Final Report

Development of Calibrated Site Amplification Models for Application in Central and Eastern North America: Collaborative Research with UCLA, UIUC, and UT

Prepared For

USGS

Under USGS/NEHRP Grant No.: G14AP00102, G14AP00103, G14AP00104

Grant Term: January 1, 2014-January 1 2016

Prepared by

Principle Investigators: Youssef Hashash, Professor, UIUC[1], hashash@illinois.edu

Jonathan P. Stewart, Professor, UCLA[2], jstewart@seas.ucla.edu

Ellen M. Rathje, Professor, UT[3], e.rathje@mail.utexas.edu

Graduate Research Assistants: Joseph Harmon, UIUC[1], harmon4@illinois.edu

Grace Parker, UCLA[2], parker@seas.ucla.edu

Boqin Xu, UT[3], boqinxu@utexas.edu

[1]UIUC
Dept. of Civil & Environmental Engineering
Newmark Civil Engineering Laboratory
2015 N Mathews Ave, Room 2230c
Urbana IL 61801

[2]UCLA
5731 Boelter Hall
Department of Civil and Environmental Engineering
Los Angeles, CA 90095-1593

[3]UT
9.227B Ernest Cockrell Jr Hall
1 University Station C1792
Austin, TX 78712-1076

September 29, 2016

CONTENTS

List of Figures

List of Tables

ABSTRACT

This report presents a suite of linear empirical and linear and nonlinear simulation-based site amplification models for Central and Eastern North America. A database of V_S measurements is collected and used to develop a geology-based V_{S30} estimation proxy procedure dependent on geologic age, prior glaciation, and topographic slope. This V_{S30} proxy procedure is used in conjunction with the NGA-East ground motion database to develop empirical linear site amplification functions conditioned on V_{S30} for glaciated and non-glaciated regions. The functional form of the linear site amplification model was guided in part by simulation results for ranges of V_{S30} where available data is sparse. A large scale study using linear, equivalent linear and non-linear site response simulations is presented. The site response simulations are developed from geologic data to capture the uncertainty and variability of site conditions of conditions representative CENA. A broad range of input ground motions representing weak as well as strong shaking expected in CENA are employed. A modular site amplification model from 1.7 million nonlinear, equivalent linear, and linear elastic 1-D site response analyses is developed with linear amplification components conditioned on V_{S30}, site natural period, and soil column depth and with nonlinear amplification components conditioned on V_{S30} and bedrock PGA and PSA. The modular nature of the model allow for the use of either the linear empirical or simulation based site amplification models in conjunction with the nonlinear site amplification model. The linear simulation based site amplification model shows strong dependency on site period in addition to V_{S30} highlighting the importance of the site period estimation.

1 INTRODUCTION

An important aspect of ground motion prediction equation (GMPE) development and in seismic design is the proper quantification of the effect of the soil site on ground motions, commonly called site effects or site amplification. Central and Eastern North America (CENA) is known as a Stable Continental Region (SCR) and GMPEs developed for SCRs have mostly been developed for hard-rock conditions which generally corresponds to rock-like shear wave velocities of $V_s > 2000$ m/s. Most available GMPEs applicable to CENA do not quantify the soft soil amplification or the effects of soil nonlinearity on site response. Site amplification is usually modeled as a sum of linear and nonlinear amplification terms as in Seyhan and Stewart (2014). The linear component site amplification is the small-strain site amplification for typically weak ground motions and a mostly linear, while the nonlinear component of site amplification occurs as a soil site exhibits strain softening, and site amplification is decreased. Current amplification functions and GMPE's that include the effect of soil amplification and nonlinearity derived from observations and simulations for the WUS may not be applicable to the geologic conditions expected in CENA. Therefore, there is a need for the evaluation of site amplification in CENA. This report develops a suite of models from simulations and empirical data for the quantification of site amplification CENA. This work is a collaborative work between the University of Illinois at Urbana Champaign (UIUC), the University of California, Los Angeles (UCLA), and the University of Texas at Austin (UT) and occurs in parallel with the development of GMPE's in the NGA-East project. This report presents the empirical linear site amplification model derivation and the development of the simulation-based site amplification models.

The development of empirical linear site amplification model is highly dependent on the V_{S30} (i.e. the time averaged shear wave velocity in the top 30 m of a soil site) of recording stations. To better constrain this site parameter, a geology-based procedure for V_{S30} estimation is developed from a database of V_S measurements in CENA. The improved estimates of V_{S30} are used with ground motion recordings to develop an empirically-based linear site amplification function.

Site response simulations have previously been used to supplement and constrain empirical site amplification models in projects such as NGA-West and NGA-West2. A large-scale parametric study of 1-D frequency-domain linear elastic (LE), frequency-domain equivalent linear (EL) and

nonlinear (NL) site response analyses is developed to produce a suite of site amplification models independent of the empirical linear models. The inputs to the 1-D site response analysis parameters are developed from data in CENA including bedrock ground motions, V_S profiles, small strain damping values, and nonlinear G/G_{max} and damping curves. V_s Profiles characteristic of CENA used in 1-D site response analyses were derived from the same database of 900 V_s Profiles from various NPP license applications and open literature used to develop the V_{S30} proxy in this study. Modulus reduction (G/G_{max}) and damping curves are quantified using the empirical model of Darendeli (2001) for using soil properties based on geological structures in CENA and are modeled with the strength-controlled GQ/H model of Groholski et. al. (2016). V_S profiles and soil nonlinear curves are randomized to consider the uncertainty and variability of CENA site conditions.

High-frequency attenuation in the Fourier Amplitude Spectrum (FAS) of S-wave acceleration can be quantified by spectral decay parameter, denoted as κ_0, and needs to be modeled to capture the high frequency response of soil sites in CENA. Input ground motions used in the analyses include a total of 246 motions, which are composed of 186 synthetic motions developed in NUREG-6729 (McGuire et al., 2001) and 61 motions generated stochastically with SMSIM (Boore, 2005) for CENA κ_0. κ_0 is well-correlated with small strain damping (D_{min}), and in this study, observations of κ_0 in CENA are used to constrain D_{min} in the 1-D simulations. In this parametric study, a total of 1.7 million LE, EL and NL site response analyses are calculated using the software DEEPSOIL. Linear site amplification is captured by the LE analyses and nonlinear amplification is captured by EL and NL analyses.

A suite of site amplification models from these analyses is developed with linear amplification components as functions of V_{S30}, natural site period (T_{nat}), and soil depth (Z), and nonlinear amplification components as functions of V_{S30} and with either bedrock peak ground acceleration (PGA) or bedrock pseudo-spectral acceleration (PSA) as the drivers of site nonlinearity.

2 PROXY-BASED V_{S30} ESTIMATION IN CENTRAL AND EASTERN NORTH AMERICA

2.1 INTRODUCTION

The Next-Generation Attenuation for central and eastern North America project (NGA-East project) developed a series of semi-empirical ground motion models (GMMs) for predicting ground motion intensity measures. These GMMs include models for earthquake source and travel path effects, and are conditional on certain site conditions (PEER 2015). All such GMMs were required to provide predictions for a reference site condition consisting of a relatively uniform shear-wave velocity (V_S) profile of 3000 m/s near the ground surface (Hashash et al., 2014). For softer site conditions, various site factors can be used that are based at least in part on the time-averaged shear wave velocity in the upper 30 m of the site (V_{S30}) (PEER 2015; Parker et al., 2016; Harmon et al., 2016). Some NGA-East GMMs do not provide a recommended site factor, but nonetheless utilize V_{S30} in connection with the definition of an alternate, softer, reference site condition of V_{S30} = 760 m/s (which is the reference value for USGS national seismic hazard maps; Petersen et al., 2016) (Yenier and Atkinson, 2015; PEER 2015). A challenge faced in the development and application of these GMMs and associated site amplification models is the lack of measured V_{S30} values at a large majority ground motion recording stations.

When no measurement of V_{S30} is available, which is the case for 94% of recording sites in the NGA-East database flatfile (Goulet et al., 2014), it becomes necessary to provide an estimate. Although it is possible to estimate site information from interpretation of recordings (Kim et al., 2016; Hassani and Atkinson, 2016), such estimates are currently possible for a relatively small number of stations due in part to requirements of multiple recordings at the same site. Moreover, a consensus has not yet emerged on the appropriateness of estimating site parameters from attributes of recordings, when the performance of the resulting GMMs are then judged against those same recordings. For these reasons, it is often necessary to estimate the logarithmic mean and standard deviation of V_{S30} via proxy methods. In the current NGA-East flatfile (Goulet et al., 2014), the considered proxies were associated with small-scale (1:2,000,000 to 1:5,000,000) geologic map categories specific to CENA (Kottke et al., 2012; hereafter Kea12), a hybrid slope-

geology proxy also derived from small-scale geologic maps for CENA (Thompson and Silva, 2013; hereafter TS13); geomorphology-based terrain categories related to V_{S30} based on data from California (Yong et al., 2012; hereafter Yea12), and a topographic gradient- V_{S30} relation developed using limited data from Memphis and Australia (Wald and Allen, 2007; hereafter WA07).

The present work was motivated by our general discomfort with the adequacy of the available proxies used to assign V_{S30} values in the development of the preliminary station database presented in Goulet et al. (2014), which was associated with the aforementioned issues of map scale and the 'borrowing' of proxies from other regions. We were also concerned with the size of the V_S data set used to evaluate proxy performance of that prior work, which was based only on measurements from ground motion stations (34 sites). With regard to geology-based proxies, we anticipate that geologic conditions identified from larger-scale maps will be more reliable, and that consideration of Wisconsin glaciation and the presence of sites in basins may influence V_{S30}. We describe below a database of sites in CENA with measured V_S, including sites with and without ground motion recording stations. We compiled geologic and terrain-based information for V_S measurement sites and query the data to develop proxy-based V_{S30} relationships. The V_{S30} assignment protocols are then updated in consideration of these results and an updated station database for NGA-East is provided as an electronic supplement (available as an electronic supplement to Parker et al. (2016)).

This report chapter is also a journal paper that has been accepted for publication in the Bulletin of the Seismological Society of America (Parker et al. 2016).

2.2 CENA V_{S30} DATABASE FROM MEASUREMENTS

We have compiled a database of 2755 VS30 values from seismic velocity measurements in CENA. We consider sites having both V_S profiles as a function of depth, and sites with only a reported V_{S30} value from measurements. The data are derived from 82 source documents including research reports, microzonation studies, and professional engineering reports for project sites (including nuclear power plants). The present database updates the earlier CENA profile database of Kea12, which had 1930 entries derived from seven source documents, and

includes many V_S profiles compiled for use in Hashash et al. (2014). A variety of measurement methods were used in developing these profiles, including downhole logging, suspension logging, and surface wave techniques. In many cases, we lacked the level of documentation required to render opinions on the relative reliability of data from different providers, and have not attempted to screen the data on this basis. Table S1, available as an electronic supplement to Parker et al. (2016), presents summary information on each entry in the database. Figure 1 shows the spatial distribution of measurement sites along with strong motion sites in the NGA-East database flatfile. There are concentrations of measurements in Ottawa, Canada, Charleston, South Carolina, and the Mississippi Embayment region.

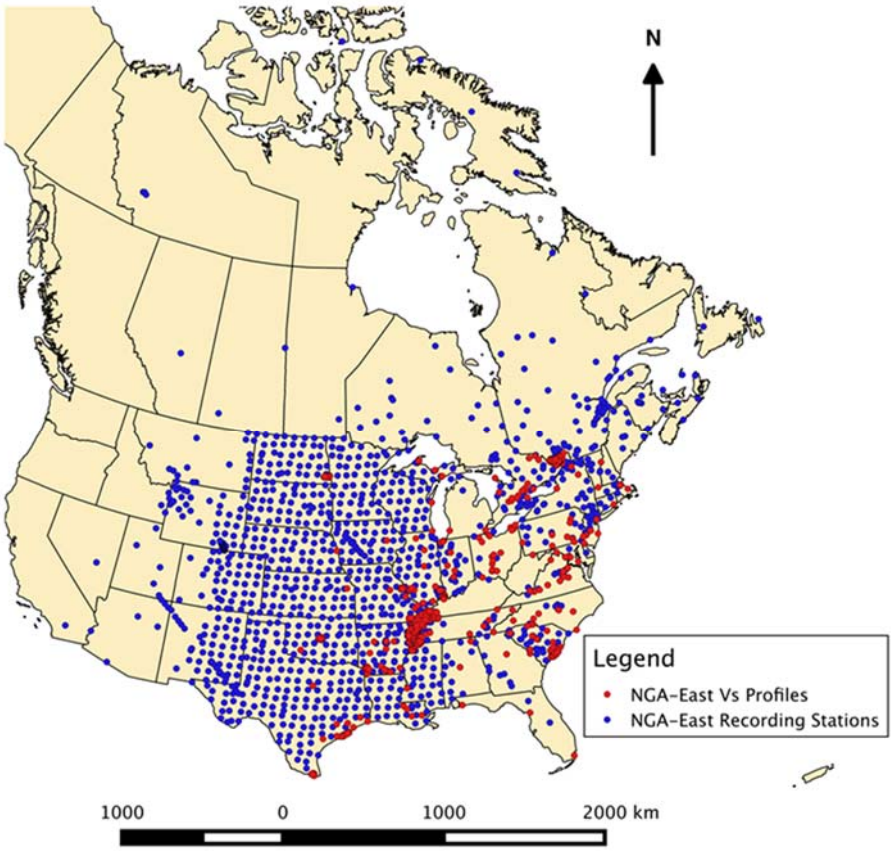

Figure 1 Locations of VS measurements in CENA included in the measurement database.

For each site in the database, we report location (latitude, longitude), measurement type, profile depth (z_p), V_{S30}, the time-averaged velocity to depth z_p (V_{SZ}), and the data source (Table S2, available as an electronic supplement to Parker et al. (2016)). Figure 2 is a histogram of

measured V_{S30} values from the database and shows that a plurality of the data sample low velocity sites (V_{S30} < 450 m/s). Concentrations of data are present in Ottawa (Canada), Charleston South Carolina, and Mississippi Embayment (1230, 326, and 535, respectively). In the earlier version of the database (Kea12), nearly all of the measurements above 450 m/s were from Ottawa (Crow et al. 2007). The present version has 583 profiles with V_{S30} > 450 m/s, 213 of which are outside of Ottawa. Due to the spatial nonuniformity of the dataset, we have considered the possibility of regional bias in VS30 values from areas with clustered profiles, as described below.

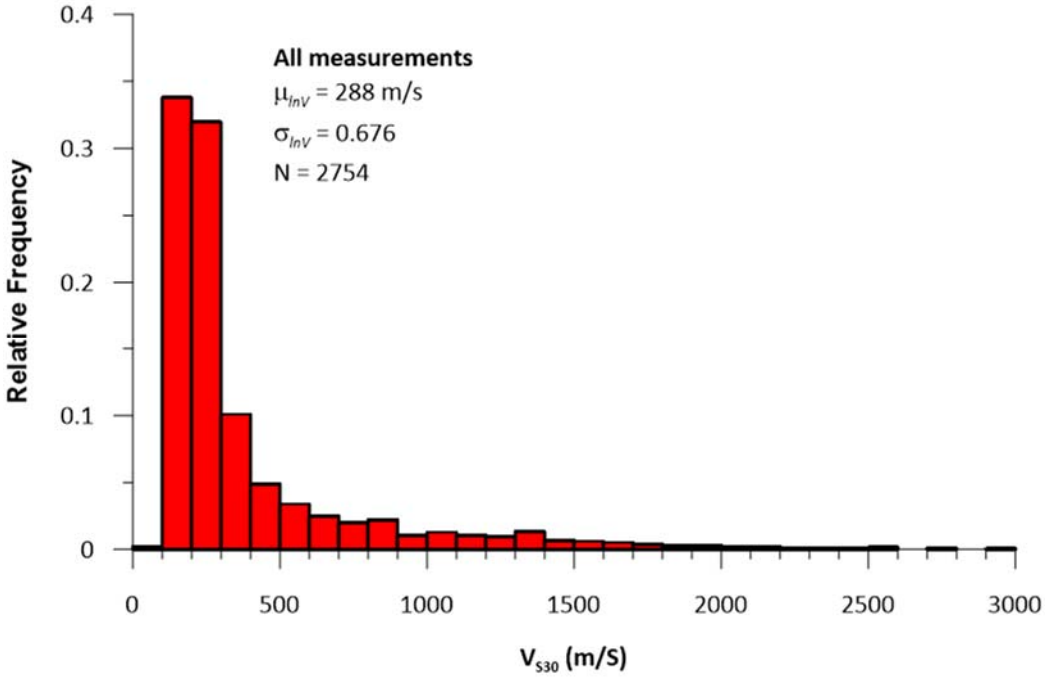

Figure 2 Histogram of all measured V_{S30} values in the CENA VS measurement database.

2.3 GEOLOGY- AND GEOMORPHOLOGY-BASED PROXIES

Information compiled for measurement sites as part of the present work includes geologic site conditions as indicated from geologic maps at larger scales than used for this application previously, an indicator of whether the profile is within the region of CENA that was overlain by the Wisconsin ice sheet during the last glaciation, indicators of whether the profiles are in various mapped basins, and indicators of whether or not the profile is in an area of data concentration (Ottawa, Charleston, or the Mississippi Embayment). In addition, geomorphology-

related parameters were compiled from digital elevation models (DEMs) at 3- and 30- arc-s resolution. The 30 arc-s DEM consists of raster files from USGS (2011); parameters compiled include geomorphic terrain categories based on procedures in Iwahashi and Pike (2007) and topographic gradient in the manner used by WA07. The 3 arc-s DEM is drawn from the NHDPlusV2 dataset (see *Data and Resources* in Parker et al. (2016)), a geospatial, hydrologic framework dataset developed with support from the Environmental Protection Agency Office of Water and the USGS. The data is available only for the contiguous U.S., and is corrected for the canopy effect. We extract topographic gradient from this DEM.

Geologic conditions were taken from geologic maps ranging in scale from 1:24,000 to 1:500,000 for locations in the United States and Canada, and from Crow et al. (2007) metadata files for locations in Ottawa, Canada. The map scale from these sources is much larger than has been used previously for proxy development (i.e., Kea12; TS13), which used 1:5,000,000 and 1:2,000,000 scale maps for the United States (Soller et al. 2009; Fullerton et al. 2003) and a 1:5,000,000 scale map for Canada (Fulton 1996). The larger scale of the maps used in the present work is expected to reduce, although not to eliminate, potential surface geology misclassifications.

Geologic maps used in this study were primarily sourced from the United States Geological Survey (USGS) national geologic map database (NGMDB; see *Data and Resources* in Parker et al. (2016)). For areas not covered by the USGS NGMDB, digital state geologic maps compiled by the USGS Division of Mineral Resources (DMR) were used. For Canada, we adopt geologic classifications from Crow et al. (2007) for Ottawa; elsewhere in Ontario we utilize the Ontario Geological Survey spatial dataset 14 (Ontario Geological Survey, 2000); and in Québec we use an online interactive map from the Sysème d'information géominière of Québec (SIGÉOM; see *Data and Resources* in Parker et al. (2016)). Table S2, available as an electronic supplement to Parker et al. 2016, provides specific map sources for each measurement site. The geologic maps sourced from the USGS NGMDB and DMR map the extent of and contacts between rock and sedimentary units, and include structural features and measurements in the area. Site-specific information compiled in the V_{S30} database (Table S2, available as an electronic supplement to

Parker et al. (2016)) includes descriptions of geologic age, geologic group, formation, and unit names where applicable, and lithologic information.

The extent of the Wisconsin glaciation was taken from Reed and Bush (2005). Any measured profile north of the extent of glaciation was given a flag of 1. Other sites to the south of the glacial limit have a flag of 0. This information was compiled because we expected glaciation to impact geologic conditions and seismic velocities in a number of ways: (1) potential overconsolidation of sediments, (2) removal of soil and weathered rock due to glacial scouring, and (3) the deposition of glacial and post-glacial sediments. We also considered the use of earlier, more extensive glacial limits (Reed and Bush 2005), but these limits affected a small number of additional sites and did not improve the predictive ability of the model.

The locations of known sedimentary basins of any age were taken from the electronic supplement of Coleman and Cahan (2012) and are listed in Table 1. The CENA V_{S30} database includes a column for basin name, where applicable. This information was compiled to enable studies of possible basin-specific biases of seismic velocities.

Table 1 Sedimentary basins, as defined by Coleman and Cahan (2012), containing measurements of V_S in CENA.

Basin Name	Number of Measurements
Appalachian Basin	34
Arkoma Basin - Ouachita Thrust Belt	2
Buried Newark Group Basins	8
Exposed Newark Group Basins	3
Forest City Basin	1
Fort Worth Basin	5
Great Smoky Mountains Rift Basin	2
Gulf of Mexico Basin	49
Illinois Basin	70
Michigan Basin	10
Midcontinent Rift	2
Mississippi Embayment	175
Reelfoot Rift	17
Rough Creek Graben	12
West Atlantic Basin	87

2.4 PROXY DEVELOPMENT METHOD

2.4.1 Grouping

The 2755 locations with measurement-based V_{S30} values were grouped by attributes to identify features that produce distinct mean V_{S30} values (taken as the exponent of the natural log mean, and denoted μ_{lnV}, which has units of m/s), standard deviations (σ_{lnV}, dimensionless), and trends with 30 arc-s slope gradient. We use the natural log of velocities because the data distribution is visually better approximated by a log-normal distribution than other distributions such as normal or beta. Attributes considered in the grouping process include geologic age, lithology, glaciation history, and location relative to known basins. Because three regions (Ottawa, Charleston, and Mississippi Embayment) have large data concentrations, we investigated statistics for these regions separately from those of otherwise similar geology to identify potentially distinct regional features.

Age was first examined by geologic era and then broken down into further subdivisions by geologic period and epoch when possible. Cenozoic was divided into Quaternary and Tertiary periods, and Quaternary was further divided into epochs: Holocene ,Pleistocene, or undivided when mapped as such (undivided indicates that the age is known to be Quaternary, but the epoch is unknown).

Well populated age bins were further broken down by lithology. This was considered for the Holocene, Pleistocene, Quaternary undivided, and Paleozoic groups. Holocene lithology bins were initially investigated for all well-populated categories (e.g. alluvial, deltaic, estuarine, eolian, marine, lacustrine, fluvial, and organic deposits); many lithology-based bins were then combined on the basis of similar statistical attributes (i.e., μ_{lnV}, σ_{lnV}, and trend with slope gradient) when possible.

The presence of Wisconsin glaciation (Reed and Bush, 2005) was investigated separately from age and lithology. Sites flagged as glaciated include locations with Holocene geology; in such cases the Holocene sediments themselves can be a product of glacial runoff, but are not subject to the overconsolidation effects of glacial unloading. By separating these sites from non-glaciated Holocene sites with similar lithology, we are in essence investigating whether the

glacially-derived sediments have unique features and possible impacts on V_{S30} of older, potentially over-consolidated layers at depth. As we look at groups that were previously glaciated compared to those that were not, we observe a significant increase in σ_{lnV}. This divergence of dispersion values was a motivating factor for considering glaciation in the formation of proxy groups along with the mean V_{S30}.

The location of a site in one of the sedimentary basins listed in Table 1 was examined to evaluate whether V_{S30} statistics for particular basin structures are distinct from otherwise similar conditions (age, lithology, glaciation).

With the many factors considered in the proxy development process, we required a systematic approach for deciding when groups or bins of V_{S30} values were statistically distinct. For this purpose, we used two types of F-tests (Snedecor and Cochran, 1989), which compare the statistical performance of submodels with that of a full model for a common data set. For example, if a full model applies to Holocene sediments, a pair of submodels could comprise glaciated and non-glaciated groups. One type of F-test uses the residual sum of squares (based on misfits from median model predictions) for the submodels (RSS_1 and RSS_2) and the full model (RSS_f). The relative performance of submodels and the full model is quantified using the difference $RSS_f - (RSS_1+RSS_2)$. If this difference is "small," then the submodels and full model fit the data about equally well, suggesting that data segregation in submodel groups is not justified. For normally distributed sets of residuals, this is interpreted using the one-way analysis of variance (ANOVA) F-statistic, which can be written as (adapted from Snedecor and Cochran, 1989; specific form used here is from Stewart et al., 2003):

$$F_1 = \frac{\left(RSS_f - (RSS_1 + RSS_2)\right) / \left((df_1 + df_2) - df\right)}{\hat{\sigma}^2} \quad (1)$$

where df_i refers to the degree of freedom for model or submodel i (one if the model consists of a simple mean, two if the model includes a slope gradient term), and

$$\hat{\sigma}^2 = \frac{RSS_1 + RSS_2}{N_f - (df_1 + df_2)} \quad (2)$$

where N_f is the number of data points in the full model. This F-statistic can be compared with the F distribution to evaluate significance level (p) for the test. Large values of p (> 0.05) are often taken to imply that the submodels are not distinct. One shortcoming of the F_1-statistic is that it does not effectively distinguish data groups having similar means but differing dispersion. For this reason, we also compute a second F-statistic (Snedecor and Cochran, 1989):

$$F_2 = \frac{\sigma_1^2}{\sigma_2^2} \tag{3}$$

for the null hypothesis that two normal populations from which samples are drawn have the same variance. As before, this statistic is compared with the F distribution and a p value is computed, which is interpreted as before (values < 0.05 indicate the sub-groups have distinct variances). If either F_1 or F_2 have p values < 0.05, the sub-groups are considered distinct.

To meet the requirement of normally populated data populations, both F-tests were performed on residuals in natural logarithmic units because V_{S30} has generally been found to be approximately log-normal (e.g., Wills and Clahan, 2006). Within each age category, alternative strategies for binning V_{S30} data were tested, with the resulting distinct sub-groups listed in Table 2. In one case (Groups 14 and 16), one of the p-values is 0.06, thus not strictly meeting the < 0.05 criteria, but are retained as distinct based on judgment driven by the different geological conditions and different means (the Group 14 mean has high uncertainty due to sparse data). At the bottom of Table 2, we also provide examples of F-test results for submodel groups that were not distinct and hence are not reflected in our recommended V_{S30} estimation procedure. Details regarding the selected groupings and the interpretation of test results are given in the *Results* section below.

Table 2 Results of F-tests performed on binned V_{S30} groups (Eqs. (1 – (3) (P = Paleozoic).

Groups*	F1	p1	F2	p2	Distinct (0) or Non-Distinct (1) Groups
1+2	4.6	<0.05	0.61	<0.05	0
1+3	6.7	<0.05	0.12	<0.05	0
1+4	54.6	<0.05	0.10	<0.05	0
2+3	0.99	0.51	0.19	<0.05	0
2+4	24.6	<0.05	0.16	<0.05	0
3+4	8.4	<0.05	0.88	0.48	0

5+6	473	<0.05	0.39	< 0.05	0
5+7	30.5	<0.05	0.30	< 0.05	0
5+8	73.2	< 0.05	0.30	< 0.05	0
6+7	55.4	< 0.05	0.77	0.24	0
6+8	33.1	< 0.05	0.77	0.25	0
7+8	2.18	< 0.05	1.00	0.98	0
9 +10	1.61	<0.05	2.05	< 0.05	0
9 +11	35.5	<0.05	1.97	< 0.05	0
10 + 11	43.6	<0.05	0.95	0.81	0
14+15	1.08	0.37	0.13	0.06	1
14+16	3.4	< 0.05	0.08	< 0.05	1
15+16	11.2	<0.05	0.64	< 0.05	0
pЄ glac. + pЄ non-Glac.	0.0017	1.0	1.20	0.68	1
P shale + P limestone	0.021	1.0	0.86	0.43	1
* See Table 3 for definition of groups					

2.4.2 Trends with Topographic Gradient

Within the various groups identified in the previous section, trends of V_{S30} with 30 arc-s topographic slope gradients (s) were investigated using semi-log, and log-log regressions:

$$ln(V_{S30}) = c_0 + c_1 s \quad (4)$$

$$ln(V_{S30}) = c_2 + c_3 ln(s) \quad (5)$$

where V_{S30} is in m/s and slope gradient s is expressed as a decimal (meters per meter). Expressions similar to Eq. (5) have been used by Thompson et al. (2014), among others.

Values of either c_1 or c_3 having zero outside the range of their 95% confidence intervals indicate statistically significant effects of gradient. When the trend with gradient is significant, either the semi-log or log-log model is selected based on visual inspection of the fit and which of the models produces lower standard deviation of residuals. In this case, the V_{S30} ln mean estimate is calculated using either Eq. (4) or (5) and the standard deviation of the fit residuals is taken as σ_{lnV}. When the trend with gradient is not significant, a gradient-independent mean is selected (μ_{lnV}).

2.5 RESULTS

Table 3 summarizes the proposed hybrid geology/slope proxy procedure for V_{S30} estimation. Rows in Table 3 are differentiated first by geologic age and the flag for Wisconsin glaciation. Within age and glaciation groups, additional sub-groups are recommended in some cases based on lithology, location, or presence within certain basins. For each sub-group, either a natural log mean and standard deviation are given or a gradient-dependent relation is given for the mean along with σ_{lnV}. Aside from geologic age, the presence (or not) of Wisconsin glaciation has the strongest effect on V_{S30} distributions, generally increasing both means and standard deviations relative to otherwise similar non-glaciated conditions. Our interpretation of the physical explanations for these trends is provided in the *Proxy Performance* section below. Additionally, V_{S30} values calculated from profiles in Ottawa differ significantly from the rest of the data across all age groups. When possible, data from Ottawa within an age group were used to create a separate recommended V_{S30} value for that region. Profiles in the Charleston and Mississippi Embayment regions were analyzed separately for comparison against the remaining data set. However, they did not differ in a statistically significant manner from otherwise similar sites, and are not considered as a separate category. Results and recommendations are described in more detail below for geologic age groups.

Table 3 Summary of proposed V_{S30} estimation procedures based on large-scale geologic maps, Wisconsin glaciation, location of site in a basin, and topographic gradient (C for Cenozoic; Q for Quaternary; H for Holocene; Pli for Pleistocene; U for undivided; T for Tertiary; M for Mesozoic; P for Paleozoic, pЄ for Precambrian).

Category							Group Moments		Gradient Relationship				
Group	Era	Period	Epoch	Wisconsin Glaciation?	Other Criteria	N	μ_{lnV} (m/s)	σ_{lnV}	Semi-Log		Log-Log		σ_{lnV}
									c_0	c_1	c_2	c_3	
1	C	Q	H	No	Alluvium, fluvial, & deltaic	308	210	0.23					
2	C	Q	H	No	All other lithology	183	221	0.29					
3	C	Q	H	Yes	In Ottawa, Canada	981	232	0.67	5.38	9.30			0.67
4	C	Q	H	Yes	Not in Ottawa, Canada	51	308	0.72			7.47	0.295	0.67
5	C	Q	Pli	No		284	271	0.36	5.47	31.4			0.31
6	C	Q	Pli	Yes	Till in Ottawa, Canada	104	777	0.57	6.51	22.4			056
7	C	Q	Pli	Yes	Other in Ottawa, Canada	60	377	0.65			7.20	0.22	0.63
8	C	Q	Pli	Yes	Not in Ottawa, Canada	63	448	0.65					
9	C	Q	U	No	Not in sedimentary basin	154	296	0.43			6.21	0.096	0.41
10	C	Q	U	No	In sedimentary basin	151	280	0.29					
11	C	Q	U	Yes	Not in sedimentary basin[1]	66	209	0.31	5.28	24.7			0.29
12	C	T				111	315	0.31			6.07	0.059	0.30

13	M					20	822	0.68					
14	P				In the Illinois Basin[2]	5	513	0.23					
15	P			No	Not in the Illinois Basin	96	684	0.61					
16	P			Yes	Not in the Illinois Basin	76	972	0.77					
17	pЄ					37	699	0.85					
18	pЄ				Site visit- hard rock confirmation		2000						

[1] Can be applied for within-basin sites with increased epistemic uncertainty (category unpopulated)

[2] Because of the small population size, the mean and standard deviation carry a larger degree of epistemic uncertainty than for other groups

2.5.1 Holocene

Of 2755 V_{S30} values from measurement, 1523 are classified as Holocene. The Holocene sites were subdivided into previously glaciated and not previously glaciated bins. The Holocene non-glaciated bin was subdivided further on the basis of lithology, with one group consisting of alluvial, fluvial, and deltaic deposits, and a second group consisting of all other lithologies (Groups 1 and 2, respectively). Figure.3a-b show that the V_{S30} histograms for these groups have non-similar means and standard deviations, which are confirmed as statistically distinct by the F-test results in Table 2. Figure 4a-b show that these groups exhibit no trend with gradient, so the recommended V_{S30} for each was taken as μ_{lnV} of the binned V_{S30} values.

The Holocene previously glaciated bin is subdivided based on location (Ottawa vs. other locations – Groups 3 and 4, respectively). Histograms for Groups 3 and 4 (Figure.3c-d) show much higher dispersion than those for Groups 1 and 2 (Figure.3a-b) and slower velocities in Ottawa (Figure.3c) than non-Ottawa locations (Figure.3d). Both Groups 3 and 4 have a statistically significant trend with gradient (Figure 4c-d). As will be discussed further below, the high dispersion in glaciated groups is a persistent feature of the data, the interpretation of which is given in the *Proxy Performance* section below.

Factors found to not be impactful for the Holocene age group included the presence of sites in sedimentary basins (Table 1) and location within Charleston or the Mississippi Embayment. These factors are considered for all other age groups as well, and are only commented on below when bins are well populated and a dependence was identified.

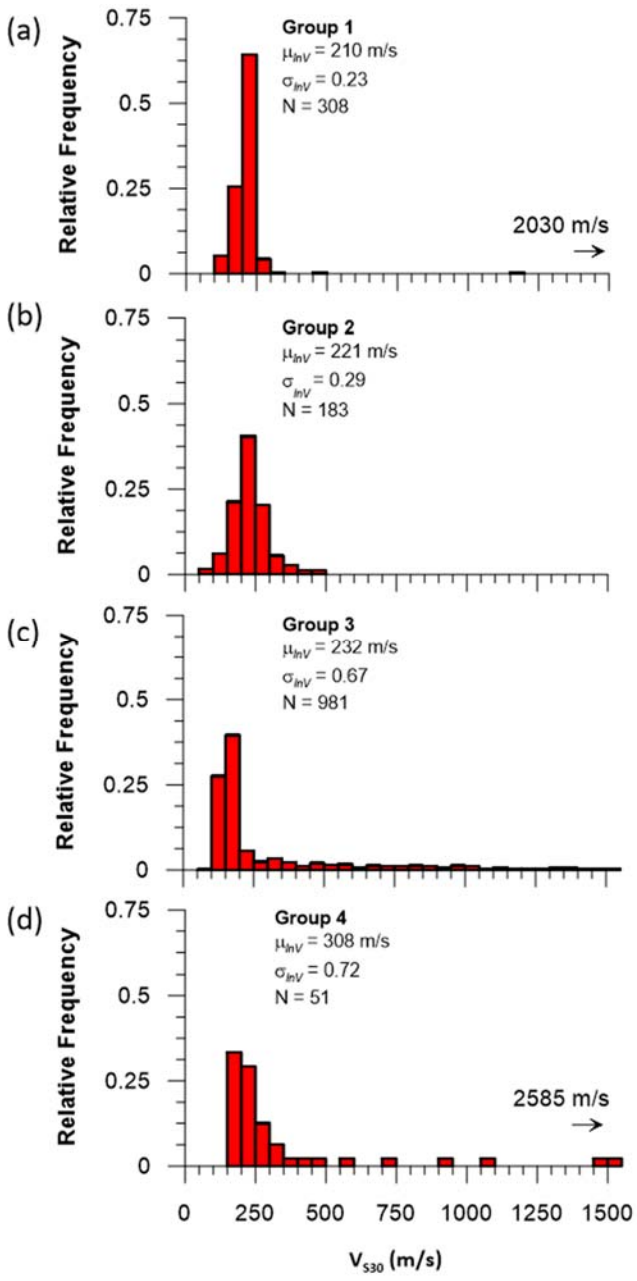

Figure.3 Histograms of V_{S30} values for Groups 1 through 4 (see Table 3).

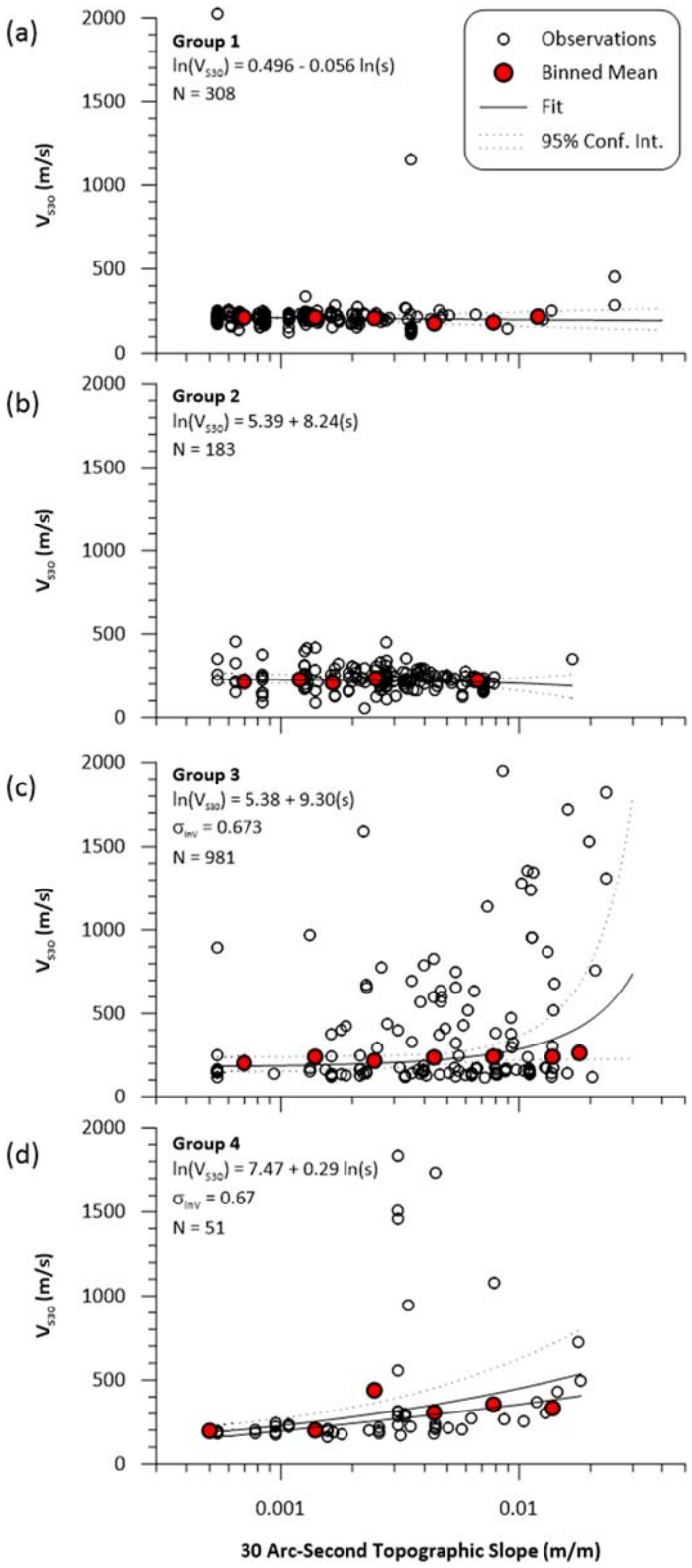

Figure 4 V_{S30} as a function of 30 arc-s topographic gradient for Groups 1 through 4 (see Table 3).

2.5.2 Pleistocene

The Pleistocene age bin contains 511 V_{S30} values from measurements, and is subdivided into previously non-glaciated locations (Group 5), locations in Ottawa (all previously glaciated, Groups 6-7), and glaciated locations outside of Ottawa (Group 8). The measurements in Ottawa were further divided by lithology, with Group 6 being for measurements on till, and Group 7 encompassing all other lithologies. Figure 5a-d show histograms for these groups, with the glaciated groups clearly having higher dispersions. Figure 6a-d show V_{S30} trends with gradient, which are not significant for Group 8, but are for the other three Pleistocene groups. This relationship is described using Eq. (4) for Groups 5 and 6, and Eq. (5) for Group 7.

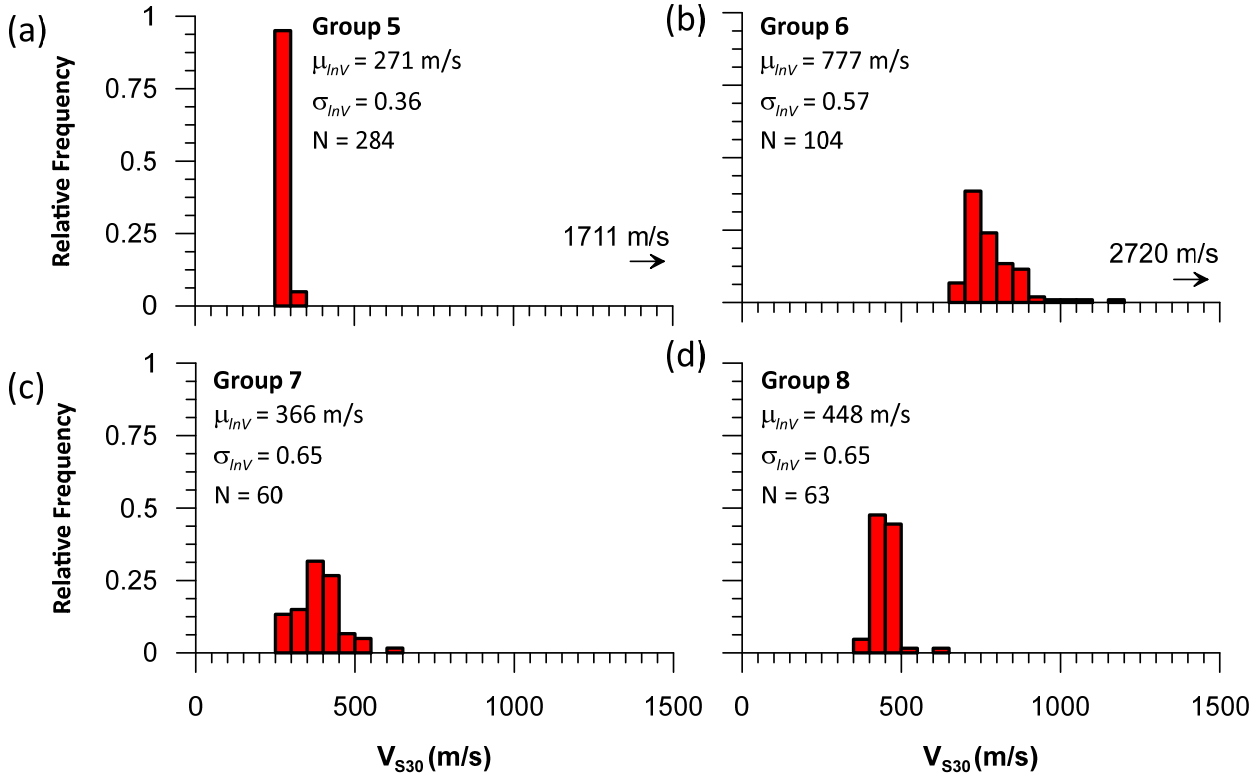

Figure 5 Histograms of V_{S30} values for Groups 5 through 8 (see Table 3).

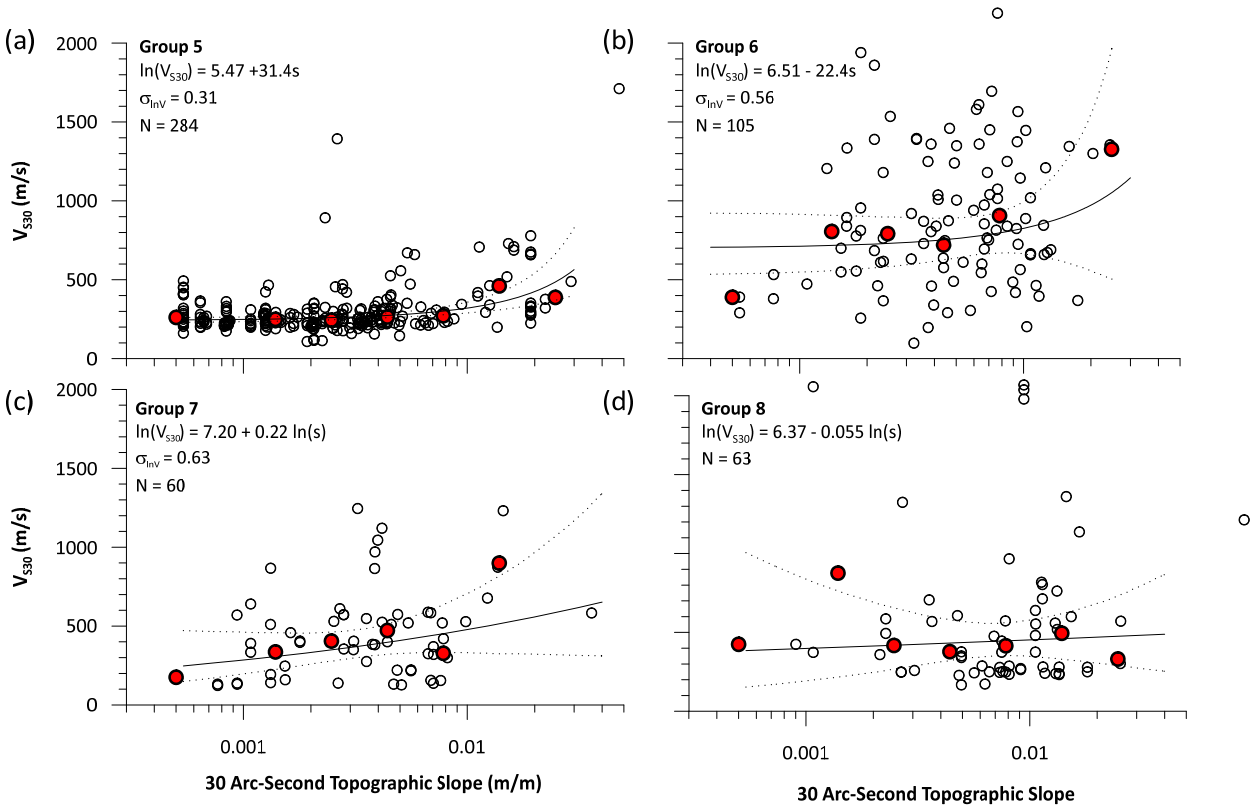

Figure 6 V_{S30} values as a function of 30 arc-s topographic gradient for Groups 5 through 8 (see Table 3). Legend from Figure 4 applies.

2.5.3 Quaternary Undivided

The Quaternary undivided (QU) age bin contains 371 V_{S30} values. This age bin was subdivided into groups based on previous glaciation, and whether or not the profile was measured in a mapped basin (Table 1). Of the four possible bins, one is not populated (previously glaciated and in-basin). Figure 7a, c and e show V_{S30} histograms for Groups 9 – 11, and Figure 7b, d and f show the gradient relationships for the same groups. Group 10 did not display a significant gradient relationship, whereas the gradient relationships in Groups 9 and 11 were fit using Eq. (5) and Eq. (4), respectively. For application purposes we recommend using the Group 11 estimates for previously glaciated basin sites.

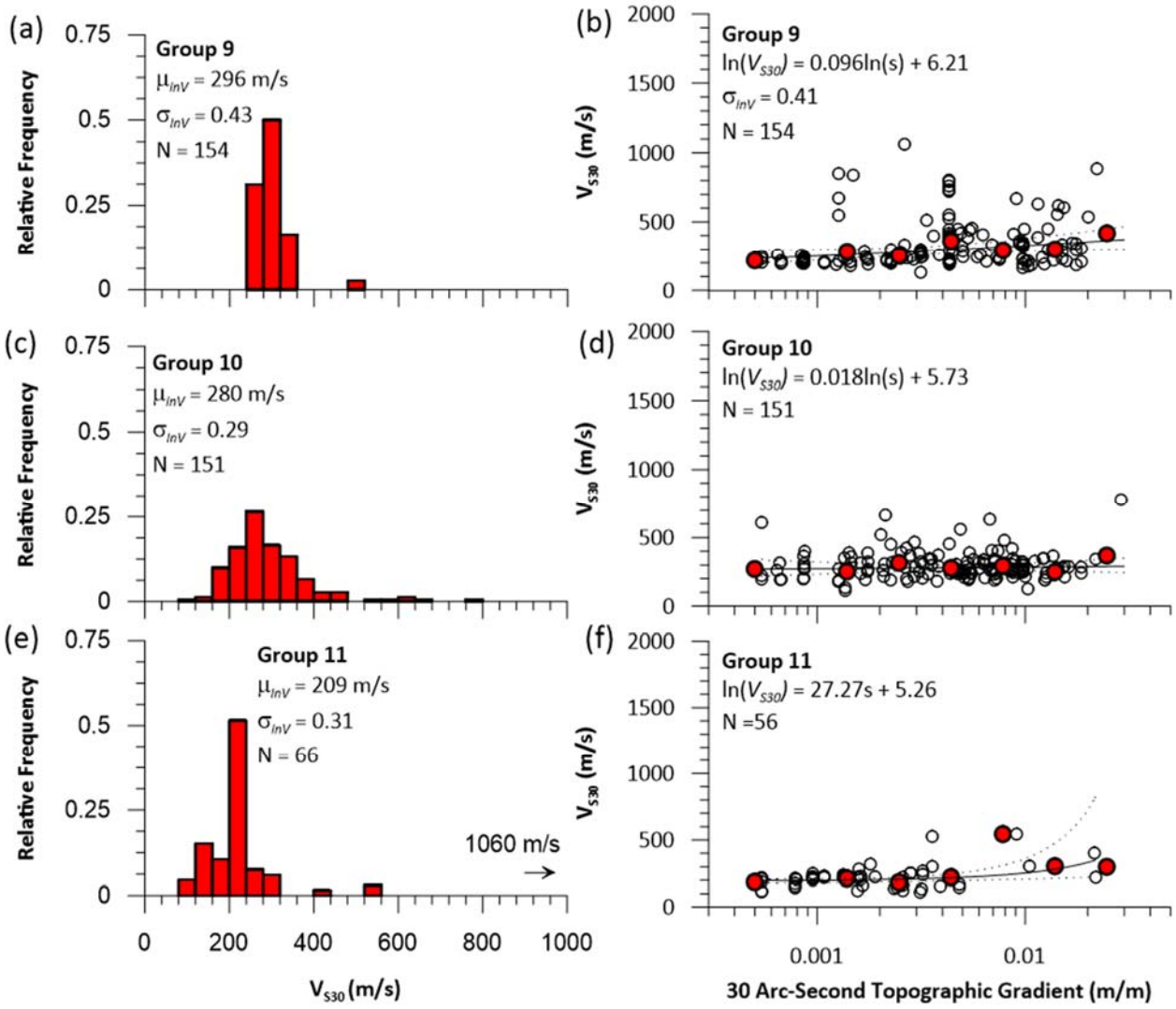

Figure 7 (a, c, e) Histogram of V_{S30} values for Groups 9 through 11 (Table 3), and (b, d, f) V_{S30} values as a function of 30 arc-s gradient for Groups 9 through 11 (Table 3), with binned means shown as filled circles. Legend from Figure 4 applies.

2.5.4 Tertiary and Mesozoic

The Tertiary age group (Group 12) contains 111 V_{S30} values, and is not subdivided further because sub-groups would be too sparsely populated. Figure 8a shows the V_{S30} histogram for Group 12, and Figure 8b shows the gradient-dependence, which is fit using the log-log relation (Eq. (5)). The CENA category statistics for Tertiary (μ_{lnV} = 315 m/s and σ_{lnV} = 0.31) indicate slightly lower velocities than multiple Tertiary categories in California (Wills and Clahan, 2006), and similar dispersion levels to those in California. The Tertiary sites in our CENA V_{S30} from

database are not glaciated, and the modest dispersion in this case appears to result from deep weathering profiles that avoids the presence of thin soft layers over firm deeper layers, which accentuates data variability.

Figure 9a shows a histogram for the Mesozoic age group (Group 13), which contains only 20 V_{S30} values from measurements. The CENA statistics for Mesozoic (μ_{lnV} = 822 m/s and σ_{lnV} = 0.68) indicate faster velocities with more dispersion than Mesozoic sites in active tectonic regions [e.g., the Franciscan complex in California has μ_{lnV} = 710 m/s and σ_{lnV} = 0.43 (Wills and Clahan, 2006); Mesozoic sites in Greece have μ_{lnV} = 590 m/s and σ_{lnV} = 0.38; (Stewart et al., 2014)]. While Mesozoic sites in our database are not glaciated, the relatively large database appears to be associated with thin, soft surficial layer effects that occur within this category (further discussion in *Proxy Performance*, below).

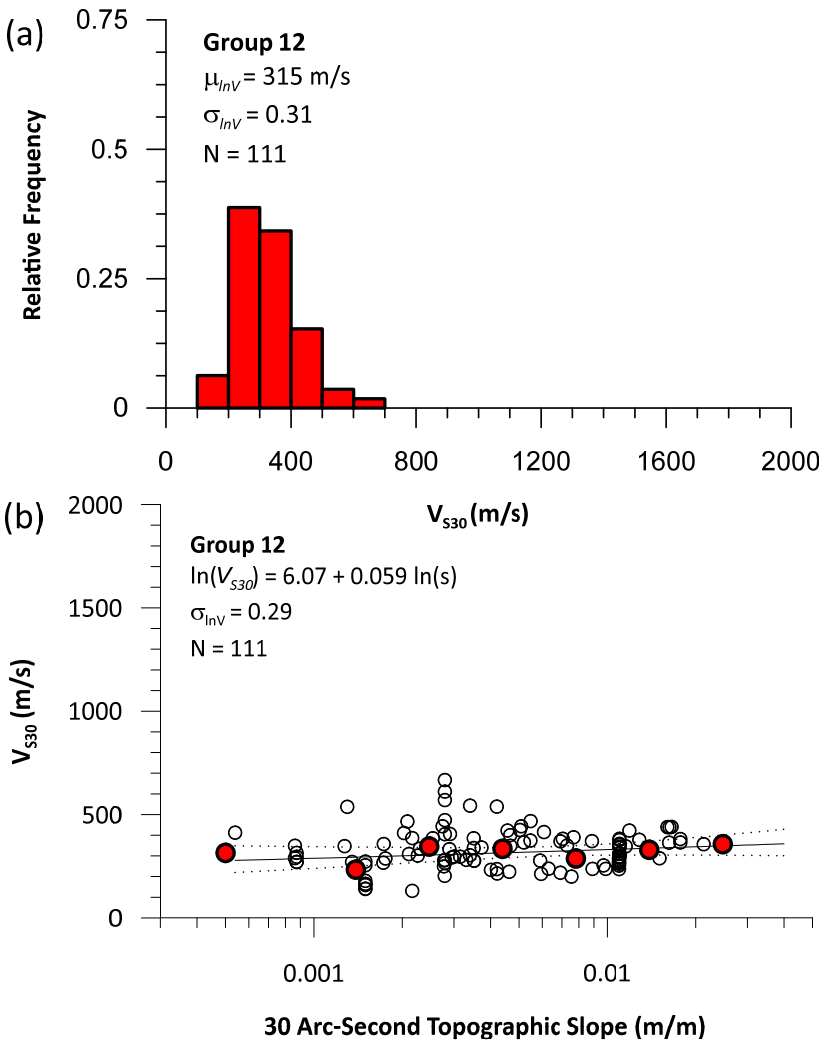

Figure 8 (a) Histogram of V_{S30} values in Group 12 (Table 3), and (b) V_{S30} as a function of slope for profiles in Group 12 (Table 3). Legend from Figure 4 applies.

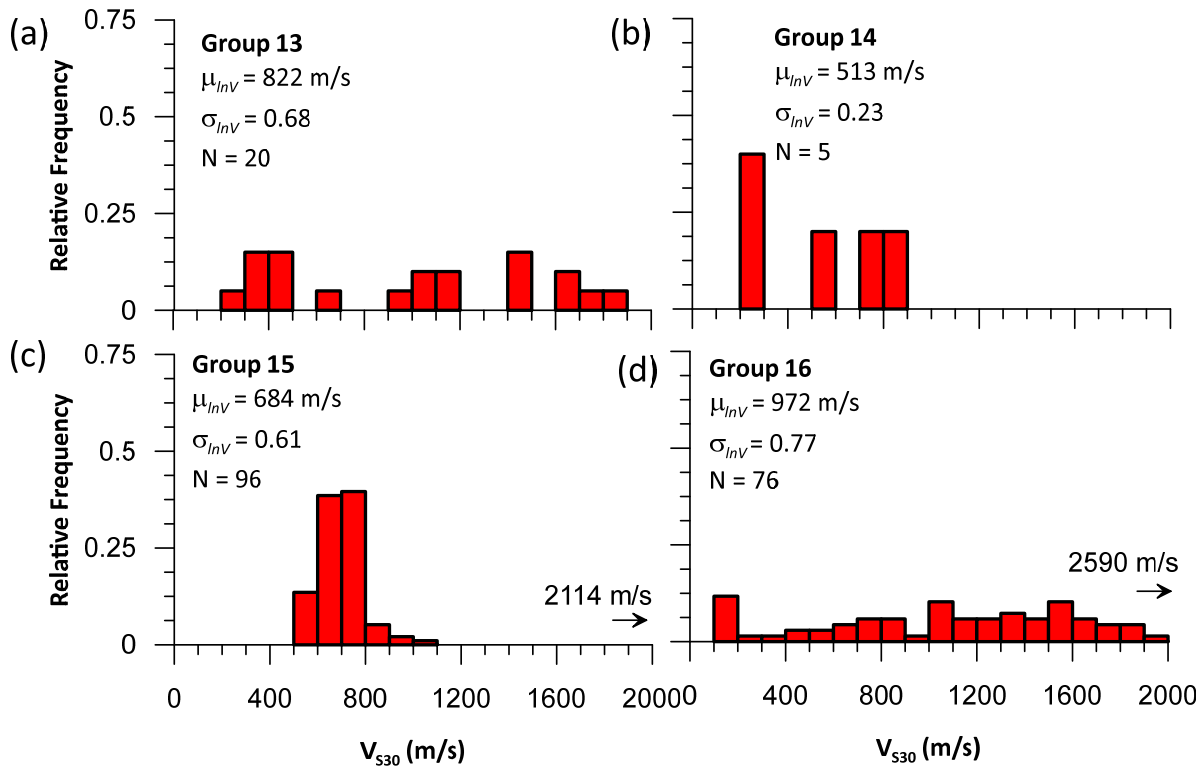

Figure 9 Histograms of VS30 values for (a) Group 13, (b) Group 14, (c) Group 15, and (d) Group 16.

2.5.5 Paleozoic

The Paleozoic age bin contains 177 V_{S30} values, and is subdivided into three groups (Groups 14-16) as shown in Figure 9b-d. Group 14 (Figure 9b) consists of Paleozoic sites in the Illinois Basin (Coleman and Cahan, 2012) and is only populated by 5 measurements. However, the log mean V_{S30} for this group is significantly lower than that of Groups 15-16 (μ_{lnV} = 513 m/s) and thus is retained as a separate group. Because Group 14 is so poorly populated, there is large epistemic uncertainty in its category mean and standard deviation. Groups 15-16 are divided in accordance with glaciation status (Figure 9c-d), and have μ_{lnV} = 684 m/s and μ_{lnV} = 972 m/s, respectively. Other basin structures (besides the Illinois basin) were not found to affect Paleozoic bin statistics. Trends with slope gradient are not significant for Paleozoic sites and hence the recommended models are reported in Table 3 as μ_{lnV} and σ_{lnV} values only.

We suspect that the velocities in Groups 14-16 are affected by a number of issues, as we would expect intact Paleozoic bedrock to have a higher shear wave velocity than those reported in Table 3. One explanation is that Paleozoic residuum, or bedrock that has weathered in place, was included in this category (as mapped by Palmer 2006). Additionally in some cases, the geologic mapping may not be recognizing a thin layer of younger, softer sediments overlying the Paleozoic materials that is affecting the value of V_{S30}. Nonetheless, we do not remove these sites from our statistical analyses for two reasons: (1) we do not have independent confirmation of the presence of non-Paleozoic sediments at these sites and (2) such potential misclassifications are inherent to the use of geologic maps (and other proxies as well), and because such misclassifications are also unavoidable for forward application, they need to be reflected in group statistics until more refined geologic site classifications become available.

2.5.6 Precambrian

The Precambrian age bin contains 37 V_{S30} values (Group 17). Figure 10 shows the histogram of V_{S30} obtained at Precambrian sites. The glaciated and non-glaciated measurements within Group 17 were determined to be non-distinct and hence were kept as a single group (Table 2 and Table 3). We suggest using Group 17 when the location in question is mapped as Precambrian bedrock, with no site visit by a geologist having taken place. If a site visit has taken place, and the mapped Precambrian bedrock is confirmed to be outcropping at the site, we suggest using a V_{S30} of 2000 m/s (Group 18, Table 3), which is based on measurements at sites with geologic conditions of this type in Ottawa city and Quebec Province (Assatourians, personal communication, 2011; based on Atkinson and Mereu, 1992).

For Group 17, there are some V_{S30} values that do not seem physically reasonable (e.g. $V_{S30} < 300$ m/s). This is a consequence of using mapped geology as a proxy for V_{S30} from measurement, as discussed in the previous section. The effects of these complexities are reflected in the large natural log standard deviation associated with the proxy estimates ($\sigma_{lnV} = 0.85$), the causes of which are discussed further in the next section.

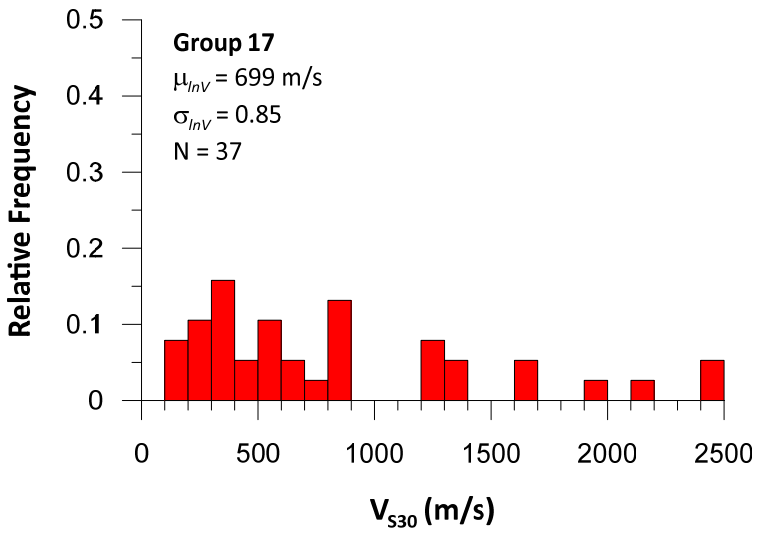

Figure 10 Histogram of VS30 values from Group 17 measurements.

2.6 PROXY PERFORMANCE

Proxy-based estimates of V_{S30} were assigned to the 2755 profiles in the database using the protocols summarized in Table 3. Residuals in natural log units were calculated as:

$$R_i = \ln(V_{S30})_i - \overline{ln(V_{S30})_\iota} \tag{6}$$

where $\ln(V_{S30})_i$ is the natural log of the V_{S30} calculated from the geophysical profile i, and $\overline{\ln(V_{S30})_\iota}$ is the proxy-based estimate for profile i (the overbar indicates that the mean is taken in natural logarithm units). Means and log standard deviations of the residuals can be computed for particular geologic conditions or for the data set as a whole; in the present case the means are expected to be near zero because the performance is evaluated using the same data set used in model development. Hence, our primary interest is in the standard deviation, σ_{lnV}.

Figure 11 shows histograms of the residuals for all profiles, previously glaciated profiles, and non-glaciated profiles. The metrics for overall proxy performance are μ_{lnV} = 0.0016 and σ_{lnV} = 0.533 (comparisons to results of other proxies are given in the next section). An important outcome of the present work is quantification of the effect of glaciation on dispersion. Non-glaciated sites have relatively modest overall dispersion (0.357) that is significantly lower than has been found previously for CENA, but which is comparable to overall proxy dispersions for

active tectonic regions (Seyhan et al., 2014). The σ_{lnV} for glaciated regions is much higher at about 0.656. Hence, the predictability of V_{S30} is better for non-glaciated than for glaciated sites. We suspect that the relative dispersion levels are caused by large impedance contrasts within the upper 30 m of glaciated sites, as seen in numerous V_S profiles measured in CENA. These sites presumably have had weathered geologic materials removed by glacial scour, with the remaining material being relatively competent and comprising the portions of the profiles below a strong impedance contrast. The relatively soft materials above the contrast have likely been laid down during or after glaciation. For sites of this type, V_{S30} is strongly correlated to the depth of materials above the impedance contrast, and because these depths are highly variable, the V_{S30} values too are strongly variable. In the absence of glaciation, sites are less likely to have these strong impedance contrasts, which could explain why the CENA proxy dispersions are comparable to those found in non-glaciated active regions. Moreover, among the non-glaciated sites, dispersion increases with age from about 0.23 for Holocene to 0.31 for Tertiary.

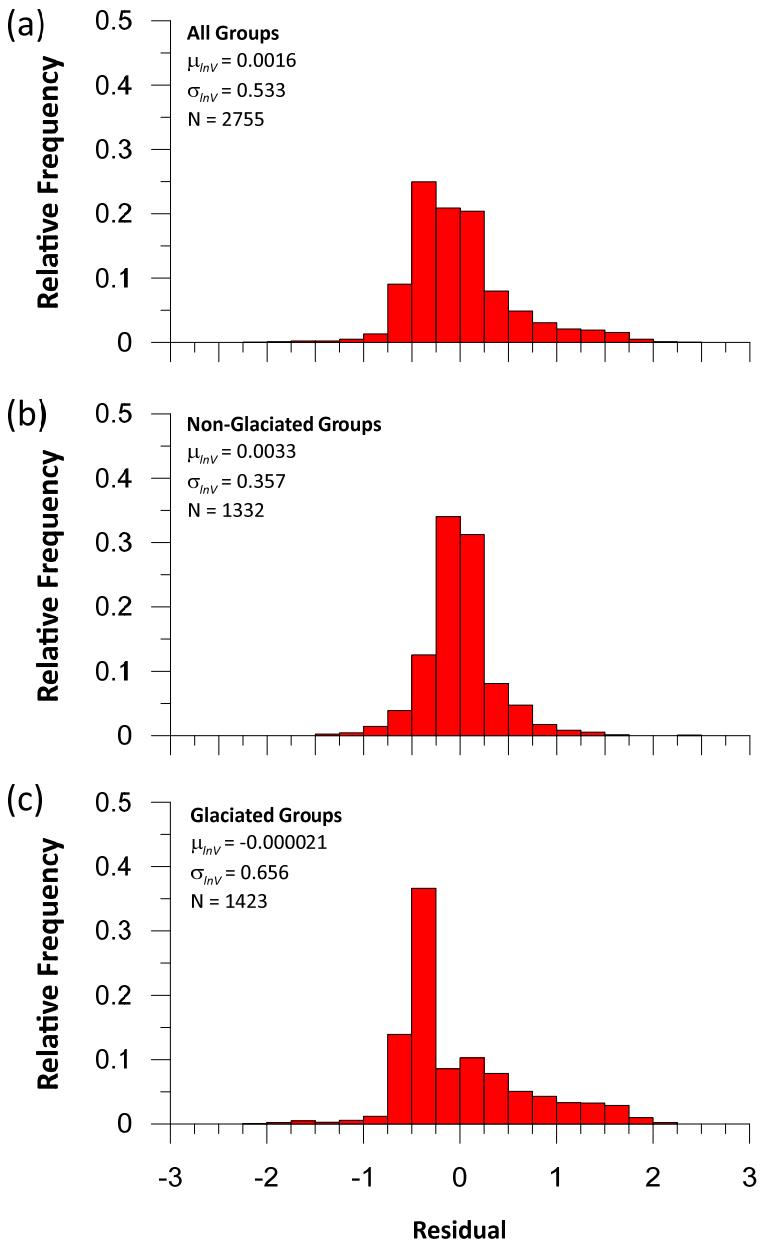

Figure 11 Comparison of residuals of V_{S30} for (a) all groups, (b) non-glaciated groups, and (c) previously glaciated groups.

Figure 12 plots residuals against 30 and 3 arc-s gradients. The 3 arc-sec gradient data capture higher resolution topography and thus include larger values of topographic slope. Results for 30 arc-s (Figure 12a) show minimal trends for gradients $\geq 3\times10^{-3}$ m/m, which is expected because

30 arc-s gradient was considered in model development. Residuals for 3 arc-s (Figure 12b) are comparable to those for 30 arc-s, with little bias. Plots similar to those in Figure 12b, but using data only for specific categories that exhibit a significant gradient effect when using 30 arc-s DEM (not shown) generally exhibit no residual trends. Hence, we conclude that our proposed hybrid-slope proxy captures gradient effects at either 30 or 3 arc-s resolution, and that the 3 arc-s gradients do not provide more predictive power than 30 arc-s gradients.

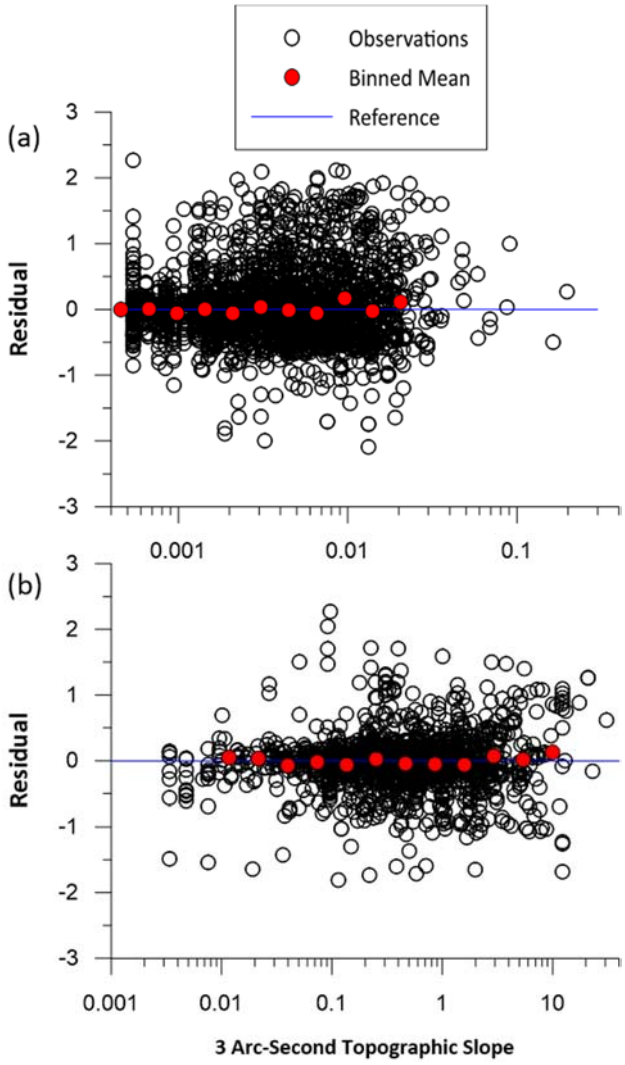

Figure 12 Proxy residuals as a function of (a) 30 arc-s topographic gradient for all measurements, and (b) 3 arc-s topographic gradient for measurements in the US, showing the binned mean of residuals as filled circles and a reference line at 0.

2.7 COMPARISON TO PRIOR WORK

As described previously, several proxy-based V_{S30} estimation procedures pre-date this work. To provide a consistent basis for comparing the proposed approach with prior relationships, we compute residuals using Eq. (6) for database sites, with the prior proxy relationships applied as published. As described in the *Geology- and Morphology-Based Proxies* section, information required to exercise each of these proxies is provided as metadata in the measurement database. The proxy relationships used in these analyses were:

a) WA07, which uses topographic gradient at 30 arc-s resolution.

b) Yea12, which uses terrain classes (site look-ups provided by A. Yong, 2012, pers. communication).

c) TS13 hybrid slope-geology using small-scale geologic maps (predicted V_{S30} values provided by E. Thompson, 2014, pers. communication).

d) Kea12 small-scale geology.

Model bias is estimated from the mean of the residuals (μ_{lnV}) and dispersion from the standard deviation of residuals (σ_{lnV}), which are evaluated over the entire set of residuals. The best-performing proxies will have relatively small biases (low μ_{lnV}) and low standard deviations. We should note here that our model was developed to best fit the dataset used for comparisons, whereas the other proxies (a-d) were not.

Figure 13 shows values of μ_{lnV} and σ_{lnV} for each proxy, including the proposed approach. All four of the previous proxy relationships have a negative bias, indicating that they overpredict the measured V_{S30} values. The Kea12 surface-geology based proxy has the lowest σ_{lnV} of 0.592, but a bias of -0.282. The WA07 ground slope based proxy has the lowest bias of -0.064, but a relatively large σ_{lnV} of 0.677. The proposed approach is unbiased (as expected), and has an overall σ_{lnV} of 0.533, which is modestly reduced from the lowest σ_{lnV} found from earlier proxies (0.592 for Kea12). The level of dispersion reduction is greater for the other proxy relations.

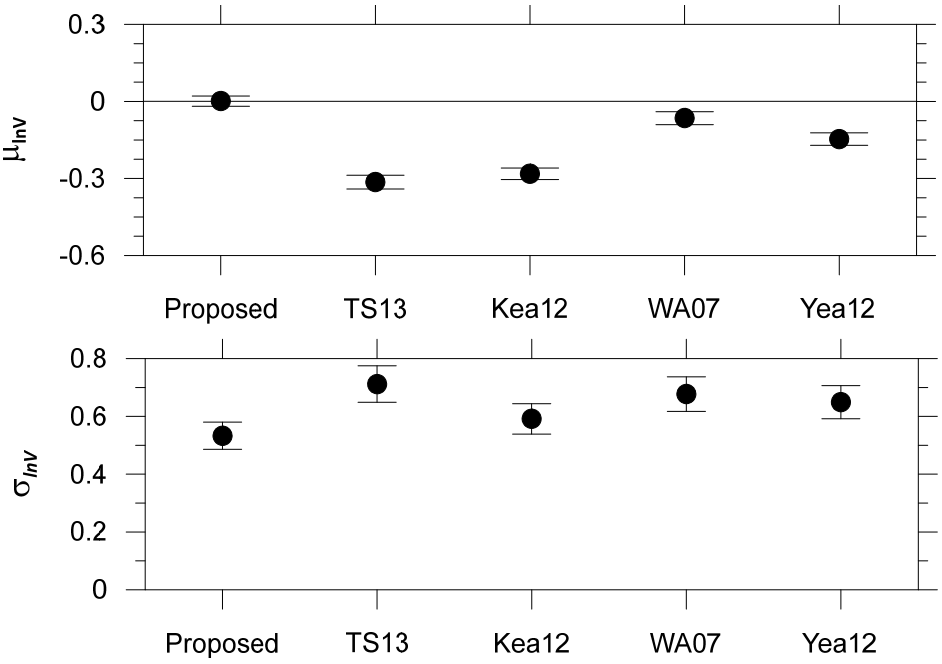

Figure 13 Comparison of log mean (top) and standard deviation (bottom) of residuals with 95% confidence intervals for existing and proposed V_{S30} proxies (TS13 = Thompson and Silva (2013); Kea12 = Kottke et al. (2012); WA07 = Wald and Allen (2007); Yea12 = Yong et al. (2012).

The similarity of the σ_{lnV} values for the Kea12 and proposed approaches suggest that either approach could be applied in forward applications. However, we propose that our method should replace Kea12 because it better distinguishes between the effects of glaciation and non-glaciation (rather than glacially-derived sediments, which can be deposited outward of glacial limits), which as discussed previously has a significant impact on σ_{lnV}. Moreover, we have more confidence in the present larger-scale surface geology assignments that we have made than in previous assignments from small-scale maps. To illustrate the significance of the geologic mapping source, we show in Figure 14a a plot of V_{S30} against topographic gradient for seemingly similar geologic categories that are well populated: the major unit of young non-glacial sediments (YN) from Kea12 [which includes alluvium (YNa), colluvium (YNc), loess (YNl), lacustrine, marine and marsh (YNm) and beach, dune, and sheet sands (YNs)], and the Holocene non-glaciated (HNG) category in the present work (encompassing all observed lithologies, Groups 1 and 2 in Table 3). The YN category in Kea12 encompasses non-glaciated sediments

from late Pleistocene and younger, whereas the HNG category in this work excludes Pleistocene conditions, only including sites with geology 11,000 years and younger. The Kea12 bin has a wide range of V_{S30} (100 to 1000 m/s) for gradients ranging from 0 to 0.1. In contrast, the HNG category in the present work has narrower ranges of V_{S30} (100 to 500 m/s) and gradient (0 to 0.02). The differences in the data are such that a strong trend of V_{S30} with gradient is present in the Kea12 category, but no trend is observed using the presently defined HNG category. Figure 14b shows trends of data residuals from both groups (computed using Eq. (6) against topographic gradient; in the case of Kea12, YNc and YNl sites are excluded from the residuals calculations due to lack of estimated mean velocities, which removes many of the highest velocity sites. The trends in Figure 14b show a trend of Kea12 residuals with topographic gradient that is not present for HNG. Moreover, the dispersion (σ_{lnV}) is lower using the present approach (0.25 as compared to 0.30 from Kea12). Our conclusion is that in this case, as in others not shown for brevity, the proposed approach based on larger-scale geologic maps better differentiates V_{S30} as represented by within-category μ_{lnV}, σ_{lnV}, and trend with gradient.

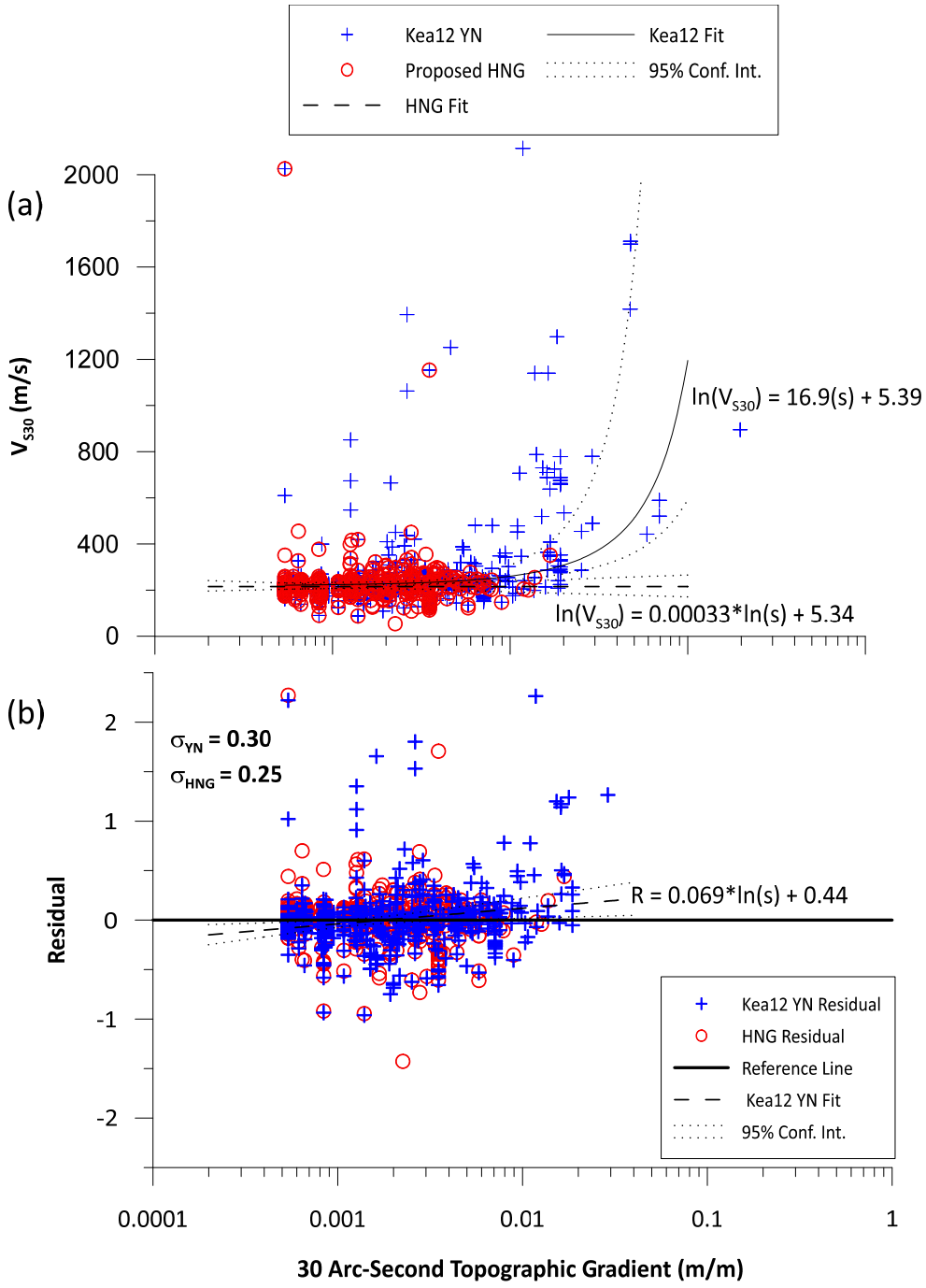

Figure 14 (a) Comparison of V_{S30} as a function of topographic gradient for the Kea12 young non-glacial (YN) category (including all sub-categories), and the Holocene non-glaciated (HNG, encompassing Groups 1 and 2) categories from the present work. Lines of best fit (Eqs. (4), (5)) are shown for both groups. (b) Comparison of residuals as a function of topographic gradient for the Kea12 YNa, YNm, and YNs categories, and the Holocene non-glaciated (HNG, encompassing Groups 1 and 2) categories from the present work.

A disadvantage of the mapping approach adopted herein is that we cannot create a map like Figure 7 of Kea12 or Figure 5 of TS13 that shows the geologic conditions across CENA. Both Kea12 and TS13 started with one continuous map source and assigned a V_{S30} value to each map unit or combinations of map units. However, this is not practical with present resources using the larger-scale maps because they are not continuous across CENA and map units are not consistently-defined across map resources. Moreover, the majority of mapped geologic units are not available as shape files that can be imported to geographic information system (GIS)-based mapping software.

2.8 IMPLEMENTATION

Best practices in site characterization are to develop full V_S profiles (extending to rock) derived from seismic data. When it is necessary to estimate V_{S30} for sites lacking such data, we have applied the P-wave seismogram method (Kim et al., 2016) when sufficient ground motion recordings are available (relationships between the frequency of the peak in horizontal-to-vertical spectral ratios and V_{S30} are an alternate approach, but have not been applied here; Hassan and Atkinson, 2016), and otherwise apply the proxy relationships in this paper. For application to V_{S30} assignments in the NGA-East station database (Table S2, available as an electronic supplement to Parker et al. (2016)), we applied the protocols below (listed in order of preference), which update those given in Section 5.5 of Goulet et al. (2014):

0. Assign mean V_{S30} from measured V_S profiles. Standard deviation taken as σ_{lnV}=0.1 per Seyhan et al. (2014).

1. Assign mean V_{S30} from known site conditions and geology based on measurements of V_S profiles at different location but the same geological condition. This assignment is only used based on a recommendation or site visit from a geologist. Standard deviation taken as σ_{lnV}=0.3, as per Goulet et al. (2014).

2. Estimate mean V_{S30} by P-wave seismogram method (Kim et al., 2016) for sites having multiple ground motion recordings and corresponding V_{S30} values from measurements. Standard deviation is taken as 0.456.

3. Estimate by hybrid slope-geology proxy developed in this paper. Mean and standard deviation taken from Table 3.

The numbers in the above list are codes provided in the station database. Of the 445 sites in the flatfile recommended by the NGA-East Technical Integration team for GMM development, 53 (12%) are Code 0 (on-site VS profile measurement), 77 (17%) are Code 1 (V_{S30} assigned after a site visit by a geologist), 10 (2%) are Code 2 (from P-wave seismogram method), and 305 (69%) are Code 3 (assigned based on the protocols in this paper).

2.9 CONCLUSIONS

Because the overwhelming majority of seismic recording stations in CENA lack measured V_S profiles, the estimation of the site parameter V_{S30} is critical for the application of strong motion data during GMM development and in the ongoing process of developing site factors. Preliminary estimates of V_{S30} were provided in the NGA-East data report (Goulet et al., 2014), which are updated herein.

We compiled a database of V_{S30} values obtained from measured V_S profiles that was not utilized in the preliminary V_{S30} assignments. When predictions from pre-existing proxy relationships are compared to the V_{S30} values in this database, significant bias and large dispersion is found, which partly motivated the present work. We compiled geologic information from larger-scale maps, supplemented by mapping that indicates glaciation/non-glaciation and the presence of sedimentary basins, which forms the basis for the present recommendations. None of this information was utilized in the development of the previous proxy relations (Kea12, TS13, WA07, Yea12).

Table 3 presents coefficients needed to apply the recommended proxy relationship. Some geologic categories take the mean V_{S30} as a simple category natural log mean, whereas others take the mean from a gradient-based model specific to the category using Eqs. (4) or (5). Values

of σ_{lnV} to accompany each mean estimate are given in Table 3. These estimates are used when more reliable, site-specific information is unavailable, as given by the implementation procedures in the previous section.

An important outcome of the present work is quantification of the effect of glaciation on dispersion. Non-glaciated groups have dispersions that are significantly lower than has been found previously for CENA (0.357), but which is comparable to proxy dispersions for active tectonic regions (Seyhan et al., 2014). The σ_{lnV} for glaciated regions is higher at 0.656. Hence, the predictability of V_{S30} is better for non-glaciated than for glaciated groups, which should be taken into consideration in the weighting of ground motion data from the two site types during GMM development.

3 EMPIRICAL LINEAR AMPLIFICATION FUNCTIONS FOR CENA

3.1 INTRODUCTION

The Next Generation Attenuation East project (NGA-East), coordinated by the Pacific Earthquake Engineering Research Center (PEER), resulted in the development of 10 ground motion models (GMMs) applicable to very hard rock reference site conditions (3 km/s, Hashash et al. 2014) in central and eastern North America (CENA). Therefore, additional models for seismic site amplification are needed to predict ground motion IMs for other site conditions, including weathered rock and soil. For past NGA projects, namely Next Generation Attenuation West2 (NGA-W2), both nonlinear and linear site amplification were developed using empirical data, with the addition of some simulations to constrain the nonlinear term (Kamai et al. 2014; Seyhan and Stewart, 2014). A similar approach combining simulation and empirical data analysis was used for evaluating the effects of basin depth (Day et al. 2008). However, the available ground motion recordings in CENA do not exhibit strong enough shaking to incite nonlinear soil behavior, and information on sediment depth is not available for CENA ground motion stations.

This chapter presents an empirically derived linear site amplification model conditioned on V_{S30} for peak ground velocity (PGV), and 5% damped, 0.01 – 10 s pseudo-spectral accelerations (PSA). This linear model can be used in conjunction with additional simulation-based model

components for the effects of nonlinearity, sediment depth, and resonance at a site period (Chapter 4).

3.2 LITERATURE REVIEW OF SITE AMPLIFICATION MODELS IN CENA

3.2.1 Previous to NGA-East

The Central and Eastern North-America (CENA) region does not contain active plate boundaries and as such is considered a stable continental region (SCR) from the standpoint of ground motion prediction. A number of existing predictive equations for earthquake ground motions in SCRs are shown in Table 4. Known as ground motion models (GMMs), these models predict the median and standard deviation of ground motion intensity measures such as peak acceleration and 5% damped pseudo-spectral acceleration conditional on magnitude, site-source distance, and site condition. The GMMs listed in Table 4 were selected by an international team of experts for consideration in the Global Earthquake Model (GEM) project prior to the completion of the NGA-East project, and as such they represent most of the models that were considered at that time to be of high quality and technically viable for SCRs. Many of these models are currently used for the USGS national hazard maps (Petersen et al., 2015) in the CENA region, namely Frankel et al. (1996), Somerville et al. (2001), Campbell (2003), Toro et al. (1997), Atkinson and Boore (2006), Tavakoli and Pezeshk (2005), Silva et al. (2002), Pezeshk et al. (2011), and Atkinson (2008).

Table 4 GMPEs for stable continental regions pre-selected for Global Earthquake Model project. Modified from Douglas et al. 2012.

	Reference	Application Region	Site Parameters		Site Amplification Function	
			Discrete categories[1]	Continuous Variables	Non-linearity	Reference site condition[2]
Stable continental regions	Atkinson (2008), Atkinson & Boore (2011)	CENA	NEHRP B/C only	-	na	NEHRP B/C
	Atkinson & Boore (2006, 2011)	CENA	Hard rock; NEHRP B/C	V_{s30}	Yes	Hard rock (V_s>2000 m/s); B/C (V_{s30}=760 m/s)
	Campbell (2003)	CENA	Hard rock only	-	na	Hard rock (V_s=2800 m/s)
	Douglas et al. (2006)	So. Norway	Hard rock only	-	na	Hard rock (V_s=2800 m/s)
	Frankel et al. (1996)	CENA	Hard rock; NEHRP B/C	-	na	Hard rock (V_s=2800 m/s)
	Raghu Kanth & Iyengar (2006, 2007)	Peninsular India	Hard rock; NEHRP A-D	-	Yes	Hard rock (V_s=3600 m/s)
	Silva et al. (2002)	CENA	Hard rock only	-	na	Mid-cont., V_s=2830 m/s; Gulf cst V_s=2310 m/s)
	Somerville et al. (2009)	Australia	Rock only	-	na	Rock (V_s=865 m/s)
	Pezeshk et al. (2011)	CENA	Hard rock only	-	na	Hard rock (V_s>2000 m/s)
	Toro et al. (1997); Toro (2002)	CENA	Hard rock only	-	na	Hard rock (V_s=2800 m/s)

[1] Reference site condition defined as having no site modification in the GMPE.

As described by Douglas et al. (2012), the models in Table 4 for SCRs are to a large extent simulation-based, meaning that they are derived wholly or in part from numerical simulations of source, path, and site effects. A subset of the methods use hybrid approaches in which simulations are combined with limited data from SCRs to develop GMMs (e.g., Atkinson, 2008; Atkinson and Boore, 2011, Campbell, 2003; Pezeshk et al., 2011).

As shown in Table 4, the GMMs for SCRs were mostly developed for hard rock conditions, which generally correspond to shear wave velocities of V_S > 2000-3000 m/s. In some cases, site amplification factors are provided to convert from hard rock conditions to the soft rock conditions of the NEHRP B/C boundary (corresponding to V_{S30} =760 m/s) As discussed in an assessment of these GMMs for the Global Earthquake Model (Stewart et al., 2015), site factors for soil conditions are generally absent, and when present are either considered unreliable (for Raghu Kanth & Iyengar, 2006, 2007) or are adopted from models for active regions (applies to Atkinson and Boore, 2006, 2011). This creates substantial uncertainty regarding the practical application of these GMMs for soil sites.

3.2.2 Site Amplification Model Development during and since NGA-East

Table 5 summarizes some of the principal attributes of ten NGA-East seed GMMs (PEER, 2015). Three of the models (Boore 2015, Darragh et al. 2015, Yenier and Atkinson 2015) are based on the point source simulation methodology. Parameters included in the simulations, especially the stress parameter and path attenuation terms, are set based on comparisons to NGA-East data. Two of the models (Pezeshk et al. 2015, Shahjouei and Pezeshk 2015) use the hybrid empirical approach of Campbell (2003), in which GMPEs for active tectonic regions (from NGA-West2; Bozorgnia et al., 2014) are modified for CENA using ratios of simulated ground motions. One model uses a conceptually similar reference empirical approach in which an active tectonic region GMPE is adjusted through residuals analysis using NGA-East data (Hassani and Atkinson 2015). Three of the models are based on direct regression of NGA-East data to develop GMMs (Al Norman and Cramer 2015, Grazier 2015, Hollenback et al. 2015). However, due to the limited parameter space covered by the data, additional information used during model building included intensity data (Al Norman and Cramer 2015) or simulations (Grazier 2015, Hollenbeck et al. 2015). Finally, one GMM consists of an inventory of finite fault simulation results (Frankel 2015).

All of the GMMs in Table 5 provide ground motion estimates for the reference site condition in CENA defined by Hashash et al. (2014). This reference condition consists of V_S = 3.0 km/s and diminutive parameter κ = 0.006 sec (κ controls the attenuation of the Fourier amplitude spectra with frequency for the high-frequency portion of the spectrum). Five of the models contain no site term and provide ground motion estimates only for the reference condition. Five models do contain a V_{S30}-based site term that is intended to capture the effects of V_{S30} on the linear site amplification. Some models used site corrections of various sorts during development, even if the models themselves do not contain a site term. As a result, there are a number of site amplification models, reflecting various approaches in their development, within the documentation for the ten NGA-East GMMs.

As shown in Table 5, the alternative approaches for estimating site amplification that were used during NGA-East GMM development included:

- Adopting models for active tectonic regions, specifically the Seyhan and Stewart (2014) model (SS14) developed for NGA-West2 (this is the site amplification model contained in the Boore et al. 2014 GMM). SS14 was used as the site term in NGA-East models (PEER, 2015) by Yenier and Atkinson 2015 and by Hassani and Atkinson 2015, and to support model development by Pezeshk et al. 2015 and Shahjouei and Pezehk 2015.

- Regression of data using a linear V_{S30}-scaling model (Al Norman and Cramer 2015; Hollenbeck et al. 2015).

- Ground response analysis simulations, typically using elastic soil conditions (Darragh et al. 2015; Graizer 2015)

These approaches for analysis of site effects for soil and soft rock sites (V_{S30} < 760 m/s) are combined with models for site amplification from 760 to 3000 m/s, as described in the next section.

Coincident with NGA-East, several investigators, working independently from the authors, have developed site amplification models for CENA conditions. Hassani and Atkinson (2016) derive the frequency of peaks in H/V spectra using CENA data, and then use those peak frequencies as predictive parameters for analysis of site effects. Not surprisingly, they find that the data-derived peaks are more effective than V_{S30} at predicting site effects in the CENA data. Aboye et al. (2015) apply equivalent-linear simulations to evaluate site factors in the Charleston, South Carolina region. Results of those simulation-based site factors are compared to simulation based site factors from the present study in Section 4.

Table 5 Summary of attributes of NGA-East median Ground Motion Models (GMMs) published by PEER (2015).

Author	Approach	Tables or equations?	Distance type[1]	Distance range (km)	M range	Site Term & Parameter	IM[2]	Site correction: V_{S30} to 760[3]	Site correction: 760 to 3000[4]
DM Boore	Point source simulations	Tables	R_{ps}	0-1200	4-8	N	-1, 0, 0.01-10	N/A	Boore, 2015
RB Darragh, NA Abrahamson, WJ Silva, N Gregor	Point source simulations	GMPE	R_{JB}	0-1000	4.5-8.5	N	-1, 0, 0.01-10	1D GRA TFs for NEHRP Cats; goes from V_{S30} to 4.68 km/s (Table 3.2)	
E Yenier and GM Atkinson	Point source simulations	GMPE	R_{ps}	0-600	3-8	Y (V_{S30})	-1, 0, 0.01-10	SS14	AB06 BC crusal amp (Atkinson, 2012)
S Pezeshk, A Zandieh, KW Campbell, B Tavakoli	Hybrid empirical	GMPE	R_{rup}	0-1000	3-8	N	0, 0.01-10	SS14 (used for validation only)	BT 2015
AD Frankel	Finite fault simulations	Tables	R_{rup}	2-1000	4.5-8	N	0, 0.01-10 (?)	N/A	Frankel et al. (1996)
A Shahjouei and S Pezeshk	Hybrid empirical	GMPE	R_{JB}	2-1000	5-8	N	-1, 0, 0.01-10	SS14 (used for validation only)	AB06 and BT2015;
N Al Norman and CH Cramer	Empirical with intensity data	GMPE	R_{rup}	<10-2000	2.5-7.7	Y (V_{S30})	-1, 0, 0.1-10	Set by regression, parameter d_1	NA
V Graizer	Empirical	GMPE	R_{rup}	0-1000	4-8.2	Y (V_{S30})	0, 0.01-10	GRA-based: Eq. 9.6	GRA-based: similar to AB06, AB11
B Hassani and GM Atkinson	Reference empirical	GMPE	R_{JB}	0-400	3-8	Y (V_{S30})	-1, 0, 0.05-10	SS14	AB06 BC crusal amp (Atkinson, 2012)
J Hollenback, N Kuehn, CA Goulet, NA Abrahamson	Empirical with finite fault simulations	GMPE (FAS); Tables (PSA)	R_{rup}	0-1200	4-8.2	Y (V_{S30})	-1, 0, 0.01-10	Set by regression, parameter c_8	Boore, 2015

1 R_{PS} = sqrt [R_{hyp}^2 + h^2]^0.5, where h is an **M**-dependent fictitious depth term; R_{JB} = horizontal distance to surface projection of fault plane; R_{rup} = rupture distance

2 IM = intensity measure. -1 = PGV, 0 = PGA, other numbers indicate oscillator periods for PSA

3 GRA = ground response analysis (simulation-based). SS14 = Seyhan and Stewart (2014), semi-empirical model for active regions

4 AB06 = Atkinson and Boore, 2006; BT 2015 = Boore and Thompson, 2015; GRA = Ground Response Analysis

3.2.3 CENA Site Amplification for V_{S30} =760 m/s Relative to the Reference Rock Condition

As shown in Table 4, GMMs for CENA have consistently used a hard rock reference site condition. Because the reference site condition for the development of national ground motion hazard maps has been V_{S30}=760 m/s since the mid-1990s (Frankel et al., 1996), there has been a long-standing need to adjust hard rock GMMs to a 760 m/s site condition. This issue has also been revisited as part of the NGA-East project.

Most of the models for the 760/3000 correction are based on ground response simulations using the square-root-impedance method (Boore, 2013), also known as the quarter-wavelength method. Nonlinear effects are not considered, which is justifiable given the fast velocities and correspondingly small strains. The parameters controlling the analysis results are the V_S profile for the V_{S30}=760 m/s site condition and the level of soil damping (expressed through diminutive parameter κ_0) that is applied during the analysis.

Figure 15 shows the V_S profile by Frankel et al. (1996) for the V_{S30}=760 m/s site condition, that was considered by Atkinson and Boore (2006). Boore (2015) also considered this profile along with a steeper-gradient OTT profile by Beresnev and Atkinson (1997). Values of diminutive parameter κ_0 used with the OTT profile are 0.005, 0.01, 0.02 and 0.03.

Figure 16 shows transfer functions for both profiles, with two results shown for the OTT profile for the two considered κ_0 values, 0.01 and 0.02. These κ_0 values were applied to the results with the Frankel et al. (1996) profile shown in Figure 16. The results show amplification for frequencies above about 0.3 Hz for the relatively low-gradient Frankel et al. (1996) profile and above about 3 Hz for the higher gradient OTT profile. In both cases, peak amplification is approximately 2-2.5 before the attenuation effective of diminutive parameter dominates at high frequencies (above ~10 Hz). Figure 17 shows PSA ratios (3000/760) for various magnitude/distance combinations and the two considered κ_0 values, which affect frequency content and hence PSA ratios. A similar model derived in the present study are presented in Section 4.5.

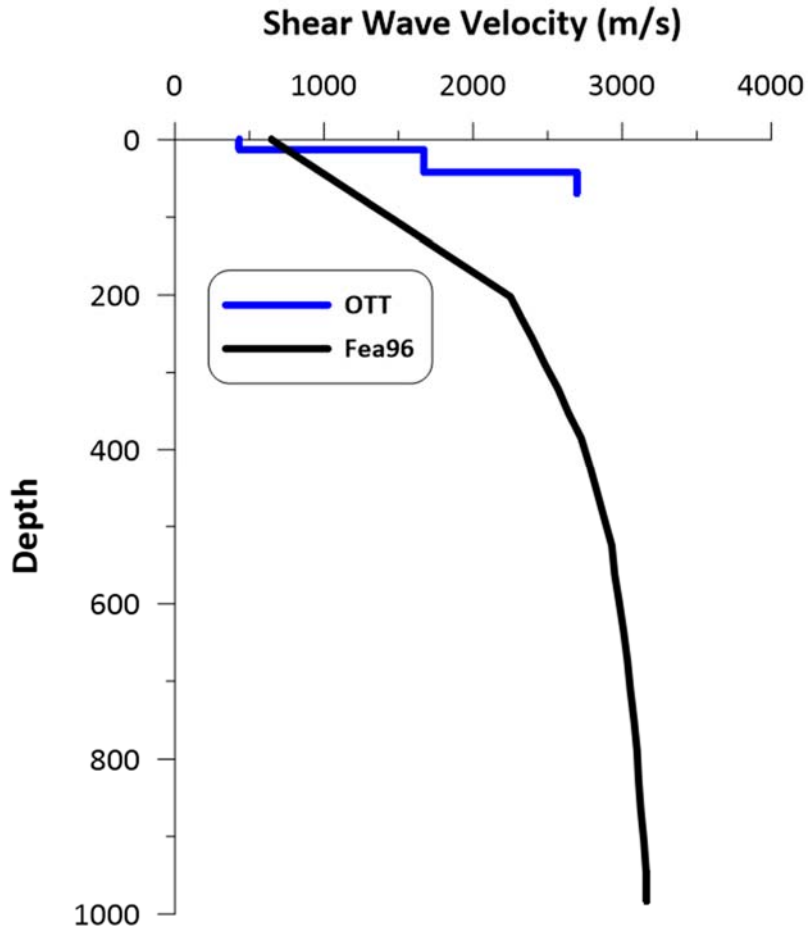

Figure 15 Shear wave velocity profiles (from Beresnev and Atkinson 1997 and Frankel et al. 1996) used for development of 760/3000 m/s amplification factors by Atkinson and Boore (2006) and Boore (2015). The Beresnev and Atkinson (1997) profile extends to a depth of 8 km, but is here truncated at 1 km.

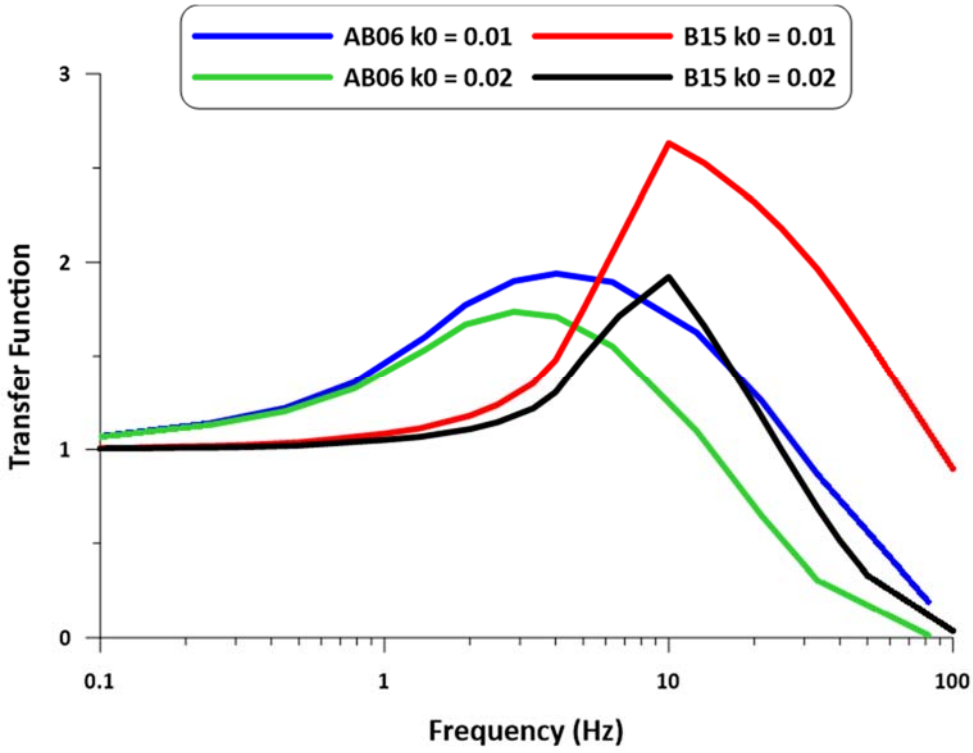

Figure 16 Fourier amplitude spectra transfer functions for 760/3000 m/s amplification from Atkinson and Boore (2006) using the Frankel et al. (1996) VS profile (κ_0 = 0.01, blue, κ_0 = 0.02, green), and Boore (2015) using the Beresnev and Atkinson (1997) OTT shear wave velocity profile (κ_0 = 0.01, red, κ_0 = 0.02, black).

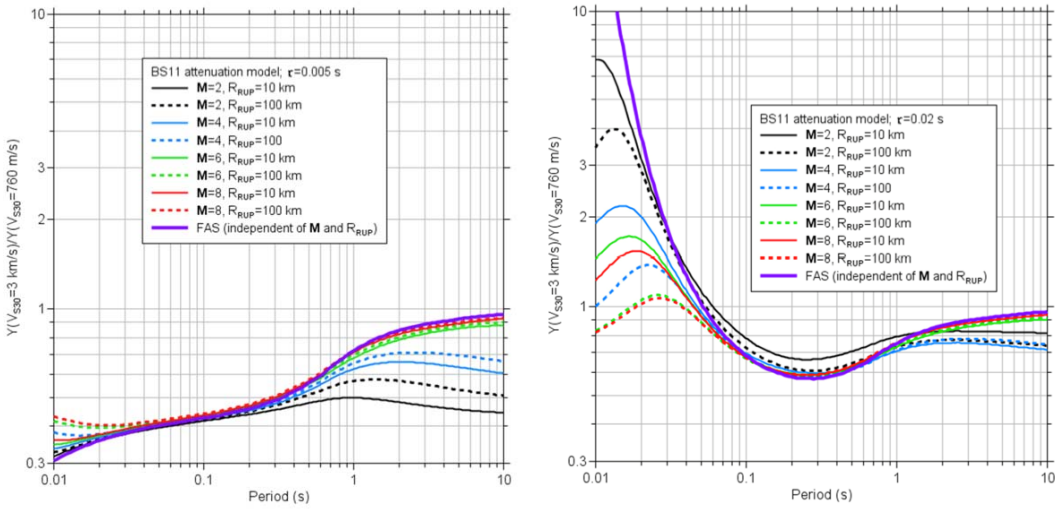

Figure 17 Ratios of PSA as a function of oscillator period for the 3000 m/s divided by 760 m/s condition, for distances of 10 and 100 km, using the Boatwright and Seekins (2011) attenuation

model and $\kappa = 0.005$ (left) and $\kappa = 0.02$ (right) for the 760 m/s site condition. A modified Frankel et al. (1996) model was used for the VS30 = 760 m/s crustal amplifications. Also shown are ratios of Fourier acceleration spectra (FAS) (Boore 2015, his Figures 18 and 21).

3.3 LINEAR EMPIRICAL MODEL DEVELOPMENT

The empirical linear model described in this chapter is the site amplification that can be inferred from NGA-East ground motion data using the non-reference site approach. The basic concept behind a non-reference site approach is that the misfit between data and a reference rock GMM can be used to evaluate trends in site amplification. The approach has been widely used in the development of site amplification models (e.g., Stewart et al., 2003; Luzi et al., 2011 Sandıkkaya et al. 2013) and site terms in GMMs in various active tectonic regions. Specifically, site amplification is taken as the within-event rock residual computed relative to the GMMs conditioned at 760 meters per second (m/s), using a mixed-effects analysis to account for model bias and event terms. The resulting site response can be considered as 'linear' when the ground motion amplitudes are predominantly small, which is the case in the present data set for CENA, as shown subsequently. This process of residual partitioning, and the data set and GMMs that were used are discussed further in the following sections. To our knowledge, this work is distinct from previous site amplification work performed prior to and during NGA-East as a result of the following two aspects: (1) we use empirical data in lieu of simulations to infer site amplification and (2) site amplification is related to a truly independent variable, V_{S30}, which in turn is derived using the most accurate estimates currently available (Chapter 2.8).

3.3.1 Ground Motion Database

The NGA-East ground motion database (available as an electronic supplement to Goulet et al. 2014) was used in model development, with some modifications. The V_{S30} values for recording stations with assignment codes 3, 4, and 5 according to Chapter 5.5 of Goulet et al. (2014) were updated using the recommended values in Table 3 of this report (Figure 18).

Additionally, the database was screened based on properties of the recordings. First according to the lowest and highest useable periods as defined and given in Goulet et al. (2014), and then secondly by the same criteria used in the development of the Yenier and Atkinson (2015) GMM: (1) $\mathbf{M} \geq 3$, (2) $R_{rup} \leq 600$ kilometers (km), (3) events with at least 3 recordings, and (4) events

with an estimate of hypocentral depth. Lastly, events and recordings from the Gulf Cost region (as defined in Goulet et al. 2014) were used, but only when both the event and recording were in the Gulf Coast region. These screening criteria affect the number of events and recordings used as a function of the PSA oscillator period (T) (Figure 19). The screened dataset for PGV in magnitude and distance space is shown in Figure 20.

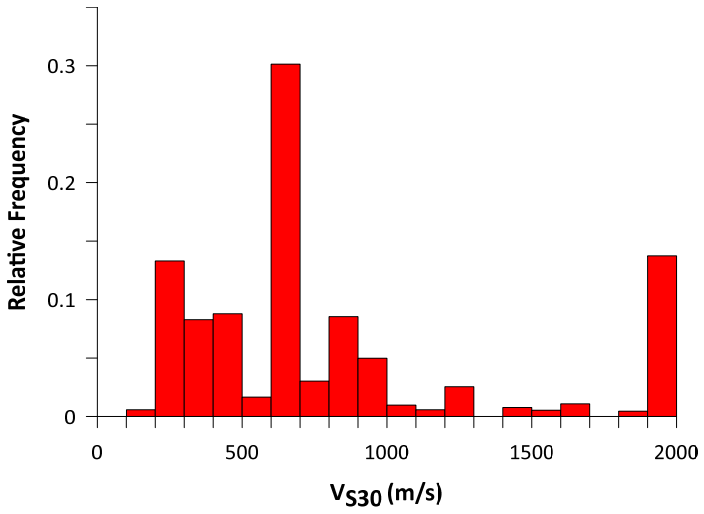

Figure 18 Histogram of V_{S30} values at stations used for PGV model development.

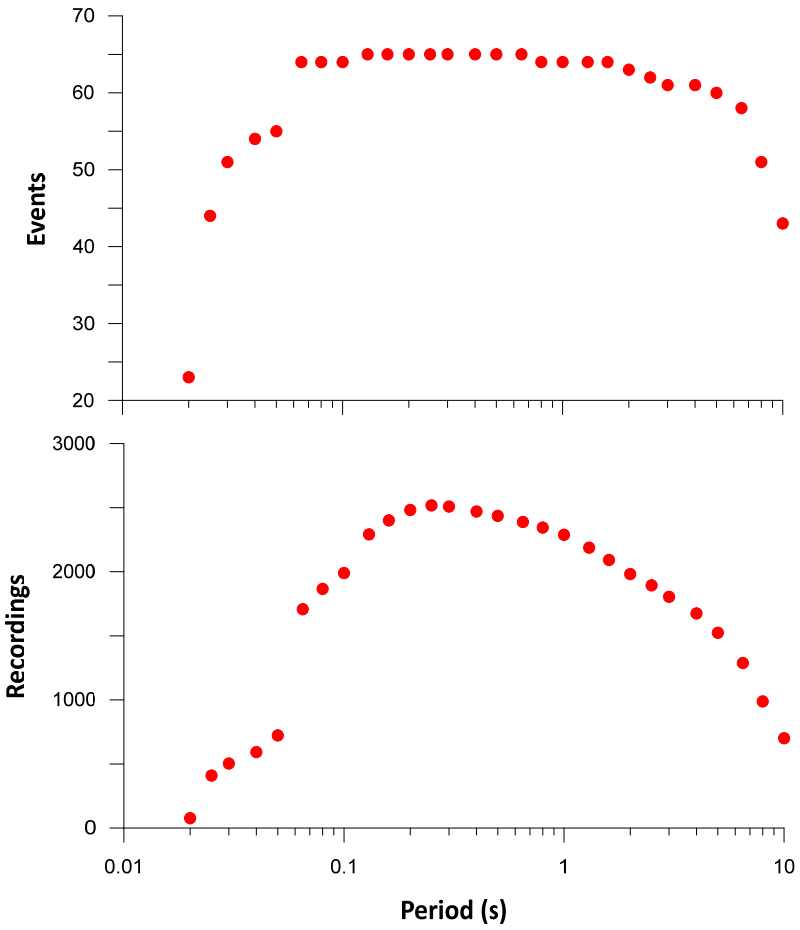

Figure 19 Earthquake events and recordings used in model development after the screening process, shown as a function of PSA oscillator period.

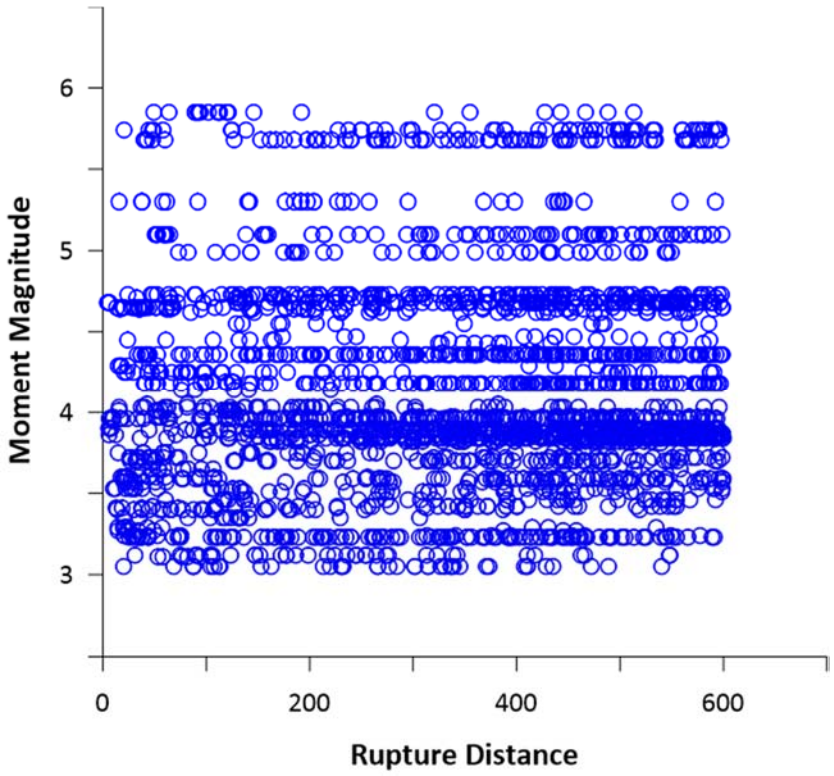

Figure 20 Post-screening ground motion data inventory used for PGV model development displayed in magnitude - distance space.

3.3.2 Rock-Conditioned Ground Motion Models

Two rock-conditioned NGA-East GMMs were used to calculate residuals in the non-reference site approach: Yenier and Atkinson (2015), and Hassani and Atkinson (2015), shown in Table 5. Both GMMs are conditioned at 760 m/s for the present calculations; therefore, our linear site amplification model is relative to a 760 m/s rock condition.

The Yenier and Atkinson (2015) GMM is based point-source (PS) simulations calibrated using ground motion data from California. This generic GMM is then adjusted for use in CENA using residuals analysis with data from the NGA-East ground motion database. The GMM provides median predictions of PGA, PGV and 5%-damped PSA at oscillator periods up to 10s, for M 3-8 and Rrup $\leq$ 600 km. The Hassani and Atkinson (2015) GMM is also based on a referenced empirical approach. The NGA-W2 Boore et al. (2014) (BSSA14) GMM, developed for active tectonic regions, was compared to ground motion data from the NGA-East database and other resources (Hassani and Atkinson, 2015). The BSSA14 GMM was then calibrated to CENA

based on the ratio of observed ground motions to GMM predictions. A comparison of the magnitude scaling of these two GMMs, along with Atkinson and Boore (2006, 2011) and Pezeshk et al. (2011) (Table 4) is shown in Figure 21

.

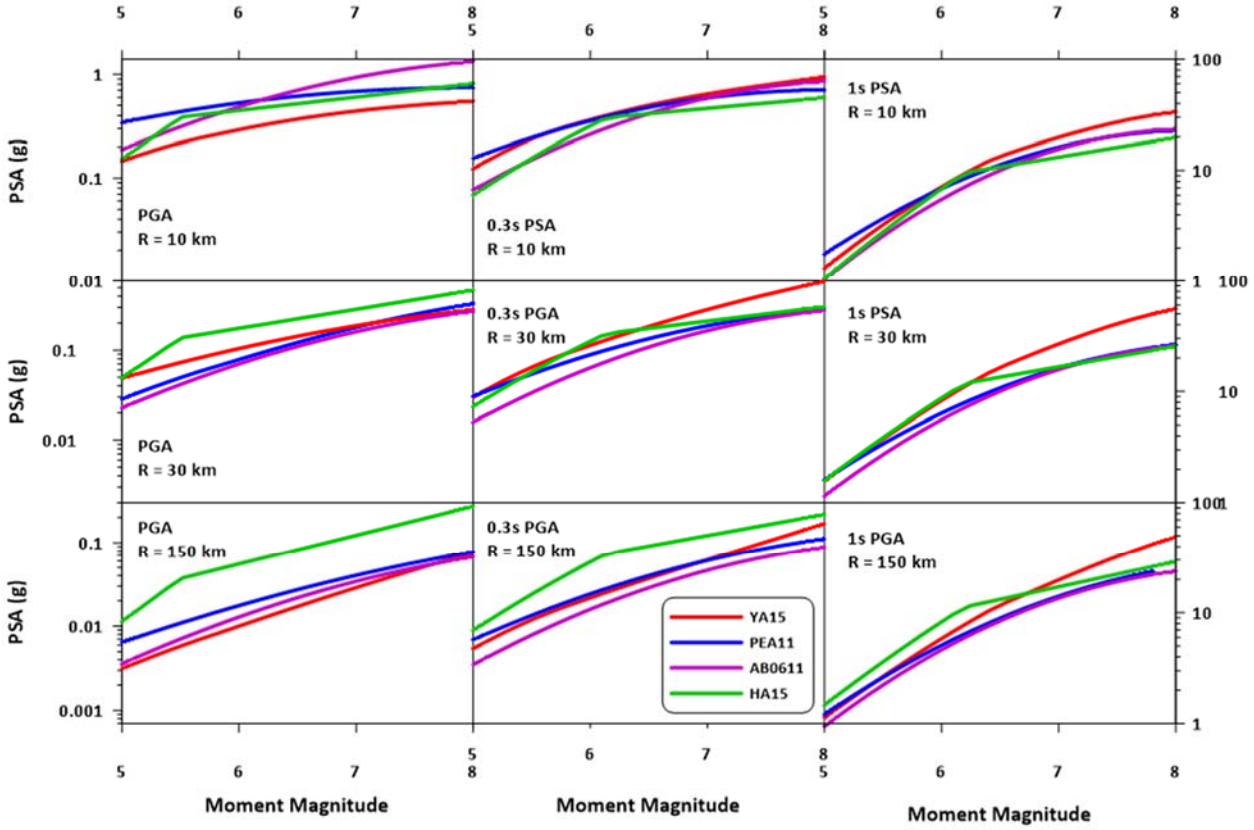

Figure 21 Comparisons of the magnitude scaling of YA15 (red), HA15 (blue), AB0611 (purple) and PEA11 (green) for PGA, 0.3s PSA, 1s PSA and 10, 30, and 100 km site-to-source distances.

Additionally, both GMMs were corrected for use in the Gulf Coast. The NGA-East GMMs as published in PEER (2015) were not applicable to events occurring in or recordings from the Gulf Coast. This was due to an observed difference in grond motion attenuation in the Gulf Coast from the rest of CENA. A PEER report (Hollenback et al. 2015) was published containing adjustment models to the NGA-East seed GMMs including Gulf Coast Adustments. Presented are two adjustments models applicable to events in the Gulf Coast that were recorded in the Gulf Coast; in other words recordings for which the path did not cross in to or out of the Gulf Coast,

but was contained fully inside of it. The so-called PEER Empirical model was developed by modeling the residual of recordings from the Gulf Coast relative to the PEER NGA-East median GMM. The second adjustment model, developed by B. Darragh, N.A. Abrahamson, W. Silva, and Gregor (DASG) is simulation-based. Simulation inputs kappa, Q_0 and stress drop, were inverted using data from the Gulf Coast region. These simulations were used to update the DASG GMM (Table 5), and the adjustment was taken as the ratio of the original and updated DASG GMMs. There is a significant difference between the empirical and simulation-based adjustment models (Figure 22) and an average of the two adjustments were applied to the GMMs used in this study.

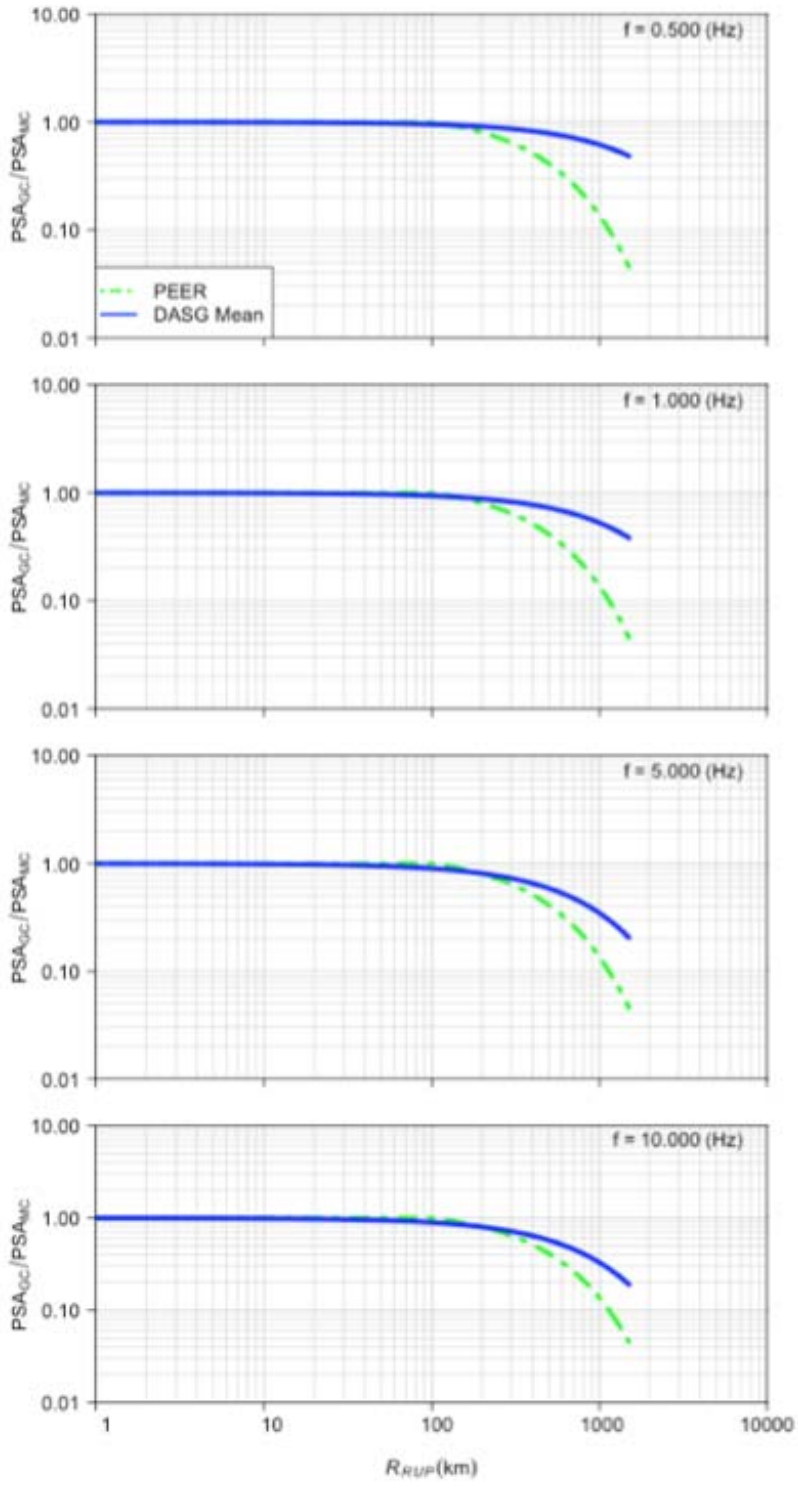

Figure 22 Comparison of the PEER empirical and DASG simulation-based Gulf Coast adjustment models to the NGA-East seed GMMs for frequencies of 0.5, 1.0, 5.0 and 10 Hz (Hollenback et al. 2015, their Figure 4.14).

3.3.3 Residual Partioning

The modeling process for linear site amplification was iterative. The first step was to calculate total residuals for our selected subset of the NGA-East ground motion database (Goulet et al. 2014) as:

$$R_{ij} = ln(Y_{ij}) - \left[\mu_{ln}(M_i, R_{ij}, 760) + F_S(V_{S30,j})\right] \quad (7)$$

where *i* refers to an event, *j* refers to a recording, Y_{ij} is an IM from recording *j* and event *i*, μ_{ln} is the natural log mean GMM prediction of that IM as a function of magnitude and distance for the reference rock site condition, and F_S is a V_{S30}-dependent site term. The rock-conditioned GMM is used without modification in all steps of the iterative process. In the first iteration, F_S is taken as the linear component of the SS14 NGA-W2 site amplification model (a "first guess" for site amplification in CENA). Once the residuals have been partitioned and regressed to obtain a new expression for F_S applicable to CENA (functional form given in Section 3.3.4), that model is used in Eq. (7) to produce new residuals, and the partitioning process is repeated. This iteration occurs until the regressed coefficients within the F_S model stabilize between iteration steps.

The residual partitioning process was performed using a mixed-effects analysis using the *lme4* package in R (Bates et al., 2015; R Development Core Team, 2008), as follows:

$$R_{ij} = c_k + \eta_i + \varepsilon_{ij} \quad (8)$$

This process isolates the mean GMM misfit, c_k, as well as event terms for each event represented in the selected dataset, η_i. An event term η_i represents the approximate difference between recordings from event *i* and the GMM median predictions. In other words, η_i represents how much higher or lower recordings from event *i* are than the average in natural log units. We are interested in removing these event terms from our residuals to isolate the component of the ground motions due to the site only. Term ε_{ij} in Eq. (7) represents the within-event residual.

Next, rock residuals (R_{Rij}) are calculated using the NGA-East GMMs (Table 5). Similar to the total residuals, except a rock-condition V_{S30} of 760 m/s is applied to the model prediction, which is equivalent to taking $F_S = 0$ in Eq. (7).

$$R_{R_{ij}} = ln(Y_{ij}) - \mu_{ln}(M_j, R_{ij}, 760) \quad (9)$$

c_k and the appropriate event terms calculated previously are then subtracted from the rock residuals to obtain the within-event rock residuals, ε_{Rij} :

$$\varepsilon_{R_{ij}} = R_{R_{ij}} - c_k - \eta_i \quad (10)$$

The average trend through these within-event rock residuals represent the empirical linear site amplification in natural log space, isolated from effects due to individual events.

3.3.4 Model Regression

The reference rock residuals, ε_{Rij}, were regressed in a least-squares fashion as a function of V_{S30}, as follows:

$$\ln(F_{lin}) = \begin{cases} c\ln\left(\frac{V_1}{V_{ref}}\right) & \text{for } V_{S30} \le V_1 \\ c\ln\left(\frac{V_{S30}}{V_{ref}}\right) & \text{for } V_1 < V_{S30} \le V_2 \\ c\ln\left(\frac{V_2}{V_{ref}}\right) & \text{for } V_{S30} > V_2 \end{cases} \quad (11)$$

The model in Eq. (11) is a piecewise linear function (in log-log space), with two horizontal segments at low and high V_{S30} (< ~300 m/s and >~1000 m/s, respectively), connected by a sloping line (Figure 23). The horizontal segment at high V_{S30} values has been observed in site amplification in active tectonic regions (Abrahamson et al., 2014; Seyhan and Stewart 2014), and a flattening of slope below V_{S30} = 200 m/s has been observed in shallow site response in Japan (Campbell and Bozorgnia 2014). Other than the Campbell and Bozorgnia finding for Japan, previous empirical site amplification studies have not identified changes in slope at low V_{S30} values.

The model building process using Eq. (11) began by fitting the model to mean ε_{Rij} values in the end ranges of V_{S30} ($V_{S30} < V1$, $V_{S30} > V2$), using values of $V1$ and $V2$ that were initially set by eye at 300 and 1300 m/s. This set slope parameter c, which controls model fit for $V1<V_{S30}<V2$. We

then adjusted *V1* and *V2* to improve fit for the central portion of the data (V_{S30} ~ 300 to 1000 m/s), as needed. These adjustments to *V1* and *V2* change slope parameter *c*. The model constrained in this manner typically does not have reference velocity V_{ref} = 760 m/s (V_{ref} represents the value of V_{S30} with natural log amplification of zero). This means that the amplification represented by the model is not referenced to the desired values of 760 m/s. This occurs as a result of trade-offs between c_k and the ε_{Rij} terms. Because site amplification represents ground motion change between site conditions, and any reference condition can be selected, we manually adjust all data points (ε_{Rij}) and the model vertically so that the model is forced to go through 0 amplification at the reference condition of 760 m/s (this sets V_{ref} = 760 m/s).

We originally considered all the CENA data together in a single regression. However, residuals analyses showed that this combined model was not capturing the different trends in the data for sites that have or have not been previously glaciated (according to the extent of the Wisconsin glaciation as defined in Reed and Bush 2005) (Figure 23). These two groups were therefore regressed separately, and each IM has two sets of model coefficients for Eq. (11): one for previously glaciated sites, and one for non-glaciated sites. The resulting models are shown in Figure 24.

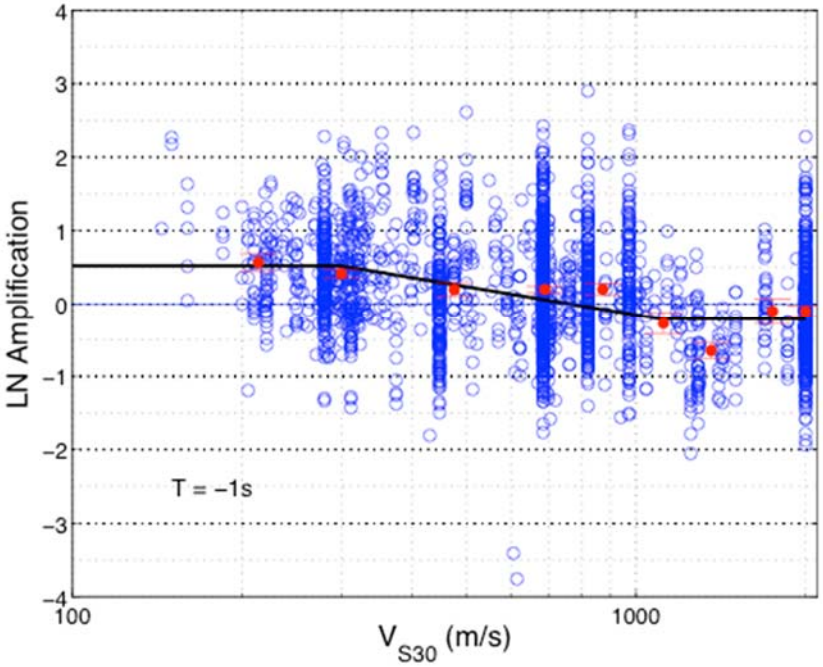

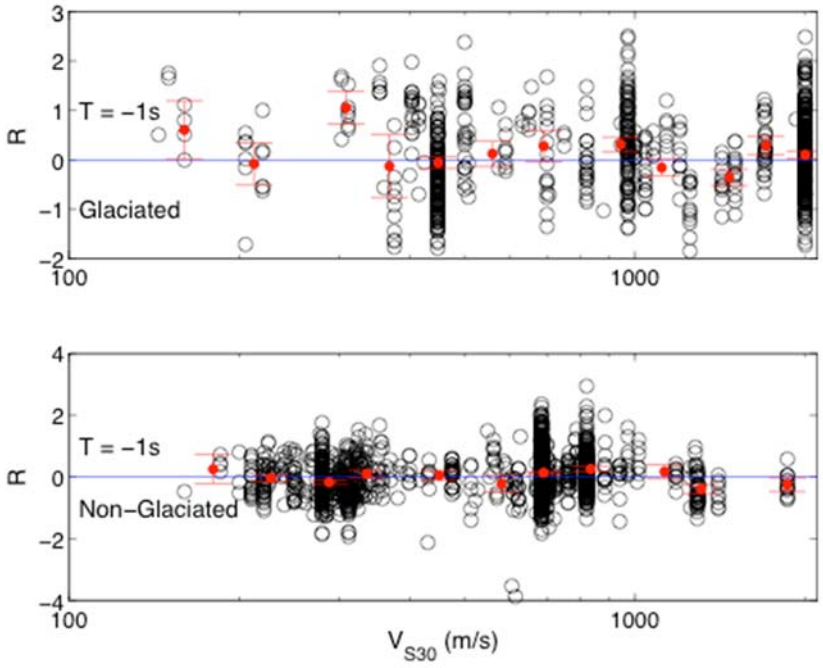

Figure 23 Best-fit PGV model using combined data from previously glaciated and non-glaciated stations (top) and residuals as a function of V_{S30} from data from previously glaciated and non-glaciated stations (bottom).

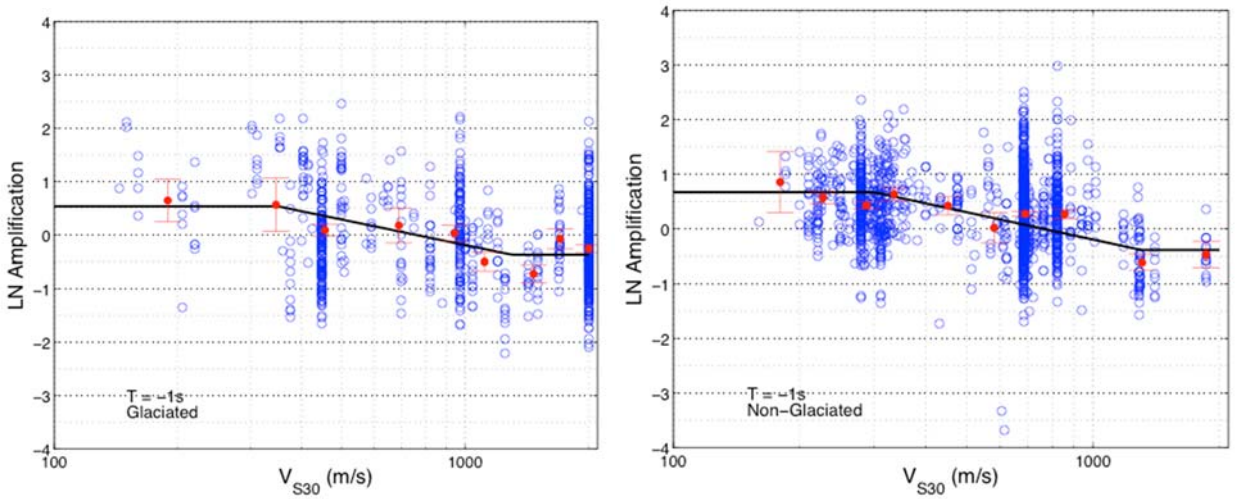

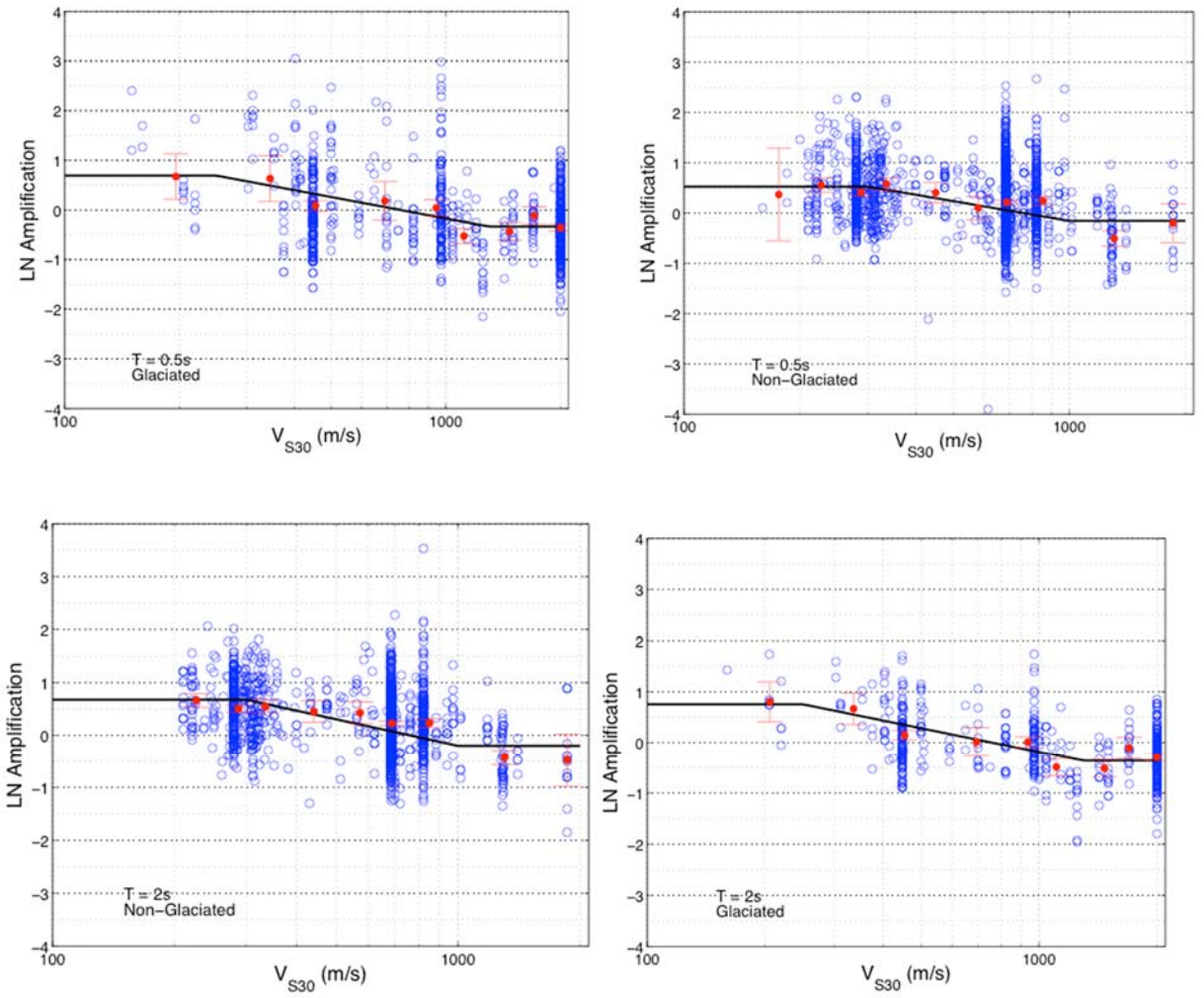

Figure 24 Linear amplification model (Eq. 3.5) and screened data for glaciated and non-glaciated sites and PGV, T = 0.5s, and T = 2s PSA. Binned means and 95% confidence intervals are shown in red.

These coefficients, as well as model sigmas, are given in Table 6 and Table 7, and shown as a function of oscillator period in Figure 25. These coefficients come directly from the analysis process and are not smoothed; smoothing will be applied in a later stage of work. Figure 25 also shows a comparison to the linear site amplification model term coefficient from Seyhan and Stewart (2014). We observe that the V_{S30}-scaling from NGA-W2 generally is steeper than that observed in CENA. This doesn't hold true at short periods (~0.065 – 0.3s) where V_{S30}-scaling is steeper than or similar to that in SS14. Additionally, the V_{S30}-scaling in CENA does not vary as a function of oscillator period as significantly as the SS14 scaling. However, it should be noted that the F_{lin} functional form used in SS14 is not the same as that used here; although both have a

slope term, *c*, it is not a direct comparison. Amplifications resulting from SS14 are compared to those resulting from the model presented here in Section 3.4.2.

Table 6 Linear amplification model coefficients and sigma for glaciated sites.

Period (s)	c	V_{ref} (m/s)	V_1 (m/s)	V_2 (m/s)	Sigma
-1	-0.691	760	350	1300	0.772
0.065	-0.873	760	350	1100	0.865
0.08	-0.706	760	350	1100	0.845
0.1	-0.670	760	300	1100	0.808
0.13	-0.629	760	250	1100	0.799
0.16	-0.611	760	350	1100	0.791
0.2	-0.654	760	300	1100	0.822
0.25	-0.697	760	250	1100	0.808
0.3	-0.672	760	350	1100	0.779
0.4	-0.727	760	300	1100	0.741
0.5	-0.708	760	250	1300	0.731
0.65	-0.623	760	250	1100	0.683
0.8	-0.678	760	250	1100	0.635
1	-0.725	760	200	1100	0.630
1.3	-0.721	760	250	1200	0.605
1.6	-0.812	760	250	1100	0.564
2	-0.798	760	250	1300	0.528
2.5	-0.679	760	250	1100	0.505
3	-0.778	760	250	1100	0.485
4	-0.693	760	300	1100	0.501
5	-0.703	760	250	1100	0.462
6.5	-0.589	760	200	1100	0.425
8	-0.657	760	250	1300	0.423
10	-0.392	760	250	1300	0.456

Table 7 Linear amplification model coefficients and sigma for non- glaciated sites.

Period (s)	c	V_{ref} (m/s)	V_1 (m/s)	V_2 (m/s)	Sigma
-1	-0.721	760	300	1300	0.664
0.065	-0.541	760	350	1300	0.751
0.08	-0.542	760	350	1300	0.749
0.1	-0.584	760	350	1300	0.740
0.13	-0.652	760	350	1300	0.736
0.16	-0.723	760	350	1300	0.727
0.2	-0.775	760	350	1300	0.725
0.25	-0.753	760	350	1300	0.710
0.3	-0.785	760	350	1300	0.719

0.4	-0.677	760	400	1300	0.675
0.5	-0.565	760	300	1000	0.652
0.65	-0.678	760	300	1300	0.639
0.8	-0.747	760	350	1300	0.637
1	-0.745	760	350	1300	0.630
1.3	-0.830	760	350	1300	0.613
1.6	-0.863	760	400	1300	0.589
2	-0.730	760	300	1000	0.590
2.5	-0.739	760	350	1300	0.545
3	-0.878	760	400	1400	0.533
4	-0.931	760	400	1300	0.552
5	-0.887	760	400	1300	0.556
6.5	-0.817	760	400	1300	0.514
8	-0.763	760	400	1400	0.474
10	-0.544	760	300	1300	0.463

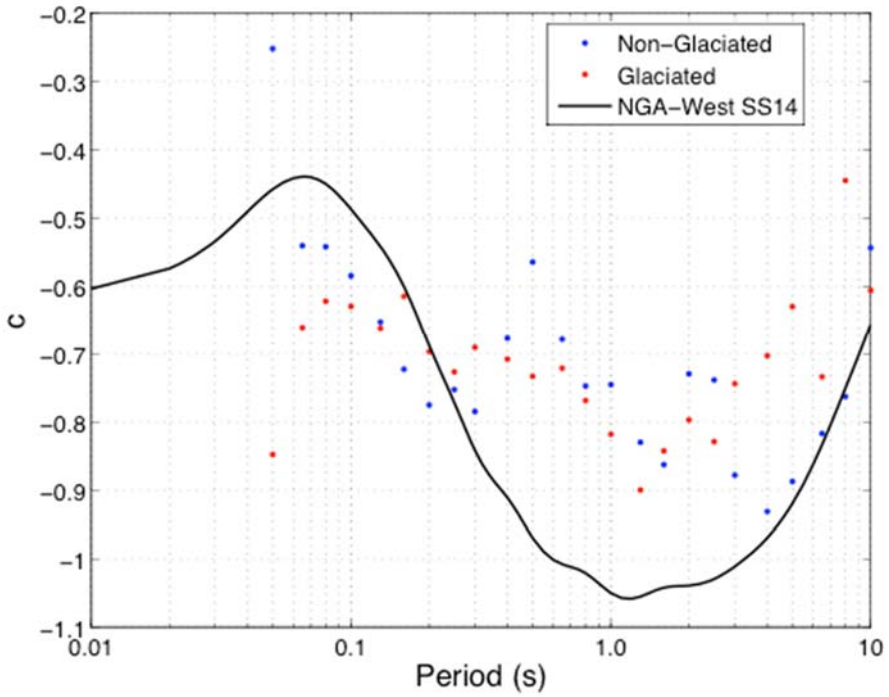

Figure 25 Slope coefficients for the glaciated (red) and non-glaciated (blue) linear site amplification models as compared to those from SS14.

3.4 RESULTS

3.4.1 Model Residuals

Residuals were computed using Eq. (7) with site amplification function (F_S) from Eq. (11) and coefficients from Table 6-Table 7. Residuals are plotted as a function of V_{S30} for the glaciated and non-glaciated models in Figure 26 for PGV, T = 0.5 and T = 2s PSA. The binned means (in red) for the non-glaciated model residuals show no appreciable bias or trends with V_{S30}, however the residuals have a positive bias for some individual bins of V_{S30} (e.g., glaciated and V_{S30} < 300 m/s).

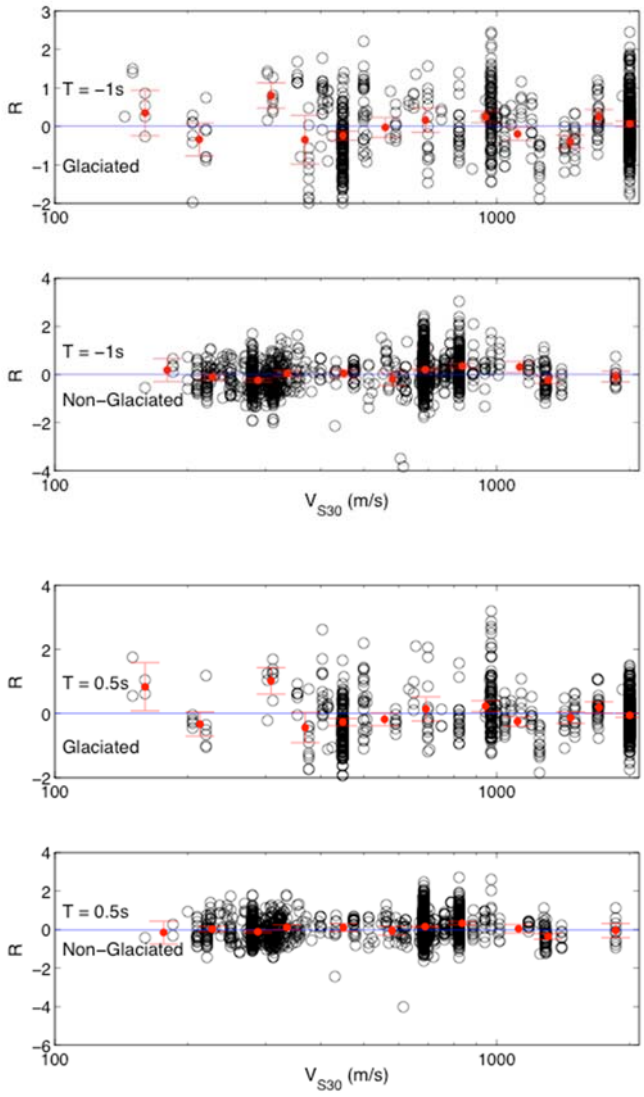

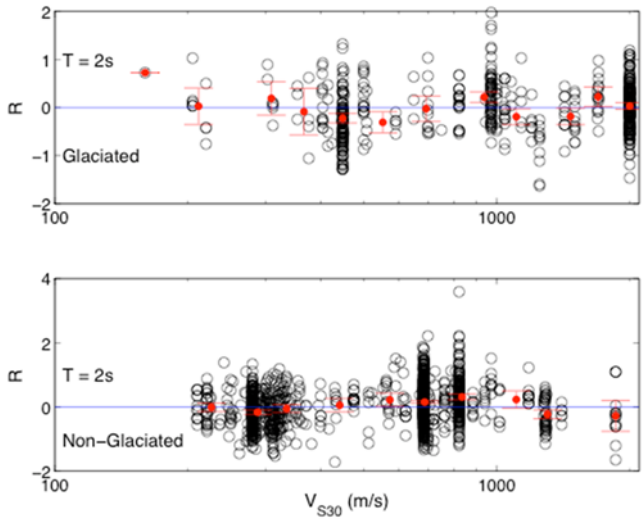

Figure 26 Glaciated and non-glaciated model residuals for PGV, T = 0.5s and T = 2s PSA, with binned means and 95% confidence intervals in red and a reference line at 0 in blue.

3.4.2 Model Performance

Figure 27 shows amplification from the glaciated model, nonglaciated model, and F_{lin} from SS14 as a function of oscillator period for a variety of V_{S30} values. Figure 27a corresponds to V_{S30} = 200 m/s, Figure 27b to V_{S30} = 400 m/s, and Figure 27c to V_{S30} = 1000 m/s. We show results for the present model over the period range 0.06 to 7 sec, due to sparseness of the data set outside of that range. The jagged appearance of the amplification functions is a result of lack of smoothing of model coefficients. This will be addressed in future work.

This task involves development of empirical site amplification factors for CENA using a non-reference site approach (e.g., Stewart et al., 2003). In this approach, site amplification is evaluated from the interpretation of data residuals:

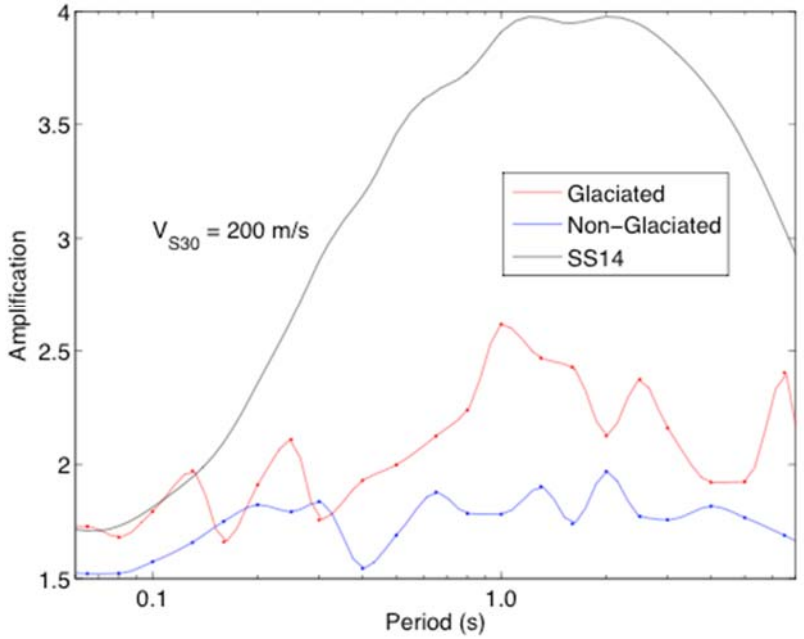
Glaciated
Non−Glaciated
SS14
V_{S30} = 200 m/s
Amplification
Period (s)
4
3.5
3
2.5
2
1.5
0.1
1.0

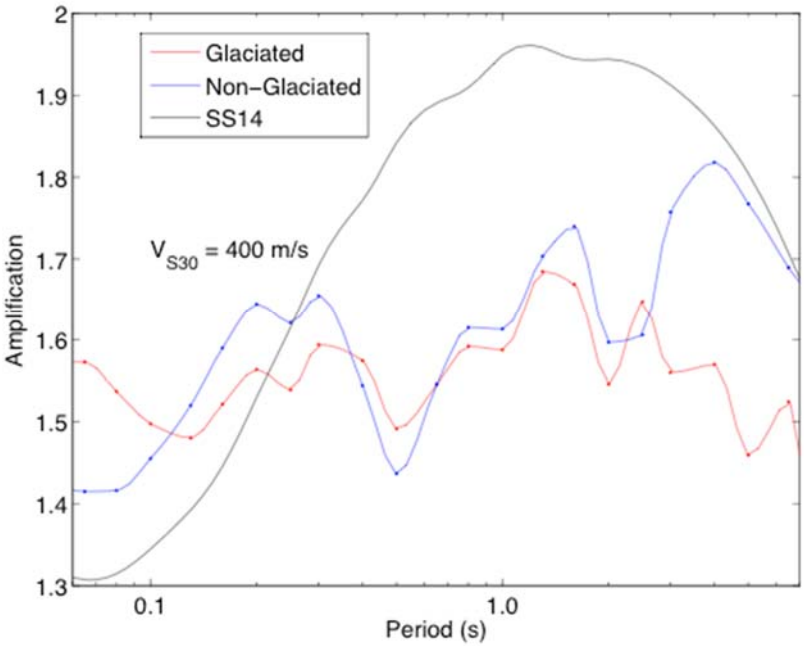
Glaciated
Non−Glaciated
SS14
V_{S30} = 400 m/s
Amplification
Period (s)
2
1.9
1.8
1.7
1.6
1.5
1.4
1.3
0.1
1.0

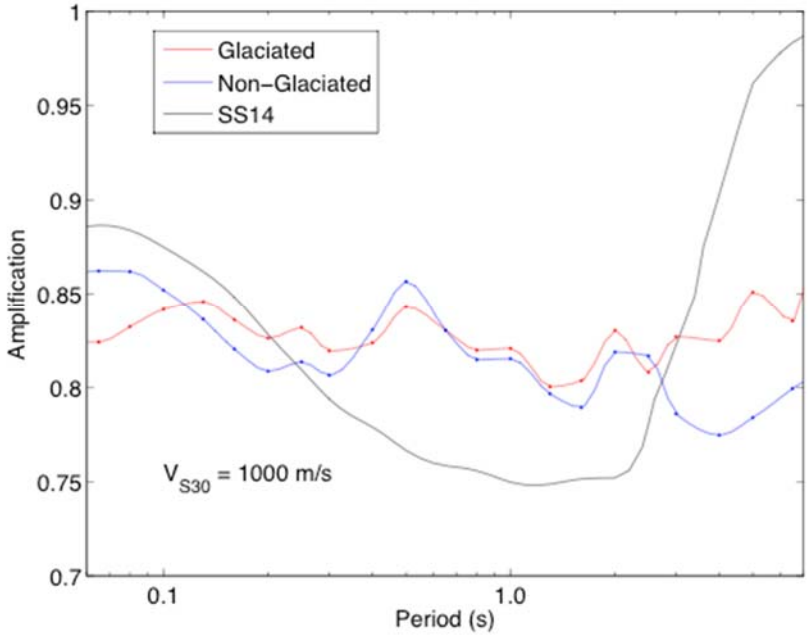

Figure 27 Amplification spectra for the glaciated model (red), non-glaciated model (blue), and SS14 (black) for VS30 = 200 m/s, 400 m/s, and 1000 m/s.

As seen in Figure 27, the models presented above predict significantly different site amplification in CENA vs active tectonic regions (SS14 model). At V_{S30} = 200 m/s linear amplification is less in CENA than that predicted by SS14. The differences between regions are less for higher velocities, (V_{S30} = 400 and 1000 m/s), but a consistent pattern is relatively period-independent site amplification in CENA vs stronger amplification features in the 0.3-3.0 period range for SS14.

Interestingly, regional variations in site amplification (between Japan, Taiwan, California, etc.) were examined by SS14 and not found. Accordingly, the appreciable differences observed here are quite significant and likely reflect the different geologic histories of stable continental regions versus active tectonic regions.

3.4.3 Effect of Glaciation

We suspect that the reason we observe a difference in site amplification behavior between glaciated and non-glaciated sites is due to the different geologic conditions, and thus different V_S profiles. Whereas sites in nonglaciated regions have V_S profiles with relatively gradual increases

in stiffness with depth (low gradient), those in glaciated regions often have much steeper gradients. Three steep gradients in glaciated regions are often controlled by large and shallow impedance contrasts. These sites presumably have had weathered geologic materials removed by glacial scour, with the remaining material being relatively competent and comprising the portions of the profiles below a strong impedance contrast. The relatively soft materials above the contrast have likely been laid down during or after glaciation.

3.4.4 Model Limitation

The model presented in this chapter has some limitations. It only accounts for linear soil behavior and does not include effects of soil nonlinearity, depth and site period that we expect influence site amplification but which cannot be constrained by observation. The broader GWG effort described in this report (Chapter 4) provides modular models for these effects that can be added to the present model in a natural log sense.

Additionally, this model should only be used for IMs including PGV and a range of PSA oscillator periods from 0.065 to 7s, and only for V_{S30} values between 150 m/s and 2000 m/s. There was not enough data outside of these oscillator period and V_{S30} ranges to constrain the model.

This model does not account for site-specific features such as kappa and details of the site condition that could be obtained for critical projects. For those cases we encourage non-ergodic site response modeling (e.g., Stewart, 2016).

Lastly, this model is for site amplification relative to 760 m/s, and therefore should be used in conjunction with predictions from GMMs with a 760 m/s rock condition, or with an additional correction for use with predictions from GMMs with a 3000 m/s rock condition as given in Section 3.2.3.

3.5 CONCLUSIONS

Although there has been significant previous work on rock-conditioned GMMs for stable continental regions (Table 4 and Table 5), models of site amplification for soil site conditions are generally absent. What models do exist are typically simulation-based using CENA conditions or

are empirical but adopted from active tectonic regions. These conditions persist to a large extent in the work performed during GMM model development for NGA-East. Those GMMs are applicable to CENA hard rock conditions (V_S = 3000 m/s; Hashash et al. 2014) or the NEHRP B/C boundary (V_{S30} = 760 m/s). This work provides empirically based site amplification models for other site conditions, including weathered rock and soil.

The empirical linear model described in this chapter is the site amplification that can be inferred from NGA-East ground motion data using the non-reference site approach. Two sets of model coefficients are regressed using a piecewise linear functional form, one for previously glaciated sites and one for non-glaciated sites. The resulting model shows a significant difference in linear site amplification between CENA and active tectonic regions (e.g. SS14). The V_{S30}-scaling is shallower in CENA and varies less as a function of PSA oscillator period. The difference in amplification between CENA and active tectonic regions is significant; it is much greater than the regional differences between different tectonic regions such as California, Taiwan and Japan.

SIMULATION BASED SITE AMPLIFICATION IN CENA

Site amplification functions are used to modify ground motions from a reference bedrock condition to a surface condition based on the geologic features of the site of interest. Site amplification has been extensively studied and evaluated empirically for seismic regions such as the Western United States (WUS) where there are abundant ground motion recordings for many sites and events. In regions of relatively lower seismicity, such as Central and Eastern North America (CENA), the lack of ground motion recordings and seismic site properties makes severely limits the empirical characterization of site amplification. Additionally differences in geologic regimes limit the use of site amplification models developed for active seismic regions for stable regions. Earthquakes in stable continental regions are usually infrequent, but still contribute to seismic hazard for infrastructure and lifelines, and a quantification of site behavior is required for engineering design and seismic hazard mapping.

The Next Generation Attenuation Relationships for Central and Eastern North America (NGA-East) project coordinated by the Pacific Earthquake and Engineering Research center (PEER) will develop models that characterize ground motions in CENA. The site effects of the ground motion models (GMM's) developed as a part of the NGA-East project for the entire CENA region are constrained by measurements at 84 of 1379 stations (Goulet et al. 2014). Site response simulations of a much larger range of site conditions and ground shaking levels are needed to supplement this very limited dataset.

Nonlinear and equivalent linear site response simulations have previously been used to develop site amplification functions and constrain empirical site amplification functions in the WUS and in CENA. In the WUS, the NGA-West project used equivalent linear simulations from Walling (2008) to constrain the nonlinearity of GMM's. The constraints on nonlinearity were updated for the NGA-West2 project by Kamai et al. (2014) for a wider range of site conditions and more versatile functional form of nonlinearity. The Kamai et al. (2014) model is designed for use within the context of GMM development, and as such, only the model coefficients related to nonlinear site amplification are provided. The linear site amplification model coefficients are intended to be regressed at the same time as other GMM model parameters.

In CENA, simulation-based site amplification functions for NEHRP-style site amplification factors have been developed for specific regions. Hashash and Moon (2011) used nonlinear site response analyses to develop depth-dependent site factors for the Mississippi Embayment, and Aboye et al. (2015) used 13,000 nonlinear and equivalent linear site response analyses to develop site amplification functions for the Charleston, South Carolina area. Neither of these sets of simulations are intended to characterize the entire CENA region, and as 1-D site response capabilities have advanced, these previous studies lack features of current best-practice nonlinear site response analyses such as constraints on shear strength and a low maximum usable frequency, f_{max}.

A large scale parametric study of 1D site response simulations to develop ergodic amplification functions for CENA is presented. The site response simulations presented in this paper will be used to develop base case (i.e. the free field amplification without basin effects) linear and nonlinear site amplification models for CENA that can be used independently of GMM development and use the current best-practice nonlinear site response analyses procedures. To capture the range of site conditions and seismic hazard in CENA, many more simulations will be used than previously. This study presents 1.7 million site response simulations compared to the next largest study of 13,000 simulations by Aboye et al. (2015). Parameters required to quantify site amplification can broadly be split into two categories: bedrock ground motion parameters and site parameters. A database of ground motions characteristic of the hard bedrock condition in CENA is developed with a range of intensities, spectral shapes, magnitudes, and distance. Site parameters are systematically varied and include V_S structure (including depth of soil material) and nonlinear soil properties. Site response analyses are computed using DEEPSOIL (Hashash et al. 2015), which provides a platform for calculation of frequency domain linear elastic (LE), equivalent linear (EL) and nonlinear (NL) 1D site response analyses.

3.6 STRUCTURE OF PARAMETRIC STUDY

Site response simulations presented in this study will be used in the development of linear and nonlinear site amplification functions for the CENA seismic region. The simulation design must therefore account for the variability in site conditions expected in CENA for the amplification functions to be usable across the entire region, and the simulation design must include parameters to constrain both the linear and nonlinear site amplification. The range of geologic

conditions in CENA is reflected by the selection and variation of ground motions and V_S profile structure which are the most influential parameters in the development of linear site amplification functions. The range of material types and properties in CENA is reflected by the selection and variation of the nonlinear site properties which are the most important parameters in the development of nonlinear site amplification functions.

The relatively low computational cost of 1-D site response simulations allows the development of a large number of simulations to capture uncertainty. Figure 28 shows a parametric pseudo-factorial tree structure for the parametric study. The parametric study tree details the approach to generating soil columns (i.e. the representation of a single site V_S and soil properties) that reflect the variability of site conditions in CENA for use in site response analyses. In total, Figure 1 represents 1,747,278 site response analyses, 582,426 of each LE, EL and NL of 70,650 unique soil profiles. The upper branch of Figure 28 represents the generation of 70,200 profiles with relatively soft soil material above reference rock as below:

- Ground Motions: 247 ground motions representative of a range of durations and intensities with frequency content characteristic of the geologic conditions in CENA.
- Representative V_S Profiles: 10 characteristic soil V_S profiles derived from measured V_S profiles in CENA
- Soil Properties: 9 geology-based combinations of soil index and strength properties. Soil properties are matched with representative V_S profiles for a total of 13 unique combinations
- Randomized V_S profiles: 30 random realizations of the V_S profile for each combination of representative soil V_S profile and corresponding soil properties. Ground motions are evenly and randomly distributed to the random V_S realizations. Each soil profile will therefore be paired with 8-9 bedrock motions and the analysis tree presented in Figure 28 is only pseudo-factorial.
- Randomized Dynamic Curves: 3 random realizations of the nonlinear curves of each random V_S profile
- Profile Depth: 10 depth bins of surficial material. The representative soil velocity profiles will extend from the ground surface to the bottom of the depth bin

- Weathered Rock Zone Model: 6 models for V_S structure of the bottom of the soil velocity profiles above the reference rock condition. All weathered rock zone models have the same soil index properties which are separate from the soil index properties of the surficial soil material
- Analysis Type: 3 analyses of the site response: frequency domain linear elastic (LE), frequency domain equivalent linear (EL) and time domain nonlinear (NL). Parameters used in the solution of the EL, NL and LE analysis methods are provided in Table 8

The lower branch of Figure 28 closely follows the structure of upper branch and represents the generation of 450 profiles without soft soil material above reference rock. Profiles generated with this branch are profiles where the weathered rock zone is at the ground surface and no soil material is present. The levels of the lower branch are analogous to the upper branch.

The sections below detail the creation of bedrock ground motions and soil profiles for use in the site response analyses following the structure of the parametric study tree shown in Figure 28.

Table 8: EL, NL, and LE analysis parameters for site response calculation. Detailed explanations of the chosen analysis parameters are available in the DEEPSOIL manual (Hashash et al. 2015)

Analysis Parameter	Analysis Type	Value
Number of iterations	EL	1
	LE	1
Shear Stress Strain Ratio	EL	0.65
Complex Shear Modulus Type	LE	Frequency Independent
	EL	Frequency Independent
Step Control	NL	Flexible
Maximum Strain Increment	NL	0.005
Time History Interpolation	NL	Linear

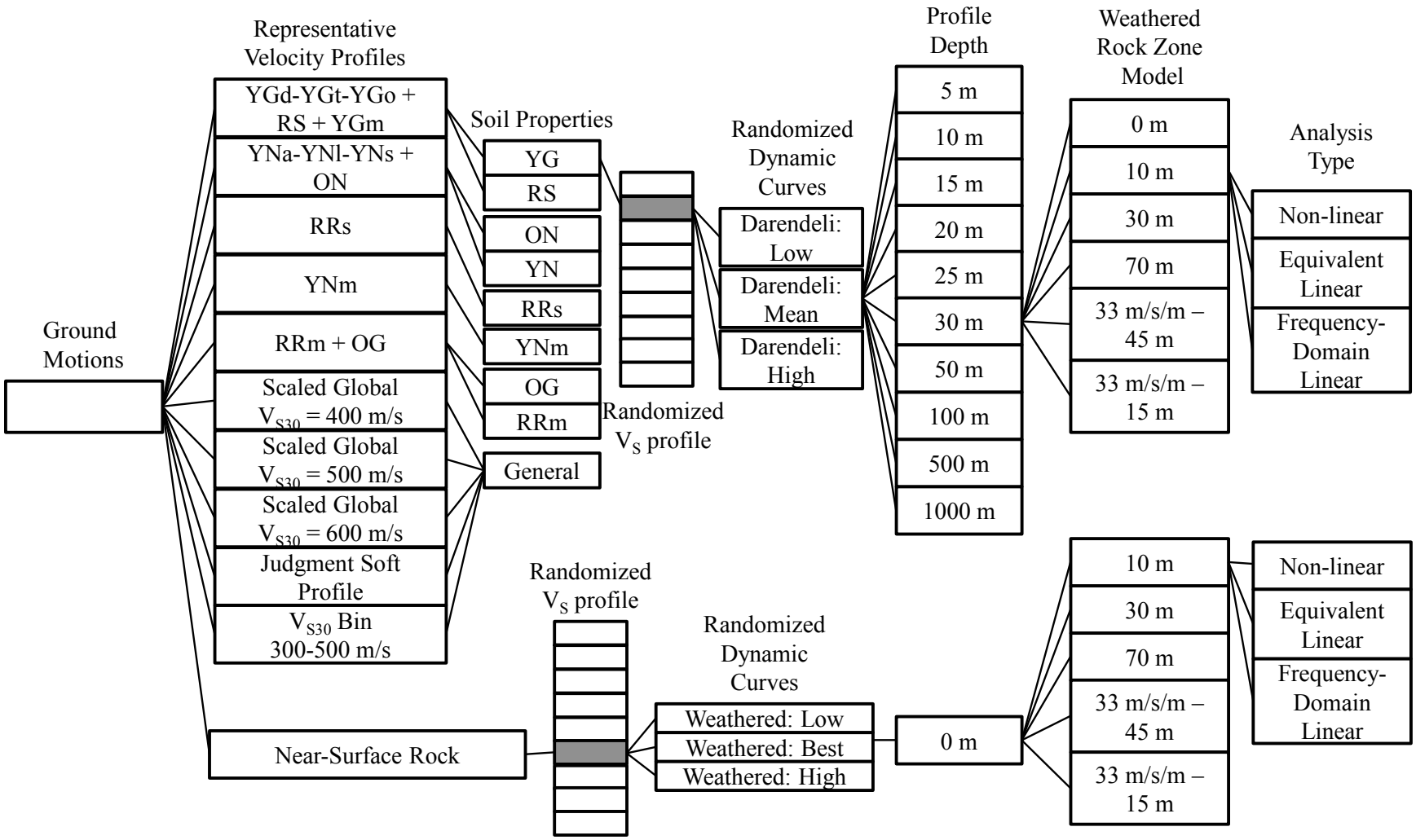

Figure 28: Parametric study analysis tree

3.7 BEDROCK GROUND MOTIONS

3.7.1 NUREG Motions:

Motions were selected from the synthetic and recorded CENA rock motions developed from WNA motions and described in NUREG-6728 (McGuire et al. 2001). The original NRC motions included 15 sets (i.e., two horizontal components) of motions for 10 magnitude/distance bins, as listed in Table 9. From these motions, only motions with time steps at least as small as 0.005 s were selected. As a result of removing motions with time steps greater than 0.005 s, each magnitude/distance bin contains a different number of motions. The resulting motion sets for each magnitude and distance bin are shown in Table 9. There are a total of 93 sets of motions (i.e., 186 horizontal motions). The median response spectra, median response spectra normalized by S_a at 0.01 s and median FAS are shown in Figure 29.

Table 9 Summary of Selected NUREG motions

M	R (km)	Number of sets*
4.5-6	0-50	0 (14)
	50-100	4 (7)
6-7	0-10	2 (5)
	10-50	1 (8)
	50-100	0 (5)
	100-200	0 (6)
7+	0-10	0 (12)
	10-50	0 (10)
	50-100	0 (10)
	100-200	0 (9)
Total		93 sets

*The number in the brackets is the number of simulated motions, while the number outside the brackets is the number of recorded motions.

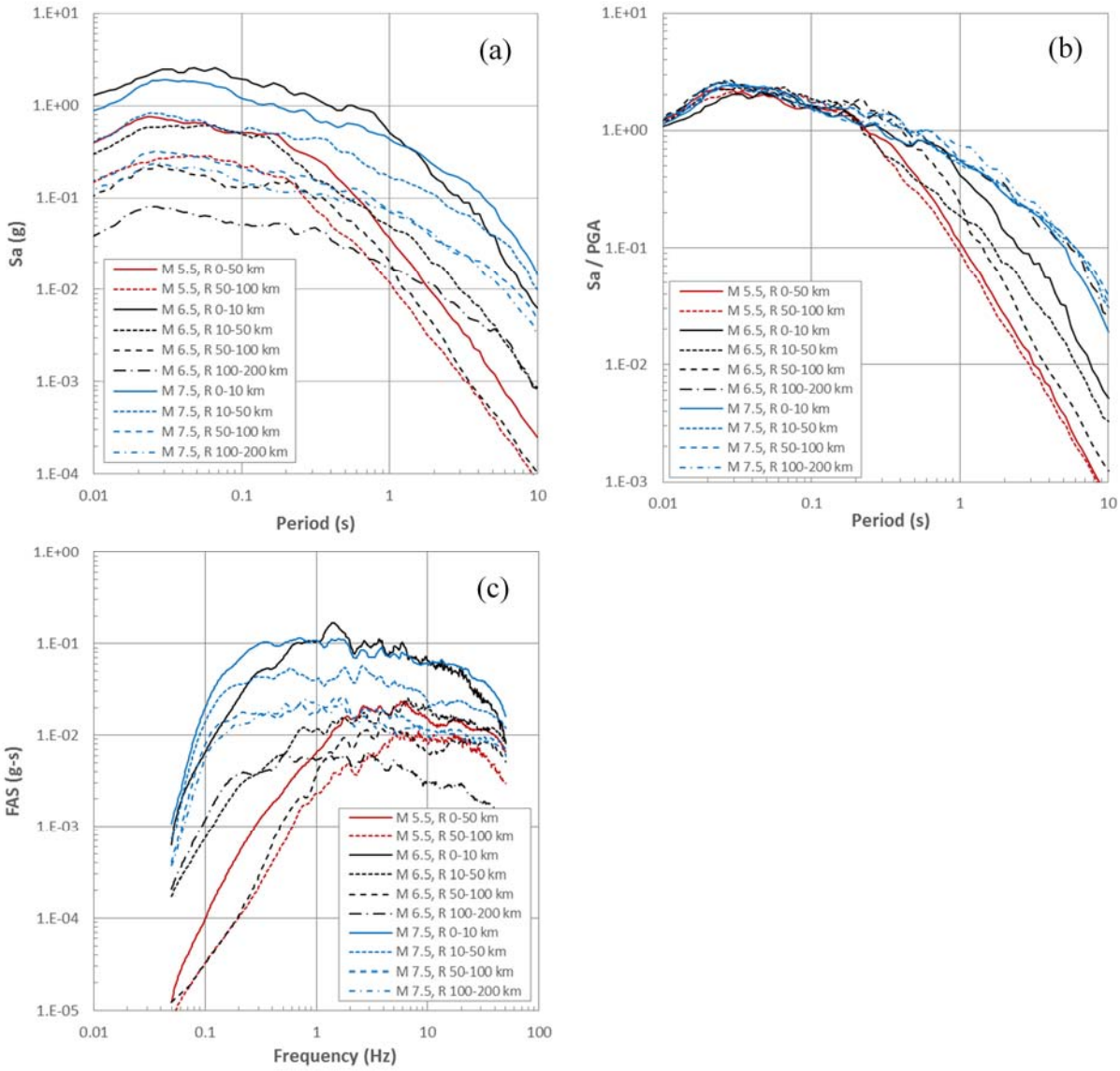

Figure 29 (a) Median response spectra, (b) median response spectra normalized by S_a at 0.001 s, and (c) median FAS for the NUREG motions

3.7.2 SMSIM Generated Motions

Rock motions appropriate for hard rock CENA conditions were stochastically generated for different earthquake magnitudes (M = 5.5, 6.5, and 7.5) and a range of distances using the program SMSIM (Boore 2005). The stochastic parameters used to generate these motions are listed in Table 10. These parameters are based on the published values of Boore and Thompson (2015).

Table 10 SMSIM Stochastic Parameters used to Generate Input Motions

General parameters	
ρ (g/cm^3)	2.8
β (km/s)	3.7
patitn	0.707
Radpat	0.55
f_s	2
Stress (bars)	400
$1/f_a$	0.5
$1/f_b$	0.5
f_max	0
kappa	0.006
dkappadmag	0
amagkref	6
f_cut	0
Nslope	8

Path duration	
nknots	8
Rdur (i)	Dur (i)
0	0
15	2.6
35	17.5
50	25.1
125	25.1
28.5	28.5
392	46
600	69.1
Slope of last segment	0.111

Crustal amplification	
namps	14
Famp (i)	Amp (i)
0.001	1
0.00783	1.003
0.0233	1.010
0.04	1.017
0.0614	1.026
0.108	1.047
0.234	1.069
0.354	1.084
0.508	1.101
1.09	1.135
1.37	1.143
1.69	1.148
1.97	1.150
2.42	1.151

For M = 5.5, 10 motions with point source distances, R, ranging from 10 km to 50 km were generated, while for M = 6.5 and 7.5, 20 motions with point source distances ranging from about 5 km to 150 km were generated (Table 11). The time step was specified as 0.004 s to maintain a Nyquist frequency of 125 Hz. The acceleration response spectra of the SMSIM motions are shown in Figure 30 and the Fourier amplitude spectra are shown in Figure 31. There are a total of 50 motions generated from SMSIM

Table 11 M and R corresponding to SMSIM motions

	M=5.5	M=6.5	M=7.5
R	10	5	6
	12.0	6	7.1
	14.3	7.2	8.4
	17.1	8.6	10
	20.4	10.2	11.8
	24.5	12.2	14
	29.2	14.6	16.6
	35.0	17.5	19.6
	41.8	20.9	23.3
	50	25.0	27.6
	/	30	32.6
	/	35.8	38.7
	/	42.8	45.8
	/	51.2	54.3
	/	61.3	64.3
	/	73.3	76.2
	/	87.7	90.2
	/	104.9	106.9
	/	125.4	126.6
	/	150	150

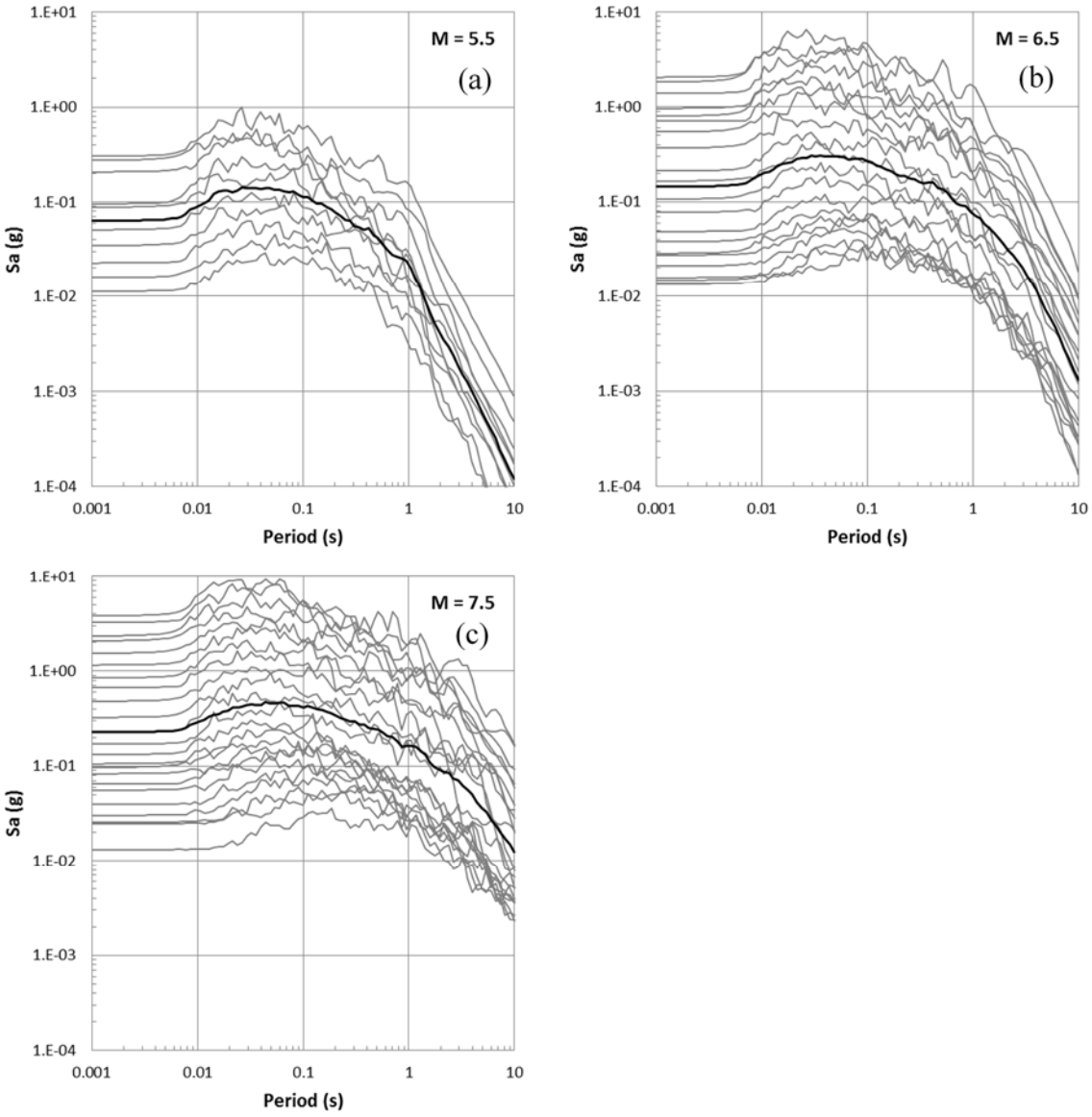

Figure 30 Acceleration response spectra of SMSIM motions at (a) M = 5.5, (b) M=6.5, (c) M=7.5

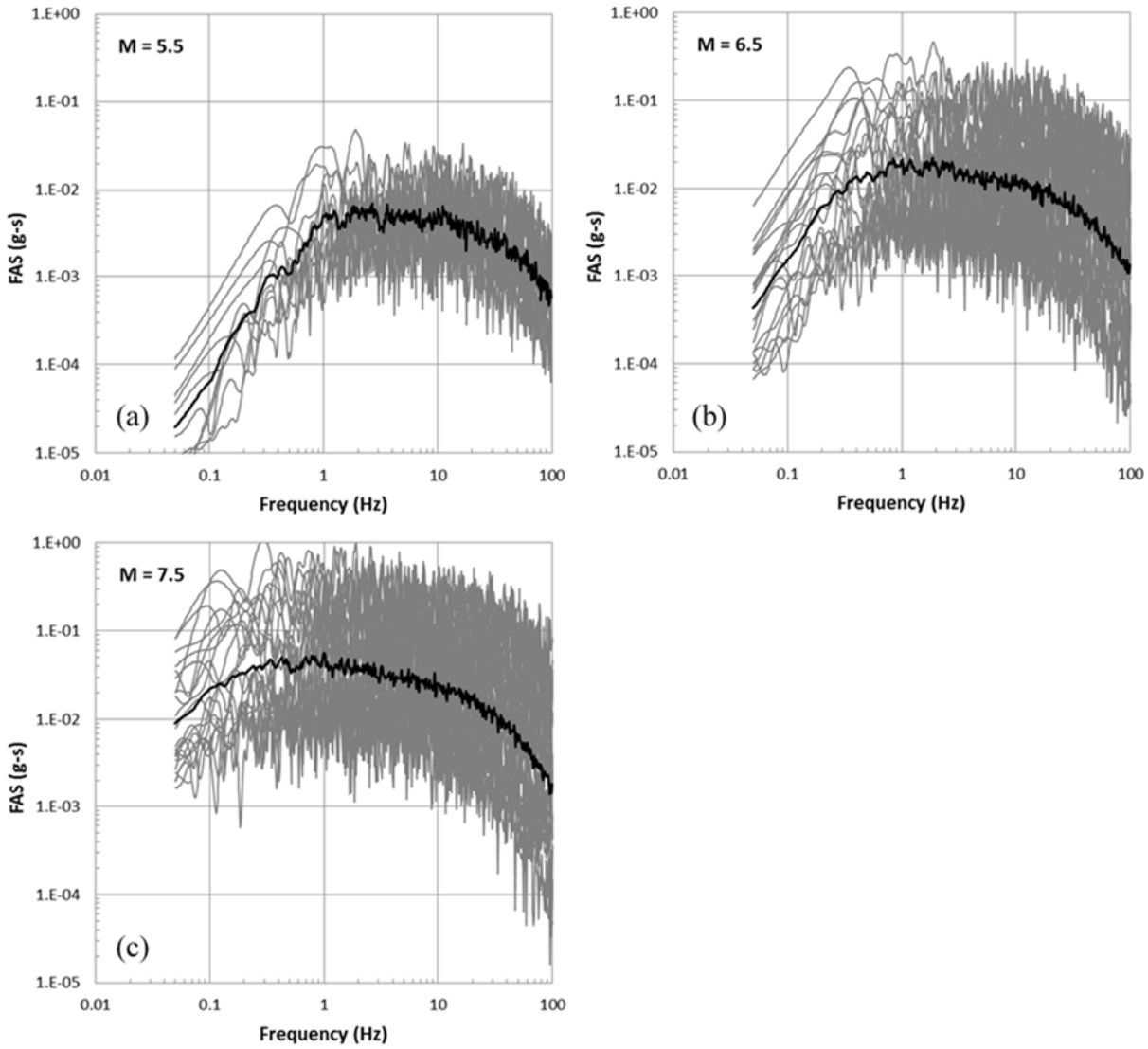

Figure 31 Fourier Amplitude Spectra of SMSIM motions at (a) M =5.5, (b) M = 6.5, (c) M=7.5

3.7.3 Composite Ground Motion Characteristics of NUREG and SMSIM Motions

The full input rock motion data set includes 236 records (186 from NUREG and 50 from SMSIM). Figure 32 plots the PGA and PGV of each motion to provide a visualization of the range of intensities of the selected motions. The motions span PGA from about 0.01 g to 4 g and PGV from 0.3 cm/s to 300 cm/s. At any value of PGA, the larger magnitude events generally have larger PGV due to the stronger long period content for larger magnitude events. The SMSIM values of PGA and PGV are consistent with those from the NUREG simulated motions.

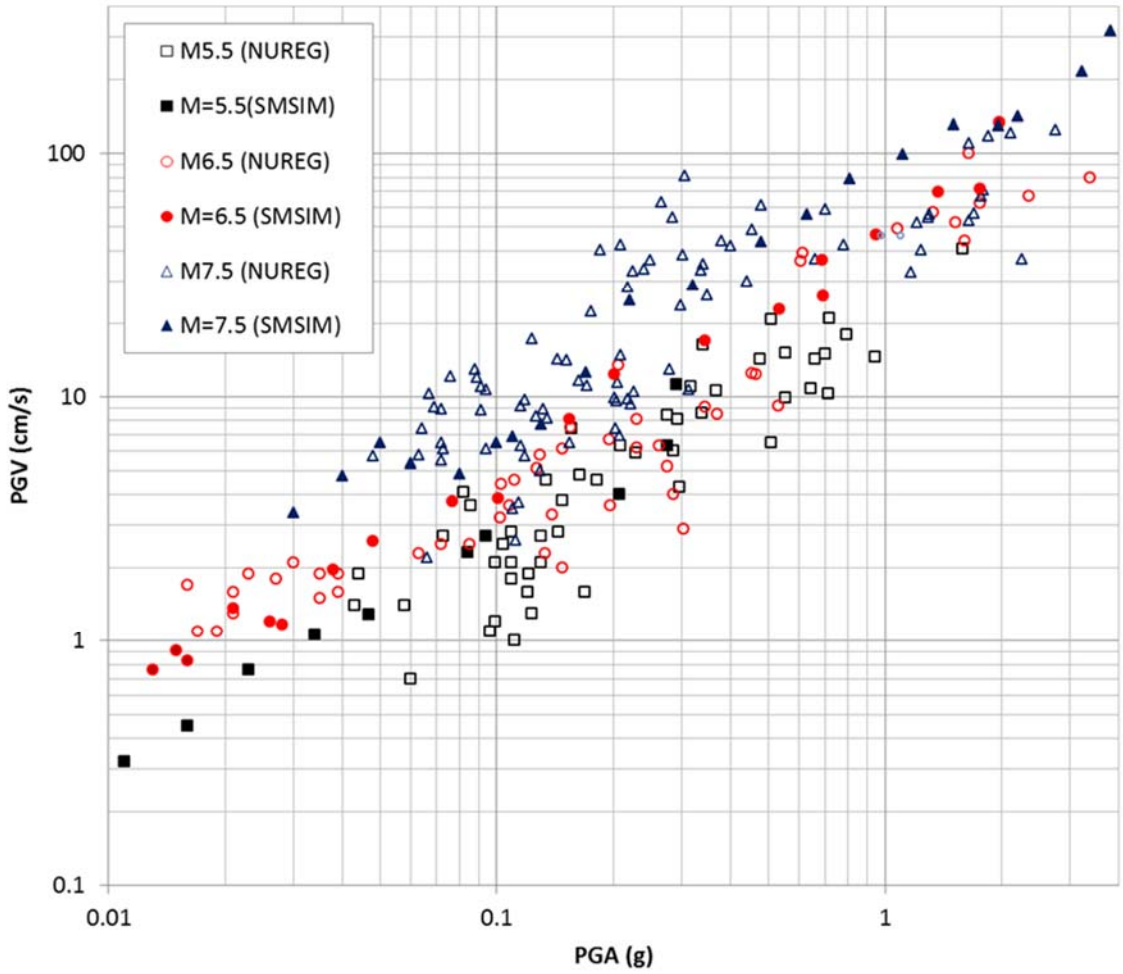

Figure 32 PGA and PGV values of selected CENA input rock motions

3.8 SOIL PROFILES

3.8.1 V_S Profiles

The V_S profiles used in this study consist of three main regions: a relatively low V_S region near the ground surface to represent soil material, a more stiff weathered rock zone under the soil region to transition to the reference rock condition, and at the bottom of the soil column the CENA reference rock condition of 3000 m/s. The depth of soil V_S region is varied to capture

different site conditions, and the combined soil V_S profile and weathered rock region are randomized to capture uncertainty in V_S.

A total of 9 characteristic V_S profiles are derived from 821 collected V_S data in CENA from literature and open file reports to represent the soil V_S behavior in CENA. A detailed description of the process used to create the characteristic V_S profiles used as inputs to randomization is presented in APPENDIX A. The steps to create the 9 characteristic V_S profiles were:

- Remove rock-like material from the V_S profiles
- Sort profiles and calculate the log-mean of V_S as a function of depth
- Smooth the log-mean profiles to remove features in the mean V_S profiles resulting from changing amounts of data as a function of depth such as sharp changes in V_S near the ground surface and regions within the profile where V_S decreases as a function of depth
- Extend the smoothed log-mean V_S profiles to a depth of 1000 m.
- Combine similar log-mean profiles

Data from 821 V_S profiles were used to create 9 characteristic V_S profiles using the above procedure and are shown in Figure 33. The characteristic V_S profiles developed fall into two categories: 5 V_S profiles (YNm, RRs, YNa-YNl-YNs+ON, RRm+OG, and YGd-YGt-YGo+RS+YGm) are derived and named after the geologic classes presented in Kottke et al. (2012) and shown in Table 12, and 4 V_S profiles (Judgement Soft, and the Scaled Global Log-Mean profiles) are judgement based derivations of the V_S profile data to capture a range of V_S behaviors as a function of depth and V_{S30} values as described in APPENDIX A. The V_{S30} of the characteristic V_S profiles is computed and shown in Table 13.

ix weathered rock models are developed to transition between the soil-like characteristic V_S profiles and the 3000 m/s CENA reference rock condition (Hashash et al. 2014). The definition of the 3000 m/s reference rock condition in Hashash et al. (2014) which uses many of the same V_S profiles in this study, also outlined properties of a weathered region above the hard bedrock condition. Weathered rock zone models either have a prescribed depth or prescribed gradient. The 4 depth-based models which have a defined thickness (0, 10, 30, and 70 m) and V_S at the top (2000 m/s) and bottom (3000 m/s) of the weathered rock zone, and the 2 gradient-based models that have a defined V_S at the top (1500 m/s and 2500 m/s) and bottom of the weathered rock zone

and gradient of V_S (33 m/s/m) within the weathered rock zone with resulting thicknesses of 45 and 15 m. The 30 m depth-based model has the same gradient of 33 m/s/m as the gradient-based models.

The weathered rock zone models are randomized simultaneously with the V_S and added to the bottom of each characteristic V_S profile at each profile depth investigated. An example of the six weathered rock zone models at the bottom of the 50m RRs characteristic V_S profile is shown in Figure 34. More details on the selection of the weathered rock zone V_S models are given in APPENDIX A.

Characteristic V_S profiles are randomized using guidelines from Toro (1995) as detailed in APPENDIX B. V_S layer thickness randomization was not performed, and randomization parameters were selected for the V_S randomization that result in perfectly correlated V_S between soil layers. These selection produce randomized V_S profiles that are lognormally distributed geometrically scaled input characteristic V_S profiles with log standard deviation, $\sigma_{lnV} = 0.2$. Numerical and other concerns about nonlinear site response analyses with V_S reversals (e.g. decreases in V_S as a function of depth) that are not shared by all authors on this report resulted in the selection of simplified parameters for the Toro (1995) model. The minimum bound of the V_S randomization is derived from the lowest measured V_S values in CENA as a function of depth in the same way as the characteristic V_S profiles and is shown in Figure 33, and the maximum bound of V_S randomization is 3000 m/s. Profiles generated with V_S values below the minimum bounding profile are re-randomized. Profiles generated with V_S values above 3000 m/s are terminated at 3000 m/s. A set of 30 V_S randomizations is made for each of the 13 combinations of characteristic V_S profiles and soil properties. The V_S randomizations are truncated at each soil depth and appended with the weathered rock zone V_S structure to produce the full V_S profile that can be assigned nonlinear soil properties.

Table 12: CENA Geology types used to sort V_S profile data collected for derivation of geology-based characteristic V_S profiles. Modified after (Kottke et al. 2012)

Major Unit and Age	Sub-Unit	Abbreviation
Old Glacial Sediments (Older than Wisconsin)	None	OG
Young Glacial Sediments (Wisconsin and younger)	Glaciomarine and Lacustrine	YGm
	Outwash and alluvium	YGo
	Tills	YGt
	Discontinuous Till	YGd
Old Non-Glacial Sediments (Mid-Pleistocene and older)	None	ON
Young Non-Glacial Sediments (Holocene and late Pleistocene)	Alluvium	YNa
	Loess	YNl
	Lacustrine, Marine and Marsh	YNm
	Beach, dune, and sheet sands	YNs
Residual Material	Residual material from metamorphic and igneous rock	RRm
	Residual material from sedimentary rock	RRs
	Residual from soils	RS

Table 13: V_{S30} of characteristic Velocity Profiles

Characteristic Profiles	V_{S30} (m/s)
YNm	240
RRs	356
YNa-YNl-YNs +ON	252
RRm + OG	391
YGd-YGt-YGo + RS + YGm	333
V_{S30} Bin = 300-500 m/s	383
Scaled Global Log-Mean to V_{S30}= 600 m/s	616
Scaled Global Log-Mean to V_{S30}= 500 m/s	513
Scaled Global Log-Mean to V_{S30}= 400 m/s	411
Judgment Soft	148

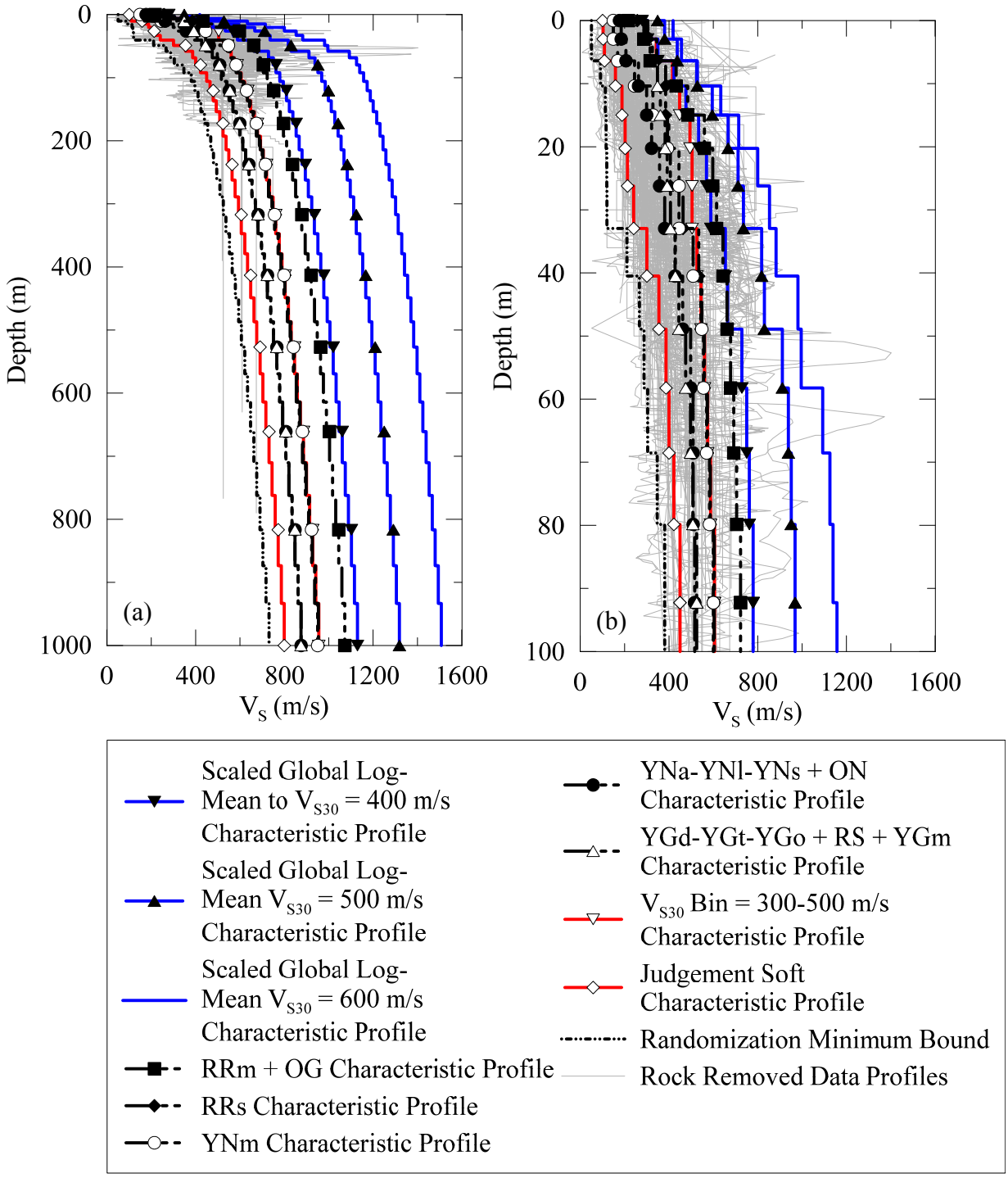

Figure 33: All characteristic profiles to 1000 m (a) and 100 m (b)

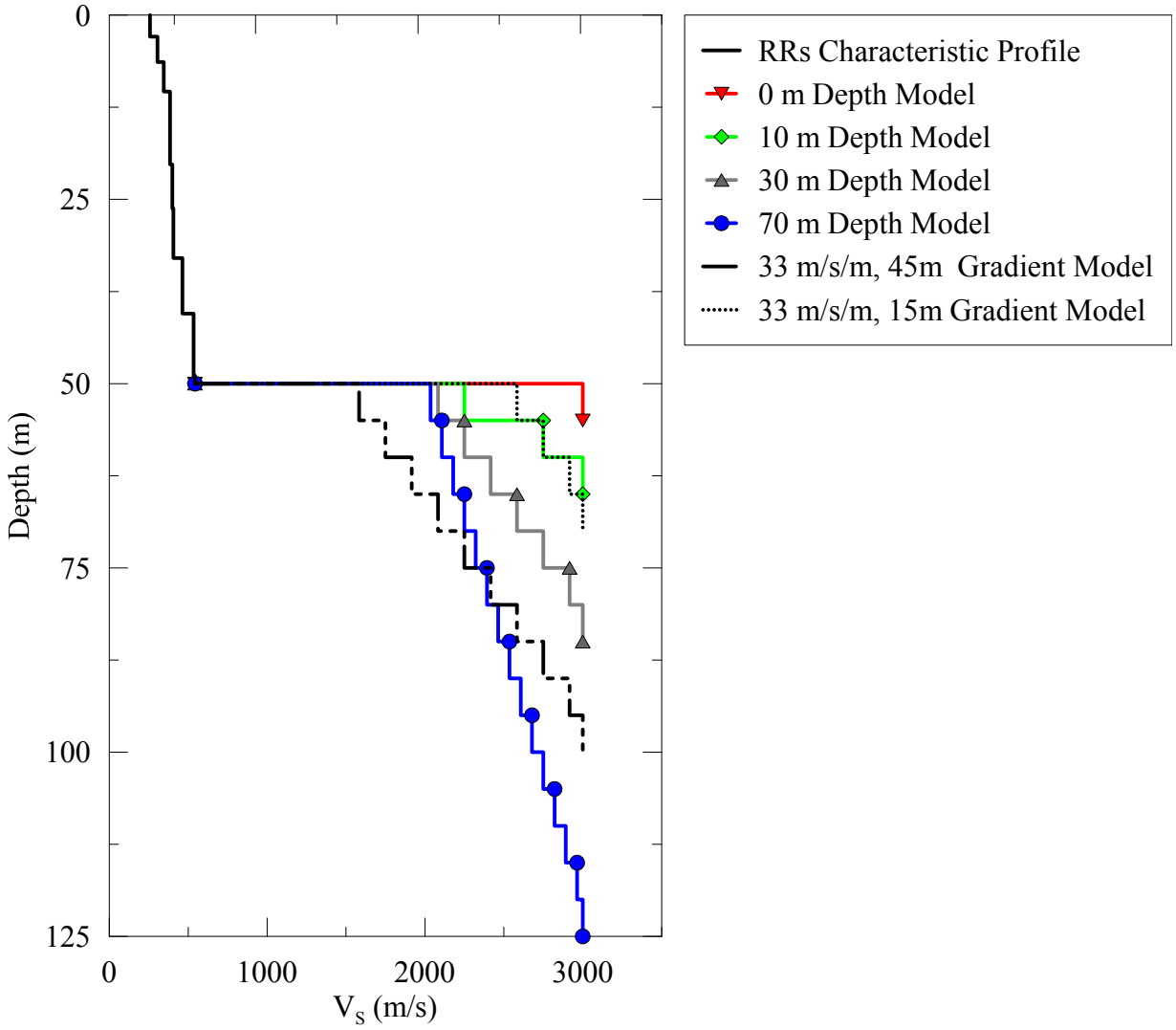

Figure 34: Weathered Rock Models applied to RRs characteristic profile at the 30 m depth bin

3.8.2 Soil Properties

Nonlinear G/G_{max} and damping curves define the nonlinear response of soil during earthquake loading. In this study, nonlinear soil properties assigned to the randomized V_S profiles (including weathered rock zone) will be created using the empirical correlations for G/Gmax and damping curves in Darendeli (2001). Darendeli (2001) requires the selection of soil index properties (i.e. plasticity index (PI) and overconsolidation ratio (OCR)) to generate G/Gmax and damping curves as a function of confining stress which can be calculated from the soil unit weight (γ) and friction angle (φ). Soil properties assigned to characteristic V_S profiles as shown in Figure 28 and

detailed in Table 14. The weathered rock zone has index properties different from the soil region of the V_S profile and also shown in Table 14. Selection of index parameters in Table 14 is detailed in APPENDIX C.

Three random realizations of soil stiffness are produced for each randomized V_S profile using the error in the G/Gmax and damping curves in Darendeli (2001) and is detailed in APPENDIX B. Randomized nonlinear curves are perfectly correlated as a function of depth, and G/G_{max} curve is perfectly negatively correlated with the Damping curve. One randomization is produced using the mean G/Gmax and Damping curves calculated from Darendeli (2001) The other two randomizations for the G/Gmax curve at a site are perfectly negatively correlated. Therefore all three realizations of soil stiffness at a site are functions of a single random number, ε. One realization uses the mean Darendeli (2001) curve, one realization has less strain softening behavior than the mean curve (+ε), and one realization has more strain-softening behavior than the mean curve (-ε).

After nonlinear curve randomization, the strength controlled GQ/H hyperbolic model is fit to the layers of the soil column. The randomized nonlinear curves produced with Darendeli (2001) in this study are difficult to directly fit with the GQ/H hyperbolic model to produce realistic nonlinear curves for two reasons: curves developed with Darendeli (2001) do not account for V_S and therefore implied shear strength of the soil layer, and the randomization procedure directly modifies the G/Gmax and Damping curves and can produce unrealistic shear stress-shear strain behaviors at large strains. To address these difficulties and produce G/Gmax and damping curves consistent with expected soil behavior, a V_S-dependent strength model is used to determine target implied shear strength values for the G/Gmax and damping curves, and a multi-step fitting procedure is used to generate fits of the GQ/H hyperbolic model that result in fits that capture the target implied shear strength at 10% while preserving the small-strain nonlinear behavior. The strength model and fitting procedure used to fit the GQ/H hyperbolic model to the nonlinear curves in the parametric study are detailed in APPENDIX C. Figure 35 shows an example of the nonlinear curve fitting procedure for the mean and +/- 1 σ random curve realizations of a soil layer.

Table 14: Selected soil properties for use in parametric study

Material	PI (%)	Unit Weight (kN/m^3)	OCR	Friction Angle (φ°)	Associated Characteristic V_S Profiles		
General	15	19	1.5	25	Scaled Global	V_{S30}-Binned	Judgement Soft
Weathered Rock Zone	5	21	3	40	Weathered Rock Zone		
Young Glaciated	15	18.9	1.3	30	YGd-YGt-YGo + RS + YGm		
Old Glaciated	20	18.6	3	30	RRm + OG		
Young Nonglaciated	20	18.5	1.3	30	YNa-YNl-YNs + ON	YNm	
Old Nonglaciated	30	19	2	30	YNa-YNl-YNs + ON		
Residual Soil from Sedimentary Rock	24	19.4	3	25	RRs		
Residual Soil from Metamorphic Rock	10	19	3	25	RRm + OG		
Residual Soil	30	19.3	3	25	YGd-YGt-YGo + RS + YGm		

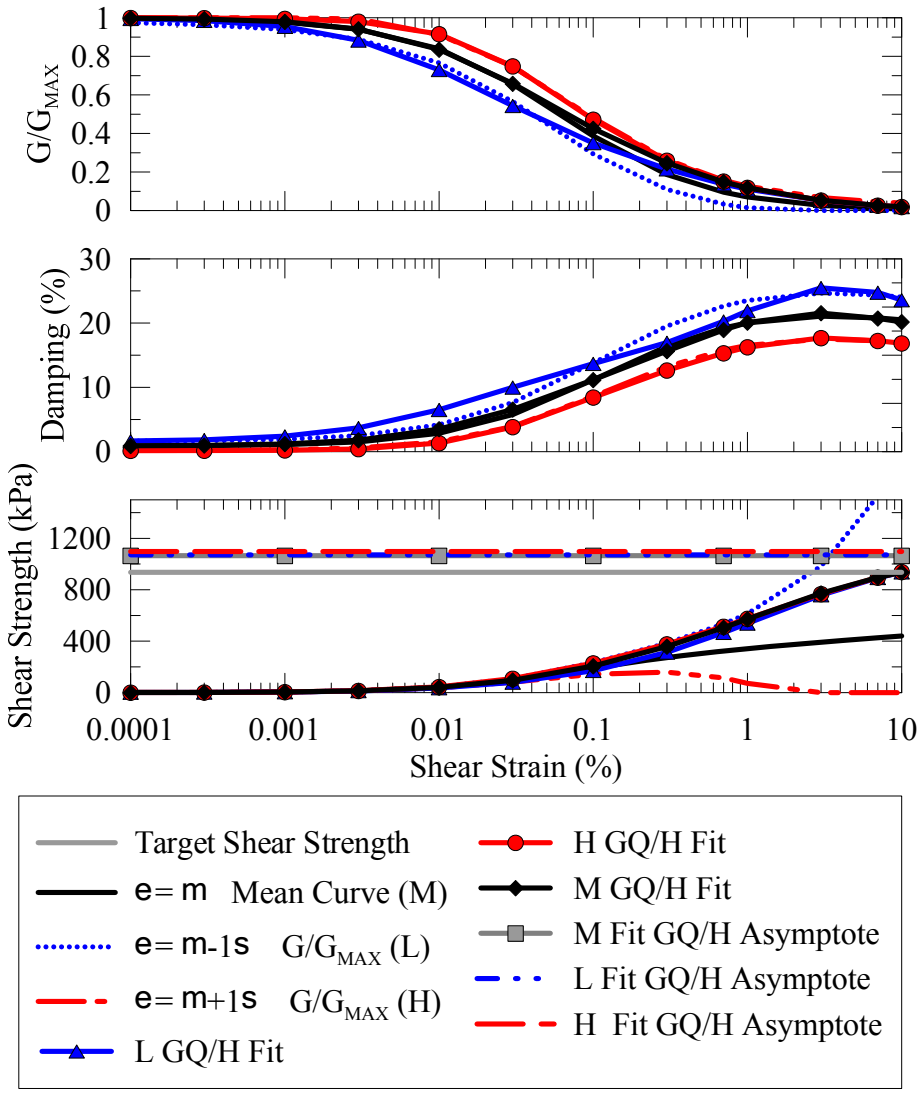

Figure 35: GQ/H Fits a soil layer with V_{S30} = 500 m/s, 50 m depth, γ = 19.0 kN/m^3, PI = 15 %, and OCR = 1.5 for the mean and +/- 1 σ G/G_{max} and damping curves from Darendeli (2001)

3.8.3 D_{min} and κ

At high frequencies the shape of the Fourier amplitude spectrum of the S-wave acceleration can be characterized by exponential decay (Anderson and Hough 1984). Anderson and Hough (1984) introduced κ as a spectral decay factor to model this exponential decay, $e^{-\pi\kappa f}$. They also observed that κ increases with distance from the source(r), and proposed a linear relationship between κ and r, $\kappa(r) = \kappa_0 + \kappa_1 * r$. In this expression, κ_0 is the zero-distance κ, representing

the attenuation of seismic waves within the geological structure beneath the site. The slope κ_1 represents the attenuation due to the horizontal propagation of seismic waves within the crust.

The value of κ_0 at the surface of a site can be computed from the shear wave velocity (V_s) profile and the anelastic attenuation factor (Q) profile using (Hough and Anderson 1988):

$$\kappa_0 = \int \frac{1}{Q(z) \cdot Vs(z)} \cdot dz \tag{12}$$

The attenuation factor, Q, can be related to the small-strain damping ratio, Dmin, which is more commonly used in engineering to represent energy dissipation. This relationship is Q = 1 / ($2D_{min}$). when considering the contribution to κ_0 from the soil layers overlying a rock half space, (12) can be modified to:

$$\kappa_0 = \kappa_{0,rock} + \int \frac{2 \cdot D_{min}(z)}{Vs(z)} \cdot dz \tag{13}$$

Thus, given the velocity profile and damping profile at a soil site and estimate of κ_0 for the underlying rock half space ($\kappa_{0,rock}$), the high frequency decay of Fourier amplitude spectrum, as modeled through the parameter κ_0, can be computed from (13).

In this study, our goal is to constrain the damping profiles used in our site response model. Specifically, κ_0 values are computed for all of the 10 baseline shear wave velocity profiles and are different approaches to model damping. These κ_0 values are compared with κ_0 values in the literature and those measured from earthquake recordings at soil sites.

3.8.3.1 κ_0 Values of Site Response Models

Ten baseline shear wave velocity models were developed as part of this study using a shear wave velocity database for the CENA (APPENDIX A). These shear wave velocity profiles represent different geologic units and are shown in Figure 36. Each of these baseline profiles is underlain with a hard-rock half space of Vs = 3,000 m/s. Analyses were performed with these profiles extending to 1,000 m, and also truncated at depths of 10 m, 30 m, 50 m, 100 m, and 500 m. The generalized properties of each of the baseline profiles in terms of Vs30, plasticity index (PI), unit weight, and over-consolidation ratio (OCR) are listed in Table 15.

Different options are available to model the profile of D_{min} for use in equation (2) to compute κ_0. From a seismological perspective, Campbell (2009) developed four models that relate Q to Vs, with the different models capturing the significant uncertainty in the data. Figure 37a shows plots of the four Q-Vs relationships. Model 1 is a linear relationship between Q and Vs across all Vs ($Q = 7.17 + 0.0276V_s$). Model 2 is the same as Model 1 except that Q_{ef} is constrained to 50 when V_s > 800 m/s. Model 3 assigns Q=10 when $Vs \leq 366\, m/s$,, and $Q = 0.00382\, V_s^{1.333}$ when $Vs > 366\, m/s$. Model 4 is the same as Model 3, except that it constrains Q = 50 when V_s > 800 m/s, similar to Model 2. Figure 37b shows the corresponding D_{min} vs. Vs relationships. The damping values generally are between 1% and 2% for Vs greater than 800 m/s, and increase to values above 3% for Vs less than about 500 m/s. For this study we used Model 1 to represent the Q-Vs relationship. Models 2 and 4 were not used because they include an instantaneous increase in Q at Vs = 800 m/s, and Model 3 was not used because of the very large damping values predicted for Vs between 100 and 500 m/s.

From a geotechnical perspective, Darendeli (2001) developed a D_{min} model based on measured values from laboratory testing of soil samples obtained from geotechnical sites. This model predicts D_{min} as a function of PI, OCR, and mean effective stress (σ_o') using $D_{min} = (0.8 + 0.0129 * PI * OCR^{-0.1}) * {\sigma_o'}^{-0.29}$. This model generally predicts D_{min} values between 0.3% and 2%, with the values decreasing with increasing depth. These values tend to be smaller than those predicted by the Campbell (2009) models. The Darendeli (2001) model predicts smaller damping because it is based on laboratory measurements of damping, which only capture material damping and not the attenuation caused by wave scattering in the field.

Using the 10 baseline Vs profiles, corresponding D_{min} profiles were developed using the Campbell (2009) Q-Vs Model 1 (Figure 38a). Using the geotechnical parameters in Table 1 and the mean effective stress computed from an assumed ground water table of 0 m and K_0= 0.5, D_{min} profiles were developed using the Darendeli (2001) model (Figure 38b). The D_{min} profiles developed from Campbell (2009) vary noticeably between the sites because the damping model is proportional to Vs, which varies considerably from site to site. The D_{min} profiles developed from Darendeli (2001) do not vary considerably between sites because the geotechnical parameters (Table 15) do not vary significantly from site to site.

As noted earlier, site response analyses will be performed with the 10 baseline profiles truncated at different depths between 10 m and 1000 m. The Vs profiles and D_{min} profiles truncated at different depths are used with equation (13) to compute k_0. For these analyses $\kappa_{0,rock}$ is taken as 0.006 s, which is consistent with the value for CENA hard rock recommended by the NGA-East Geotechnical Working Group (Campbell et al. 2014). Figure 39 shows the computed k_0 values as a function of soil depth for the Campbell (2009) and Darendeli (2001) damping profiles. For both damping models, k_0 increases with soil depth due to the increase in the travel path over which the damping acts. However, the k_0 values derived from the Campbell (2009) damping model are significantly larger and vary more considerably among the sites than the values derived from the Darendeli (2001) model. This effect is a direct result of the differences in the D_{min} profiles shown in Figure 38.

Table 15 General properties of the baseline profiles

Sites	V_{S30} (m/s)	PI	Unit Weight (kN/m^3)	OCR
Soft	148	15	19	1.5
Ynals+ON	252	20	18.5	1.3
YNM	240	15	19	1.5
Bin 300-500	383	15	19	1.5
RRM+OG	391	10	19	3
RRS	356	24	19.4	3
RS+YGdto+Ygm	333	15	18.9	1.3
Scaled 400	411	15	19	1.5
Scaled 500	513	15	19	1.5
Scaled 600	616	15	19	1.5

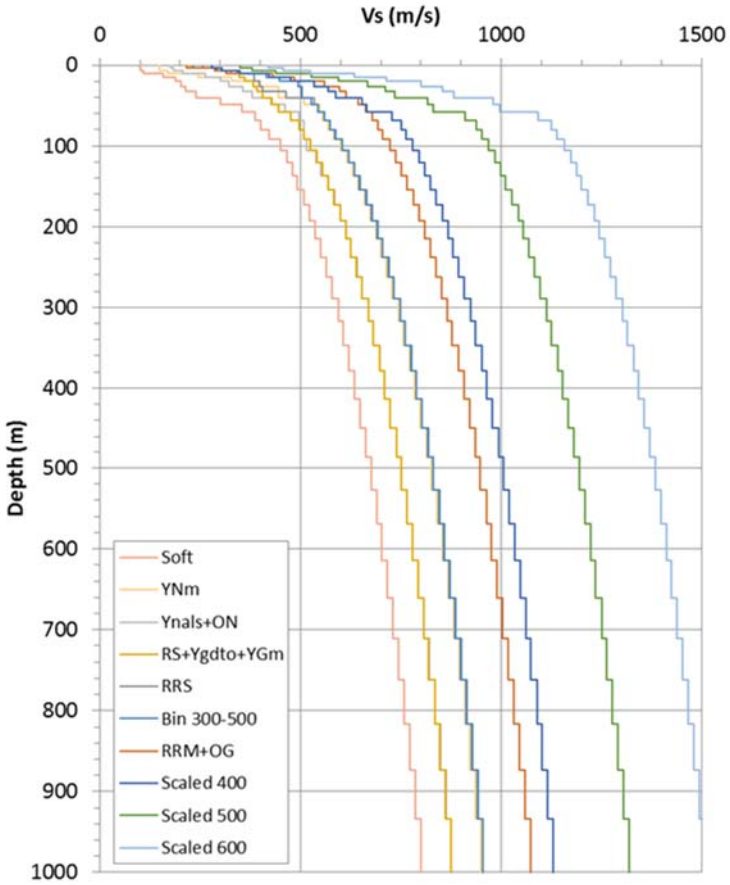

Figure 36 General properties of the baseline profiles

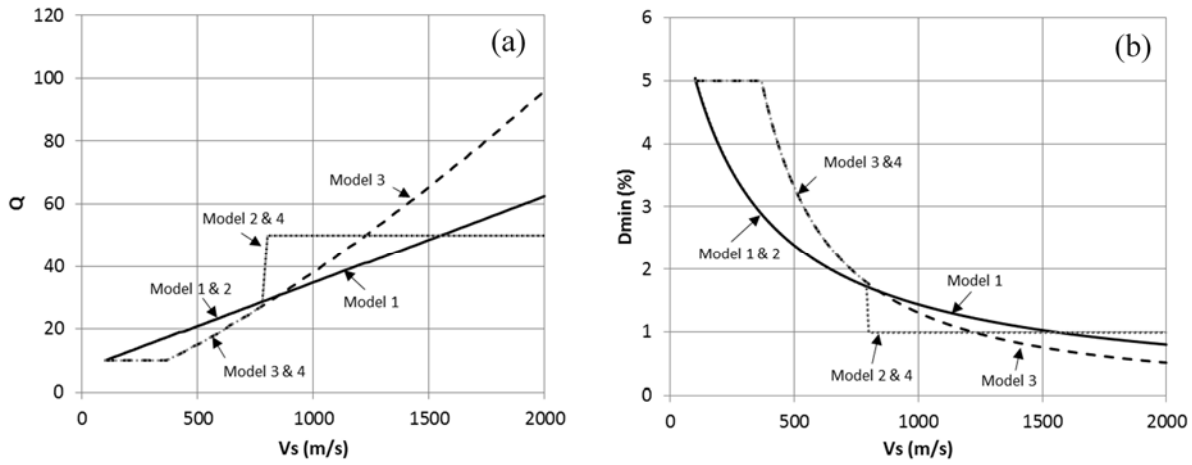

Figure 37 Attenuation (Q) models from Campbell (2009) in terms of (a) Q vs. V_s; (b) D_{min} vs. V_s

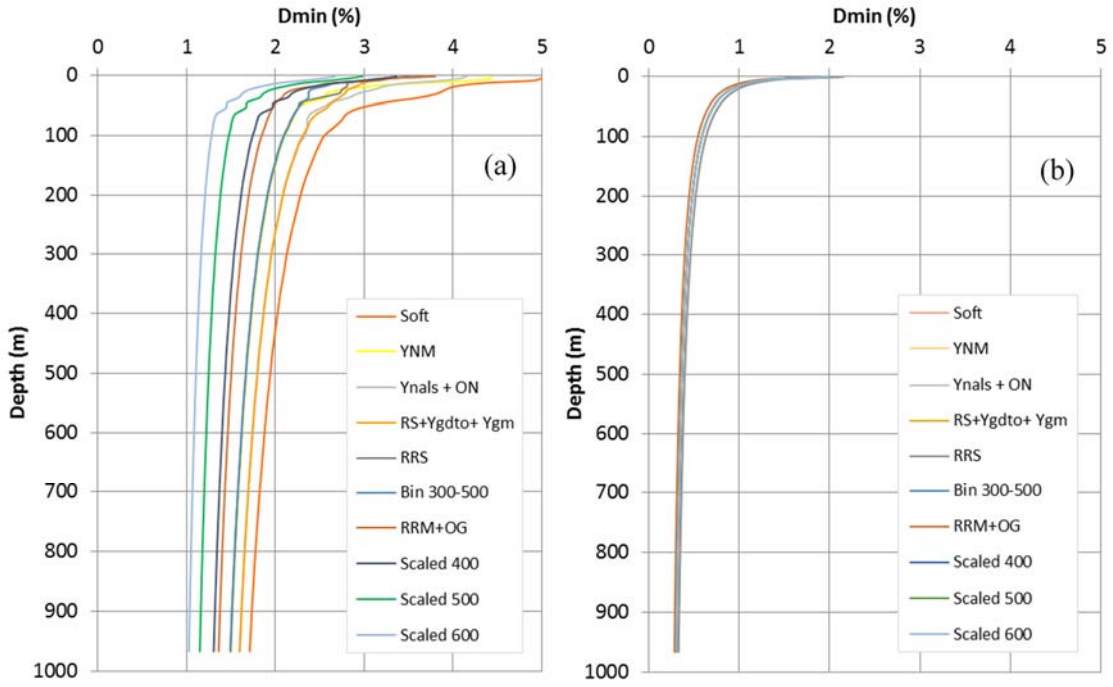

Figure 38 D_{min} vs. Depth from (a) Campbell (2009) $\mathrm{Q} - V_s$ Model 1; (b) Darendeli (2001) D_{min} model

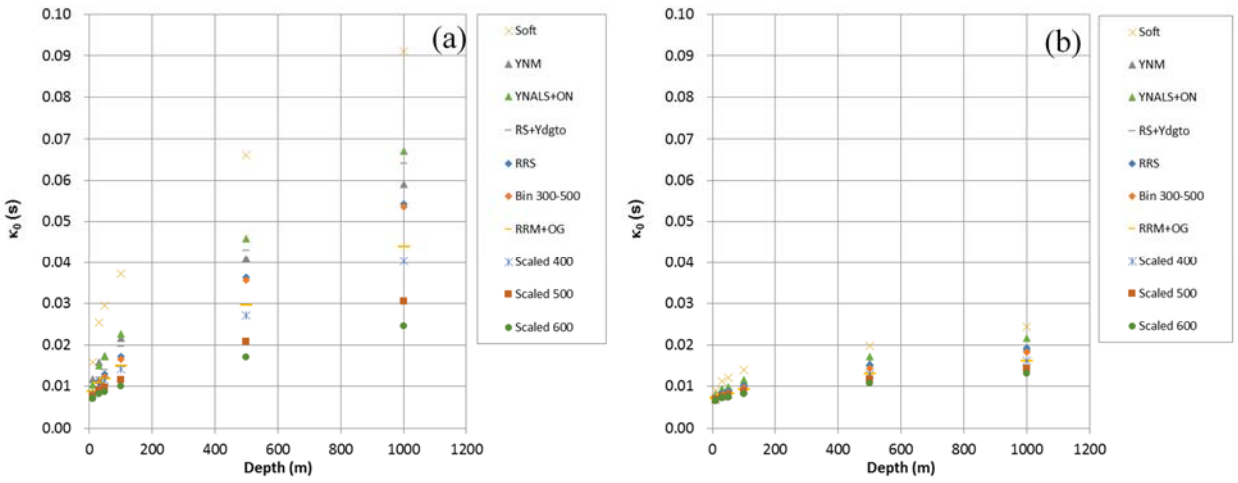

Figure 39 κ_0 as a functional of soil depth for 10 baseline Vs models and damping from (a) Campbell (2009) Q-Vs Model 1 and (b) Darendeli (2001) D_{min} Model

3.8.3.2 Comparisons of κ_0 Values of Site Response Models and κ_0 Values from Other Sources

To evaluate the two damping models within the context of κ_0, the computed values in Figure 39 are compared with values published in the literature and those computed directly from ground motion recording computed as part of this project.

Campbell (2009) developed a linear relationship between κ_0 and the depth of sediments (H_{sed}) for selected site profiles in CENA:

$$\kappa_0(\mathrm{s}) = 0.005 + 6.05\mathrm{x}10^{-5} * H_{sed}(m) \tag{14}$$

The κ_0 values from equation (14) are compared with those computed for the 10 baseline profiles for the different damping models in Figure 40. The κ_0 values derived from the Campbell (2009) damping model (Figure 40a) agree well with the range from equation (14), although the scatter is large and at larger depths the κ_0 values of the models are mostly smaller than those predicted by (14). It should be noted that some of the favorable agreement is due to the fact that equation (14) was derived as part of the same study that recommended the Q-Vs relationship (i.e, Campbell 2009). The κ_0 values derived from the Darendeli (2001) damping model (Figure 40b) agree well with equation (14) at depths less than 100 m, but these values are significantly smaller than those predicted by equation (14) at larger depths. This result is due to the small depth dependence in κ_0

that is produced by the Darendeli (2001) D_{min} model. Based on the results in Figure 40, the damping model derived from Q-Vs Model 1 of Campbell (2009) is considered most appropriate for the analyses in this study.

Various researchers have used ground motion recordings to calculate κ_0. There are different ways to compute κ_0 from recordings (Ktenidou et al. 2014). For this study, the acceleration slope method was used in which the log-linear slope of the Fourier Amplitude Spectrum of acceleration is related to κ_0. Surface and borehole recordings from KiK-net sites in Japan were used and multiple recordings at each site, representing events recorded at different distances, were analyzed. Only M_w greater than 3.5 and distances less than 150 km were used, and a regional distance-dependence for κ was assumed from Van Houtte et al. (2011) to correct the log-linear slope to κ_0.

Many studies of κ_0 have shown that κ_0 increases with decreasing V_{S30} (e.g., Chandler 2006, Van Houtte et al. 2011). Figure.41 plots the κ_0 values from the 10 baseline Vs profiles and damping from Campbell (2009) Q-Vs Model 1, along with the κ_0 values derived from 39 KiK-Net sites analyzed as part of this study. For each baseline profile six κ_0 values are shown which represent the different truncation depths. The larger κ_0 values correspond with the larger depths. For each KiK-Net site κ_0 values are shown for both the surface and borehole recordings, and the values are plotted at the surface and borehole V_{S30} values, respectively. Also shown in Figure.41 are the $\kappa_0 - V_{S30}$ relationships proposed by Chandler et al. (2006), Edwards et al. (2011), and Van Houtte et al. (2011). These relationships are only applicable down to V_{S30} of about 350 m/s.

The κ_0 values of the 10 baseline profiles in Figure.41 generally match the κ_0 values from the KiK-net recordings at V_{S30} less than 400 m/s. At larger V_{S30} or at small V_{S30} and smaller depths, the κ_0 values of the baseline profiles are smaller than those from the KiK-net recordings and those predicted by the various $\kappa_0 - V_{S30}$ relationships. However, none of the KiK-net recording sites encountered hard rock near the surface, and thus the KiK-net data do not include the very shallow soil conditions represented by some of the truncated baseline profiles.

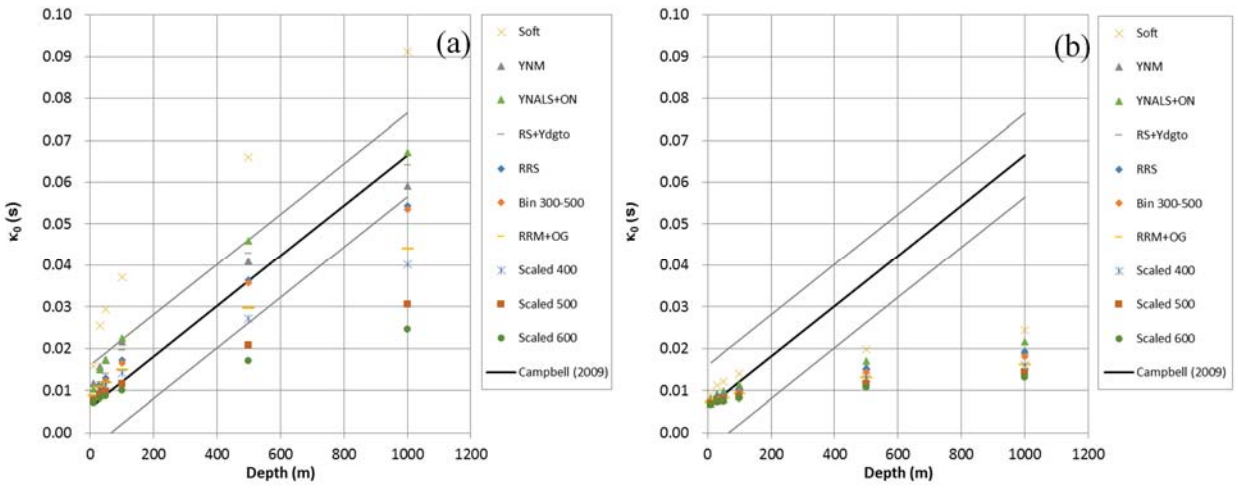

Figure 40 Comparison of Campbell (2009) κ_0 – depth model with κ_0 values for 10 baseline Vs models and damping from (a) Campbell (2009) Q-Vs Model 1 and (b) Darendeli (2009) D_{min} model

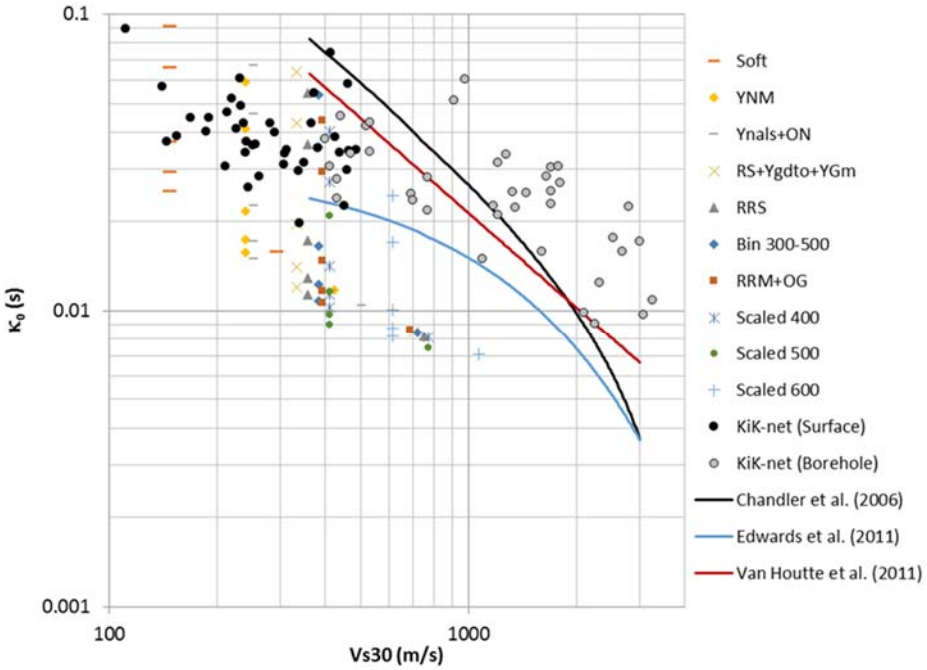

Figure.41 Comparison of κ_0 vs. Vs30 from different sources. κ_0 from site response profiles using Campbell (2009) Q-Vs Model 1, κ_0 from surface and borehole recordings from Kik-net sites, and κ_0-Vs30 relationships proposed in the literature.

3.9 SITE RESPONSE VERIFICATION

Simulation results from this parametric study are used in aggregate form to develop ergodic site amplification models for use in engineering and seismology in Part II of this study. This section presents a sample of site amplification results from three sites to verify that the procedurally-generated site amplification analyses in DEEPSOIL behave as expected on a site-specific basis. Properties for the three soil columns are given in Table 16 and the profiles are simulated with NL, EL and LE analyses in DEEPSOIL for the motions given in Table 17.

Profile 1 has the lowest V_{S30} of the profiles presented in this section with V_{S30} = 198 m/s. It is a soil column with 50 m of soil material above the 3000 m/s bedrock with no weathered rock zone. It has a site natural period of 0.83 s. This profile is randomization realization 3 of 30 generated for the judgement-based soft V_S profile.. This profile was simulated with ground motions ranging from 0.015 g to 1.24 g PGA. The surface response spectra and amplification as a function of depth from the NL, EL, and LE simulations are shown in Figures 42 and 43, respectively.

Profile 2 has V_{S30} of 434 m/s. It is a soil column with 20 m of soil above a 30 m weathered rock zone. It has a site natural period of 0.26 s. This profile is randomization realization 15 of 30 generated for the YNals+ON characteristic V_S profile. This profile was simulated with ground motions ranging from 0.07 g to 1.09 g PGA. The surface response spectra and amplification as a function of depth from the NL, EL, and LE simulations are shown in Figures 44 and 45, respectively.

Profile 3 has the highest V_{S30} of the profiles presented in this section with V_{S30} = 608 m/s. It is a soil column with 10 m of soil material above the weathered rock zone and has a site natural period of 0.212 s. The 30 m depth-based weathered rock zone V_S model is truncated where the V_S reaches 3000 m/s. This profile is randomization realization 10 of 30 generated for the characteristic V_S profile YGdto+RS+YGm. This profile was simulated with ground motions ranging from 0.02 g to 2.24 g PGA. The surface response spectra and amplification as a function of depth from the NL, EL, and LE simulations are shown in Figures 46 and 47, respectively.

The simulation results presented in Figures 42 through 47 suggest that the procedurally-generated soil columns are behaving as expected at all levels of shaking. The relative behaviors

of the NL, LE, and EL analyses, the soil column strain and PGA response as a function of depth and bedrock motion intensity, and amplification at the natural period of the soil column for weak motion shaking all demonstrate typical behavior.

The LE analyses are representative of the small-strain response of the soil column, and for very low levels of bedrock motion intensity, the LE analyses will converge with both the EL and NL analyses for a sufficiently high profile layer resolution. At higher levels of shaking, the EL and NL analyses will begin to diverge from the LE analyses, and at very high levels of shaking the EL and NL analyses will diverge from each other. The V_S of the soil column and bedrock motion intensity both contribute to the divergence of the EL and NL site response analyses (Kim et al. 2015), and for softer site (lower V_{S30}) more divergence is expected for a bedrock motion intensity measure. Figures 42, 44, and 46 all show good agreement in the spectral response for ground motions with very low levels of shaking (i. e. low PGA) between the LE analyses and the EL and NL analyses. At higher levels of shaking for each site, the LE, EL, and NL analyses all begin to diverge and are largest at the highest levels of shaking. The soil column response as a function of depth shown in Figures 43, 45, and 47 also demonstrates that for various profile V_{S30} values, low levels of ground motion shaking show little divergence between the analysis types. At the strongest levels of shaking, the EL and NL analyses diverge most significantly from the LE analyses, and diverge less significantly from each other.

Three different weathered rock conditions are represented in Profiles 1, 2, and 3. Profile 1 has a thin weathered rock zone of just 5 m because it was truncated at 3000 m/s after V_S randomization. Profile 2 has no weathered rock zone, and the soil column is directly above the 3000 m/s bedrock half-space condition. Profile 3 has 30 m of weathered rock between the 3000 m/s bedrock half-space condition and the soil profile. In Figure 43 showing Profile 1, there is a sharp decrease in maximum strain just below the 50 m of soil in the weathered rock material. In Figure 47 the 30 m weathered rock zone has significantly lower maximum strain values than the soil above. The differences between the LE, EL and NL analyses are also most pronounced in the lower V_S soil material than the higher V_S weathered rock material.

Profile 1, Profile 2, and Profile 3 all exhibit higher amplification around the site natural period than at other locations in the response spectrum. Figures 42, 44, and 46 show peaks in the surface

response spectra near the natural period of each site, 0.84, 0.26, and 0.21 s respectively, for the LE, EL, and NL analyses. For the EL and NL analyses at higher levels of shaking, there is less noticeable amplification in the EL and NL analyses near the natural site period than for the LE analysis. As shaking intensifies at a site and the soil begins to strain, its stiffness decreases, changing the natural period of the site as a function of time. It is expected that for more intense shaking, the amplification near the natural period of the site will decrease.

Table 16: Soil column properties for select analysis results. Material properties for each geology class are given in Table 14

Characteristic V_S profile	Geology	Rand.	G/G_{max} Curve	Z (m)	Weathered Rock	V_{S30} (m/s)	T_{nat}	Profile
SOFT	General	R3	$\varepsilon > 0$	50	30 m Depth	198	0.837	1
YNals+ ON	YN	R15	$\varepsilon < 0$	20	0 m depth	434	0.262	2
RS+ YGdto+ YGm	YG	R10	$\varepsilon > 0$	10	30 m Depth	608	0.212	3

Table 17: Ground motion properties for select analysis results. Motions are paired with profiles from Table 16 by Profile number.

Motion	PGA (g)	PGV (m/s)	Duration (s)	Mag.	Distance (km)	Motion Source	Profile
Nrcm65Ra_G06000	0.464	0.1228	29.975	6.5	5	NUREG	1
Nrcm65Rb_A-Lvl000	0.230	0.0809	39.995	6.5	30	NUREG	1
Nrcm65Rd_Ma1130	0.015	0.0167	35.965	6.5	150	NUREG	1
Nrcm75Ra_Brn090	1.236	0.4023	24.96	7.5	5	NUREG	1
Nrcm75Rd_Tap067-N	0.090	0.1100	79	7.5	150	NUREG	1
Nrcm75Rd_Kau078-W	0.113	0.0365	89.995	7.5	150	NUREG	1
Smsimm5.5_M5.5R35	0.022	0.0074	131.068	5.5	35	SMSIM	1
Smsimm6.5_M6.5R61.3	0.027	0.0114	131.068	5.5	61.3	SMSIM	1
Nrcm55Rab_Dcf180	0.286	0.0595	13.6	5.5	25	NUREG	2
Nrcm65Ra_S1280	1.095	0.4607	20.56	6.5	5	NUREG	2
Nrcm65Rc_A-Csh090	0.072	0.0245	39.99	6.5	75	NUREG	2
Nrcm65Rd_Ma2130	0.026	0.0181	29.485	6.5	150	NUREG	2
Nrcm75Ra_Izt180	0.401	0.4183	29.995	7.5	5	NUREG	2
Nrcm75Rc_Nsk-E	0.126	0.0829	40.995	7.5	75	NUREG	2
Smsimm6.5_M6.5R17.5	0.337	0.1670	131.068	6.5	17.5	SMSIM	2
Nrcm55Rab_B-Kod270	0.180	0.0459	18.495	5.5	25	NUREG	3
Nrcm55Rc_1125S08L	0.133	0.0461	29.65	5.5	75	NUREG	3
Nrcm55Rc_1125S20L	0.147	0.0376	20.645	5.5	75	NUREG	3
Nrcm65Rb_L-Bpl070	0.195	0.0672	25.95	6.5	30	NUREG	3
Nrcm75Ra_Lcn345	2.248	0.3694	48.12	7.5	5	NUREG	3
Nrcm75Rd_Tap060-N	0.090	0.0875	64.995	7.5	150	NUREG	3
Smsimm5.5_M5.5R12	0.269	0.0620	65.532	5.5	12	SMSIM	3
Smsimm6.5_M6.5R87.7	0.020	0.0133	131.068	6.5	87.7	SMSIM	3

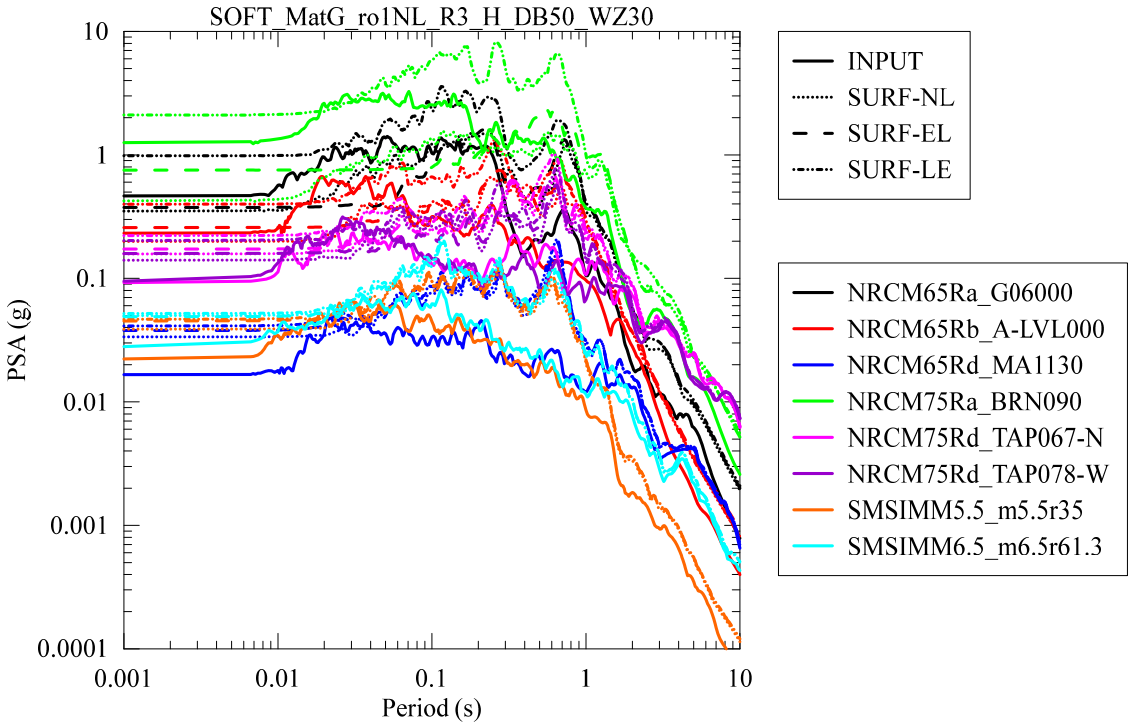

Figure 42: Simulation results for Profile 1. Profile characteristics given in Table 16, motion characteristics given in Table 17

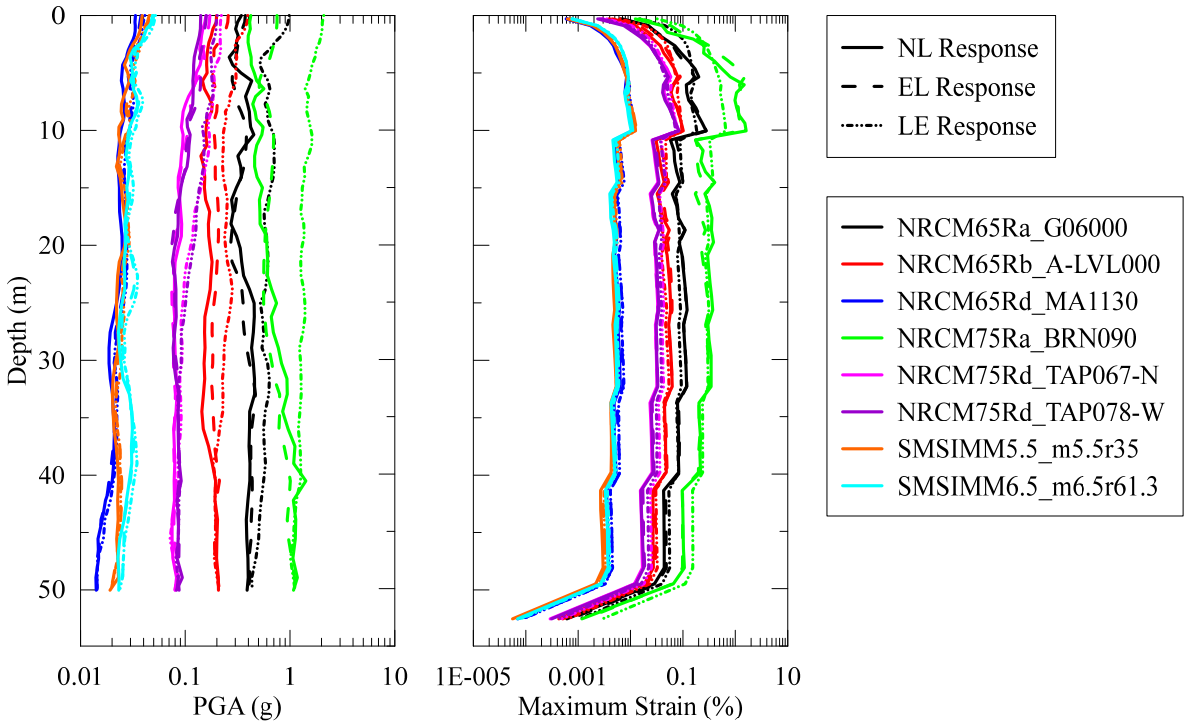

Figure 43: Simulation results for Profile 1 as a function of depth. Surface spectral response shown in Figure 42, profile characteristics given in Table 16, motion characteristics given in Table 17

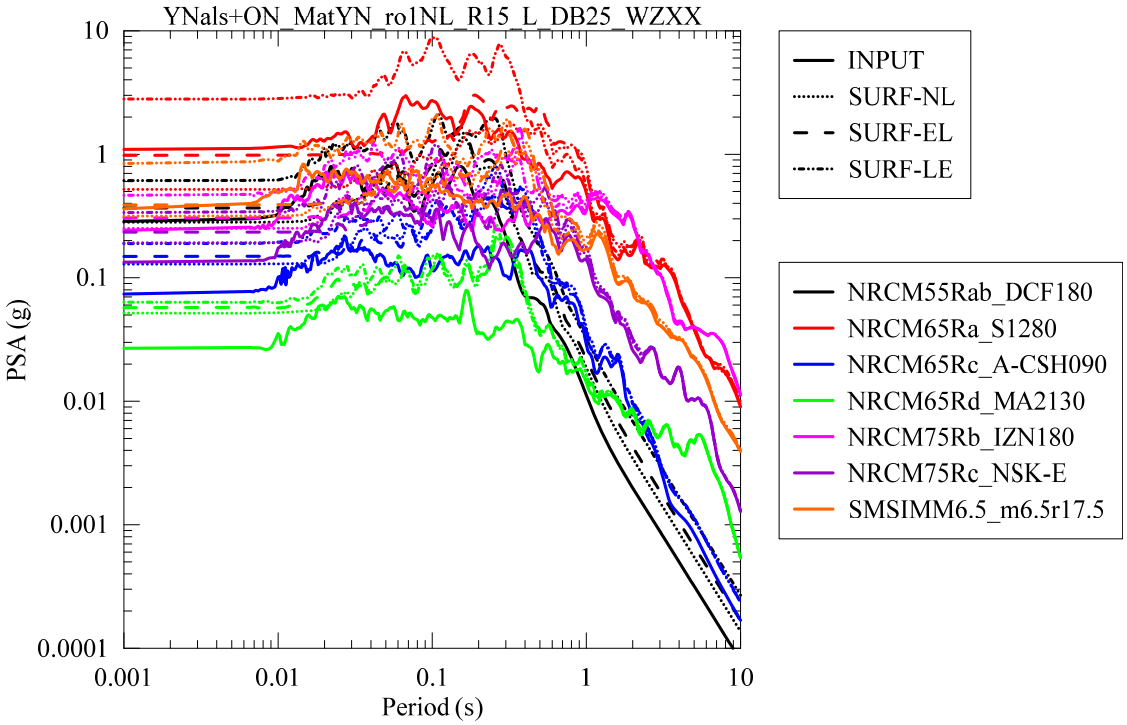

Figure 44: Simulation results for Profile 2. Profile characteristics given in Table 16, motion characteristics given in Table 17

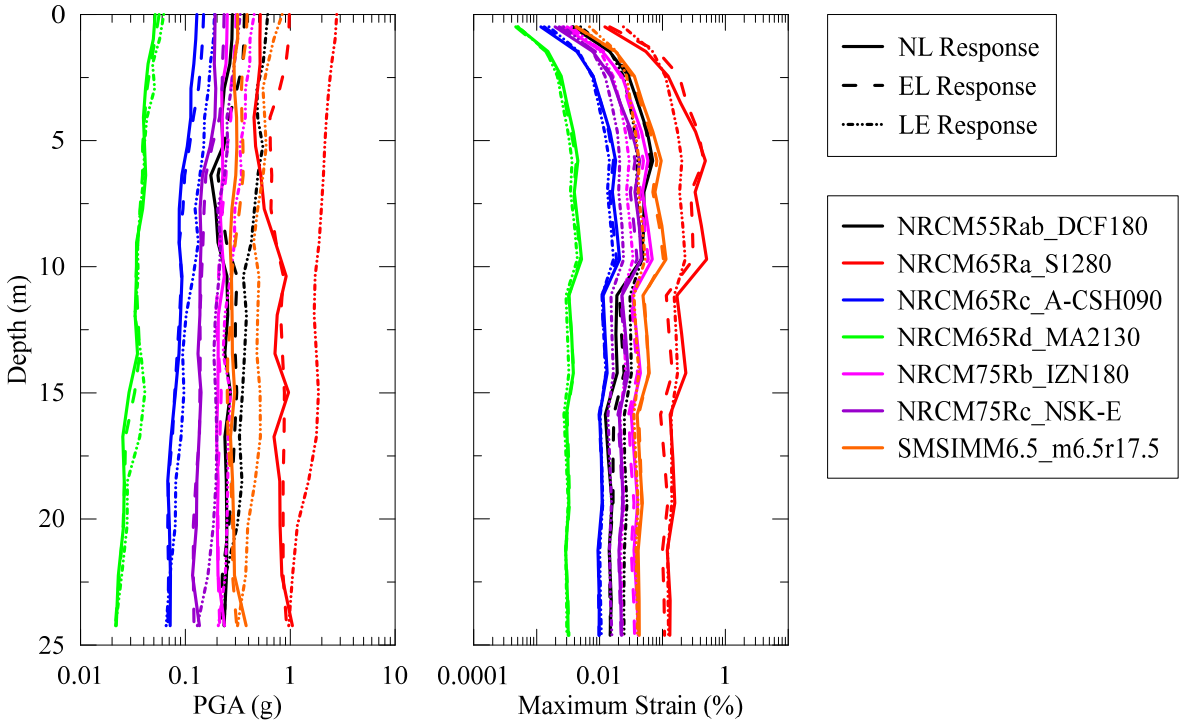

Figure 45: Simulation results for Profile 2 as a function of depth. Surface spectral response shown in Figure 44, profile characteristics given in Table 16, motion characteristics given in Table 17

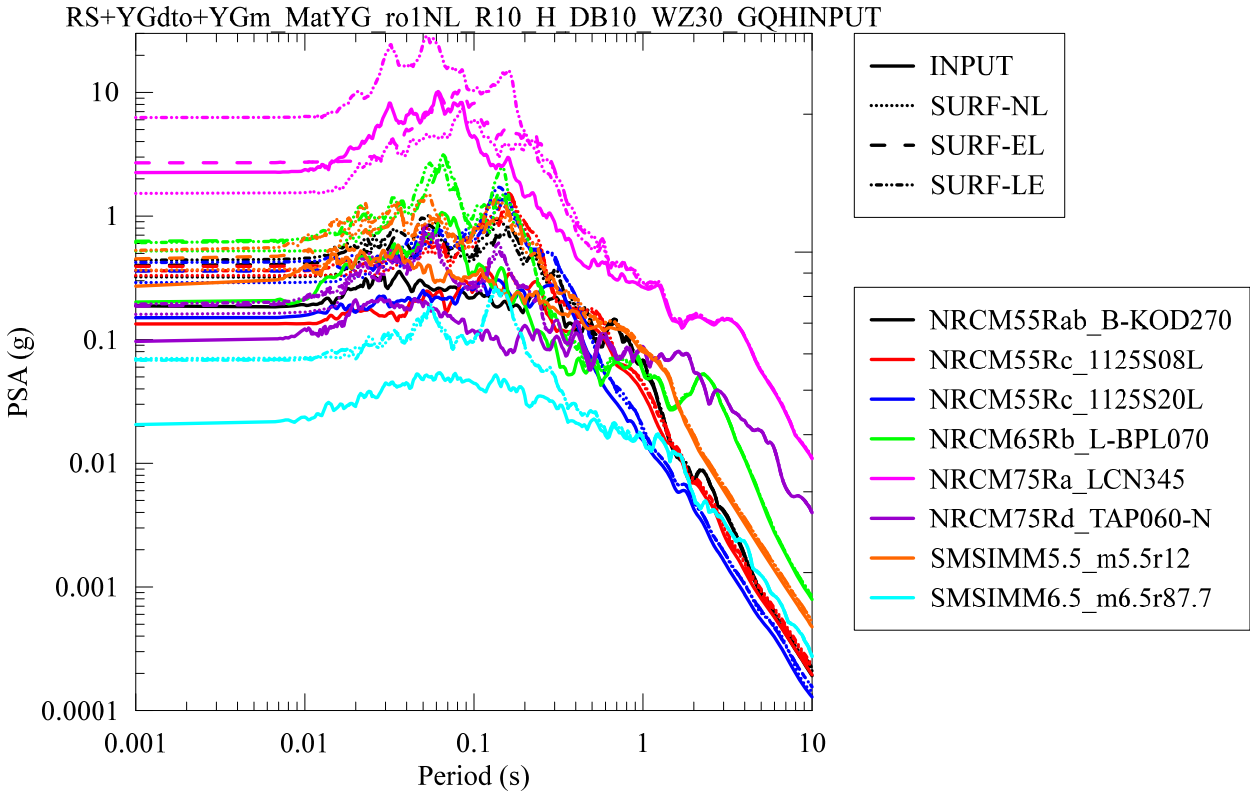

Figure 46: Simulation results for Profile 3. Profile characteristics given in Table 16, motion characteristics given in Table 17

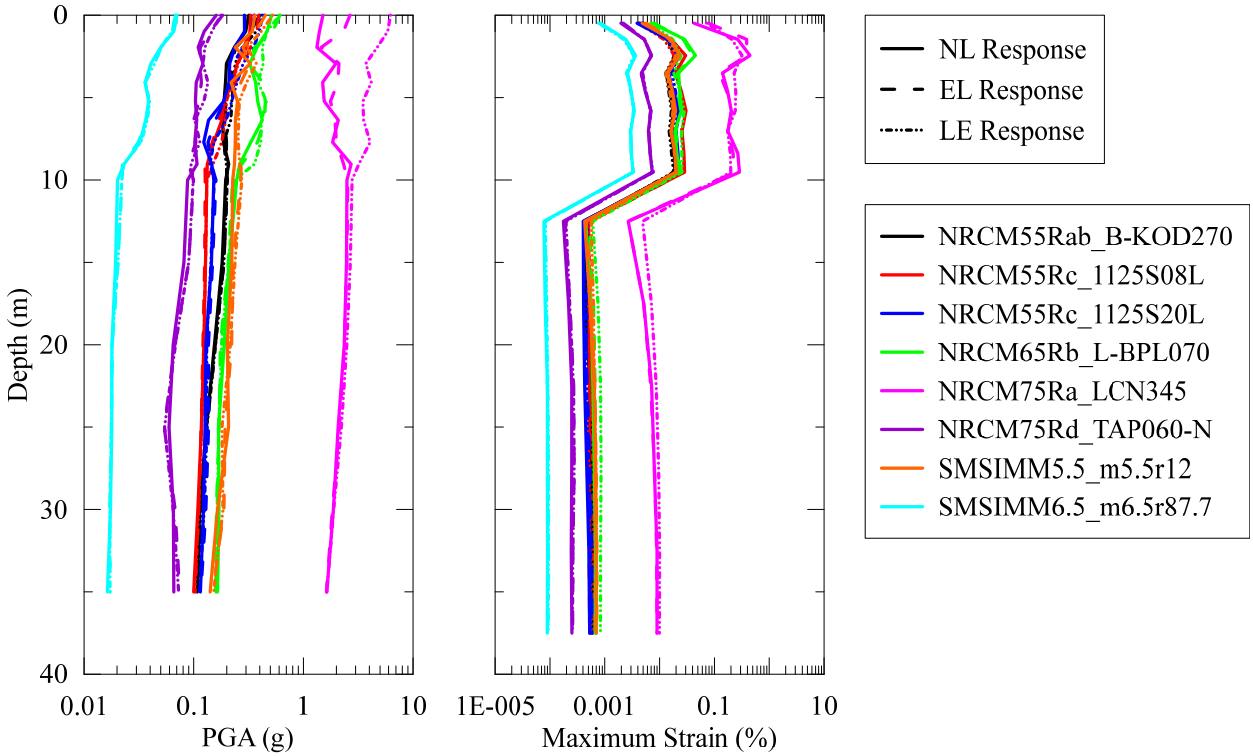

Figure 47: Simulation results for Profile 3 as a function of depth. Surface spectral response shown in Figure 46, profile characteristics given in Table 16, motion characteristics given in Table 17

4 RESPONSE SPECTRUM SITE AMPLIFICATION MODELS

In the Western United States (WUS), amplification factors are typically developed for the response spectrum and not the Fourier Amplitude Spectrum. This section presents linear and nonlinear site amplification factors and models resulting from the parametric study presented in Chapter 3.6 from simulations. The response spectrum amplification absent of multidimensional and basin effects, ($F_{S,B}$) is commonly represented as the sum of a linear amplification component (F_{lin}) and a nonlinear site amplification (F_{nl}) component as given in (after Seyhan and Stewart (2014) as

$$F_{S,B} = \ln(F_{lin}) + \ln(F_{nl}) \tag{15}$$

The linear amplification component is the intensity-independent site amplification for a linear site condition. The linear amplification in the response spectrum has up to three model terms for V_{S30}, depth of soil, and site natural period as shown in (16).

$$\ln(F_{lin}) = f(V_{S30}) + f(Z_{Soil}) + f(T_{nat}) \quad (16)$$

where Z_{soil} is the depth of soil, and T_{nat} is the site natural period. The full response spectral amplification model is given in (17).

$$F_{S,B} = \ln(F_{lin}) + \ln(F_{nl}) = f(V_{S30}) + f(Z_{Soil}) + f(T_{nat}) + f(NL) \quad (17)$$

where the nonlinear amplification component is represented as a function of soil stiffness and ground motion intensity characteristics, *f(NL)*.

Components of the RS amplification model are evaluated both together and independently for situations where data to evaluate the full model may not be obtainable. Table 18 shows the amplification coefficient models to be derived from the simulation dataset. Model terms shown in Table 18 can be combined to form complete site amplification models as shown in Table 19.

Models L1-L5 shown in Table 19.are intensity-independent linear site amplification models from linear elastic simulations for sites in CENA. Model L1 is a site amplification model dependent only on V_{S30}. Models L2 and L3 are amplification models with coefficients for Z_{soil} and T_{nat} respectively calculated after the effects of V_{S30} have been removed through the regression of the L1 coefficients as shown in Table 18. The Z_{soil} and T_{nat} terms in models L2 and L3, respectively are usable with amplification models from other sources such as those CENA such as those presented in Section 3.3. Linear models L4 and L5 are amplification models with simultaneously-regressed model terms for V_{S30} and Z_{soil} (L4) and V_{S30} and T_{nat} (L5), respectively.

Two kinds of nonlinear site amplification models are represented in Table 19 for each of two different ground motion intensity measures. Models of the form L+N are site amplification models with independently calculated linear and nonlinear coefficients. The L amplification terms are calculated from the linear elastic site response simulation as shown in Table 18. The N amplification terms are regressed from the difference between the NL GQ/H site response simulation and the LE site response simulation. The K1 and K2 linear and nonlinear site amplification model terms are regressed simultaneously from the NL GQ/H site response simulations using PSA or PGA, respectively, as the intensity measure for nonlinear site amplification. The N1 and K1 models use period-dependent pseudo-spectral acceleration (PSA) values of the bedrock motion and N2 and K2 models use the period-independent peak ground

acceleration (PGA) of the bedrock motion as the intensity measure for nonlinear site effects. The derivations of each of the terms for the models described in Table 19 are detailed in Section 4.

Table 18: Amplification Coefficient models

Amplification Component	Simulation Data	Component Subscript	Component Model Terms
V_{S30}	$\ln(amp)_{LE}$	L1	$f(V_{S30})_{L1}$
Z_{Soil} (after V_{S30})		L2	$f(V_{S30})_{L1} + f(Z_{soil})_{L2}$
T_{nat} (after V_{S30})		L3	$f(V_{S30})_{L1} + f(T_{nat})_{L3}$
V_{S30} + Z_{Soil} (simultaneous)		L4	$f(V_{S30})_{L4} + f(Z_{soil})_{L4}$
V_{S30} + T_{nat} (simultaneous)		L5	$f(V_{S30})_{L5} + f(T_{nat})_{L5}$
NL (PSA)	$\ln(amp)_{GQ/H} - \ln(amp)_{LE}$	N1	$f(NL)_{N1}$
NL (PGA)		N2	$f(NL)_{N2}$
V_{S30} + T_{nat} + NL(PSA) (simultaneous)	$\ln(amp)_{GQ/H}$	K1	$f(V_{S30})_{K1} + f(T_{nat})_{K1} + F(NL)_{K1}$
V_{S30} + T_{nat} + NL(PSA) (simultaneous)		K2	$f(V_{S30})_{K2} + f(T_{nat})_{K2} + F(NL)_{K2}$

Table 19: Response Spectral Amplification Models from simulations

Amplification Model	Model Terms	Amplification Type
L1	$f(V_{S30})_{L1}$	Linear
L2	$f(V_{S30})_{L1} + f(Z_{soil})_{L2}$	Linear
L3	$f(V_{S30})_{L1} + f(T_{Nat})_{L3}$	Linear
L4	$f(V_{S30})_{L4} + f(Z_{soil})_{L4}$	Linear
L5	$f(V_{S30})_{L5} + f(T_{Nat})_{L5}$	Linear
L1 + N1	$f(V_{S30})_{L1} + f(NL)_{N1}$	Nonlinear (PSA)
L2 + N1	$f(V_{S30})_{L1} + f(Z_{soil})_{L2} + f(NL)_{N1}$	Nonlinear (PSA)
L3 + N1	$f(V_{S30})_{L1} + f(T_{Nat})_{L3} + f(NL)_{N1}$	Nonlinear (PSA)
L4 + N1	$f(V_{S30})_{L4} + f(Z_{soil})_{L4} + f(NL)_{N1}$	Nonlinear (PSA)
L5 + N1	$f(V_{S30})_{L5} + f(T_{Nat})_{L5} + f(NL)_{N1}$	Nonlinear (PSA)
L1 + N2	$f(V_{S30})_{L1} + f(NL)_{N2}$	Nonlinear (PGA)
L2 + N2	$f(V_{S30})_{L1} + f(Z_{soil})_{L2} + f(NL)_{N2}$	Nonlinear (PGA)
L3 + N2	$f(V_{S30})_{L1} + f(T_{Nat})_{L3} + f(NL)_{N2}$	Nonlinear (PGA)
L4 + N2	$f(V_{S30})_{L4} + f(Z_{soil})_{L4} + f(NL)_{N2}$	Nonlinear (PGA)
L5 + N2	$f(V_{S30})_{L5} + f(T_{Nat})_{L5} + f(NL)_{N2}$	Nonlinear (PGA)
K1	$f(V_{S30})_{K1} + f(T_{Nat})_{K1} + f(NL)_{K1}$	Nonlinear (PSA)
K2	$f(V_{S30})_{K2} + f(T_{Nat})_{K2} + f(NL)_{K2}$	Nonlinear (PGA)

4.1 V_{S30} SCALING

The V_{S30} scaling component, $f(V_{S30})$, of the site amplification models shown in Table 19 is given in (18).

$$\ln(amp) = \begin{cases} V_c < V_{S30} & 0 \\ V_L < V_{S30} < V_c & c_1 \log\left(\frac{V_{S30}}{V_c}\right) \\ V_{S30} < V_L & c_1 \log\left(\frac{V_{S30}}{V_c}\right) + c_2 \log\left(\frac{V_{S30}}{V_L}\right) + c_3 \log\left(\frac{V_{S30}}{V_L}\right)^2 \end{cases} \quad (18)$$

where coefficients c_1, c_2 and c_3 describe the period-dependent V_{S30} scaling in the model, V_c is a limiting velocity above which ground motions show no amplification relative to the 3000 m/s bedrock condition, and V_L is a limiting velocity below which amplification does not scale linearly with the log of V_{S30}. The V_{S30} scaling model component given in (18) has three regions of behavior, a departure from commonly used V_{S30} scaling functions for the WUS such as in Walling et al.(2008) and Seyhan and Stewart (2014).

Above the V_c limiting velocity, there is no dependency of site amplification on V_{S30}. V_c as presented in (18) maintains the same definition as in equation 2 of Seyhan and Stewart (2014) if $V_{ref} = V_c$. Above V_c there is negligible change in the site amplification relative to the 3000 m/s reference rock condition. Between V_c and V_L, the site amplification scales linearly with the log of V_{S30}. Linearity in site amplification as a function of V_{S30} is commonly seen in amplification functions in the WUS and other regions. Below V_L the V_{S30} scaling term has a curved region. In the region $V_{S30} < V_L$, the c_1 and c_2 terms ensure a continuous function of V_{S30}, and the c_3 term determines the degree of curvature. At low periods, the simulations reveal a decrease in site amplification as V_{S30} decreases. At longer periods, the magnitude of c_3 decreases, and the site amplification becomes more linear with the log of V_{S30}.

The V_{S30} scaling given in (18) and regressed for the linear elastic simulation data, model L1 in (18), is shown for several response spectral periods in Figure 48. Coefficients for the L1 site amplification coefficients are shown graphically in Figure 49 and provided in tabular form in APPENDIX D

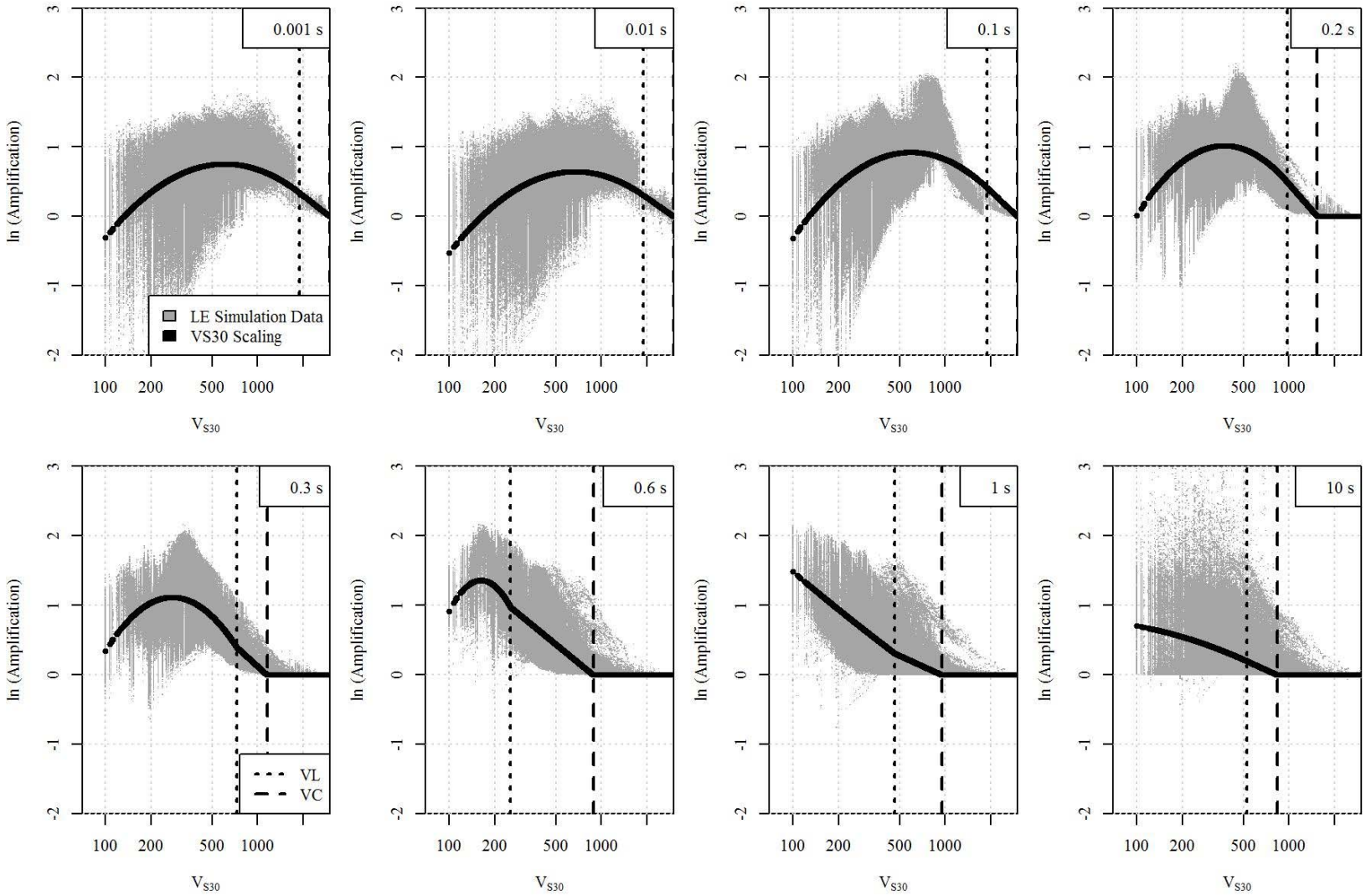

Figure 48: L1 Site amplification function for response spectral periods 0.001, 0.01, 0.1, 0.2, 0.3, 0.6, 1 and 10 s.

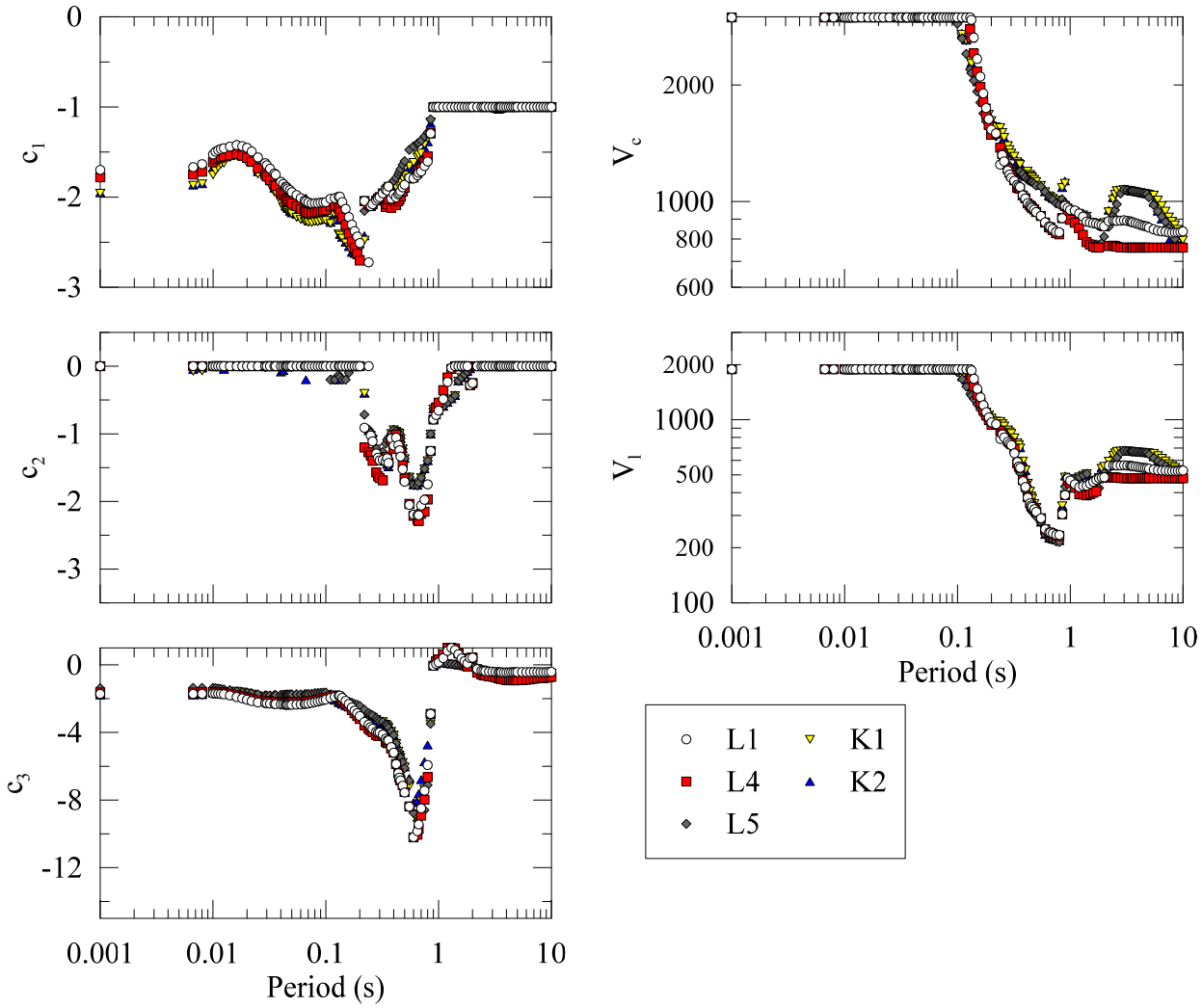

Figure 49: Response Spectral Coefficients for f(V_{S30})

4.2 DEPTH EFFECTS

The effects of soil column depth, $f(Z_{Soil})$, of site amplification for the models shown in Table 19 is given in (19).

$$\ln(amp) = \begin{cases} Z < 30 & 0 \\ Z \geq 30 & c_4(Z - 30\ m)^2 \end{cases} \quad (19)$$

where c_4 describes the period-dependent depth effects, and Z is the soil depth to weathered rock in meters.

The depth effects of site amplification given in (19) provide a correction for sites deeper than 30 m. At low periods, c_4 is negative and represents a decrease in the amplitude of ground motion at a site due to the damping of a very deep soil column. At longer periods, c_4 becomes positive and represents an increase in the amplitude of ground motions for deeper sites due to resonance effects.

Model L2 and L4 in Table 19 include effects of depth on linear site amplification and are shown graphically for several response spectral periods in Figures 50 and 51, respectively. Model coefficients for models L2 and L4 are shown graphically in Figure 52 and provided in tabular form in APPENDIX D.

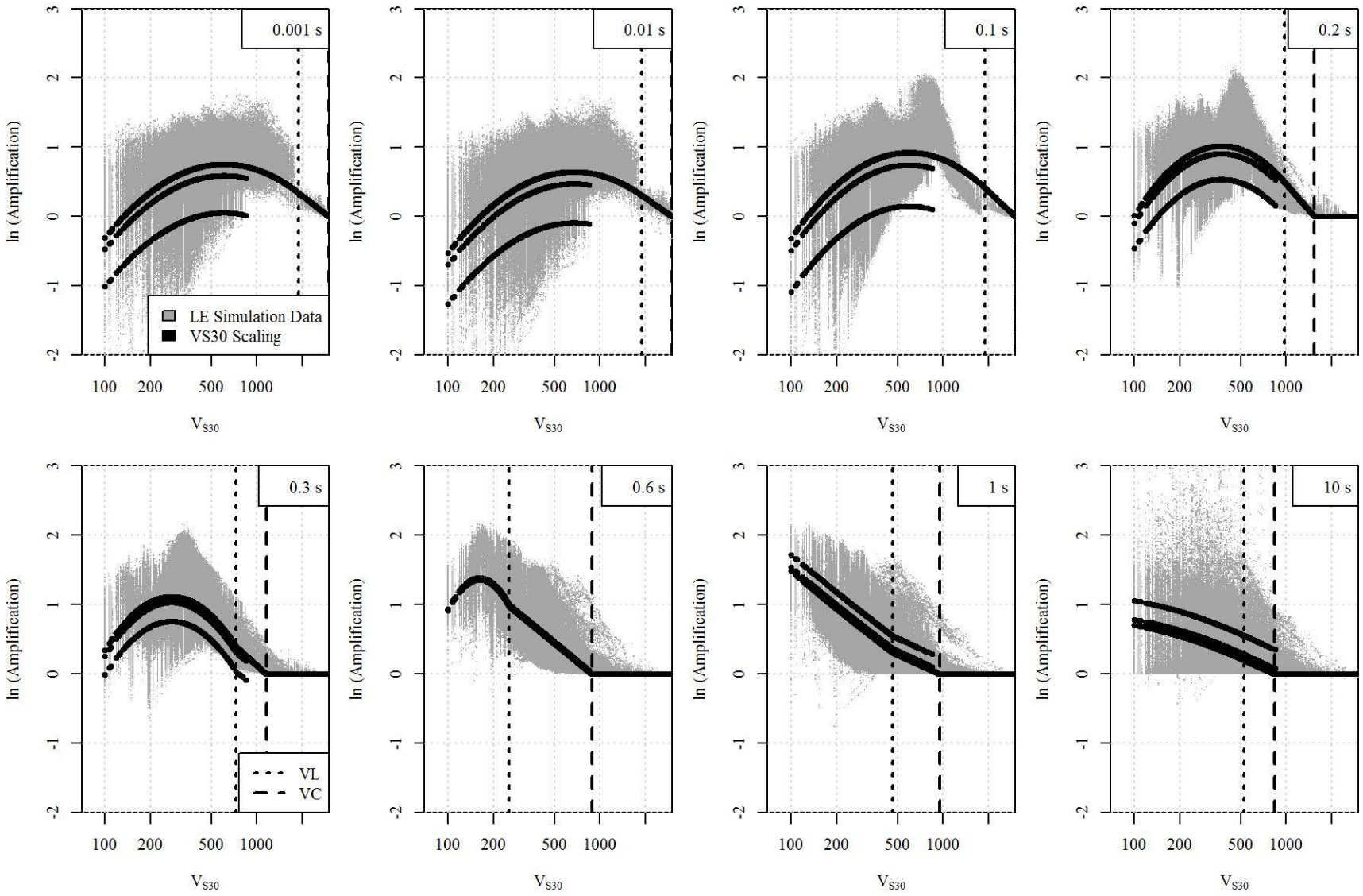

Figure 50: L2 Site Amplification Function

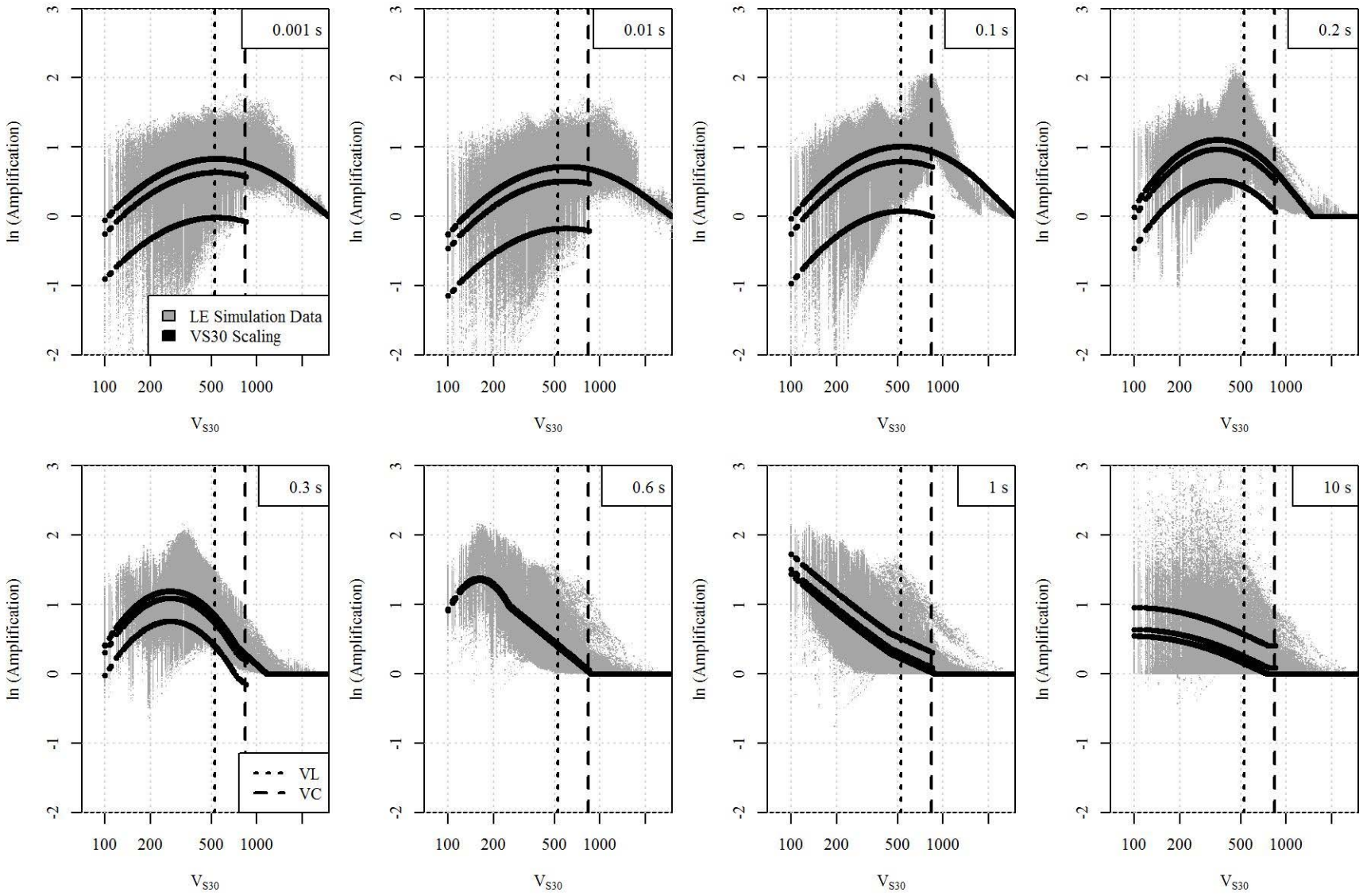

Figure 51: L4 Site Amplification Function

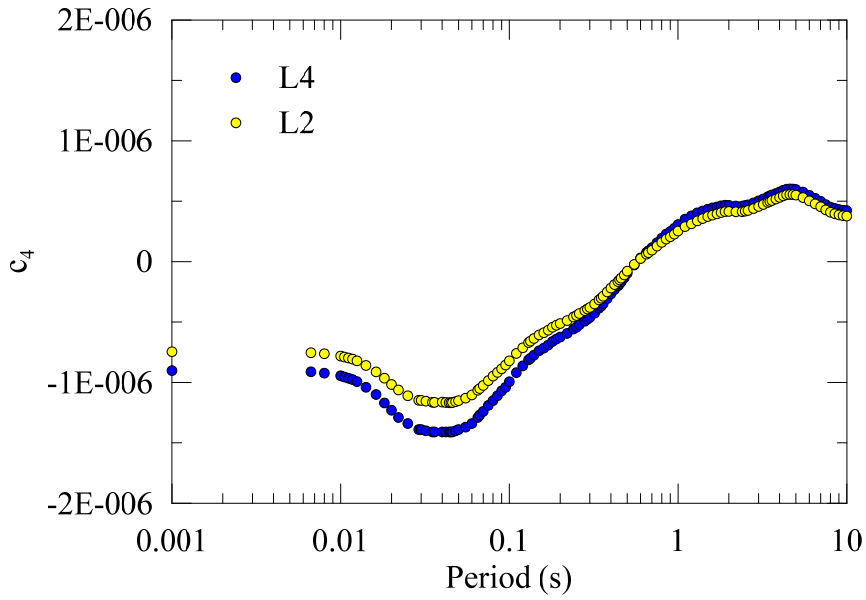

Figure 52: Response Spectral Coefficients for f(Z)

4.3 NATURAL PERIOD EFFECTS

The effects of the site natural period, $f(T_{nat})$, of site amplification shown in Table 19 is given in (20).

$$\ln(amp) = \begin{cases} T_{OSC} < 0.01 & c_6 T_{nat} \\ T_{OSC} \geq 0.01 & c_5 R + c_6 T_{nat} \end{cases} \tag{20}$$

where c_5 and c_6 describe the period dependent natural period effects, T_{OSC} is the response spectrum frequency under consideration, T_{nat} is the soil column natural frequency, and R is given by (21).

$$R = \frac{2}{\sqrt{3\alpha}\pi^{\frac{1}{4}}}\left(1 - \frac{(\beta)^2}{\alpha^2}\right)\exp\left(\frac{(\beta)^2}{2\alpha^2}\right) \tag{21}$$

where α is a regression coefficient and β is given (22).

$$\beta = log10\left(\frac{T_{OSC}}{T_{nat}}\right) - log10(0.81) \tag{22}$$

The natural period effects in (20) have two components. The c_5 component is an amplification term that takes the functional form of a Riker wavelet (commonly called the "Mexican Hat" wavelet). The c_6 component is amplification linear with T_{nat}. The Riker wavelet and linear with T_{nat} come from residuals of site amplification after V_{S30} scaling effects are removed (e.g. residuals of model L1) shown in Figure 53 for 12 periods between 0.001 s and 10 s. Residuals in Figure 53 are plotted as a function of response spectral period divided by site natural period (T_{OSC} / T_{nat}).

For response spectral periods near the site natural period ($T_{OSC} = T_{nat}$), strong resonance effects can be seen for almost all frequencies and are captured in the site amplification model using a Riker Wavelet using (21). The Riker wavelet function has three main components: amplitude, width, and peak location The amplitude and width of the Riker wavelet is determined through regression of site response analysis data at each response spectral period and is represented by c_5 and α, respectively. The location of the peak residuals of V_{S30} scaling do not occur at values of (T_{OSC} / T_{nat}) = 1 and instead occur at (T_{OSC} / T_{nat}) = 0.81. The location of the peak of the Riker wavelet in (21) is defined in (22) including this offset. The value of (T_{OSC} / T_{nat}) = 0.81 was determined as the mean value of the location of the first peak of the residuals as shown in Figure 53 and is stable at the site periods of interest for geotechnical engineering. The Riker wavelet natural period effect on amplification is not observed for very low periods ($T_{OSC} < 1.0$) as seen in Figure 53 and so is not included for this range in (20). For T_{nat} less than 1 s the peak width is fairly constant, but widens slightly for larger periods as seen in the lines for 3 and 10 s T_{nat} in Figure 53.

The c_6 component of amplification in (20) captures the effects of deep sites with long T_{nat}. The c_6 amplification captures the observed residual behavior between $T_{OSC}/T_{nat} = 0.001$ and $T_{OSC}/T_{nat} = 0.1$ in Figure 53. The effects of the c_6 amplification are most noticeable for sites with low V_{S30} and can be seen in Figures 54 and 55 at 0.001 s. At 0.001 s, there is no contribution of the c_5 component of amplification in (20), and the effect of the c_6 component of amplification can be seen by comparing Figures 54 and 55 to Figure 48.

Models L3 and L5 in Table 19 include the effects of T_{nat} on linear site amplification and are shown graphically for several response spectral periods in Figures 54 and 55, respectively.

Model coefficients for models L3 and L5 are shown graphically in Figure 56 provided in tabular form in APPENDIX D.

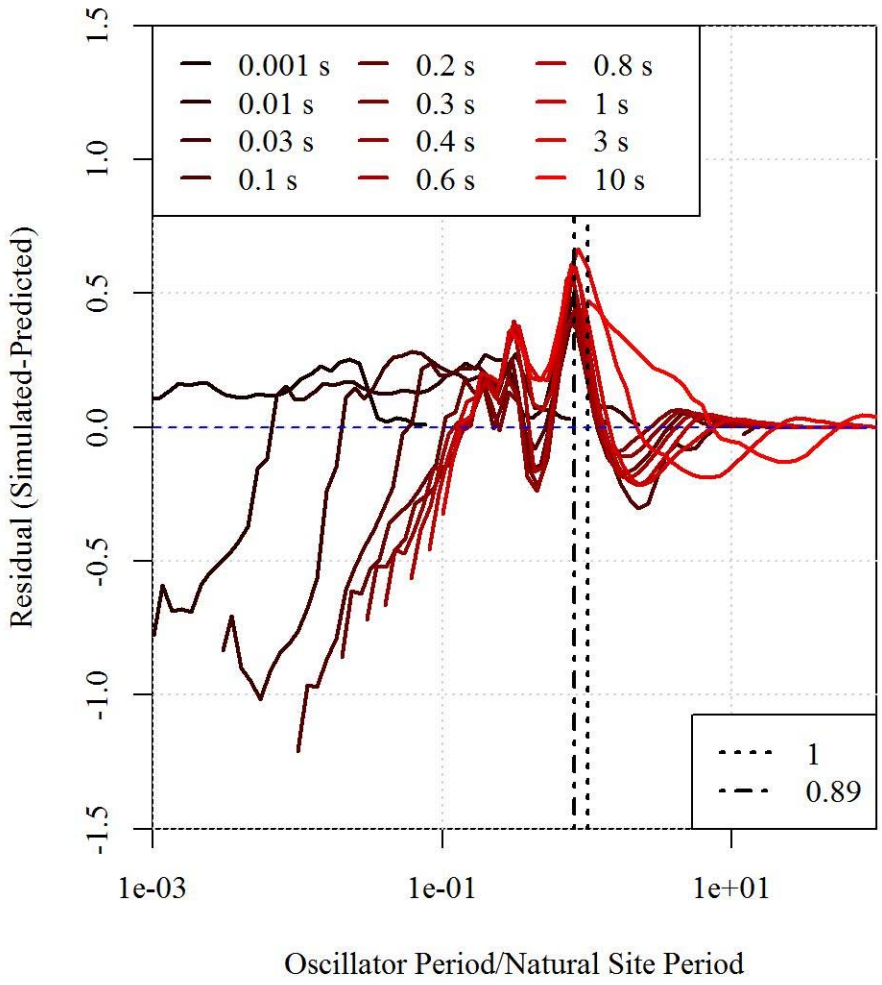

Figure 53: Natural Period Residuals after VS30 scaling for periods 0.001 s to 10 s

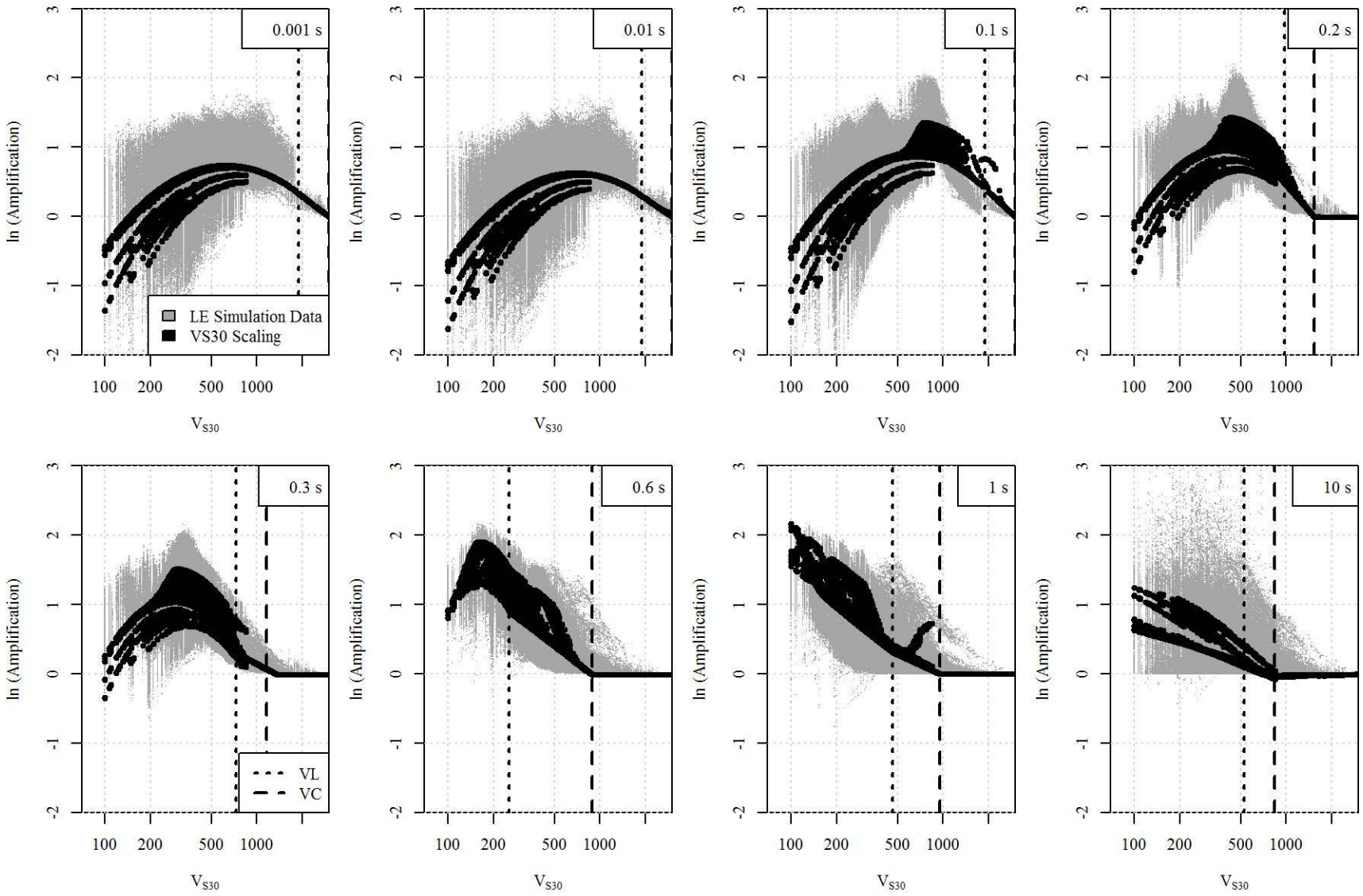

Figure 54: L3 Site Amplification Function

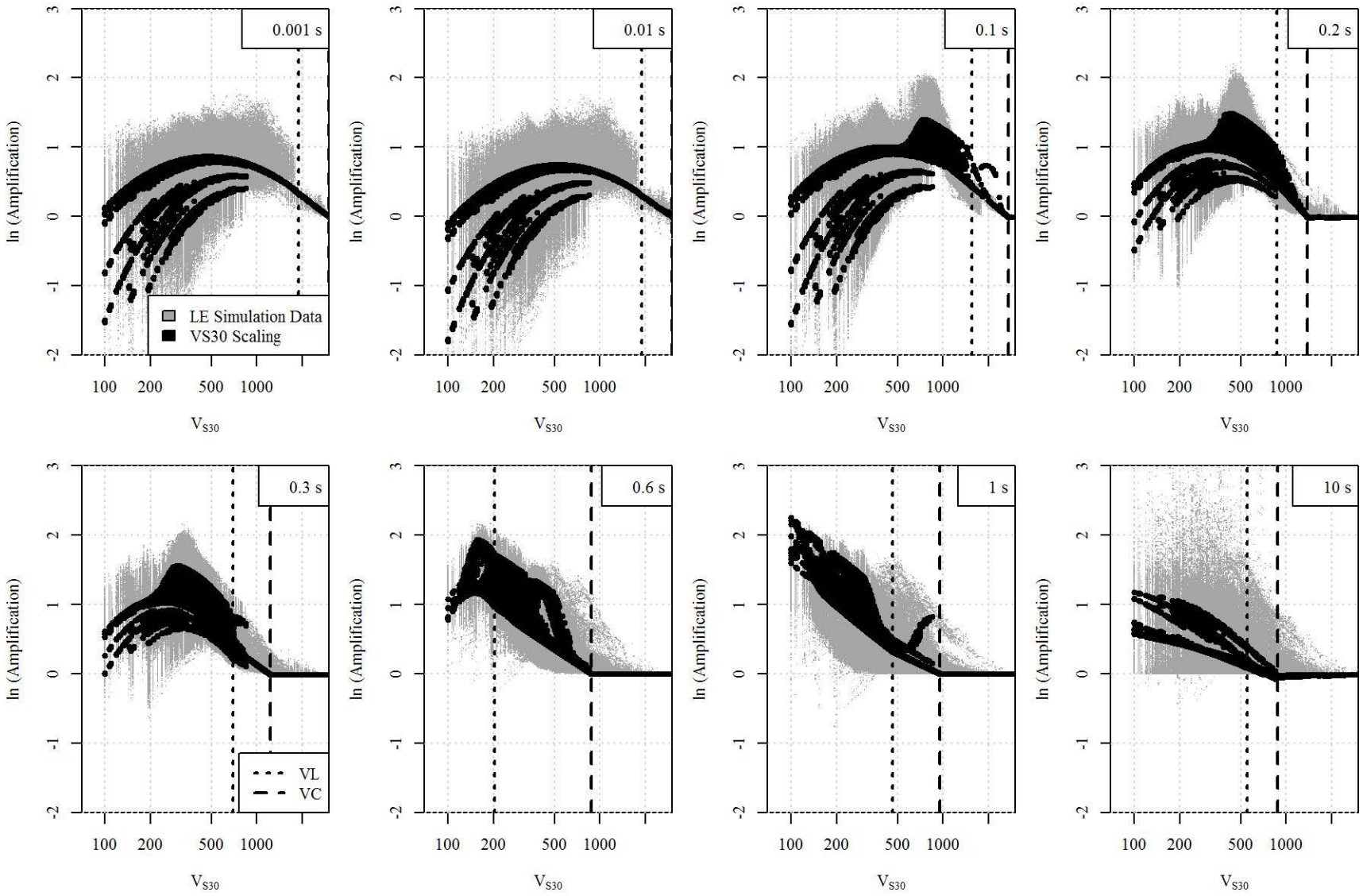

Figure 55: L5 Site Amplification Function

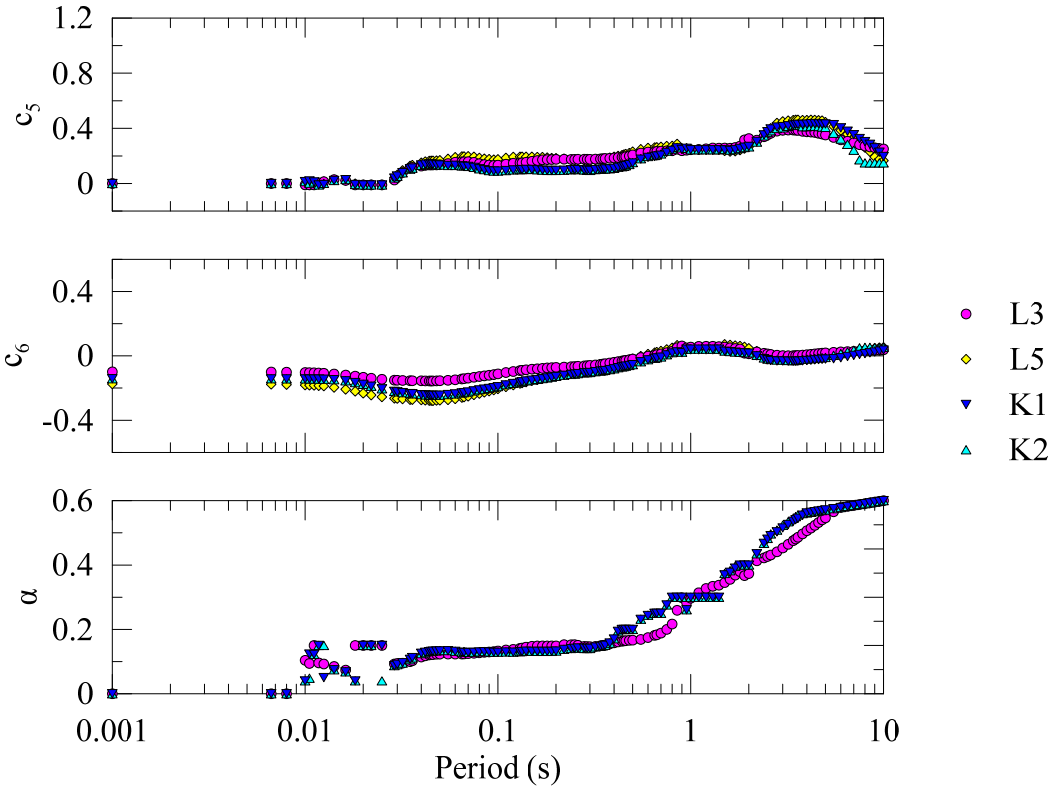

Figure 56: Response Spectral Coefficients for f(T_{nat})

4.4 NONLINEAR SITE EFFECTS

The nonlinear site amplification, $f(NL)$, shown in Table 19 is given by eq. (23) and (24), modified from Chiou and Youngs (2008) and Seyhan and Stewart (Seyhan and Stewart 2014)

$$\ln(amp) = \begin{cases} f_2 \ln\left(\frac{I_r + f_3}{f_3}\right) & V_{S30} < V_c \\ 0 & V_{S30} \geq V_c \end{cases} \quad (23)$$

Where f_2 and f_3 describe the nonlinear site effects and I_r is an intensity measure of the 3000 m/s bedrock condition ground motion that drives site nonlinearity. The f_2 coefficient is given as a function of V_{S30} in (24).

$$f_2 = f_4\left[\exp\left\{f_5\left(\min\left(V_{S30}, V_{ref}\right) - 360\right)\right\} - \exp\left\{f_5\left(V_{ref} - 360\right)\right\}\right] \quad (24)$$

Where f_4 and f_5 describe the effect of V_{S30} on the nonlinear site effects, and V_c is the reference rock condition of 3000 m/s from the V_{S30} scaling. For the N1 and N2 models, V_c from the L1 site

amplification model is used, for the K1 and K2 models, V_c is regressed simultaneously with the nonlinear amplification coefficients.

The functional forms for the nonlinear site amplification given in eq. (23) and (24) have two departures from the functional form proposed in Chiou and Youngs (2008) and adapted in Seyhan and Stewart (Seyhan and Stewart 2014): the removal of an f_1 intercept in (23) and the adjustment of V_{ref} in (24) to the CENA reference rock condition of 3000 m/s described in Hashash et al. (2014) from the 1130 m/s in Chiou and Youngs (2008) and 760 m/s Seyhan and Stewart (Seyhan and Stewart 2014).

The first change in (23) is the removal of an f_1 intercept. In the simulation data of this study, direct comparisons are possible between linear and nonlinear site response analyses, and the simulations will converge for very low levels of earthquake intensity. In previous sets of simulations such as Walling et al. (2008), nonlinear site amplification is typically regressed as amplification as a function of ground motion intensity, and in empirically-derived nonlinear site amplification, there is no observation of a simultaneous linear site response and nonlinear site response for high levels of shaking. In those studies, the nonlinear site amplification requires an additional coefficient, f_1, to describe the difference between the observed nonlinear site amplification and the modeled linear site amplification. In this study, the nonlinear site amplification can be modeled independently of the linear site amplification model by direct comparison of the linear site response analysis and the nonlinear site response analysis.

Two kinds of site amplification models with nonlinear site effects are provided, L+N type and K type as shown in Tables 18 and 19. The L+N model type uses linear amplification terms from LE analyses, and nonlinear amplification terms from the difference between NL GQ/H analyses and the corresponding LE analyses. The parametric study tree as shown in Figure 28 has one of each LE, EL and NL site response analyses conducted for each profile and motion combination. Figure 57 (a) and (b) show the fitting of the N1 and N2 model coefficients, respectively, to simulation data at 0.1 s. Figures 58 and 59 show the N1 and N2 nonlinear site amplification term. Figures 61 and 62 show the estimated K1 and K2 site amplification and simulated GQ/H nonlinear site response for all simulations in this parametric study as a function of V_{S30},

respectively. The coefficients for the *f(NL)* amplification are shown graphically in Figure 60 and provided in tabular form in APPENDIX D.

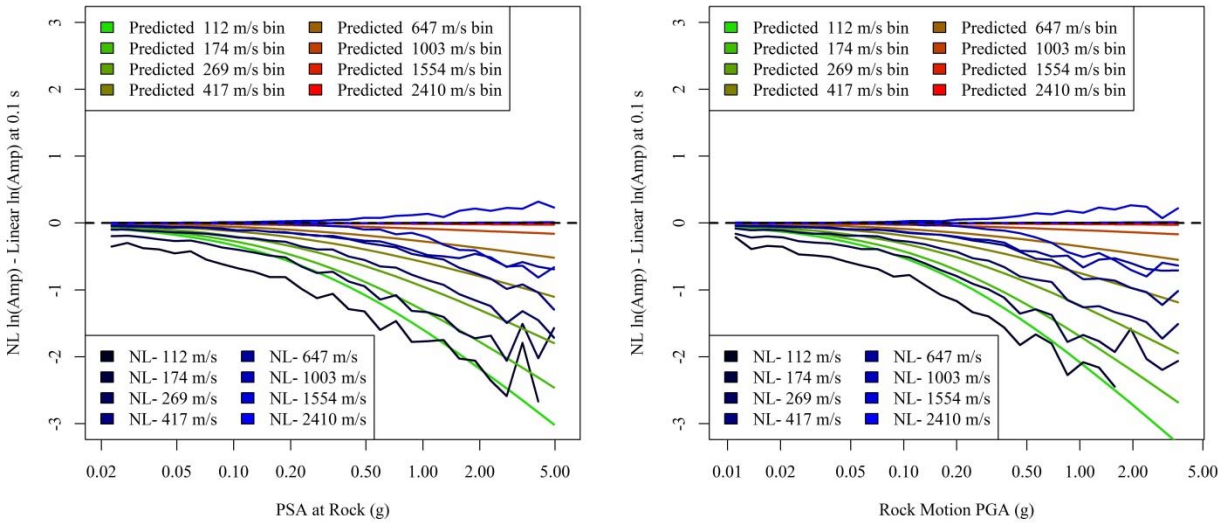

Figure 57: Nonlinear site amplification at 0.1 s as a function of PSA (N1) (a) and PGA (N2) (b)

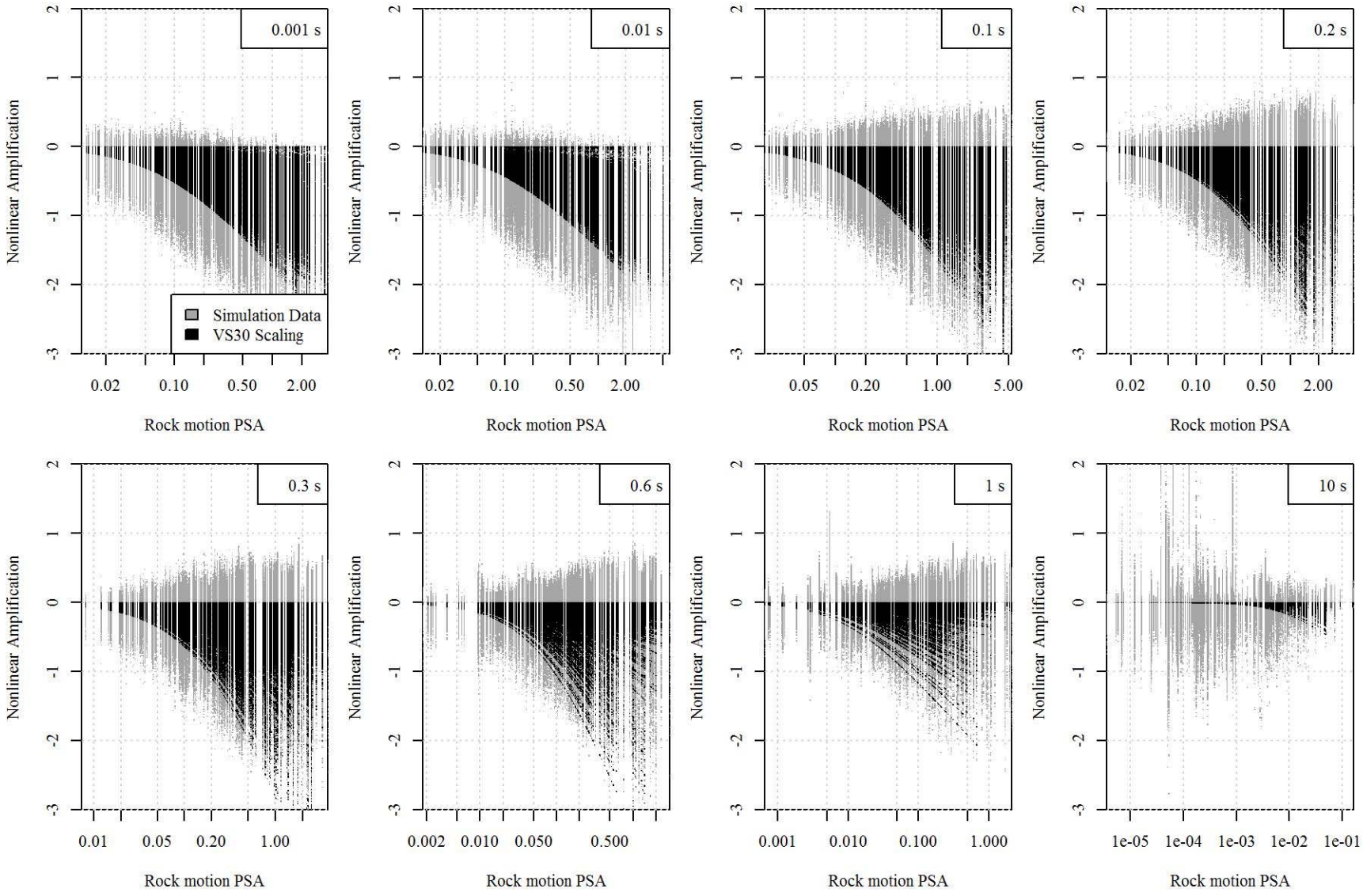

Figure 58: N1 Nonlinear site amplification model

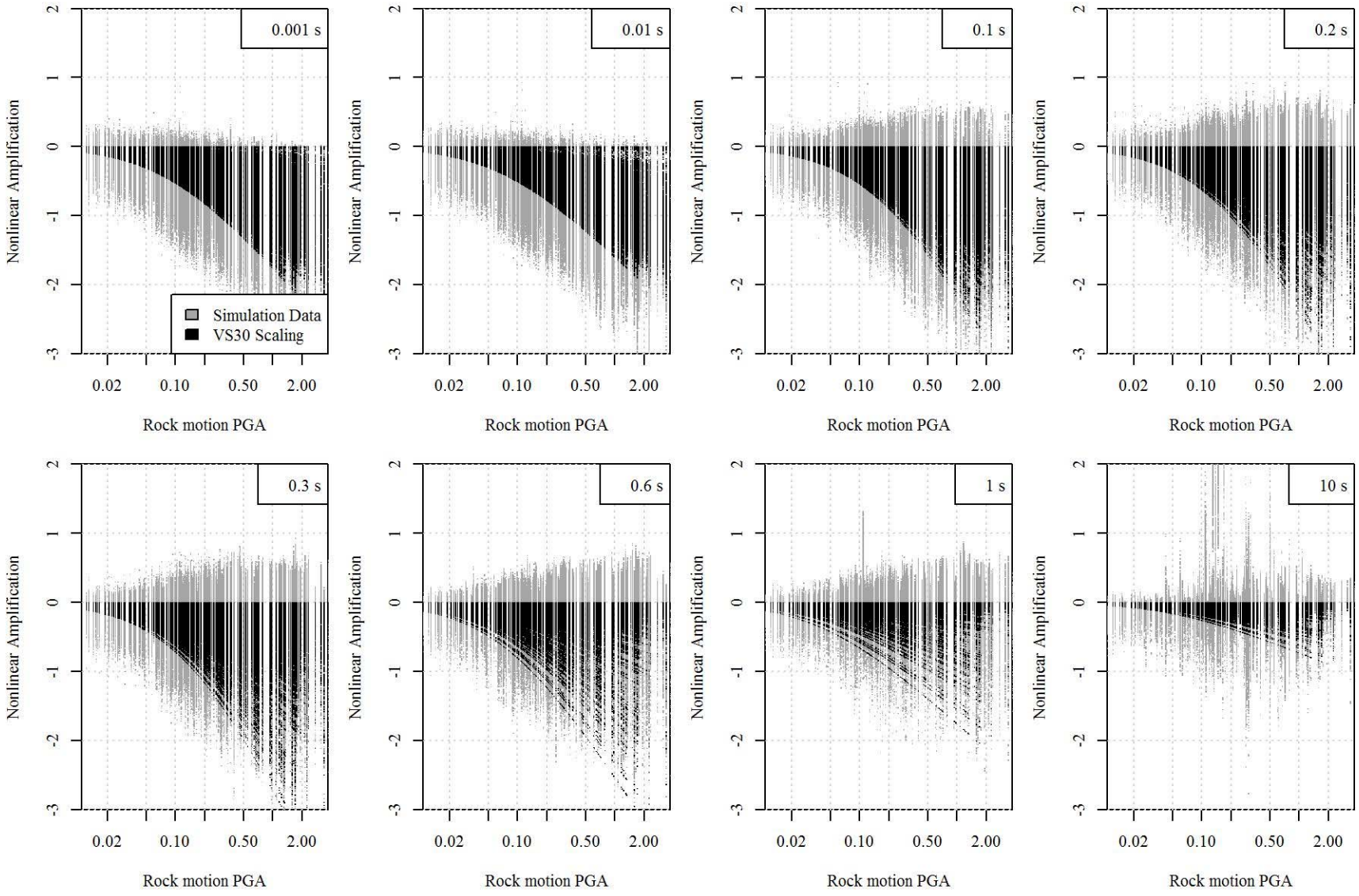

Figure 59: N2 Nonlinear site amplification model

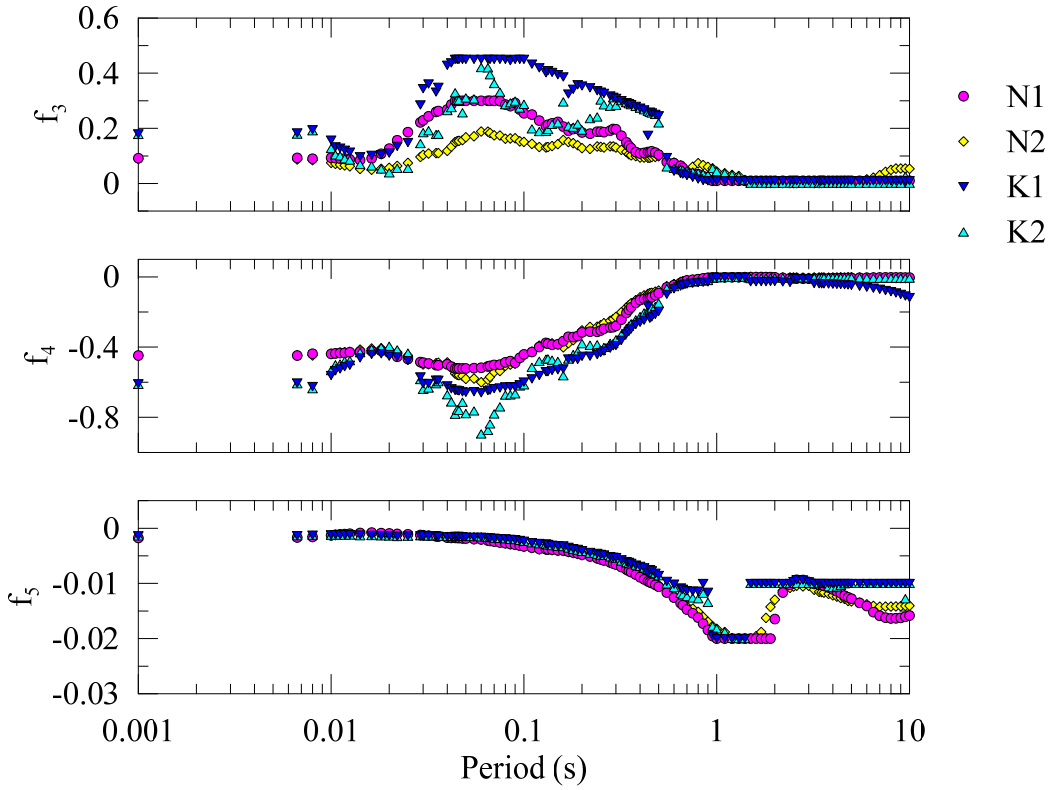

Figure 60: Response Spectral Coefficients for f(NL)

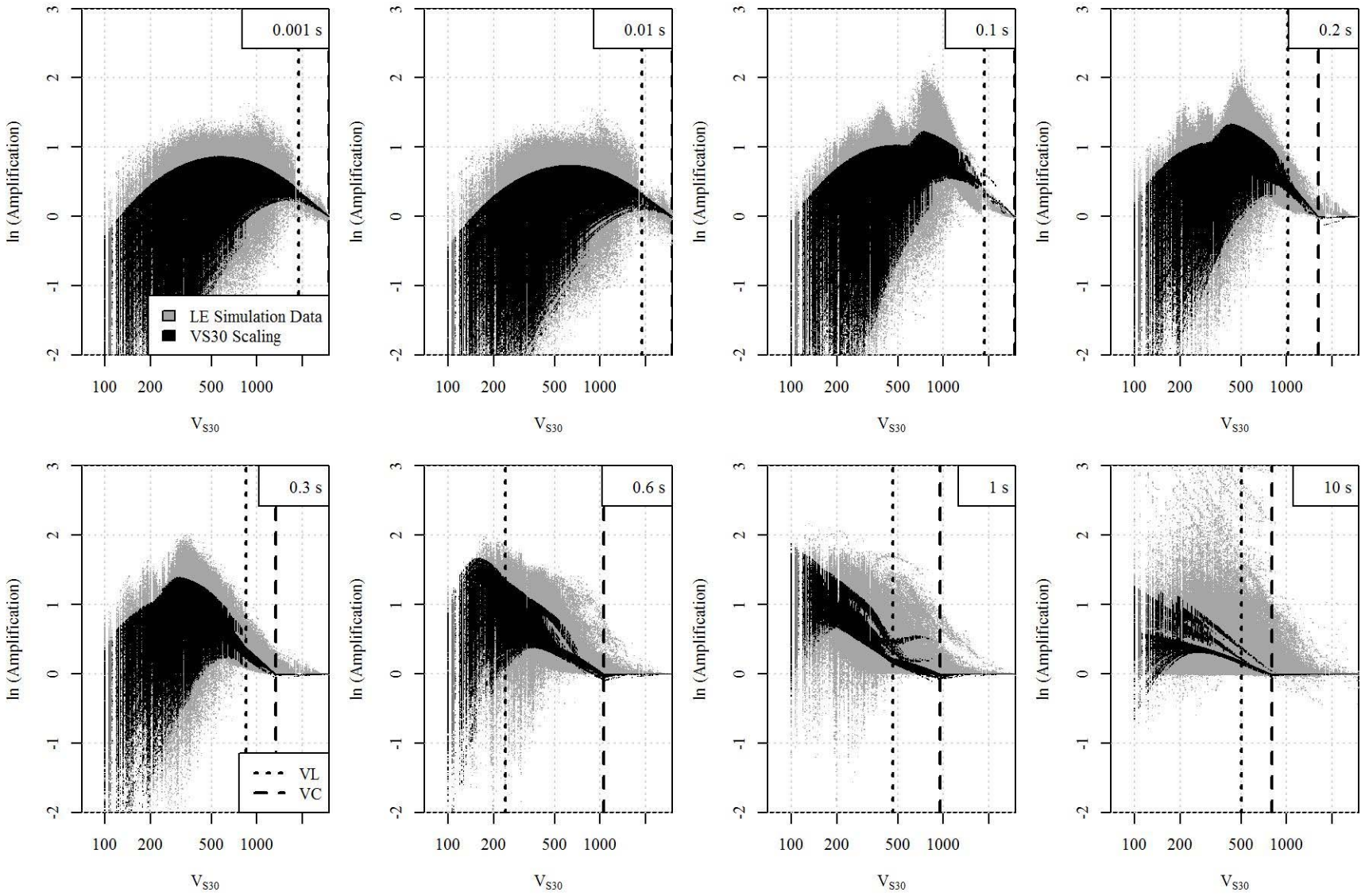

Figure 61: K1 site amplification model

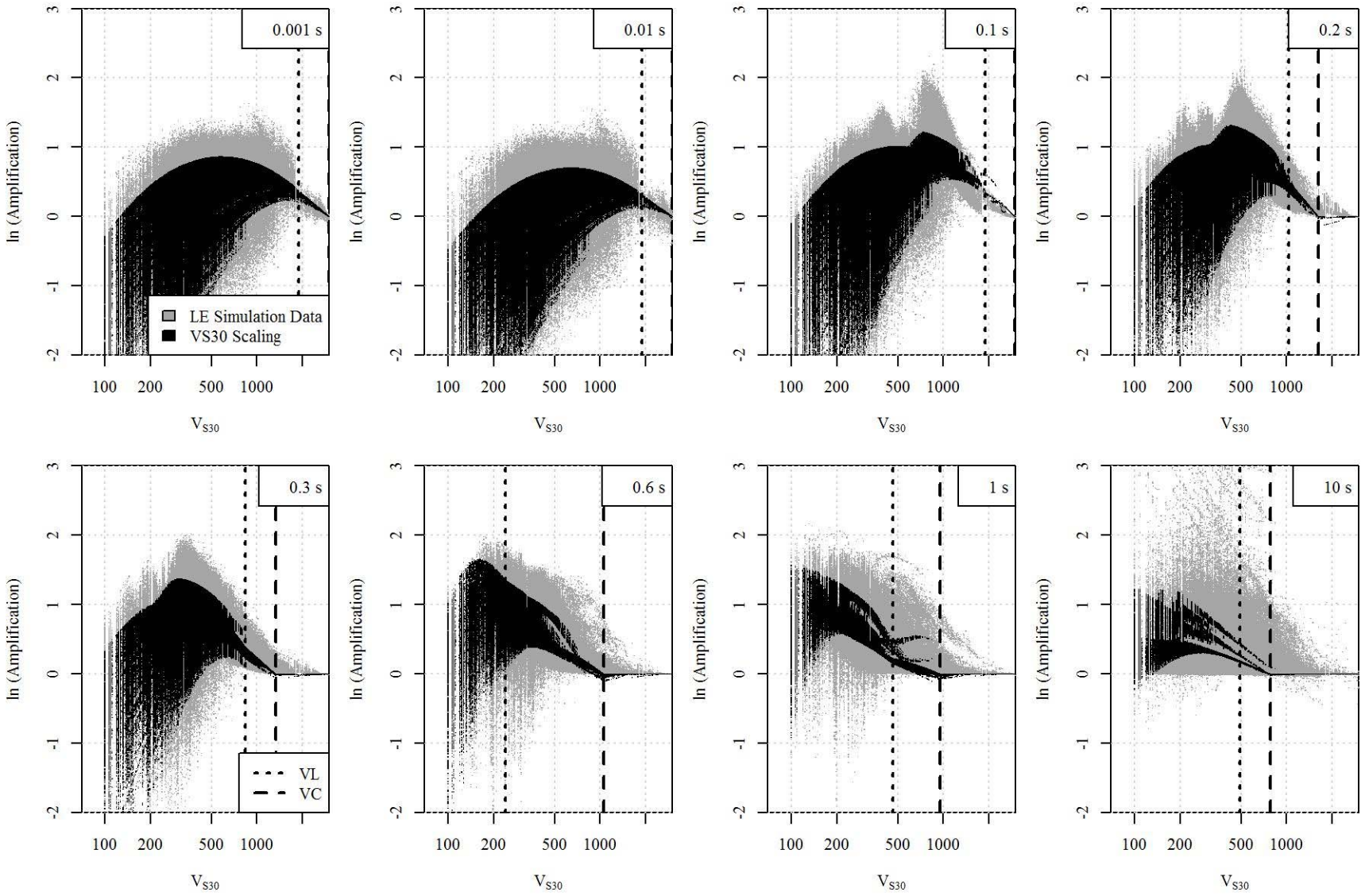

Figure 62: K2 site amplification model

4.5 AMPLIFICATION RELATIVE TO 760 M/S

The difference in site amplification behavior relative to 3000 m/s rock condition in CENA and relative to 760 m/s rock condition in the WUS is of particular interest to the developers of seismic hazard maps and GMPE's. The site response analyses conducted in this parametric study are used to develop period-dependent coefficients of average amplification of sites with V_{S30} near 760 m/s relative to the 3000 m/s CENA bedrock condition. Figure 63 shows two sets of coefficients derived from linear elastic site response analyses that describe the amplification of sites with V_{S30} near 760 m/s, and is included in tabular form in APPENDIX E.

The depth-independent coefficients shown in Figure 63 are calculated from the log average amplification of all linear elastic simulations for soil profiles with V_{S30} between 700 and 800 m/s. The depth-dependent coefficients shown in Figure 63 are calculated from the log average amplification of all linear elastic simulations for soil profiles withV_{S30} between 700 and 800 m/s for each depth bin considered in the parametric study tree in Figure 28. These coefficients represent the amplification for sites with a V_{S30} near 760 m/s relative to a 3000 m/s bedrock condition at some known depth. The calculated V_{S30} of all profiles used in these analyses includes soil material, weathered rock, and 3000 m/s bedrock material.

The coefficients presented in this study can serve as a way to correct site amplification models developed for a 760 m/s site condition to a 3000 m/s site condition or vice versa through the use of (25).

$$f(amp)_{760} = f(amp)_{3000} - C_{760-3000} \tag{25}$$

Where $f(amp)_{760}$ is the site amplification relative to a 760 m/s reference condition, $f(amp)_{3000}$ is the site amplification relative to a3000 m/s reference condition, and $C_{760\text{-}3000}$ is the mean amplification of sites with V_{S30} near 760 m/s relative to a 3000 m/s reference condition (i.e. the 760 to 3000 m/s correction provided in APPENDIX E)

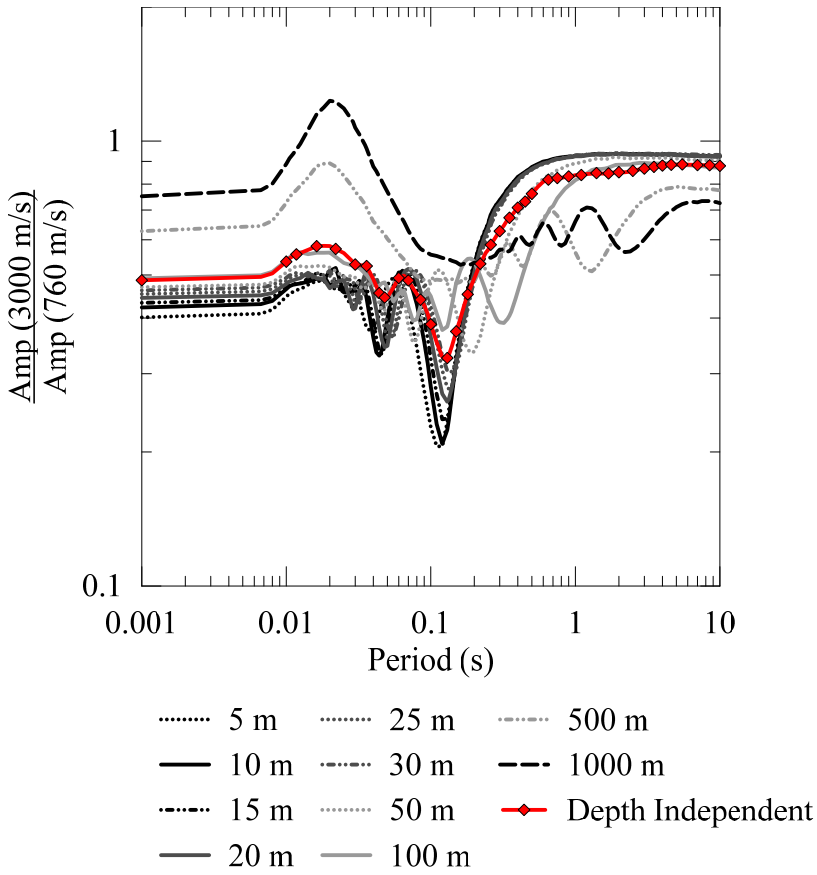

Figure 63: Adjustment for 7600-3000 m/s by depth to 3000 m/s bedrock

4.6 MODEL EVALUATION

The linear and nonlinear site amplification modes developed in this study are modular functions intended to be usable with different amounts of site information. If site natural period or depth to weathered rock are available, more advanced model forms for linear (L models as shown in Table 18) amplification can be used. The nonlinear site amplification models (L+N models and K models as shown in Table 18) are provided for two different drivers of nonlinearity: PSA and PGA. A discussion of the relative effect on error of adding amplification terms to the site amplification model or regressing terms separately or simultaneously is provided in APPENDIX F.

4.6.1 Applicability range of response spectral models

The site response model presented in (15) is not intended for use for all levels of ground motion shaking and all soil profiles. For all linear models, the simulations used to develop the model

terms are all linear elastic simulations as presented in Figure 28. For all nonlinear amplification models, the simulations used were the GQ/H analyses with maximum strains resulting from the site response analysis in any soil layer being less than 1% shear strain. For the GQ/H analyses with shear strains larger than 1%, the N model terms are regressed without effects from the corresponding linear elastic simulation. The K models only use analyses with maximum shear strains of less than 1%.

The response spectral models presented in Table 19 are applicable for sites with V_{S30} > 200 m/s and ground motions with PGA values < 1.0 g. Sites with V_{S30} values less than 200 m/s require detailed modeling of the soil V_S structure and shear stress-strain behavior to accurately describe site behavior. The ergodic site amplification functions presented here are not appropriate for very soft sites. For strong levels of ground shaking with PGA values greater than 1.0 g, the 1-D assumption used in site response analysis can become invalid as multidimensional and basin effects begin to influence observed site amplification.

4.6.2 Site-Specific comparisons of amplification model to simulation data

Regression coefficients and amplification models developed up to this point have been evaluated on the period-independent performance in capturing the ergodic site amplification behavior across all sites used in the parametric study. This section will compare the shape of the site amplification and response spectra from the regressed amplification models to computed site amplification for a single soil profile and motion combination. The amplification from the simulation for the soil profile will be compared to all similar analyses in the parametric study. An analysis is considered to have similar if it has a V_{s30} within 20%, the same depth to weathered rock, and a bedrock motion PGA within 30%.

The site response analysis under investigation is a randomization of the RS+YGdYGtYGo+YGm characteristic V_S profile with 25 m of soil material above the 30 m gradient weathered rock zone model and negative G/G_{max} ε from the nonlinear curve randomization. The soil profile has a V_{S30} of 377 m/s with T_{nat} of 0.36 s. This profile is paired with a bedrock ground motion from NUREG (McGuire et al. 2001) 55Rab_B-KOD180 from an M 5.5 earthquake at 0-50 km distance and has

a PGA of 0.4 g. The site amplification of the soil profile is shown in Figures 64, 65, and 66. The response spectra corresponding to the site amplification for the soil profile is shown in Figures 67, 68, and 69. There are 2676 simulations similar to the soil profile.

Figure 64 shows the predicted amplification for the soil profile from the linear site amplification functions and compares to the linear elastic simulation of the soil profile. The L1 and L2 amplification models for this site are identical. The L2 site amplification model uses the same V_{S30} scaling as the L1 site amplification model and a depth-dependent correction if the site has greater than 50 m. the soil profile has a depth of 25 m so there is no depth-dependent correction for the L2 amplification model. The L4 amplification model has only minor differences from the L1 and L2 amplification models. The L3 and L5 models have different shapes than the other amplification models around the natural period of the site. The L3 and L5 models both show relative increases in the amplification near the natural period of the site as a result of the Riker wavelet term in the natural period amplification function.

Figure 65 shows the L+N nonlinear amplification functions calculated for the soil profile calculated from GQH analyses. The EL analysis result for the soil profile is also shown in Figure 65. The same amplification features of the linear models in Figure 64 are present in Figure 65. the soil profile is a simulation of a bedrock ground motion with PGA of 0.4 g and nonlinear effects are expected and can be observed by the lower site amplification in the nonlinear amplification when compared to the linear amplification at high frequencies. The error of the N1 and N2 site amplification terms for PSA and PGA, respectively, is very similar, and the corresponding plots (b) and (a) in Figure 65 show only slight differences in the level of amplification and no differences in the shape of the amplification functions.

Figure 66 shows the K nonlinear amplification functions for the soil profile. The notable difference between the model amplification in Figure 65 and Figure 66 is the amplitude of the peak of the amplification near the natural period of the soil column. The peak of the natural period amplification in the L+N models is derived from the linear component of amplification independently of the nonlinear amplification. The L+N models do not evaluate nonlinearity near T_{nat} of the soil column differently than nonlinearity at other periods within the profile, while the K models consider the nonlinearity at the same time as the peak of amplification near the soil

column natural period. The peak in the nonlinear K models is expected to be less dramatic than the L+N nonlinear models as a result. However, neither the L+N nor the K amplification models consider any changes in T_{nat} that may occur for a soil column as a result of soil nonlinearity, and the width of the natural period of the K models may widen as a result.

The response spectra corresponding to the L linear amplification models for the soil profile is shown in Figure 67 and compared with the LE site response analysis. Figure 68 shows the response spectra corresponding to the L+N nonlinear amplification. The nonlinear effects on the site amplification can be seen clearly in the high frequency range of Figure 68 when compared to Figure 67. The negative amplification of the response spectrum at high frequency is the result of the nonlinearity in the model from the N coefficient. The natural period effects of the L3+N and L5+N amplification model when evaluated with the response spectrum are also clear. The L1+N, L2+N, and L4+N amplification models near the natural period of the soil column have the same shape as the input ground motion spectrum with a relative decrease in spectral acceleration at 0.4 s. The amplification models that include the effects of natural period (L3+N and L5+N) more accurately capture the site amplification behavior and spectral shape observed in the simulations near the natural period. Figure 69 shows the response spectra for the K model amplification compared to the EL and NL site response analyses for the soil profile. The response of the K models for the soil profile are similar to the L+N models shown in Figure 68 without as strong natural period effects as seen in the difference between Figures 65 and 66.

4.6.3 Comparison of NGA-East GWG CENA Site Amplification Models

This study presents a suite of models that exhibit differences previously published literature. The NGA-East GWG site amplification models each use coefficients developed with a range of regression methodologies for varying amounts of site and bedrock motion data. The NGA-East GWG models also use different functional forms than models developed using primarily WUS data for the effects of V_{S30}, and nonlinear site amplification for the GWG models uses different coefficients than the WUS models.

The L1 V_{S30} scaling model uses a different functional form than the log-linear with V_{S30} functional form commonly used in the WUS. Figure 70 shows the L1 model with the BSSA14, and CS05 (Choi and Stewart 2005) amplification models for V_{S30} values of 200, 400, and 760

m/s and the AB11 amplification model for site class A (1500 m/s) and site class BC (760 m/s). The BSSA14 (Boore et al. 2013), CS05, and AB11 (Atkinson and Boore 2011) amplification functions are all developed for a 760 m/s reference condition and not the 3000 m/s reference condition of CENA of the L1 model, so the models are converted to be relative to 3000 m/s in Figure 70 by using the conversion procedure above and APPENDIX E. The models relative to the WUS reference condition all exhibit a decrease in amplification as a function of V_{S30} at all periods. The L1 amplification model shows a decrease in amplification for higher V_{S30} at longer periods, but at shorter periods, shows an increase in amplification for higher V_{S30}. This fundamentally different behavior results from the curved region of the V_{S30} amplification in the L1 model (i.e. the c_2 and c_3 terms).

The L1+N2 amplification model is compared to the CS05 model for site amplification as a function of V_{S30} and PGA in Figure 71. The L1+N2 model and the CS05 model both include the effects of site nonlinearity as the same function of V_{S30} with PGA as the driver of soil nonlinearity. The change in site amplification at stronger shaking is more pronounced for the L1+N2 site amplification model than the CS05 model at low periods, but at long periods, the CS05 model exhibits more nonlinearity.

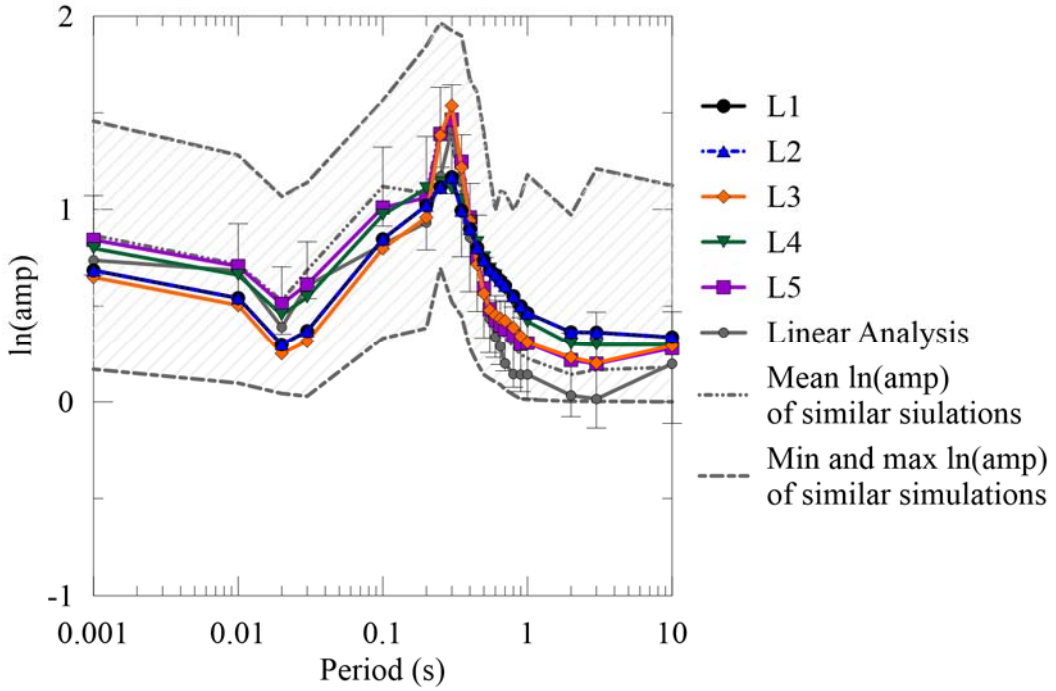

Figure 64: Linear site amplification functions compared to LE simulations for Profile A and similar sites. Error bars represent +/- 1 standard deviation of ln(amp) for 2676 similar sites.

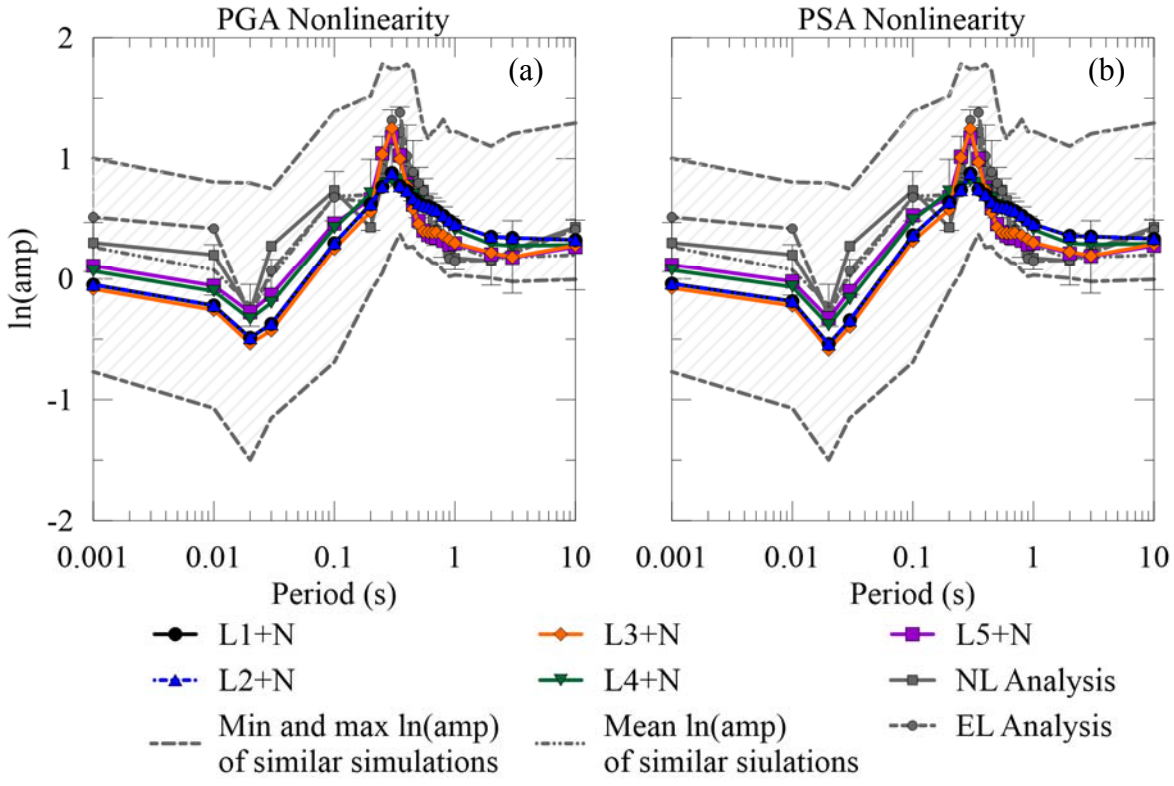

Figure 65: Nonlinear site amplification functions for PGA (a) and PSA (b) with L+N model form compared to NL simulations for a selected soil profile and similar sites. Error Bars represent +/- 1 standard deviation of ln(amp) of 2676 similar sites.

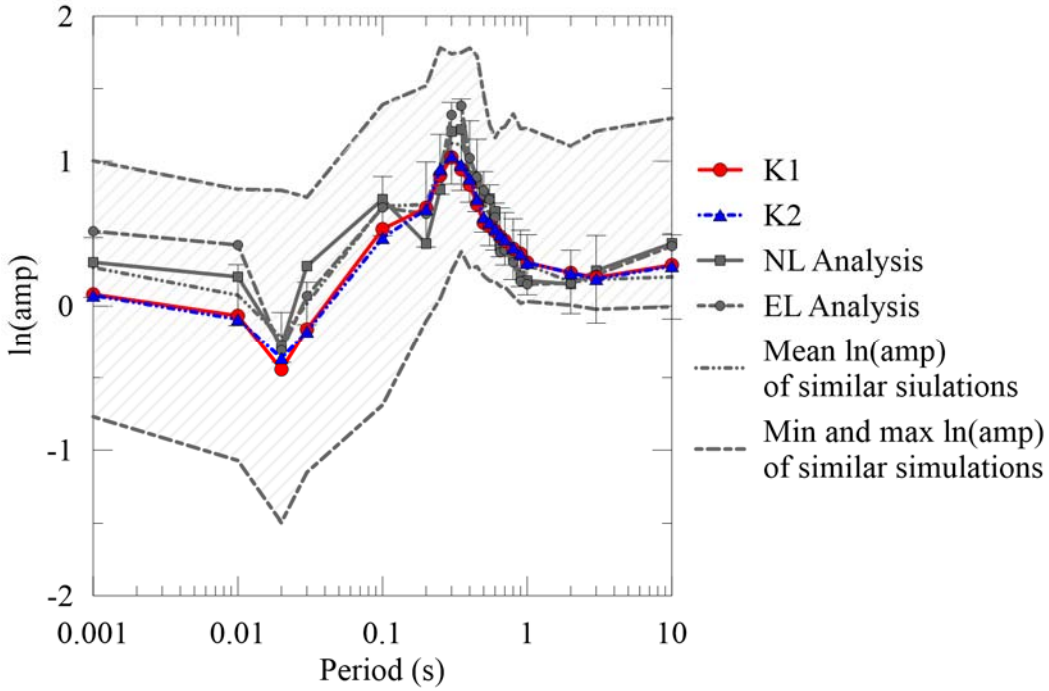

Figure 66: Nonlinear site amplification functions with K model form compared to NL simulations for a selected soil profile and similar sites. Error Bars represent +/- 1 standard deviation of ln(amp) of 2676 similar sites.

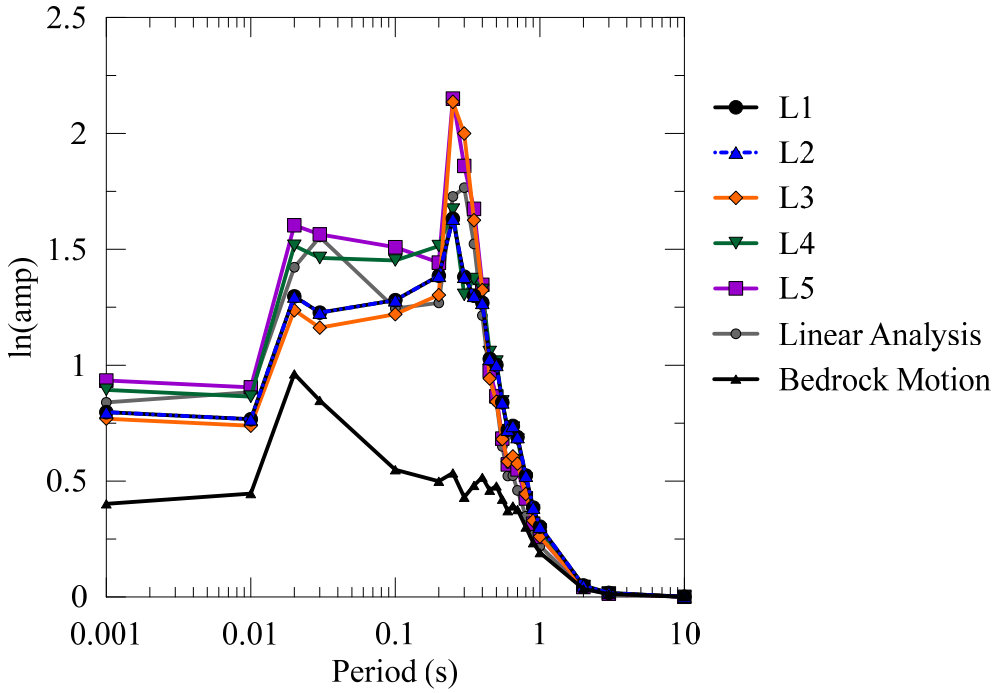

Figure 67: Response spectra resulting from linear site amplification functions compared to LE simulation of a selected soil profile.

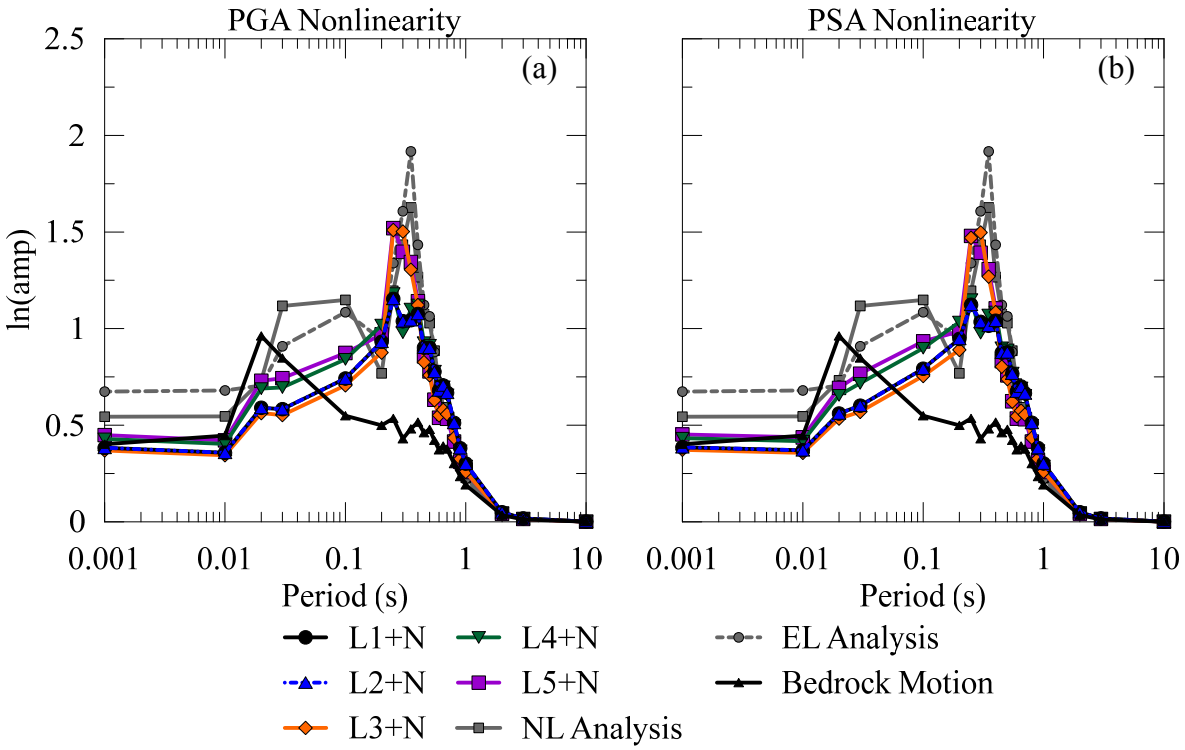

Figure 68: Response spectra resulting from L+N nonlinear site amplification functions compared to NL and EL simulation of a selected soil profile for PGA (a) and PSA (b) drivers of nonlinearity.

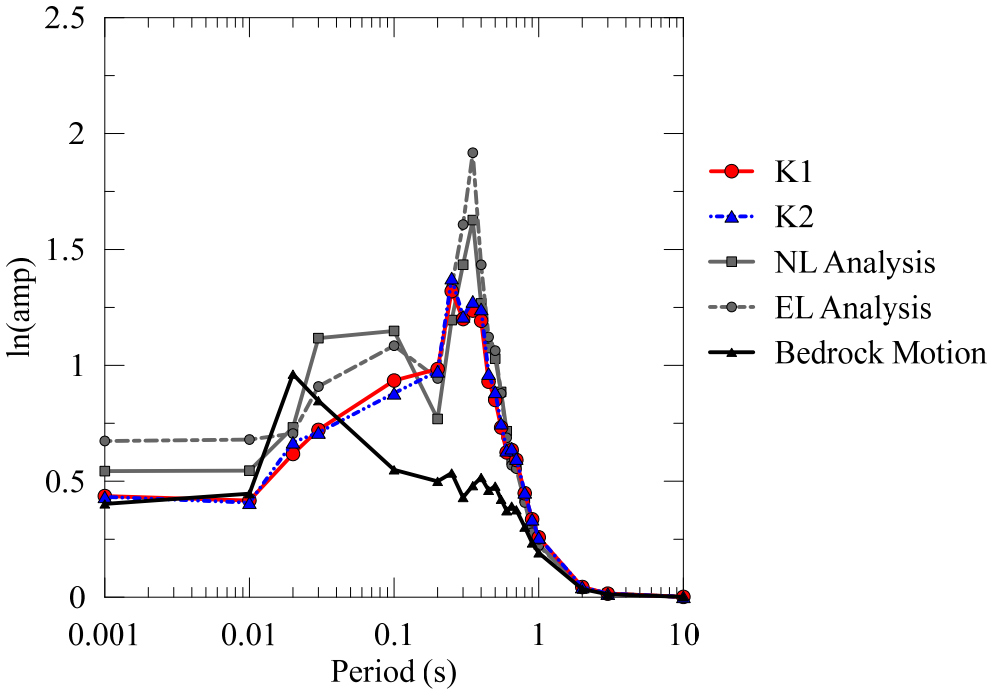

Figure 69: Response spectra resulting from K nonlinear site amplification functions compared to NL and EL simulation of a selected soil profile.

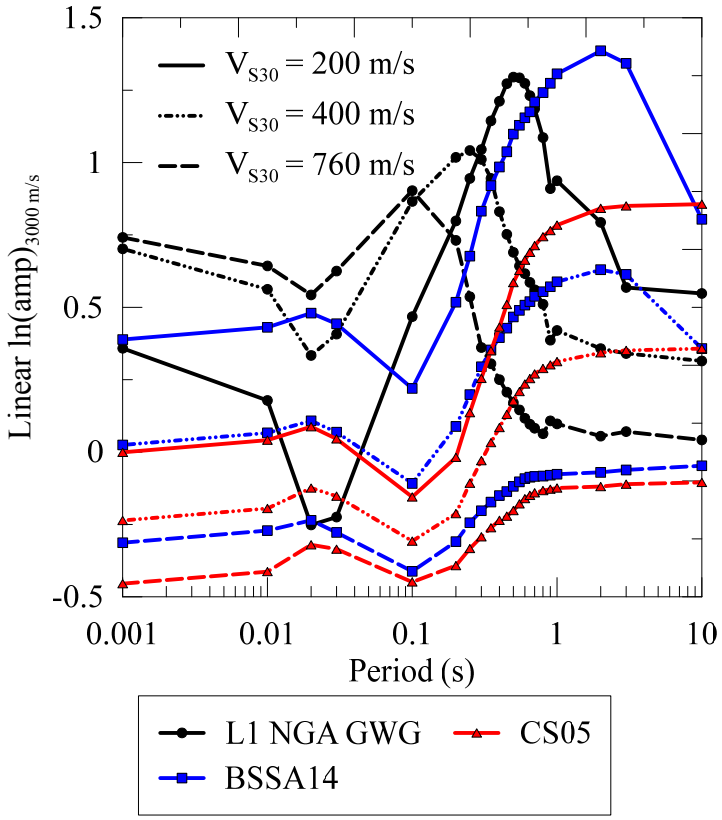

Figure 70: Comparison of Vs30 Scaling Models relative to 3000 m/s. CS05 and BSSA14 have been corrected to a 3000 m/s condition using the $C_{760\text{-}3000}$ presented in this study

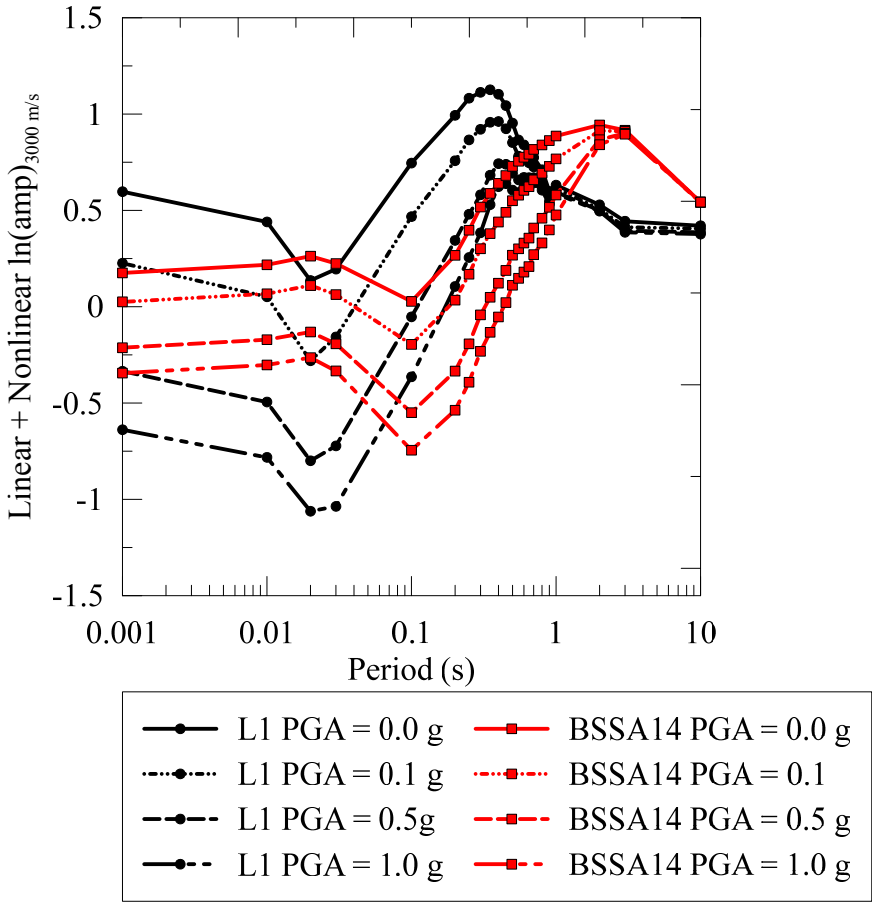

Figure 71: Comparison of site nonlinearity of models relative to 3000 m/s. CS05 and BSSA14 have been corrected to a 3000 m/s condition using the $C_{760\text{-}3000}$ presented in this study

5 CONCLUSIONS

Ground motion prediction equation (GMPE) development and seismic engineering design requires the proper modelling of site effects on ground motions. Previously available GMPEs and site factors developed for CENA do not quantify the region-specific soft soil amplification or the effects of soil nonlinearity on site response. In this report, a suite of empirical and simulation-based site amplification models for CENA is presented. A geology-based proxy procedure for V_{S30} is developed from a database of V_{S30} obtained from measured V_S Profiles and supplemented with geologic information from larger-scale maps to differentiate glaciated/non-glaciated regions and the presence of sedimentary basins. This study reveals the importance of the effects of glaciation on dispersion of V_{S30} in that non-glaciated regions display dispersions that are significantly lower than have been found previously for CENA (σ_{lnV} = 0.357) but comparable to proxy dispersions for active tectonic regions. For glaciated regions, σ_{lnV} is much higher (σ_{lnV} = 0.656) and thus the predictability of V_{S30} is better for non-glaciated than for glaciated regions.

An empirical linear site amplification model is developed for CENA by using ground motion measurements at recording stations with the geology-based proxy procedure for V_{S30}. Previous models, are either simulation-based using CENA conditions or are empirical for considering active tectonic regions. The developed model quantifies site amplification at recording stations extracted from NGA-East ground motion data using the non-reference site approach. The model reveals more significant differences in linear site amplification between CENA and active tectonic regions (e.g. SS14) than exist between different active tectonic regions such as California, Taiwan and Japan. The linear empirical amplification model form at low V_S values was guided in part by the linear amplification models derived from the results of the large-scale site response simulation study.

A large-scale parametric study of 1-D LE, EL and NL site response analyses developed from CENA site conditions are conducted to produce an additional suite of linear and nonlinear site amplification models. The input parameters to the site response analysis are extracted from data compiled for CENA including bedrock ground motions, V_S Profiles, small strain damping values, and nonlinear G/G_{max} and damping curves. Characteristic V_S profiles are developed and matched with geology-based soil properties and nonlinear dynamic curves quantified using the empirical

model of Darendeli (2001) and modeled with the strength-controlled GQ/H model of Groholski et. al. (2016).

High frequency response of soil sites in CENA is captured by spectral decay factor, κ_0 and represented in the selection of ground motions and soil D_{min}. A of 246 bedrock ground motions are selected for analyses composed of 186 synthetic motions from NUREG-6729 (McGuire et al., 2001) and 61 motions stochastically generated by SMSIM (2005). κ_0 is well-correlated with small strain damping (D_{min}) and D_{min} profiles for soil sites are developed using both Darendeli (2001), proposing that D_{min} as a function of PI, OCR, and mean effective stress (σ_o'), and Campbell (2009). The correlations from Darendeli (2001) produced D_{min} values that tended to be smaller than those predicted by the Campbell (2009) models because Darendeli (2001) quantifies damping by laboratory measurement which includes only material damping and ignores the attenuation caused by wave scattering in the field. This difference in D_{min} for these two models results in the prediction of larger κ_0 values by Campbell (2009) with more considerable variation among the sites than the κ_0 values derived from the Darendeli (2001) model. The parametric study parameters result in 1.7 million LE, EL and NL site response analyses in which linear site amplification is quantified by LE analyses and nonlinear site amplification is captured by EL and NL analyses.

Site amplification from these site amplification analyses is captured by a model including linear amplification components as functions of V_{S30}, natural site period (T_{nat}) and soil depth (Z). Nonlinear site amplification is modelled as functions of V_{S30} and with either bedrock PGA or bedrock PSA as the driver of site nonlinearity. This detailed interpretation of site amplification results in a total of 17 models, 5 models for linear site amplification and 12 models for nonlinear site amplification. The simulation based linear site amplification model shows significant dependence on site period highlighting the need to quantify this parameter.

6 ACKNOWLEDGEMENTS

This study was supported by the U.S. Geological Survey (USGS). Any opinions, findings, and conclusions or recommendations expressed in this material are those of the authors and do not necessarily reflect those of the organizations listed above. The authors would like to thank Michael Musgrove, Okan Ilhan, Sissy Nikolaou, Cheryl Moss, Albert Kottke, and Byungmin Kim for their contribution to this work.

7 REFERENCES

Aboye, S. A., R. D. Andrus, N. Ravichandran, A. H. Bhuiyan and N. Harman (2015). "Seismic Site Factors and Design Response Spectra Based on Conditions in Charleston, South Carolina." Earthquake Spectra **31**(2): 723-744.

Anderson, N. and T. Thitimakorn (2004). A 2-D MASW Shear-Wave Velocity Profile along a Test Segment of Interstate I-70, St. Louis, Missouri, RDT 04-012, Missouri Department of Transportation: 34 pages.

Anderson, N., d. Hoffman, W. Liu, R. Luna, R. Stephesnson and T. Thitimakorn (2005). Comprehensive Shear-Wave Velocity Study in the Polar Bluff Area, Southeast Missouri, RDT 05-006, Missouri Department of Transportation: 197 pages.

Anderson, N., G. Chen, S. Kociu, R. Luna, T. Thitimakorn, A. Malovichko, D. Malovichko and D. Shylakov (2003). Vertical Shear-Wave Velocity Profiles Generated from Spectral Analysis of Surface Waves: Field Examples, Missouri Department of Transportation.

Andrus, R. D., C. D. Fairbanks, J. Zhang, W. M. Camp Iii, T. J. Casey, T. J. Cleary and W. B. Wright (2006). "Shear-Wave Velocity and Seismic Response of Near-Surface Sediments in Charleston, South Carolina." Bulletin of the Seismological Society of America 96(5): 1897-1914.

Ashland, F. X. and N. G. McDonald (2003). Interim Map Showing Shear-Wave-Velocity Characteristics of Engineering Geologic Units in the Salt Lake City, Utah, Metropolitan Area.

Atkinson, G. M. and D. M. Boore (2011). "Modifications to Existing Ground-Motion Prediction Equations in Light of New Data." Bulletin of the Seismological Society of America **101**(3): 1121-1135.

Atkinson, G. M., and R.F. Mereu (1992). The Shape of Ground Motion Attenuation Curves in Southeastern Canada. *Bul. Seismol. Soc. Am.* **82** 2014-2031.

Atkinson, GM (2008). Ground-Motion Prediction Equations for Eastern North America from a Referenced Empirical Approach: Implications for Epistemic Uncertainty, *Bull. Seism. Soc. Am.*, 98, 1304–1318.

Atkinson, GM and DM Boore (2006). Earthquake Ground-Motion Prediction Equations for Eastern North America, *Bull. Seism. Soc. Am.*, **96**(6), 2181–2205.

Bates D., M. Maechler, B. Bolker, and S. Walker (2015). Fitting Linear Mixed-Effects Models Using lme4. *Journal of Statistical Software*, **67**(1), 1-48.

Bauer, R. A. (2004). Central U.S. Shear-Wave Velocity Database with Accompanying Geological/Geotechnical Information of Nonlithified Geologic Materials, External Grant Award Number 04-HQ-GR-0074, U.S. Geological Survey.

Beresnev, I. A. and G. M. Atkinson (1997). "Shear-Wave Velocity Survey of Seismographic Sites in Eastern Canada: Calibration of Empirical Regression Method of Estimating Site Response." Seismological Research Letters 68(6): 981-987.

Boore, D. M. (2013). The Uses and Limitations of the Square-Root Impedance Method for Computing Site Amplification, *Bull. Seismol. Soc. Am.* **103**, 2356--2368.

Boore, D., and W. Joyner (1997). Site Amplifications for Generic Rock Sites, *Bull. Seism. Soc. Am.* **87,** 327–341.

Boore, D., J. P. Stewart, E. Seyhan and G. A. Atkinson (2013). NGA-West2 Equations for Predicting Response Spectral Accelerations for Shallow Crustal Earthquakes, Pacific Earthquake Engineering Research Center. **2013**.

Boore, D.M. (2015). Adjusting Ground-Motion Intensity Measures to a Reference Site for Which V_{S30}=3000 m/s, *PEER Report 2015/06*, Pacific Earthquake Engineering Research Center, University of California, Berkeley, CA. Available at: http://www.daveboore.com/

Boore, D.M. and E.M. Thompson (2015). Revisions to Some Parameters Used in Stochastic-Method Simulations of Ground Motion, *Bull. Seism. Soc. Am.*, **105**, 1029—1041.

Boore, D.M., J.P. Stewart, E. Seyhan, and G.M. Atkinson (2014). NGA-West 2 Equations for Predicting PGA, PGV, and 5% Damped PSA for Shallow Crustal Earthquakes, *Earthquake Spectra*, 30, 1057-1085.

Bozorgnia, Y., N.A. Abrahamson, L.A. Atik, T.D. Ancheta, G.M. Atkinson, J.W. Baker, J. W., A. Baltay, D.M. Boore, K.W. Campbell, B.S.J. Chiou, and R. Darragh (2014). NGA-West2 research project. *Earthquake Spectra*, **30**(3), 973-987.

Brandenberg, S. J., N. Bellana and T. Shantz (2010). "Shear Wave Velocity as Function of Standard Penetration Test Resistance and Vertical Effective Stress at California Bridge Sites." Soil Dynamics and Earthquake Engineering 30(10).

Calvert Cliffs 3 Nuclear Project LLC. UniStar Nuclear Operating Services LLC (2011). Calvert Cliffs, Unit 3: Combined Licensing Agreement: Final Safety Analysis Report, Revision 8, http://www.nrc.gov/reactors/new-reactors/col/calvert-cliffs/documents.html.

Campbell, K.W. (2003). Prediction of Strong Ground Motion Using the Hybrid Empirical Method and Its Use in the Development of Ground-Motion (Attenuation) Relations in Eastern North America, *Bull. Seism. Soc. Am*., **93**(3), 1012–1033.

Campbell, K.W. and Y. Bozorgnia (2014). NGA-West2 Ground Motion Model for the Average Horizontal Components of PGA, PGV, and 5% Damped Linear Acceleration Response Spectra. *Earthquake Spectra* **30**(3), 1087-1115.

Chiou, B. S. J. and R. R. Youngs (2008). NGA model for average horizontal component of peak ground motion and response spectra, Pacific Engineering Research Center.

Choi, W. K. (2008). Dynamic Properties of Ash-Flow Tuffs., University of Texas, Austin.

Choi, Y. and J. P. Stewart (2005). "Nonlinear site amplification as function of 30 m shear wave velocity." Earthquake spectra **21** (1): 1-30.

Coleman, J. L., Jr., and S. M. Cahan (2012). Preliminary Catalog of the Sedimentary Basins of the United States. *Open-File Report 2012–1111*, U.S. Geological Survey, 27 p. (plus 4 figures and 1 table available as separate files) Available online at http://pubs.usgs.gov/of/2012/1111/.

Crow, H., M. Pyne, J. A. Hunter, S.E. Pullan, D. Motazedian, and A. Pugin (2007). Shear Wave Measurements for Earthquake Response Evaluation in Orleans, Ontario. *Geological Survey of Canada. Open-File*, *5579*, 192.

Dames and Moore (1974). Site Parameter study: Gassar Seismic Design for General Atomic Company. Report No. 2395-001-02. San Franciso, CA.

Darendeli, M. B. (2001). Development of a new family of normalized modulus reduction and material damping curves Ph. D., University of Texas at Austin.

Day, SM, RW Graves, J Bielak, D Dreger, S Larsen, KB Olsen, A Pitarka, and L Ramirez-Guzman, 2008. Model for Basin Effects on Long-Period Response Spectra in Southern California. *Earthquake Spectra*, **24**, 257-277.

Detroit Edison Company (1994). Fermi Unit 3, Combined License Application, Part 2: Final Safety Analysis Report, Revision 2, http://www.nrc.gov/reactors/new-reactors/col/fermi/documents.html.

Dickenson, S. E. (1994). Dynamic Response of Soft and Deep Cohesive Soils During the Loma Prieta Earthquake of October 17, 1989. 9504791 Ph.D., University of California, Berkeley.

Dominion Virginia Power (2009). North Anna Unit 3, Combined License Application, Part 2: Final Safety Analysis Report, Revision 3, http://www.nrc.gov/reactors/new-reactors/col/north-anna/documents.html.

Douglas J, F Cotton, C Di Alessandro, DM Boore, NA Abrahamson, and S Akkar (2012). Compilation and Critical Review of GMPEs for the GEM-PEER Global GMPEs Project, *Proc. 15th World Conference on Earthquake Engineering*, Lisbon, Portugal.

Duke Energy (2010). William States Lee III Nuclear Station Units 1 and 2, Combined License Application, Part 2: Final Safety Analysis Report, Revision 3, http://www.nrc.gov/reactors/new-reactors/col/lee/documents.html.

Entergy Operations Florida Inc. (2011). Grand Gulf, Unit 3: Combined Licensing Agreement: Final Safety Analysis Report, Revision 0, http://www.nrc.gov/reactors/new-reactors/col/grand-gulf/documents.html.

Entergy Operations Inc (2008). River Bend Station 3, Combined License Application, Part 2: Final Safety Analysis Report, Revision 0, http://www.nrc.gov/reactors/new-reactors/col/river-bend/documents.html.

Exelon Generation Company (2006). Clinton, Early Site Planning Application: Part 2, Site Safety Analysis Report, Revision 0, http://www.nrc.gov/reactors/new-reactors/esp/clinton.html.

Exelon Nuclear Texas Holdings LLC (2008). Victoria County Station Units 1 and 2, Combined License Application, Part 2: Final Safety Analysis Report, Revision 0, http://www.nrc.gov/reactors/new-reactors/col/victoria/documents.html.

FEMA (1997). NEHRP recommended provisions for seismic regulations for new buildings and other structures, Part I**:** 337p.

Florida Power and Light Company (2010). Turkey Point Units 6 and 7, Combined License Application, Part 2: Final Safety Analysis Report, Revision 3, http://www.nrc.gov/reactors/new-reactors/col/turkey-point/documents.html.

Frankel, A, C Mueller, T Barnhard, D Perkins, E Leyendecker, N Dickman, S Hanson, and M Hopper, (1996). National Seismic Hazard Maps: Documentation, *Open-File Rept. 96-532*, USGS, 69 pp.

Fullerton, D. S., C. A. Bush and J. N. Pennell (2003). Map of surficial deposits and materials in the eastern and central United States (east of 102 degrees West longitude). IMAP.

Fulton, R. J. (1996). Surficial Materials of Canada, Geological Survey of Canada, Natural Resources Canada. Ottawa. Map 1880A, Scale 1:5,000,000.

Fumal, T. E. (1978). Correlations between Seismic Wave Velocities and Physical Properties of Near-Surface Geologic Materials in the Southern San Francisco Bay Region, California. Open-File Report.

Ge, J., J. Pujol, S. Pezeshk and S. Stovall (2007). "Determination of Shallow Shear-Wave Velocity at Mississippi Embayment Sites Using Vertical Seismic Profiling Data." Bulletin of the Seismological Society of America 97(2): 614-623.

Gomberg, J., B. Waldron, E. Schweig, H. Hwang, A. Webbers, R. VanArsdale, K. Tucker, R. Williams, R. Street, P. Mayne, W. Stephenson, J. Odum, C. Cramer, R. Updike, S. Hutson and M. Bradley (2003). "Lithology and shear-wave velocity in Memphis, Tennessee." Bulletin of the Seismological Society of America 93(3): 986-997.

Goulet, C. A., T. Kishida, T. D. Ancheta, C. H. Cramer, R. B. Darragh, W. J. Silva, Y. M. A. Hashash, J. A. Harmon, J. P. Stewart, K. E. Wooddell and R. R. Youngs (2014). PEER NGA-East Database, Pacific Earthquake Engineering Research Center**:** 124.

Groholski, D. R., Y. M. A. Hashash, B. Kim, M. Musgrove, J. A. Harmon and J. P. Stewart (2015). "A Simplified Non-Linear Shear Model to Represent Small-Strain Nonlinearity and Soil Strength in One-Dimensional Seismic Site Response Analysis."

Groholski, D. R., Y. M. A. Hashash, B. Kim, M. Musgrove, J. Harmon and J. P. Stewart (2016). "Simplified Model for Small-Strain Nonlinearity and Strength in 1D Seismic Site Response Analysis." Journal of Geotechnical and Geoenvironmental Engineering **0**(0): 04016042.

Hamilton, E. L. (1976). "Shear-Wave Velocity versus Depth in Marine Sediments; a Review." Geophysics 41(5): 985-996.

Hardin, B. O. and V. P. Drnevich (1972). "Shear Modulus and Damping in Soils: Design Equations and Curves." Journal of Soil Mechanics and Foundations 98(SM7): 289-324.

Harmon, J. A., Y. M. A. Hashash, J. P. Stewart, E. M. Rathje, K. W. Campbell, W. Silva, G. A. Parker, and B. Xu (2016). A Site Amplification Model for Central and Eastern North America from Linear Elastic and Nonlinear Site-Response Simulations [abstract]. In: Proceedings of the Seismological Society of America Annual Meeting; 2016 Apr 20-22; Reno NV. California (CA): SSA; Abstract 16-537

Hashash, Y. M. A. and D. Park (2001). "Non-linear one-dimensional seismic ground motion propagation in the Mississippi embayment." Engineering Geology **62**(1-3): 185-206.

Hashash, Y. M. A. and S. Moon (2011). Site amplification factors for deep deposits and their application in seismic hazard analysis for Central U.S., USGS. **USGS/NEHRP Grant: G09AP00123:** 91 pages.

Hashash, Y. M. A., A. R. Kottke, J. P. Stewart, K. W. Campbell, B. Kim, C. Moss, S. Nikolaou, E. M. Rathje and W. J. Silva (2014). "Reference Rock Site Condition for Central and Eastern North America." Bulletin of the Seismological Society of America **104**(2): 684-701.

Hashash, Y. M. A., M. I. Musgrove, J. A. Harmon, D. Groholski, C. A. Phillips and D. Park (2015). DEEPSOIL V6.1, User Manual. Urbana, IL, Board of Trustees of University of Illinois at Urbana-Champaign.

Hassani, B. and G. M. Atkinson (2016). Applicability of the Site Fundamental Frequency as a V_{S30} Proxy for Central and Eastern North America, *Bull. Seismol. Soc. Am.*, **106**, doi: 10.1785/0120150259.

Hassani, B., and Atkinson, G. M. (2015). Referenced Empirical Ground Motion Model for Eastern North America. *Seismological Research Letters*, ***86***(2A), 477-491.

Herrmann, R. B. and D. J. Crossley (2008). Shear-Wave Velocity Determination for Metropolitan St. Louis Focal Mechanism, USGS Grant 05HQGR0046, U.S. Geological Survey: 44 pages.

Hoar, R. J. and I. Kenneth H. Stokoe (1982). In Situ Seismic Wave Velocities and Dynamic Analysis for CFH Compressor Foundations, Kenneth E. Tand & Associates: 99 pages.

Hoffman, D., N. Anderson and D. Rogers (2008). St. Louis Metro Area Shear-Wave Velocity Testing, External Grant Award Number: 06HQGR0026, U.S. Geological Survey: 24 pages.

Hollenback, J., W. J. Silva, R. B. Darragh, N. A. Abrahamson (2015). Adjustment for Gulf Coast and Mississippi Embayment Region. *In* NGA-East: Adjustments to Median Ground-Motion Models for Central and Eastern North America. *PEER Report 2015/08,* Pacific Earthquake Engineering Research Center, Berkeley, CA. Available online at: http://peer.berkeley.edu/publications/peer_reports.html.

Jaume, S. C. (2006). "Shear Wave Velocity Profiles via Seismic Cone Penetration Test and Refraction Microtremor Techniques at ANSS Strong Motion Sites in Charleston, South Carolina." Seismological Research Letters 77(6): 771-779.

Jeon, S. Y. (2008). Dynamic and Cyclic Properties in Shear of Tuff Specimens from Yucca Mountain, Nevada, University of Texas, Austin.

Kaka, S. I. (2005). Development of Ontario ShakeMaps. Doctor of Philosophy, Carleton University.

Kamai, R. N. A. Abrahamson, and W. J. Silva (2014). Nonlinear Horizontal Site Amplification for Constraining the NGA-West2 GMPEs. *Earthquake Spectra*, **30**(3), pp. 1223-1240.

Kayen, R. E., B. A. Carkin, S. C. Corbett, A. S. Zangwill, L. Lai and I. Etstevez (2013). Seismic-Shear Wave Velocity and Ground Motion Amplification Factors for 50 Sites Affected by the Mineral, Virginia M5.8 Earthquake of 23 August 2011, U.S. Geological Survey.

Kim, B., Y. M. A. Hashash, E. M. Rathje, J. P. Stewart, S. Ni, P. G. Somerville, A. R. Kottke, W. J. Silva, and K. W. Campbell (2016). Subsurface Shear-Wave Velocity Characterization Using P-Wave Seismograms in Central and Eastern North America. *Earthquake Spectra*, **32**, 143-169.

Kim, B., Y. M. A. Hashash, J. P. Stewart, E. M. Rathje, J. A. Harmon, M. I. Musgrove, K. W. Campbell and W. J. Silva (2015). "Relative Differences between Nonlinear and Equivalent-Linear 1D Site Response Analyses." Earthquake Spectra **0**(0): null.

Kokusho, T., Y. Yoshida and Y. Esashi (1982). "Dynamic Properties of Soft Clay for Wide Strain Range." Soils Found. 22(4): 1–18.

Kondner, R. L. and J. S. Zelasko (1963). Hyperbolic stress-strain formulation of sands. Second pan American Conference on Soil Mechanics and Foundation Engineering, Sao Paulo, Brazil.

Kottke, A. R. and E. M. Rathje (2011). Draft of Technical Manual for Strata.

Kottke, A.R., Y. M. A. Hashash, J. P. Stewart, C. J. Moss, S. Nikolaou, E. M. Rathje, W. J. Silva, and K. W. Campbell (2012). Development of Geologic Site Classes for Seismic Site

Amplification for Central and Eastern North America. *Proc. 15th World Conf. on Earthquake Eng.*, Sept 24-28, 2012, Lisbon, Portugal. Paper No. 4557.

Lester, A. P. (2005). An Examination of Site Response in Columbia, South Carolina: Sensitivity of Site Response to Rock Input Motion and the Utility of Vs30, Virginia Polytechnic Institute and State University.

Lew, M. and K. Campbell (1985). Relationships Between Shear Wave Velocity and Depth of Overburden. Proceedings of Measurement and Use of Shear Wave Velocity for Evaluating Dynamic Soil Properties, Denver, Colo, American Society of Civil Engineers.

Liu, H. P., Y. Hu, J. Dorman, T. S. Chang and J. M. Chiu (1997). "Upper Mississippi Embayment Shallow Seismic Velocities Measured in Situ." Engineering Geology 46(3-4): 313-330.

Luminant Generation Company LLC (2009). Comanche Peak Nuclear Plants 3 and 4, Combined License Application, Part 2: Final Safety Analysis Report, Revision 1, http://www.nrc.gov/reactors/new-reactors/col/comanche-peak/documents.html.

Luzi, L., R. Puglia, F. Pacor, M. R. Gallipoli, D. Bindi and M. Mucciarelli (2011). Proposal for a Soil Classification Based on Parameters Alternative or Complementary to V_{S30}. *Bull Earthquake Eng,* 9: 1877.

Marcuson, W. F. and H. E. Wahls (1972). "Time Effects on Dynamic Shear Modulus of Clays." J. Soil Mech. and Found. Div. 98(12): 1359-1373.

Matasovic, N. (1993). Seismic response of composite horizontally-layered soil deposits Ph.D. Thesis, University of California, Los Angeles.

McGuire, R. K., W. J. Silva and C. J. Costantino (2001). Technical Basis for Revision of Regulatory Guidance on Design Ground Motions: Hazard- and Risk-consistent Ground Motion Spectra Guidelines (NUREG/CR-6728). R. M. Kenneally.

Menq, F. Y. (2003). Dynamic Properties of Sandy and Gravelly Soils Ph.D, University of Texas at Austin.

Mohanan, N., C. Fairbanks, R. Andrus, W. Camp, T. Cleary, T. Casey and W. Wright (2006). Electronic Files of Shear-Wave Velocity and Cone Penetration Test Measurements from the Greater Charleston Area, South Carolina, USGS Award Number 05HQGR0037, United States Geological Survey: 19 pages.

Moos, D. and M. D. Zoback (1983). "In Situ Studies of Velocity in Fractured Crystalline Rocks." Journal of Geophysical Research 88(B3): 2345-2358.

Nine Mile Point Nuclear Project LLC and UniStar Nuclear Operating Services LLC (2011). Nine Mile Point, Unit 3: Combined Licensing Agreement: Final Safety Analysis Report, Revision 1, http://www.nrc.gov/reactors/new-reactors/col/nine-mile-point/documents.html.

Odum, J. K., R. A. Williams, W. J. Stephensen and D. M. Worley (2003). Near-Surface S-Wave and P-Wave Seismic Velocities of Primary Geological Formations on the Piedmont and Atlantic Coastal Plain of South Carolina, USA, Open-File report 03-043, U.S. Geological Survey: 14 pages.

Ohio Geological Survey (2011). Seismic Refraction Analyses of Shallow Subsurface Geologic materials (http://www.dnr.state.oh.us/OhioGeologicalSurvey/SurficialGeology/tabid/7124/Default.aspx).

Ohta, Y. and N. Goto (1978). "Empirical Shear Wave Velocity Equations in Terms of Characteristic Soil Indexes." Earthquake Engineering & Structural Dynamics 6(2): 167-187.

Olson, S. M. and Y. M. A. Hashash (2009). Geotechnical Seismic Engineering New 1-70 Mississippi River Bridge St. Louis, Missouri to St. Clair County, Illiois, HNTB Corporation: 296 pages.

Ontario Geological Survey (2000). Quaternary Geology, Seamless Coverage of the Province of Ontario; Ontario Geological Survey, Data Set 14 - Revised.

Pacific Earthquake Engineering Research Center (2015). NGA-East: Median Ground-Motion Models for Central and Eastern North America. *PEER Report 2015/04*. PEER, Berkeley, CA. Available online at: http://peer.berkeley.edu/publications/peer_reports.html.

- Boore, DM, Chapter 2: Point-Source Stochastic-Method Simulations of Ground Motions for the PEER NGA-East Project.
- Darragh, RB, NA Abrahamson, WJ Silva and N Gregor, Chapter 3: Development of Hard Rock Ground-Motion Models for Region 2 of Central and Eastern North America.
- Yenier, E and GM Atkinson, Chapter 4: Regionally-Adjustable Generic Ground-Motion Prediction Equation based on Equivalent Point-Source Simulations: Application to Central and Eastern North America.
- Pezeshk, S, A Zandieh, KW Campbell and B Tavakoli, Chapter 5: Ground-Motion Prediction Equations for CENA Using the Hybrid Empirical Method in Conjunction with NGA-West2 Empirical Ground-Motion Models.
- Frankel, AD, Chapter 6: Ground-Motion Predictions for Eastern North American Earthquakes Using Hybrid Broadband Seismograms from Finite-Fault Simulations with Constant Stress-Drop Scaling.
- Shahjouei, A and S Pezeshk, Chapter 7: Hybrid Empirical Ground-Motion Model for Central and Eastern North America using Hybrid Broadband Simulations and NGAWest2 GMPEs.
- Al Noman, MN and CH Cramer, Chapter 8: Empirical Ground-Motion Prediction Equations for Eastern North America.
- Grazier, V, Chapter 9: Ground-Motion Prediction Equations for the Central and Eastern United States.
- Hassani, B and GM Atkinson, Chapter 10: Referenced Empirical Ground-Motion Model for Eastern North America.
- Hollenback, JK, N Kuehn, CA Goulet and NA Abrahamson, Chapter 11: PEER NGA-East Median Ground-Motion Models.

- Palmer, J.R. (2006). Surficial material geologic map of the Wentzville 7 1/2' quadrangle, St. Charles County, Missouri: Missouri Department of Natural Resources, Division of Geology and Land Survey, Open-File Map OFM-06-518-GS, scale 1:24,000

Parker, G., Harmon, J., Stewart, J. P., Hashash, Y. M. A., Kottke, A. R., Rathje, E. M., Silva, W. J., Campbell, K. W. "Proxy-Based V_{S30} Estimation in Central and Eastern North America." *Bulletin of the Seismological Society of America*. 2016. Accepted.

Parker G.A., J. P. Stewart, Y. M. A. Hashash, E. M. Rathje, K. W. Campbell, W. Silva, J. A. Harmon, and B. Xu, (2016). Empirical Seismic Site Amplification in Central and Eastern North America from NGA-East Ground Motion Database [abstract]. In: Proceedings of the Seismological Society of America Annual Meeting; 2016 Apr 20-22; Reno NV. California (CA): SSA; 2016. Abstract 16-586.

Pehlivan, M., Y. M. A. Hashash, H. J., E. M. Rathje, J. P. Stewart, W. J. Silva, K. Campbell and S. Nikolaou (2015). Influence of Shear Wave Velocity Reversals on One-Dimensional Site Response of Spatially Varied Profiles 6th International Conference on Earthquake Geotechnical Engineering. Christchurch, New Zealand.

Petersen, M.D., M.P. Moschetti, P.M. Powers, C.S. Mueller, K.M. Haller, A.D. Frankel, Y. Zeng, S. Rezaeian, S.C. Harmsen, O.S. Boyd, N. Field, R. Chen, K.S. Rukstales, N. Luco, R.L. Wheeler, R.A. Williams, and A.H. Olsen (2015). The 2014 United States National Seismic Hazard Model. *Earthquake Spectra*, **31**, S1-S30.

Pezeshk, S, A Zandieh, and B Tavakoli (2011). Hybrid Empirical Ground-Motion Prediction Equations for Eastern North America using NGA Models and Updated Seismological Parameters, *Bull Seism. Soc. Am.*, **101**(4), 1859-1870.

Progress Energy Carolinas, I. (2011). Progress Energy Harris Nuclear Units 2 & 3, Combined License Application, Part 2: Final Safety Analysis Report, Revision 3, http://www.nrc.gov/reactors/new-reactors/col/harris/documents.html.

Progress Energy Florida Inc. (2011). Levy County, Units 1 and 2: Combined Licensing Agreement: Final Safety Analysis Report, Revision 2, http://www.nrc.gov/reactors/new-reactors/col/levy/documents.html.

PSEG Power, L., and PSEG Nuclear, LLC (2011). PSEG Site, Early Site Planning Application: Part 2, Site Safety Analysis Report, Revision 0, http://www.nrc.gov/reactors/new-reactors/esp/pseg.html.

R Core Team (2015). R: A Language and Environment for Statistical Computing. Vienna, Austria, R Foundation for Statistical Computing.

R Development Core Team (2008). R: A Language and Environment for Statistical Computing. *R Foundation for Statistical Computing*, Vienna, Austria. ISBN 3-900051-07-0. Available online at: http://www.R-project.org.

Raghu Kanth, STG and RN Iyengar (2006). Seismic Hazard Estimation for Mumbai City, *Current Science*, **91**(11), 1486–1494.

Raghu Kanth, STG and RN Iyengar (2007). Estimation of Seismic Spectral Acceleration in Peninsular India, *J. Earth System Science*, **116**(3), 199–214.

Read, K., H. El Naggar and D. Eaton (2008). "Site-Response Spectra for POLARIS Station Sites in Southern Ontario and Quebec." Seismological Research Letters 79(6): 776-784.

Reed, J.C., and C.A. Bush (2005). Generalized Geologic Map of the United States, Puerto Rico, and the U.S. Virgin Islands. *USGS National Atlas Small-Scale Collection*. Available online at: http://pubs.usgs.gov/atlas/geologic/.

Rosenblad, B. L. (2006). Deep Shear-Wave Velocity Profiles of Mississippi Embayment Sediments Determined from Surface Wave Measurements, USGS Award Number: 06HQGR0131, U.S. Geological Survey: 23 pages.

Salomone, L. A., J. F. Hamel and R. P. Kassawara (2012). EPRI (2004, 2006) Ground-Motion Model (GMM) Review Project: Shear Wave Velocity Measurements at Seismic Recording Stations. Draft Report. EP-P43952/C19088. Palo Alto, California, EPRI.

Sandıkkaya, M. A., S. Akkar, and P.Y. Bard (2013). A Nonlinear Site Amplification Model for the Next Pan European Ground Motion Prediction Equations. *Bull. Seismol. Soc. Am*, **103**(1), 19-32.

Santagata, M. and Y. I. Kang (2007). "Effects of Geologic Time on the Initial Stiffness of Clays." Engineering Geology 89(1-2): 98-111.

Schneider, J. A., P. W. Mayne and G. J. Rix (2001). "Geotechnical Site Characterization in the Greater Memphis Area Using Cone Penetration Tests." Engineering Geology 62(1-3): 169-184.

Seed, H. B. and I. M. Idriss (1970). Soil Moduli and Damping Factors for Dynamic Response Analyses. Berkeley, College of Engineering University of California Berkeley.

Seyhan, E. and J. Stewart (2014). "Semi-Empirical Nonlinear Site Amplification from NGA-West2 Data and Simulations." Earthquake spectra **30**(3): 1241-1256.

Seyhan, E., J.P. Stewart, T.D. Ancheta, R.B. Darragh, and R.W. Graves (2014). NGA-West 2 Site Database*, Earthquake Spectra*, **30**, 1007-1024.

Silva, WJ, N Gregor, and R Darragh (2002). Development of Regional Hard Rock Attenuation Relations for Central and Eastern North America, Pacific Engineering and Analysis, El Cerrito, California, 57 pp.

Snedecor, G.W. and W.G. Cochran (1989). *Statistical Methods*, 8th edition, Ames, Iowa: Blackwell Publishing Professional. ISBN 978-0-8138-1561-9.

Soller, D.R., M.C. Reheis, C.P Garrity, and D.R.Van Sistine (2009). Map Database for Surficial Materials in the Conterminous United States, *U.S. Geological Survey Data Series 425,* scale 1:5,000,000. Available at: http://pubs.usgs.gov/ds/425/.

Somerville, PG, N Collins, NA Abrahamson, RW Graves and C Saikia (2001). Earthquake Source Scaling and Ground Motion Attenuation Relations for the Central and Eastern United States. Final Report to the U.S. Geological Survey, Contract No. 99HQGR0098.

South Carolina Electric & Gas (2011). V. C. Summer Nuclear Station Units 2 & 3, Combined License Application, Part 2: Final Safety Analysis Report, Revision 5, http://www.nrc.gov/reactors/new-reactors/col/summer/documents.html.

Southern Nuclear Operating Company (2008). Vogtle Units 3 and 4, Combined License Application, Part 2: Final Safety Analysis Report, Revision 3, http://www.nrc.gov/reactors/new-reactors/col/vogtle.html

Stewart, J. P., A. H. Liu, and Y. Choi (2003). Amplification Factors for Spectral Acceleration in Tectonically Active Regions. *Bull. Seismol. Soc. Am.*, **93,** 332-352.

Stewart, JP (2016). "Joyner Lecture: Site Response Uncertainty and Its Implications for Seismic Risk Characterization," EERI 2016 Annual Meeting, San Francisco, CA; SSA 2016 Annual Meeting, Reno, NV *Seismological Research Letters*, **87:2B**, pp 516 (abstract).

Stewart, JP, J Douglas, M Javanbarg, Y Bozorgnia, NA Abrahamson, DM Boore, KW Campbell, E Delavaud, M Erdik, and PJ Stafford (2015). Selection of Ground Motion Prediction Equations for the Global Earthquake Model, *Earthquake Spectra*, **31**, 19-45.

Stokoe II, K. H. (1983). In Situ Seismic Wave velocities Pinopolis West dam, Part 1: Crosshole seismic testing, South Carolina Public Service Authority: 188 pages.

Stokoe II, K. H. and E. turner (1983). In Situ Seismic Wave Velocities, Southwestern Laboratories, Inc.

Stokoe II, K. H. and Y. J. Mok (1987). In Situ Seismic Wave Velocities: S. R. Bertron Power Plant, Houston, Texas, Ulrich Engineers: 90 pages.

Stokoe II, K. H., J. A. Bay and M. D. Fuhriman (1992). Crosshole Seismic Measurements Savnnah River Site Replacement Tritium Facility, Bechtel Incorporated.

Stokoe II, K. H., J. A. Bay, B. L. Rosenblad, S.-K. Hwang and M. R. Twede (1994). In Situ Seismic and Dynamic Laboratory Measurements of Geotechnical Materials at Queensboro Bridge and Roosevelt Island, Steinman, Boynton, Gronquist and Birdsall.

Stokoe II, K. H., S. H. H. Lee and T. S. H. Ni (1985). In Situ Seismic Wave Velocities and Foundation Vibration Measurements, Converse Consultants.

Stokoe II, K. H., S. Nazarian and E. Turner (1983). In Situ Seismic Wave Velocities by Crosshole and Surface Wave Methods, Southwestern Laboratories, Inc: 81 pages.

Stokoe II, K. H., Y.-J. Mok, J. Bay and R. Lopez (1989). In Situ Seismic Wave Velocities: Cheveron Styrene Expansion, St. James, Louisiana, Dames & Moore: 29 pages.

STP Nuclear Operating Company (2011). South Texas Project Units 3 & 4, Combined License Application, Part 2: Final Safety Analysis Report, Revision 5, http://www.nrc.gov/reactors/new-reactors/col/south-texas-project/documents.html.

Street, R., E. Woolery, Z. Wang and J. Harris (1995). "A Short Note on Shear-Wave Velocities and other Site Conditions at Selected Strong-Motion Stations in the New Madrid Seismic Zone." Seismological Research Letters 66(1): 56-63.

Sykora, D. W. and J. J. Davis (1993). Site-Specific Earthquake Response Analysis for Portsmouth Gaseous Diffusion Plant, Portsmouth, Ohio, U.S. Army Corps of Engineers: 113 pages.

Sykora, D. W. and K. H. Stokoe (1983). Correlations of in Situ Measurements in Sands of Shear Wave Velocity, Soil Characteristics, and Site Conditions. Geotechnical engineering report, University of Texas at Austin. Geotechnical Engineering Center.

Tavakoli, B and S Pezeshk (2005). Empirical-Stochastic Ground-Motion Prediction for Eastern North America, *Bull. Seism. Soc. Am*. **95**, 2283–2296.

Tennessee Valley Authority (2009). Bellefonte Nuclear Plants 3 & 4, Combined License Application, Part 2: Final Safety Analysis Report, Revision 1, http://www.nrc.gov/reactors/new-reactors/col/bellefonte/documents.html.

Terzaghi, K., R. B. Peck and G. Mesri (1996). Soil Mechanics in Engineering Practice. New York, Wiley.

Thompson, E. M. and W.J. Silva (2013). Development of a Hybrid Slope-Geology Method of Estimating VS30 for Central and Eastern North America. Report to USGS. Available at: http://earthquake.usgs.gov/research/external/reports/G12AP20003.pdf.

Thompson, E.M., W.J. Wald, C.B. Worden (2014). A V_{S30} Map for California with Geologic and Topographic Constraints, *Bull. Seismol. Soc. Am*. **104**, 2313–2321.

Toro, G. R. (1995). Probablistic Models of Site Velocity Profiles for Generic and Sitespecific Ground-Motion Amplification Studies. Upton, New York, Brookhaven National Laboratory.

Toro, GR, NA Abrahamson, and JF Schneider (1997). Model of Strong Ground Motions from Earthquake in Central and Eastern North America: Best Estimates and Uncertainties, *Seism. Res. Ltrs*, **68**, 41–57.

Union Electric Company (2009). Callaway Plant Unit 2, Combined License Application, Part 2: Final Safety Analysis Report, Revision 2, http://www.nrc.gov/reactors/new-reactors/col/callaway/documents.html.

UniStar Nuclear Services LLC (2010). Bell Bend Nuclear Power Plant, Combined License Application, Part 2: Final Safety Analysis Report, Revision 2, http://www.nrc.gov/reactors/new-reactors/col/bell-bend/documents.html.

Wald, D. J. and T. I. Allen (2007). Topographic Slope as a Proxy for Seismic Site Conditions and Amplification. *Bull. Seisol. Soc. Am.*, **97**, 1379-1395.

Walling, M., W. Silva and N. Abrahamson (2008). "Nonlinear Site Amplification Factors for Constraining the NGA Models." Earthquake spectra **24**(1): 243-255.

Wilder, B. D. (2007). SASW Testing in the Salt Lake Valley, UT Master of Science, The University of Texas at Austin.

Wills, C. J. and K. B. Clahan (2006). "Developing a Map of Geologically Defined Site-Condition Categories for California." Bulletin of the Seismological Society of America 96(4 A): 1483-1501.

Woolery, E. W. and Z. Wang (2005). Seismic Velocity Measurements at Expanded Seismic Network Sites, UK/KRCEE Doc#: P8.3 2005, U.S. Department of Energy.

Xia, J., R. D. Miller, C. B. Park, J. A. Hunter, J. B. Harris and J. Ivanov (2002). "Comparing Shear-Wave Velocity Profiles Inverted from Multichannel Surface Wave with Borehole Measurements." Soil Dynamics and Earthquake Engineering 22(3): 181-190.

Yamada, S., M. Hyodo, R. Orense and S. V. Dinesh (2008). "Initial Shear Modulus of Remolded Sand-Clay Mixtures." Journal of Geotechnical and Geoenvironmental Engineering 134(7): 960-971.

Yee, E., J. P. Stewart and K. Tokimatsu (2013). "Elastic and Large-Strain Nonlinear Seismic Site Response from Analysis of Vertical Array Recordings." Journal of Geotechnical and Geoenvironmental Engineering **139**(10): 1789-1801.

Yenier, E, and G. M. Atkinson (2015). Regionally Adjustable Generic Ground Motion Prediction Equation Based on Equivalent Point Source Simulations: Application to Central and Eastern North America. *Bull. Seismol. Soc.Am.*, **105**, 1989-2009.

Yong, A, S. E. Hough, J. Iwahashi, and A. Braverman (2012). A Terrain Based Site Conditions, Map of California with Implications for the contiguous United States. *Bull. Seismol. Soc. Am.*, **102,** 114-128.

Zen, K., H. Yamazaki and Y. Umehara (1987). Experimental Study on Dynamic Properties of Soils for Use in Seismic Response Analysis. Rep. of Port and Harbor Research Institute. Yokosuka, Japan, Port and Harbor Research Institute. 26.

APPENDIX A DEVELOPMENT OF CHARACTERISTIC LOG-MEAN INPUT SHEAR WAVE VELOCITY PROFILES

Extensive work has been done to characterize the V_S structure of CENA for use in site response analyses including the reference rock condition. Much of the work in this study builds on the report of reference rock condition of CENA in Hashash et al. (2014) including use of much the shear wave velocity (V_S) profile data collected for that study.

The V_S of a soil column has a significant impact on both the linear and nonlinear site response. To characterize V_S across CENA, 821 V_S profiles from literature and public reports were collected and analyzed. The list of references for the V_S profiles collected is shown in Table 20. The profiles are from a variety of locations in the central and eastern United States and Canada as shown in Figure 72.

The characteristic input V_S profiles to the randomization scheme are developed as follows:

- Remove rock-like material from the V_S profiles
- Sort profiles and calculate the log-mean as a function of depth
- Smooth the log-mean profiles to remove features resulting from changing amounts of data as a function of depth
- Extend the smoothed log-mean profiles to a depth of 1000 m.
- Combine similar log-mean profiles

Once the characteristic V_S profiles are developed, they are merged with a weathered rock zone to model the transition of V_S from a soil condition to the reference rock condition.

A.1 REMOVAL OF ROCK-LIKE MATERIAL

Rock-like material (i.e. material with high V_S) is sampled in many of the collected V_S profiles. Rock-like material is addressed with the weathered rock zone, soil column depth, and bedrock branches of the parametric study. A procedure is needed to remove the rock-like material from the collected V_S profiles prior to combining them into characteristic profiles. A V_S value of 760 m/s is on the boundary between NEHRP site classes B and C FEMA (1997)and is typically

considered the reference rock condition for the Western United States. Rock-like material was removed from the V_S profile data by truncating the profile at the deepest V_S values greater than 800 m/s or at the deepest increase of more than 500 m/s between adjacent V_S values to capture the high impedance contrasts expected between rock and soil material. The values of 800 and 500 m/s for the removal of rock-like data are judgment based. Material with a V_S greater than 760 m/s would be classified into NEHRP site class B and is considered as rock for WUS site amplification. A jump in 500 m/s or greater in V_S suggests a significant change in stiffness between geologic layers. Figure 73 shows the results of this rock-removal process for the geologic classes YGd, YGo, and YGt.

A.2 SORT PROFILES AND CALCULATE THE LOG-MEAN AS A FUNCTION OF DEPTH

V_{S30} values in CENA can be related to surficial geology age and origin (Kottke et al. 2012). An investigation by Kottke et al. (2012) found that surficial geology classifications could be used as a proxy for time-averaged shear wave velocity in the top 30 m of soil (V_{S30}). Surficial geology information from Fullerton et al. (2003) for the United States and Fulton (1995) for Canada was used to develop geologic classes of surficial materials in CENA that shared similar V_S characteristics for use in site amplification. The CENA geology classifications from Kottke et al. (2012) are shown in Table 12 and will be adopted for this study

V_S profile data collected does not provide even coverage of all geologic classes shown in Table 12. Some geologic sub-units with similar velocity and geologic characteristics were combined to create more stable log-mean profiles. In Figure 74 the rock-removed velocity profiles from geology classes YGd, YGo, and YGt are combined to increase the stability of the log-mean (e.g. the log-mean does not significantly change with the addition or removal of data). Additional geologic sub-units that are combined in this way are: ONa, ONc, ONl, and ONm; OGm, OGo, and OGt; and YNa, YNl, and YNs.

Once sorted, the log-mean of the V_S profiles was calculated as a function of depth. Log-Mean V_S values were calculated at a 1 m interval from 0 m to 10 m depth, then at a 5 m interval below

10 m. The log-mean V_S profiles to 100 m are shown in Figures 75 through 84 for each of the geologic classes.

Certain characteristics of V_S profiles to be used as inputs to randomization schemes for the parametric study are desirable, and the strict log-mean V_S profiles of the collected data needed to be adjusted to have these characteristics. The log-mean V_S profiles were adjusted to be monotonically increasing with depth. If a region of the log-mean profiles would exhibit a decrease in V_S with depth, the V_S is held constant with depth over the affected layers. The log-mean V_S profiles also had abrupt changes in V_S with depth reduced. Because of the dependency of the shape of the log-mean V_S profiles on the number of V_S profiles collected at each depth, the final adjustments to the characteristic V_S profiles are made near the ground surface and at depth where the number of collected V_S profiles controls the shape of the log-mean profile. At the ground surface, abrupt changes in V_S were ignored and the characteristic profiles were extrapolated to the ground surface depth from a deeper area where there is more data and the mean V_S is better constrained. At depth, where there is little V_S data, or where the V_S data available only comes from one or two sites, the profile extrapolation technique described in Section A.3 is used. Typically if there are fewer than five collected V_S profiles for a given depth, profile extrapolation is used. Figure 74 shows an example of the log-mean V_S profile of the collected data, and its adjustment for use as a characteristic profile in the parametric study.

A.3 DEPTH EXTENSION OF CHARACTERISTIC PROFILES

Of the V_S profile data collected, none reaches a depth of 1000 m, the greatest soil profile depth to be considered in this study. V_S profiles are commonly fit to an equation of the form

$$\log(V_S) = n_v \times log(z) + C \tag{26}$$

where V_S is shear wave velocity, z is depth or confining pressure, and C is a constant (Sykora 1983 , Darendeli 2001, Menq 2003). A review of literature using this functional form to fit was performed; sources are shown in Table 22. The functional form of shear wave velocity shown in (26) was fit using a least-squares method to the log-mean velocity profiles of each combined geologic classification described in Section A.2 and the n_v values are shown with the literature values of n_v in Figure 85.

When the log-mean of all rock-removed velocity profiles is fit to (26), $n_v = 0.293$ which falls in the range of values observed in literature. The value of C in (26) can be adjusted to cause the fit profile intersect the log-mean profile where the profile terminates, as shown in Figure 86. Characteristic profiles are extrapolated to depths beyond where there is reliable data from the slope of the curve with $n_v = 0.293$ fit to the log-mean of all velocity profile data shown in Figure 86. This extension procedure can be applied consistently to characteristic profiles and results in reasonably-shaped velocity profiles. An example of a characteristic profile extension from 20 m to 100 m is shown in Figure 74.

A.4 CALCULATION OF ADDITIONAL CHARACTERISTIC V_S PROFILES

Additional characteristic V_S profiles for use in site response analyses are derived from the log mean of collected velocity profile data at discrete depths across geologic classes and values of V_{S30}, from scaling the log mean profile of all collected V_S profiles, and using engineering judgment to come up with a soft V_S profile. The characteristic V_S profiles from the binning, judgment, and scaling procedures are used to provide coverage of V_S not captured by collected data, but desired for use in developing site amplification functions.

The characteristic profiles derived from the geologic classes presented in Kottke (2012) do not provide the coverage of higher V_S values observed in the data, and do not provide sufficient coverage of V_{S30} desired for use in the parametric study. Three additional velocity profiles were created by uniformly scaling the adjusted (through the process detailed in Section A.2) log-mean profiles calculated from all collected V_S profiles to produce characteristic profiles with V_{S30} values of 400 m/s, 500 m/s, and 600 m/s. The scaled global mean profiles are shown in Figure 89.

A characteristic profile was also created from the log-mean velocity profile of rock-removed velocity profile data with V_{S30} values between 300 m/s and 500 m/s to capture more intermediate V_S behavior. The characteristic V_S profile from binning by V_S is shown in Figure 84.

To capture the lower V_S values observed in the data, an additional judgment-based profile was created from the lower bound of the collected rock-removed profile data and the adjusted log-mean binned velocity profile from the rock-removed velocity profile data with V_{S30} values

between 0 m/s and 300 m/s. The soft judgment-based profile was created by taking the geometric mean of the lower bound and binned profile and imposing a few additional constraints. The maximum increase in velocity between 5 m layers is 30 m/s and velocity is monotonically increasing with depth. The V_{S30} of the soft judgment profile is 142 m/s. Figure 88 shows the binned and minimum bound velocity profiles and the judgment-based soft velocity profile.

The adjusted log mean V_S profiles calculated for the similar geology classes described in Section A.2 were combined to reduce the number of characteristic velocity profiles for use in site response analysis. The combined profiles were created by taking the log-mean of the two or three adjusted log-mean profiles similar in V_S structure. Geology-sorted adjusted log-mean profiles combined in this way are RRm and OG (shown in Figure 92), YNa-YNl-YNs and ON (shown in Figure 90), and YGd-YGt-YGo, RS, and YGm (shown in Figure 91).

A.5 WEATHERED ROCK ZONE VELOCITY STRUCTURE

Above the hard reference rock conditions in CENA is a zone of weathered rock of varying thickness and velocity structure. To capture the range of characteristics of the weathered zone in the parametric study, six velocity gradients and zone thicknesses are selected to reach the V_S = 3000 m/s value of reference rock. Four depth-based velocity structures in the weathered rock zone are selected to capture observed weathered-rock zone thicknesses and two gradient-based models are selected to capture varying impedance ratios at the top of the weathered rock zone.

The depth-based structures all have median V_S at the top of the weathered zone of 2000 m/s. This is a typical value as described in Hashash et al. (2014). The chosen thicknesses of the weathered rock zone are 0 m, 10 m, 30 m, and 70 m. The gradient-based structures all have a constant V_S gradient with depth of 33 (m/s)/m. This value was selected to capture variability in the V_S of the top of the weathered rock zone. For V_S values of 1500 and 2500 m/s at the top of the weathered rock zone, the chosen gradient model results in thicknesses of the weathered rock zone of 45 m and 15 m, respectively. Figure 93 shows a comparison of the selected weathered rock zone models with the collected data from the report on reference rock condition.

All weathered rock models will be applied to the bottom of each characteristic V_S profile for each depth bin in the parametric study. The weathered rock models will be randomized as a part of the characteristic velocity profile.

A.6 TABLES

Table 20: List of V_S profiles references.

•Anderson et al. (2003) •Anderson and Thitimakorn (2004) •Anderson et al. (2005) •Andrus et al. (2006) •Bauer et al. (2004) •Beresnev and Atkinson (1997) •Calvert Cliffs 3 Nuclear Project LLC and UniStar Nuclear Operating Services LLC (2011) •Dames and Moore (1974) •Detroit Edison Company (2010) •Dominion Virginia Power (2009) •Duke Energy (2010) •Entergy Operations Florida Inc. (2011) •Entergy Operations Inc. (2008) •Exelon Generation Company (2006) •Exelon Nuclear Texas Holdings LLC (2008) •Florida Power and Light Company (2010) •Ge et al. (2007) •Gomberg et al. (2003) •Herrmann and Crossely (2008) •Hoar and Stokoe (1982) •Hoffman et al. (2008) •Jaume (2006) •Kaka (2005) •Lester (2005) •Liu et al. (1997) •Luminant Generation Company LLC (2009) •Mohanan et al. (2006) •Moos and Zoback (1983) •Nine Mile Point Nuclear Project LLC and UniStar Nuclear Operating Services LLC (2011)	•Odum et al (2003) •Ohio Geologic Survey (2011) •Olson and Hashash (2009) •Progress Energy Carolinas (2011) •Progress Energy Florida Inc. (2011) •PSEG Power (2011) •R. Kayen 2012, Written Communication •Read et al. (2008) •Rosenblad (2006) •Salomone et al. (2012) •Santagata and Kang (2007) •Shneider et al. (2001) •South Carolina Electric & Gas (2011) •Southern Nuclear Operating Company (2008) •Stokoe (1983) •Stokoe and Mok (1987) •Stokoe and Turner (1983) •Stokoe et al. (1983) •Stokoe et al. (1985) •Stokoe et al. (1989) •Stokoe et al. (1992) •Stokoe et al. (1994) •STP Nuclear Operating Company (2011) •Street et al. (1995) •Sykora and Davis (1993) •Tennessee Valley Authority (2009) •Union Electric Company (2009) •UniStar Nuclear Services LLC (2010) •Woolery and Wang (2005) •Xia et al. (2002)

Table 21: CENA Geology types for site amplification (Kottke et al. 2012)

Major Unit and Age	Sub-Unit	Abbreviation
Old Glacial Sediments (Older than Wisconsin)	Glaciomarine and Lacustrine	OGm
	Outwash and alluvium	OGo
	Tills	OGt
Young Glacial Sediments (Wisconsin and younger)	Glaciomarine and Lacustrine	YGm
	Outwash and alluvium	YGo
	Tills	YGt
	Discontinuous Till	YGd
Old Non-Glacial Sediments (Mid-Pleistocene and older)	Alluvium	ONa
	Colluvium	ONc
	Loess	ONl
	Lacustrine, Marine and Marsh	ONm
Young Non-Glacial Sediments (Holocene and late Pleistocene)	Alluvium	YNa
	Colluvium	YNc
	Loess	YNl
	Lacustrine, Marine and Marsh	YNm
	Beach, dune, and sheet sands	YNs
Residual Material	Residual material from metamorphic and igneous rock	RRm
	Residual material from sedimentary rock	RRs
	Residual from soils	RS
Not Classified	Not Classified	NC

Table 22: List of references of n_v values.

Ashland, F.X. and McDonald, N. G., (2003)	Marcuson, W. E., and Wahls, H. E. (1972)
Brandenberg et al (2010)	Menq, F.-Y. (2003)
Choi, W.K. (2008)	Ohta, Y., & Goto, N. (1978)
Dickenson, S. E. (1994)	Rosenblad, B.L. (2009)
Fumal, T. E. (1978)	Seed, H. B., & Idriss, I. M. (1970)
Hamilton, E. L. (1976)	Sykora, D. W., and K. H. Stokoe. (1983)
Hardin et al (1972)	Wills, C. J., & Clahan, K. B. (2006)
Jeon, S. Y. (2008)	Yamada et al (2008)
Kokusho et al (1982)	Wilder (2007)
Lew, M., and Campbell, K. W. (1985)	Zen et al (1987)

A.7 FIGURES

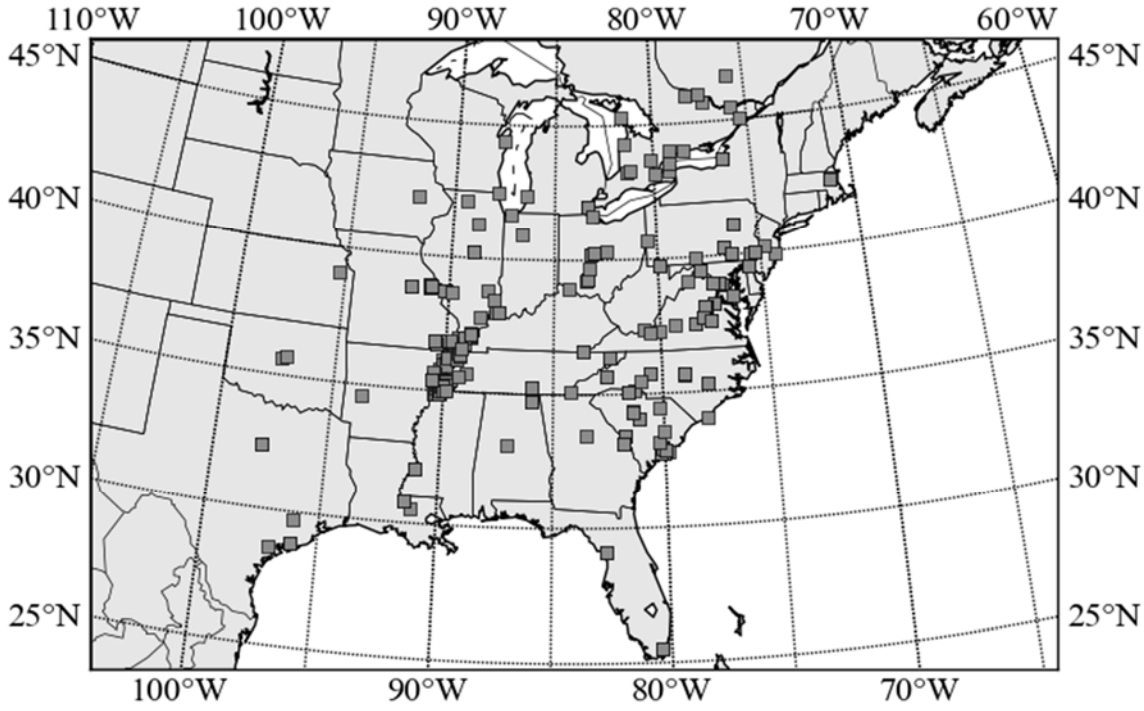

Figure 72: Locations of V_S profiles in CENA from literature and open file reports.

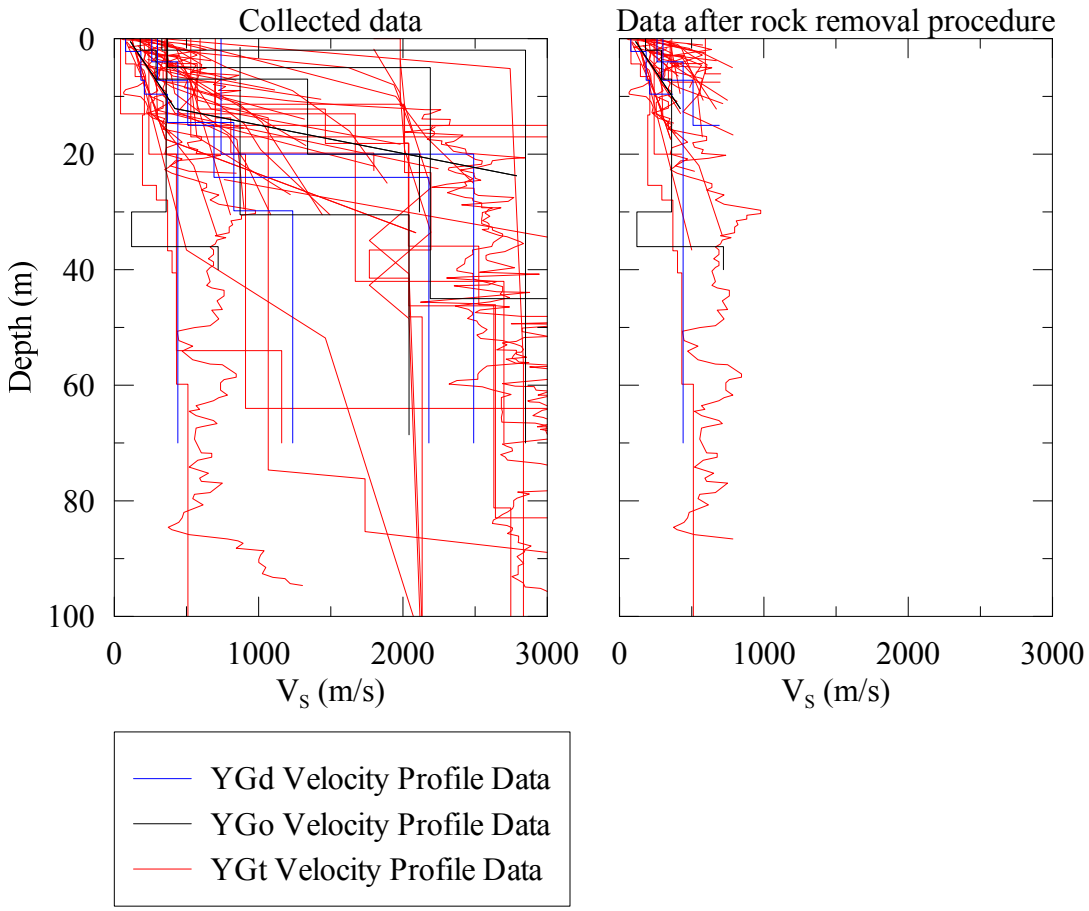

Figure 73: Results of rock removal procedure for velocity profiles collected in geologic classes YGd, YGo, and YGt.

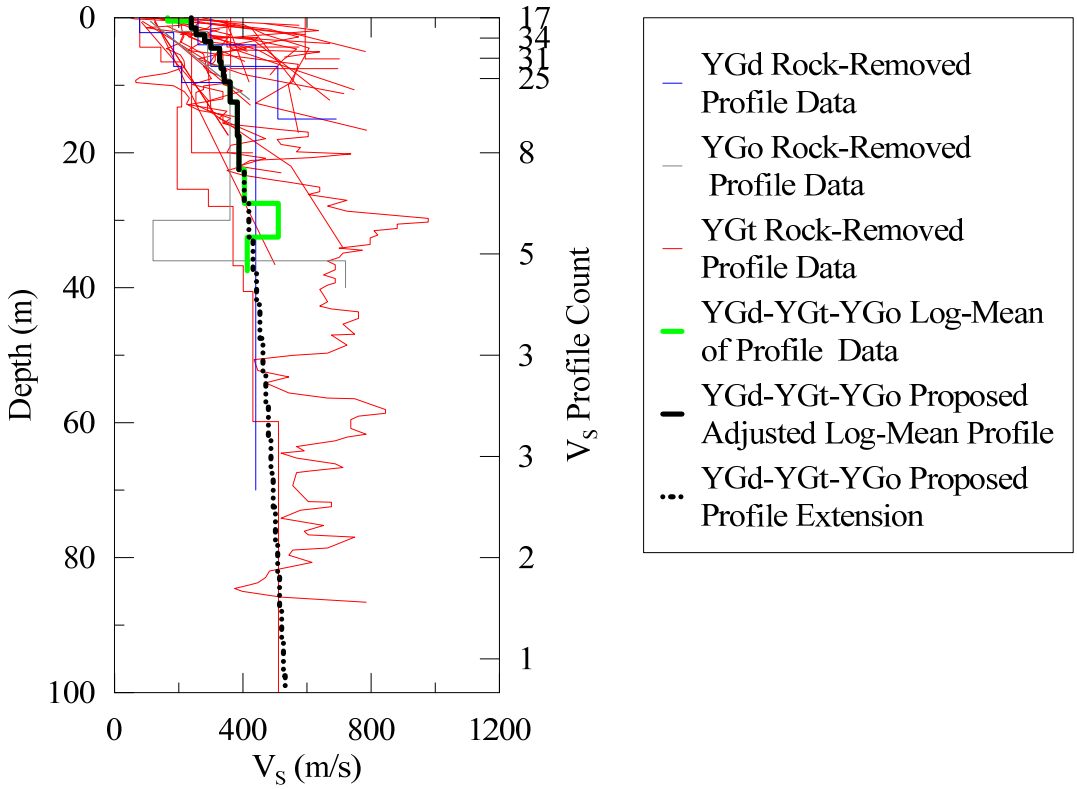

Figure 74: YGd-YGt-YGo adjusted log mean velocity profile. Profile data and log mean of geologic classes YGd, YGo, and YGt shown

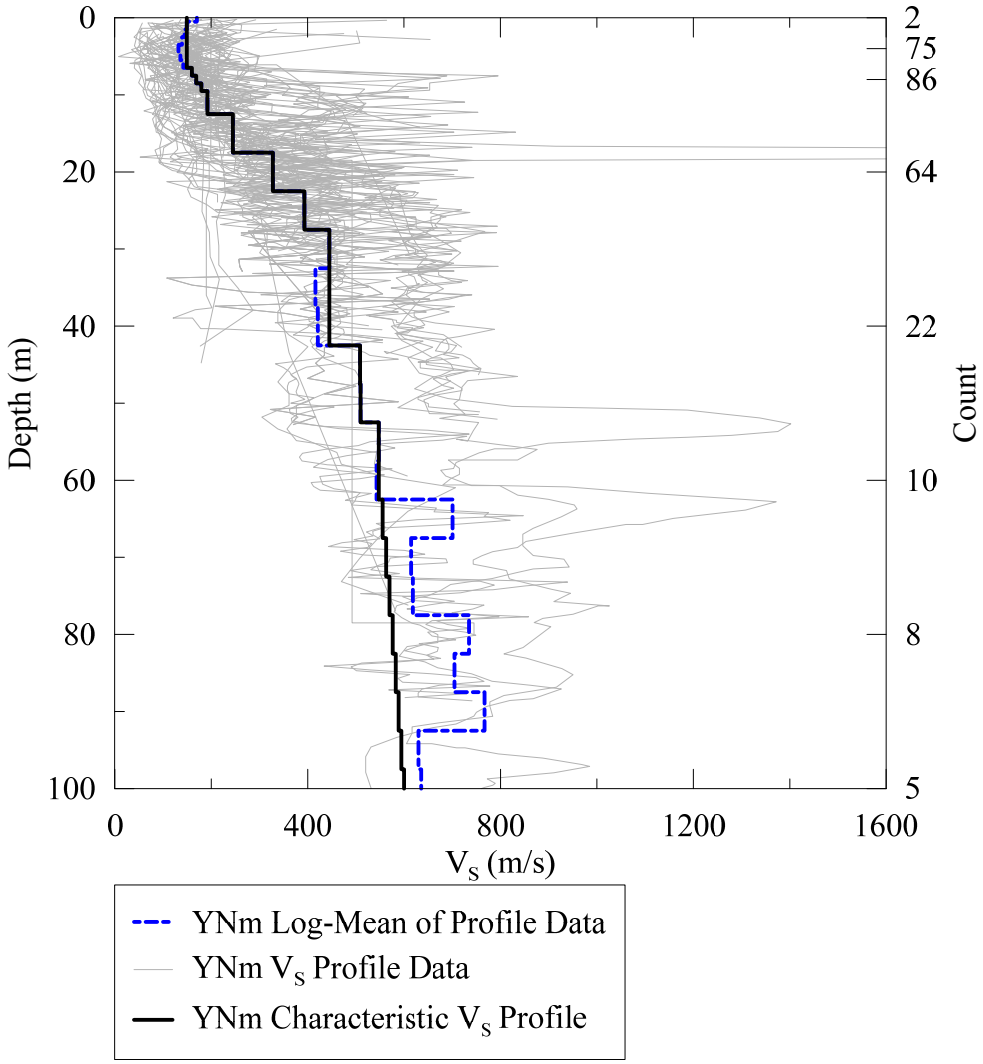

Figure 75: YNm Representative V_S profile

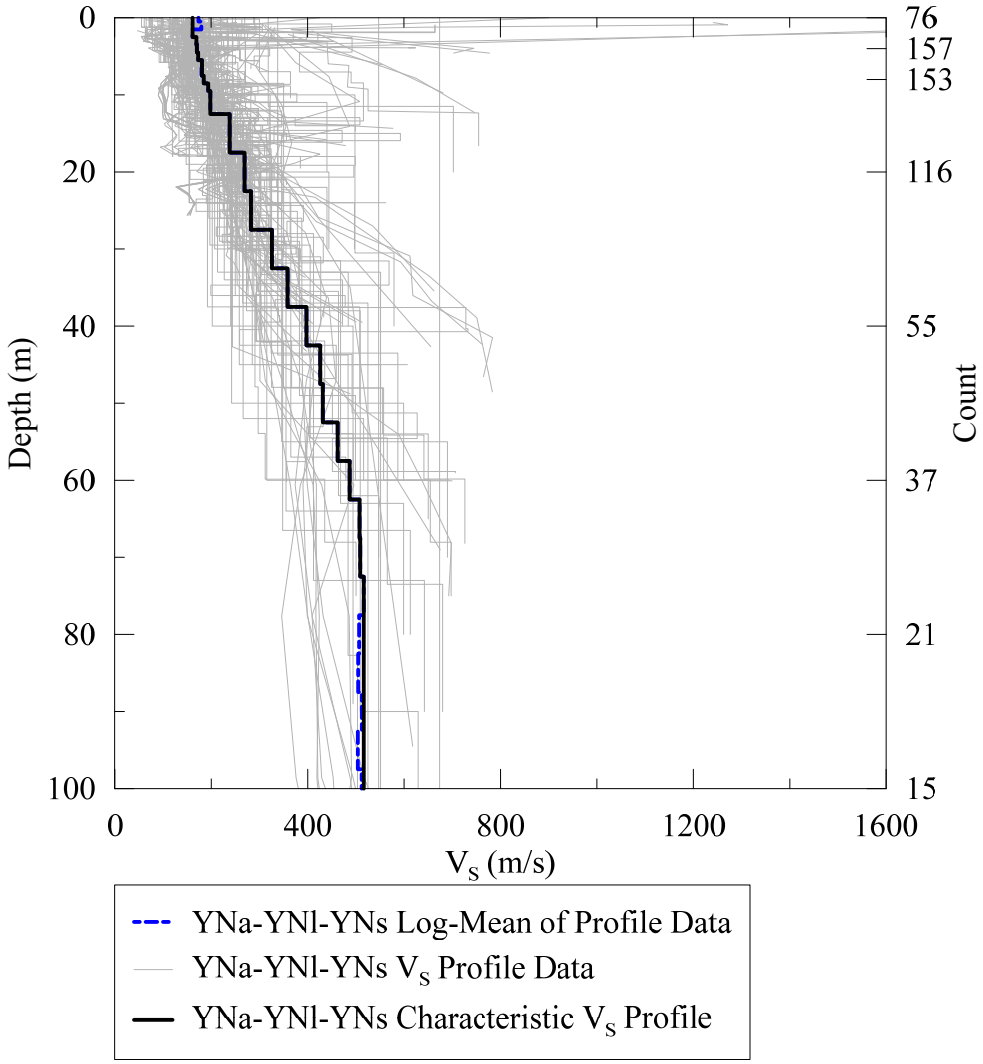

Figure 76: YNa-YNl-YNs Representative V_S Profile

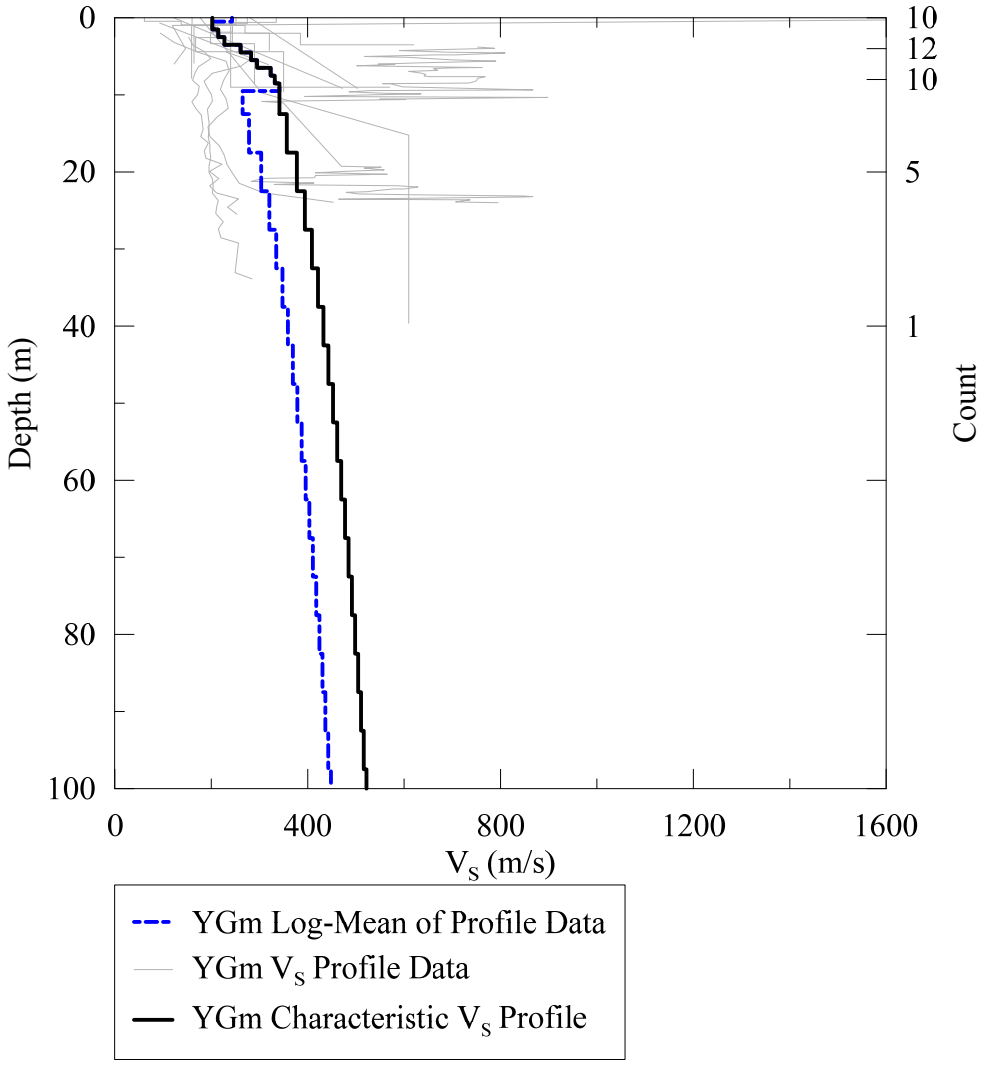

Figure 77: YGm Representative VS Profile

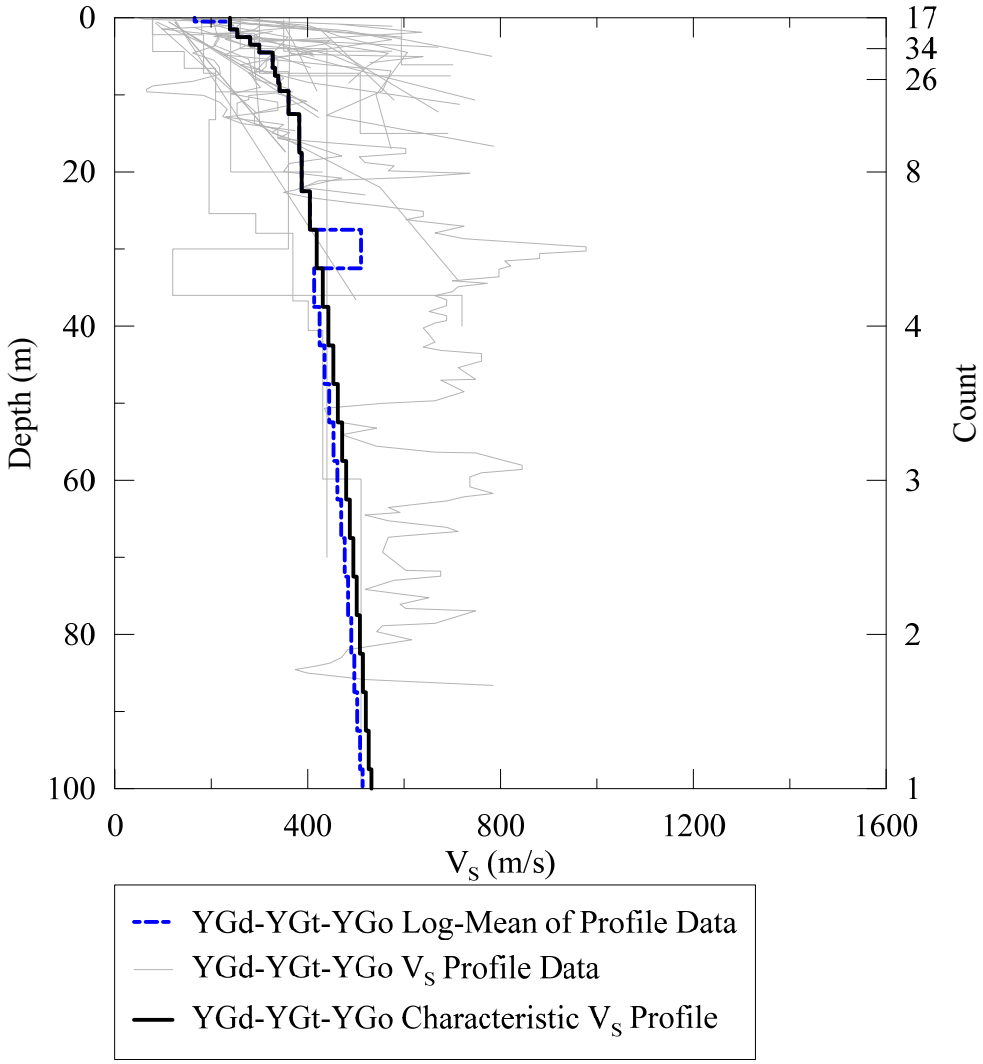

Figure 78: YGd-YGt-YGo Representative VS Profile

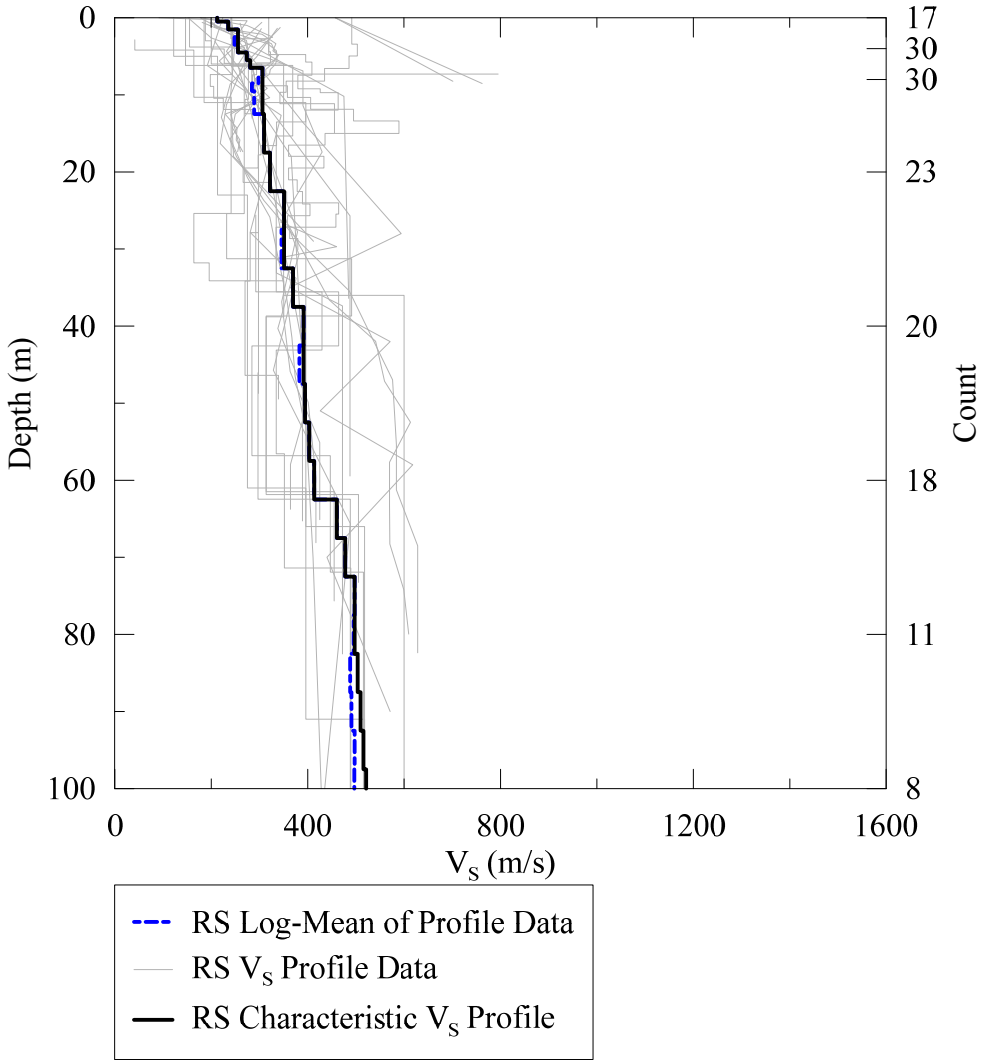

Figure 79: RS Representative VS Profile

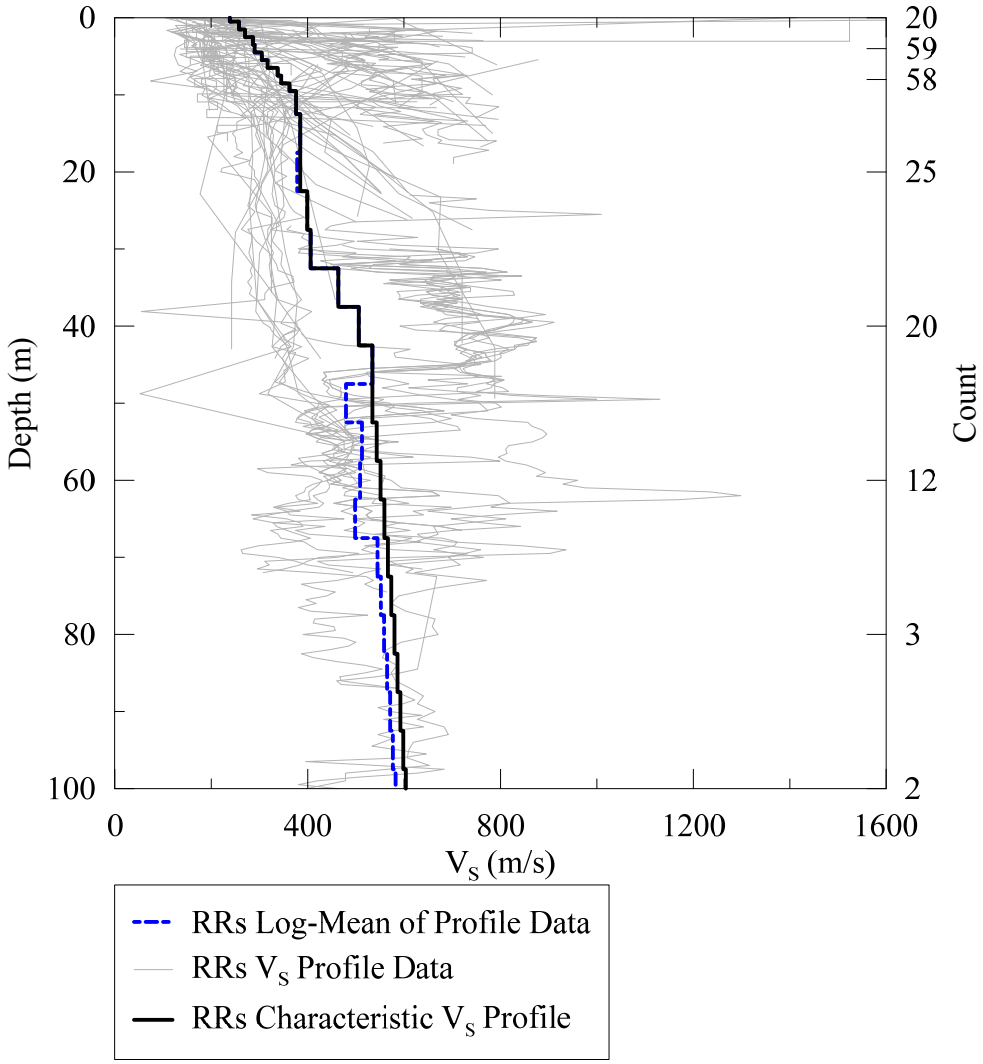

Figure 80: RRs Representative VS Profile

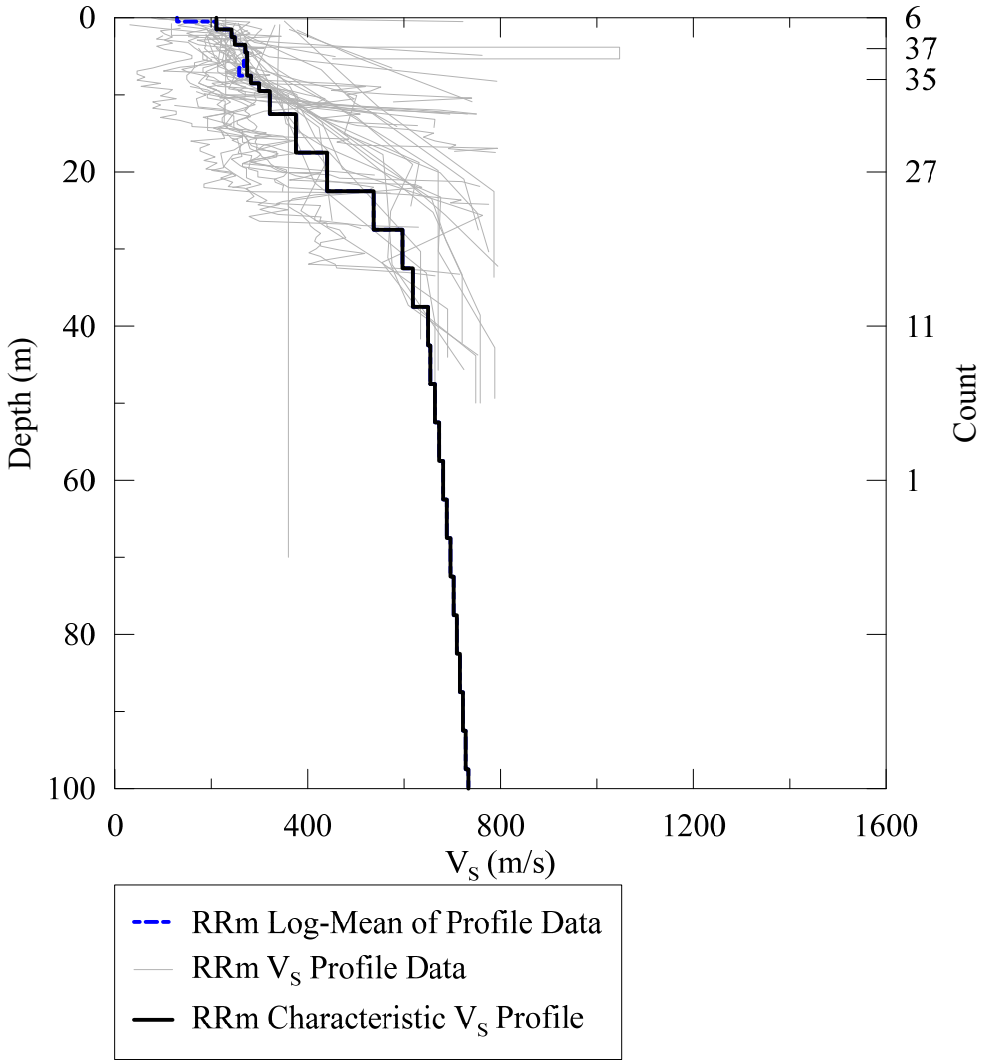

Figure 81: RRm Representative VS Profile

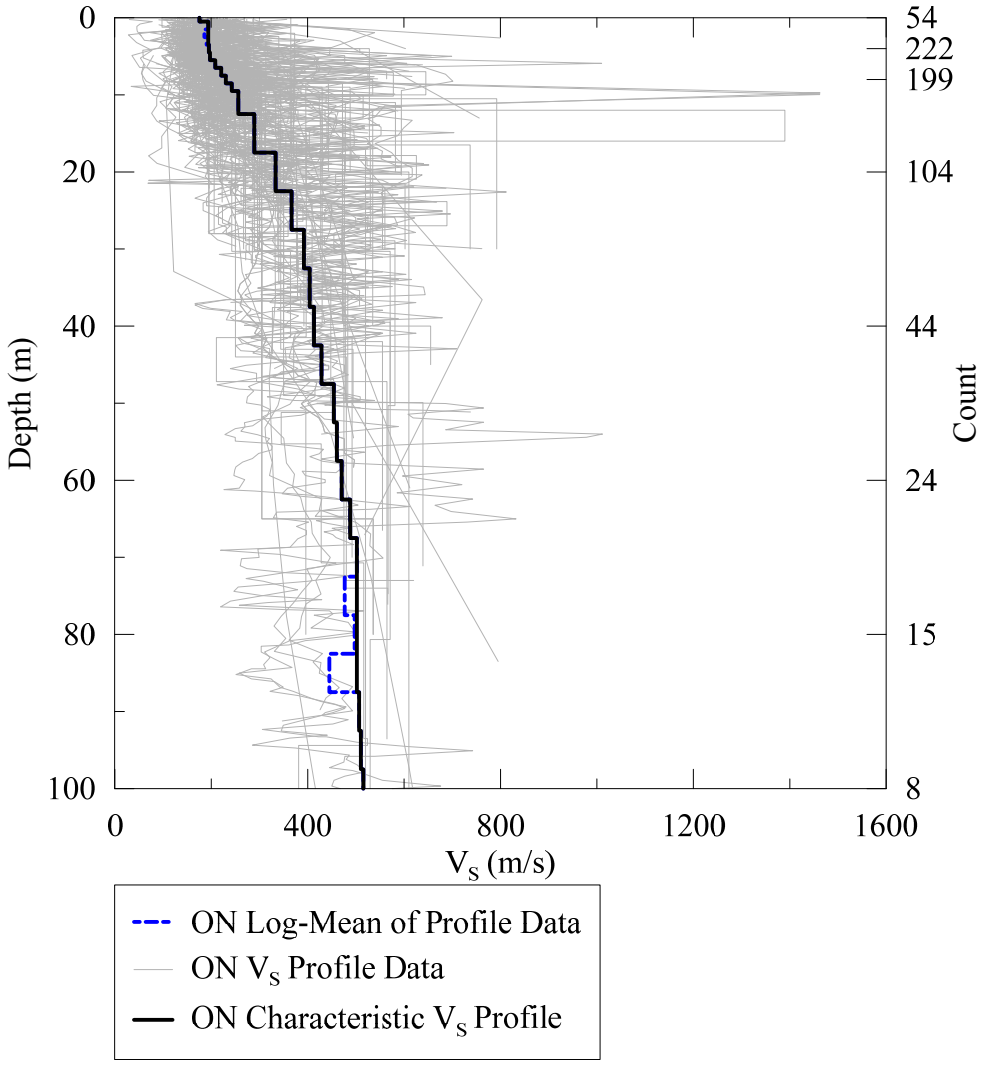

Figure 82: ON Representative VS Profile

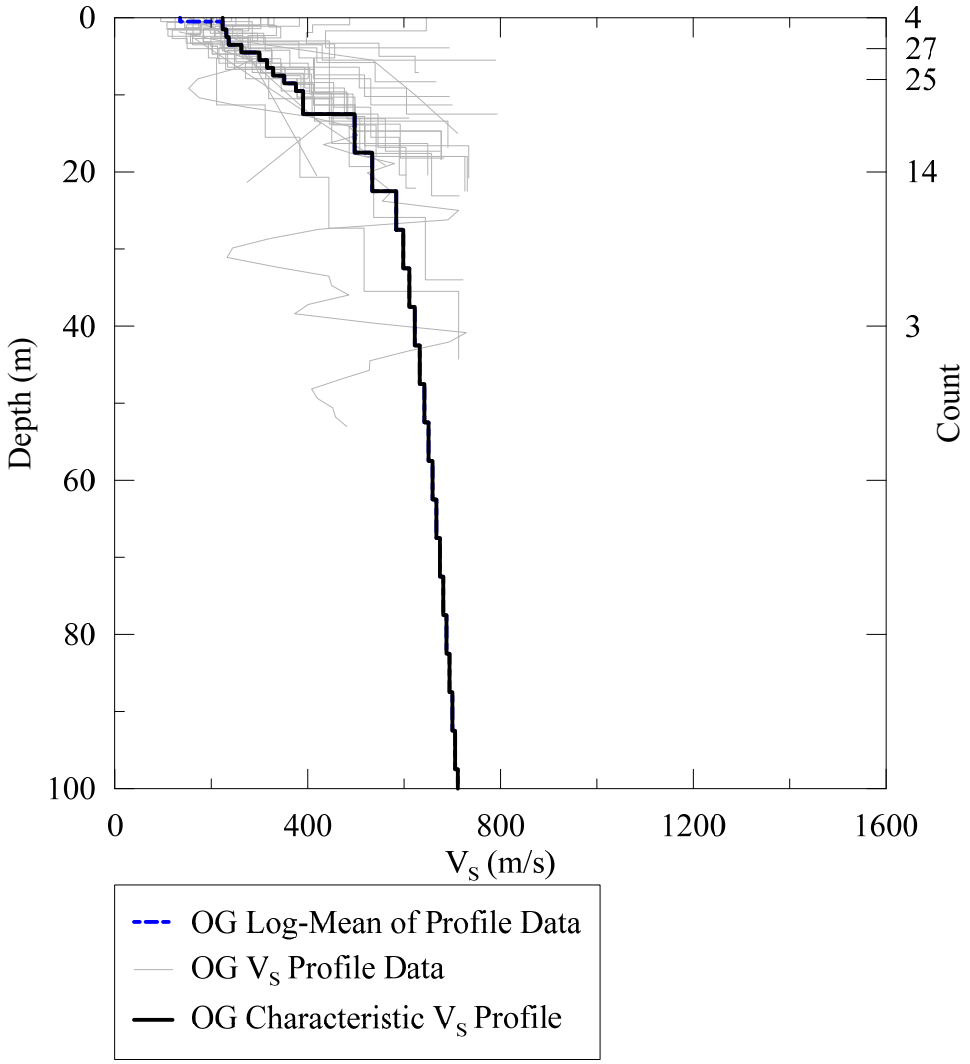

Figure 83: OG Representative VS Profile

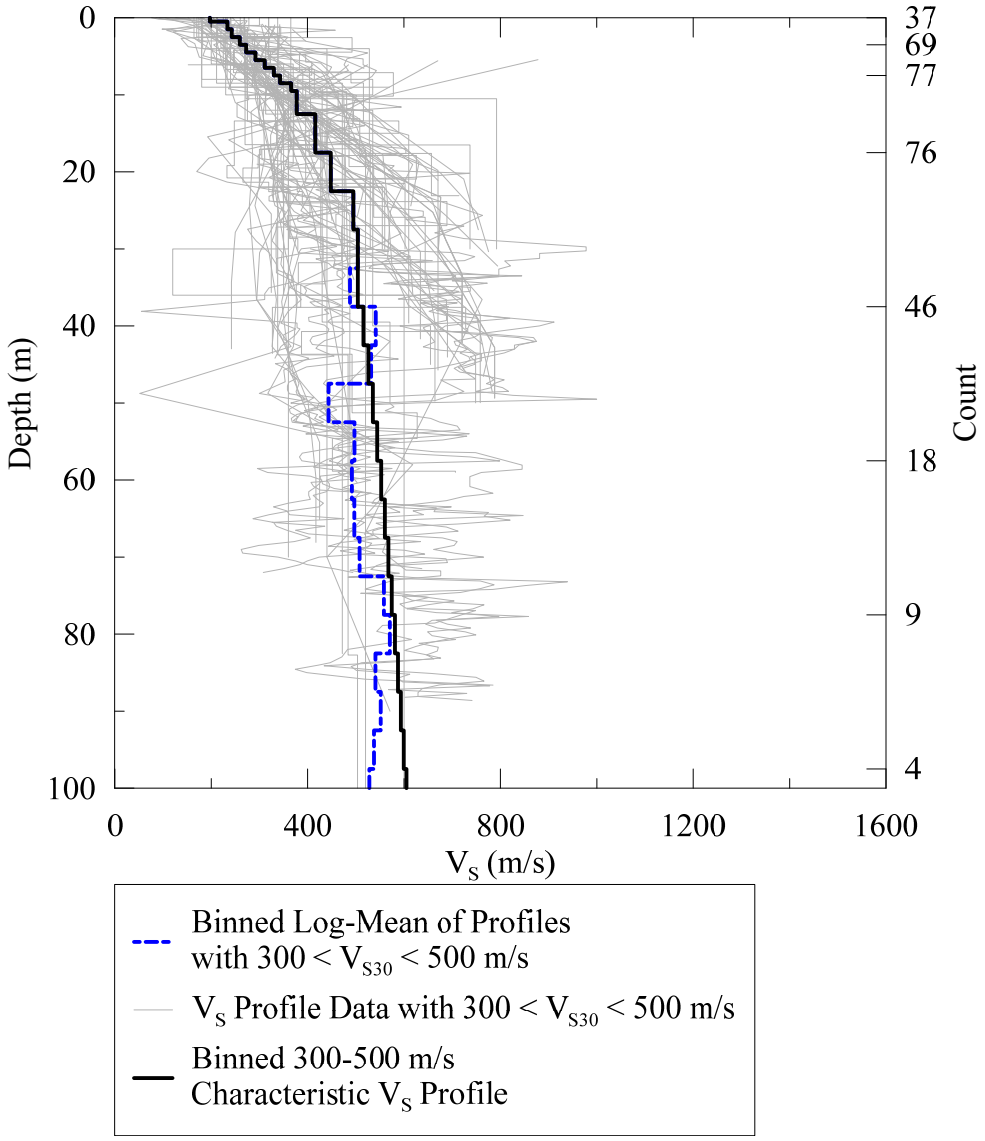

Figure 84:Representative VS Profile of Binned data with 300 m/s < VS30 < 500 m/s

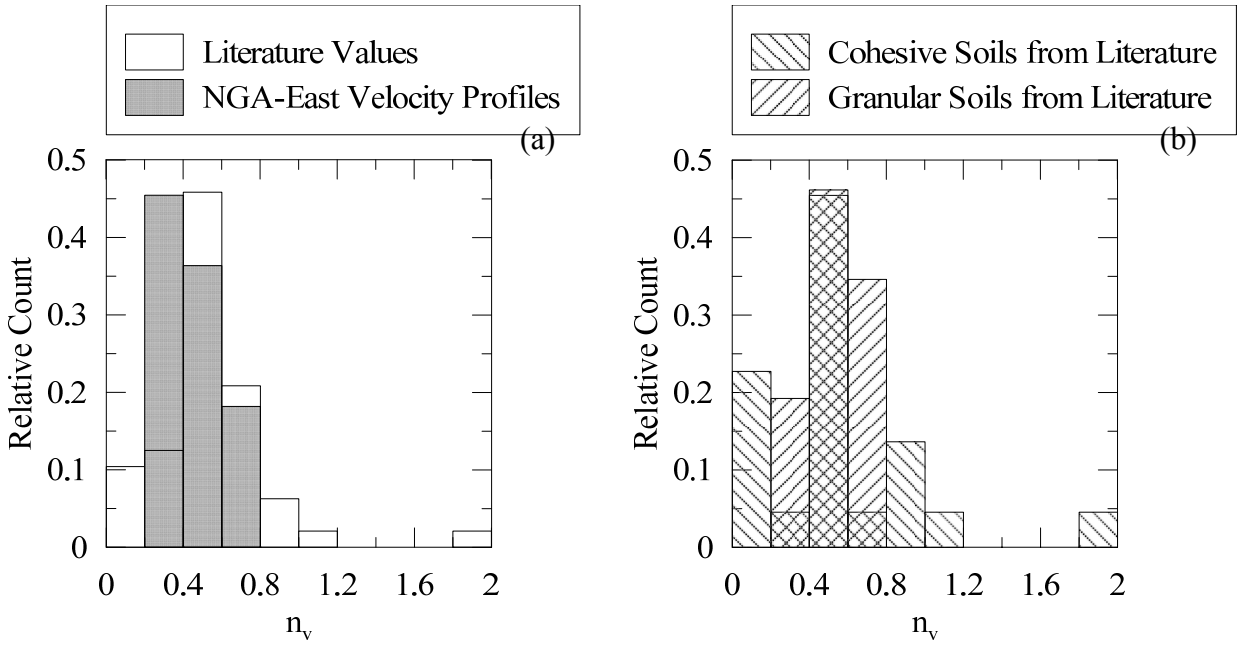

Figure 85: Relative histograms of n_v values from literature and collected velocity profiles. Relative histograms shown for cohesive and granular soils in literature where soil classification is known.

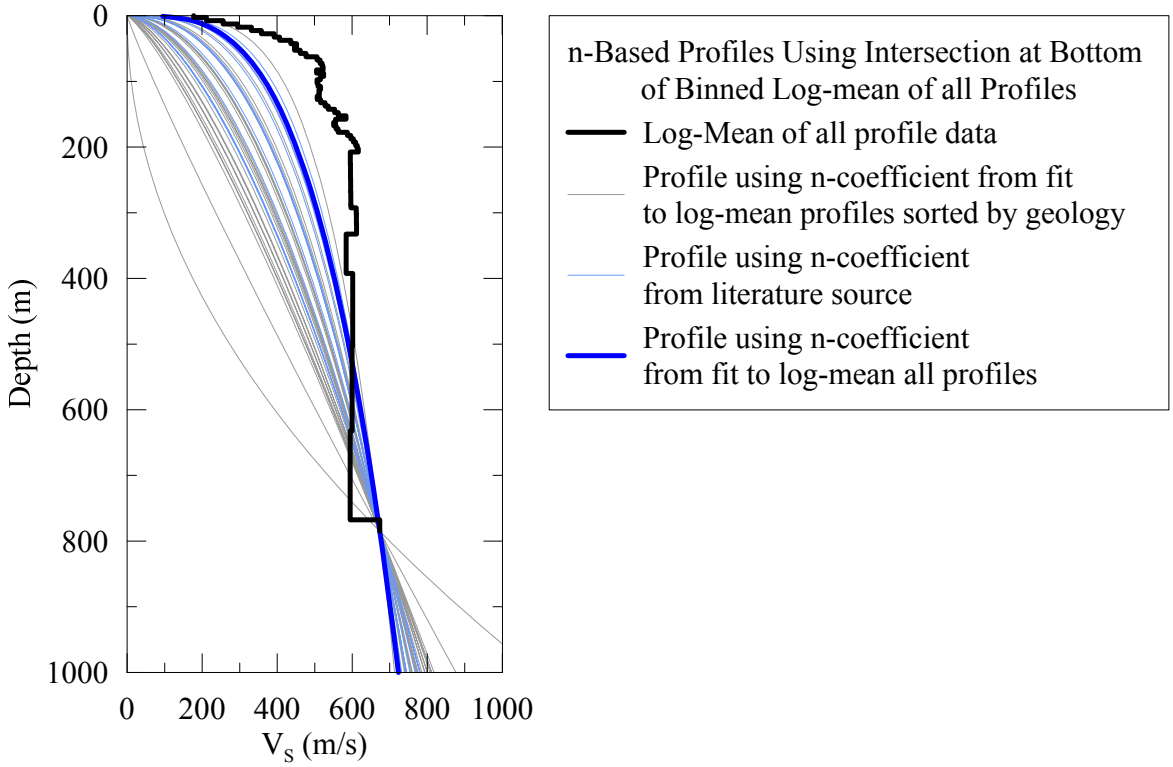

Figure 86: Velocity profiles generated for literature and data n_v-coefficient values fit to the termination point of the log-mean of all velocity profile data

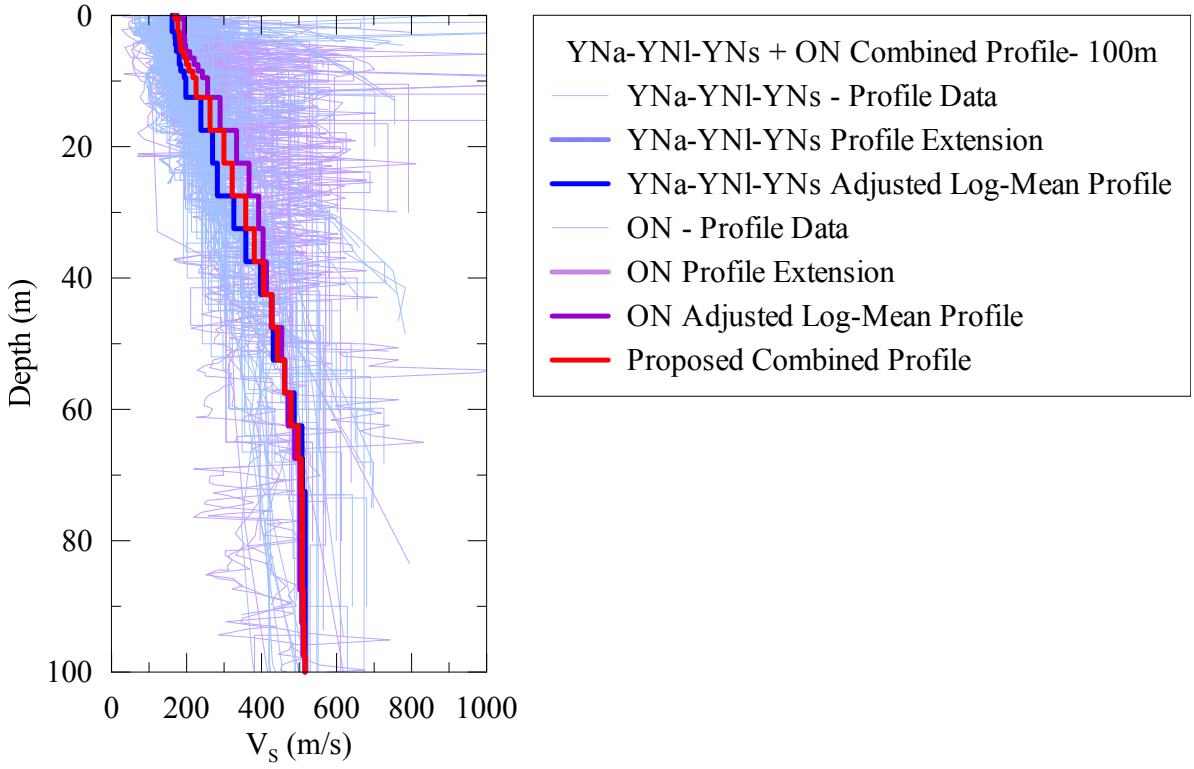

Figure 87: Combination of two adjusted log-mean V_S profiles into one characteristic V_S profile

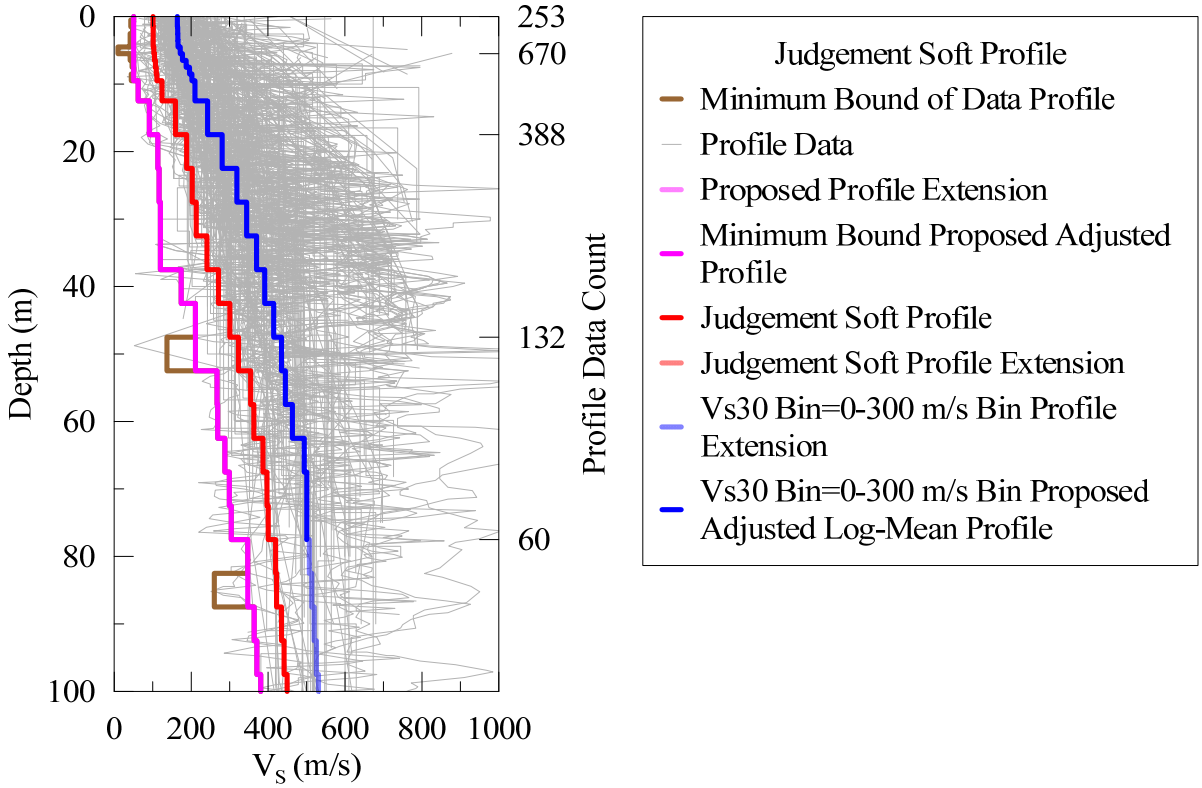

Figure 88: Creation of Judgment Soft profile for use as a characteristic profile in parametric study from the minimum bound profile and the adjusted log mean of rock-removed velocity profiles with V_{S30} values between 0 and 300 m/s

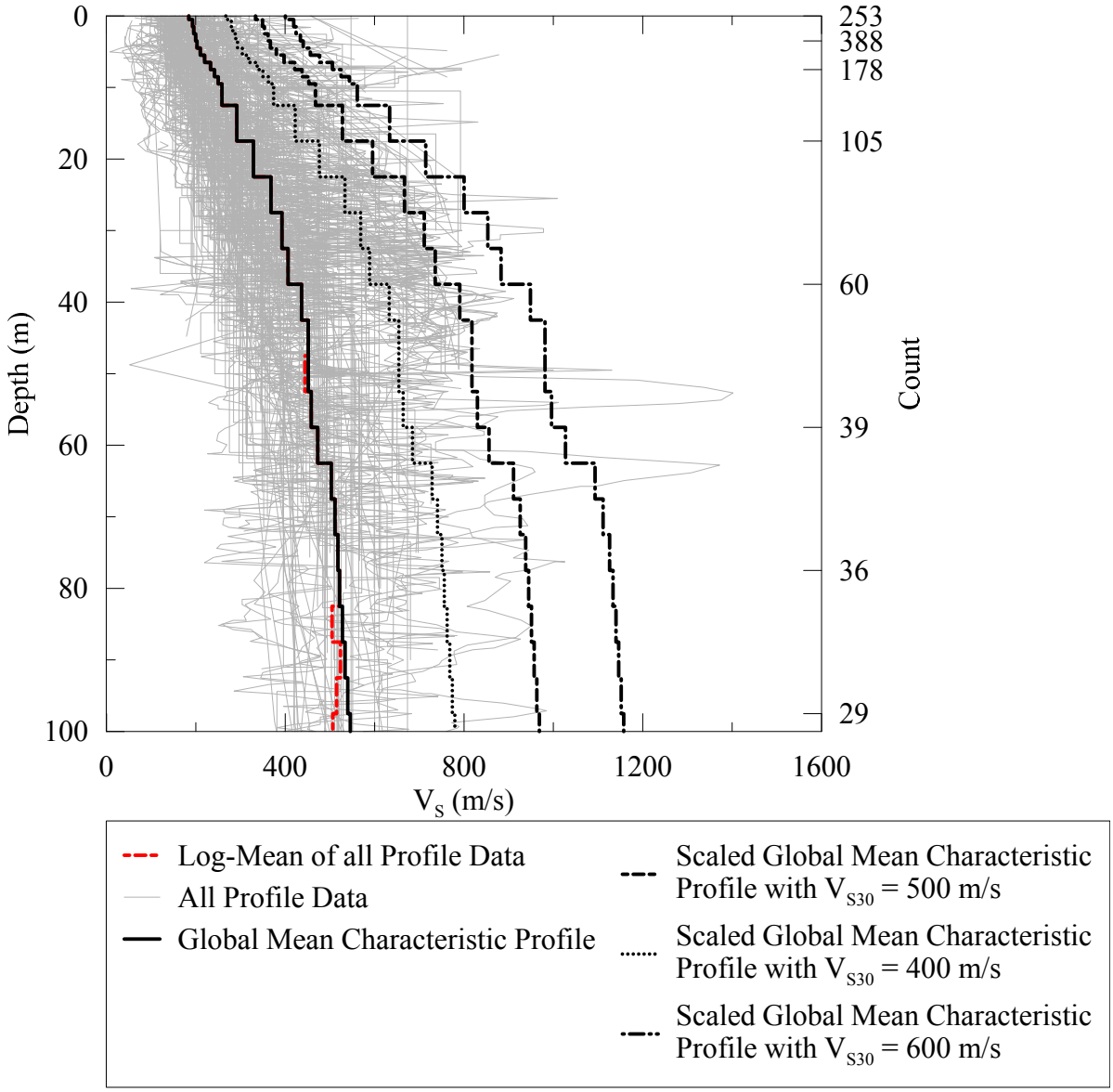

Figure 89: Representative VS Profiles from scaled global log-mean profile

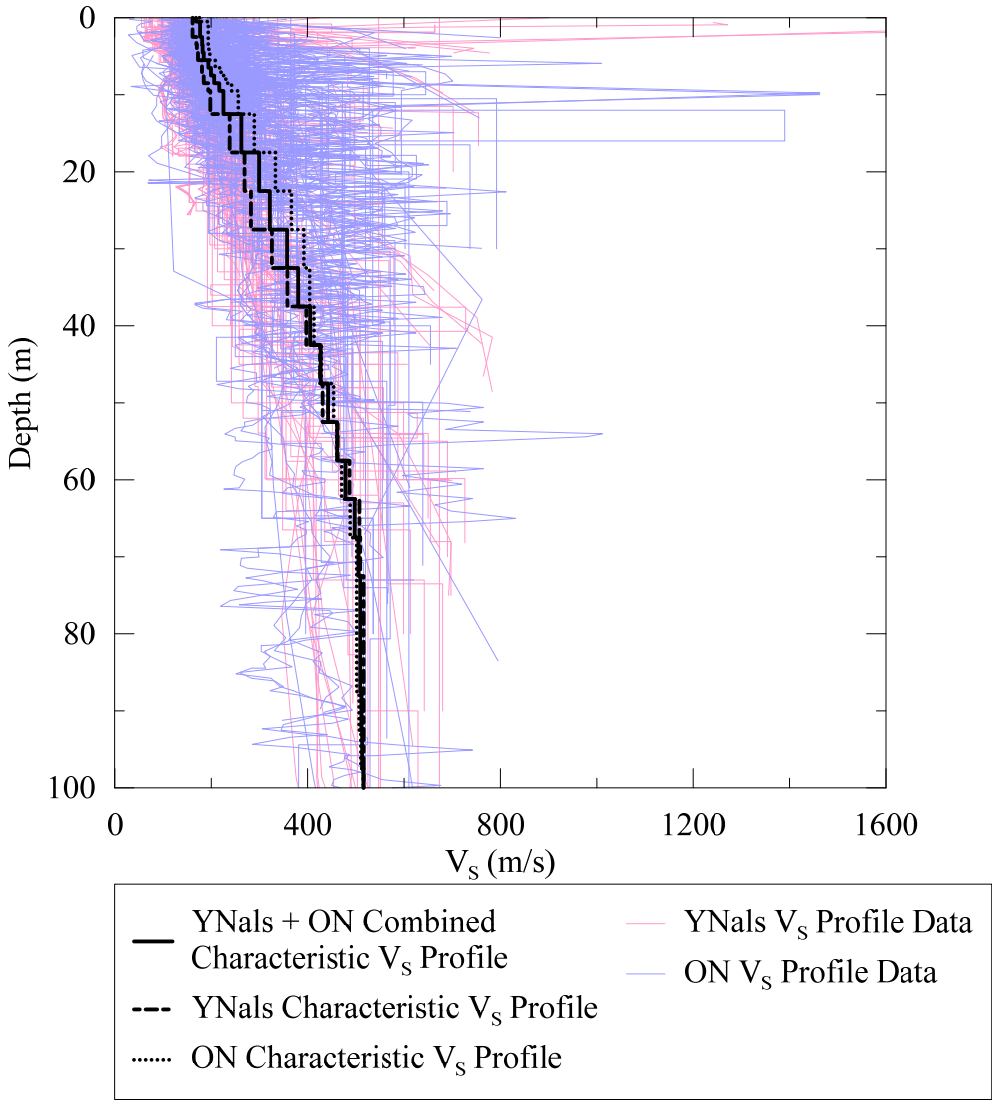

Figure 90: Combination of YNa-YNl-YNs profile and ON profile for YNals+ON Representative Profile

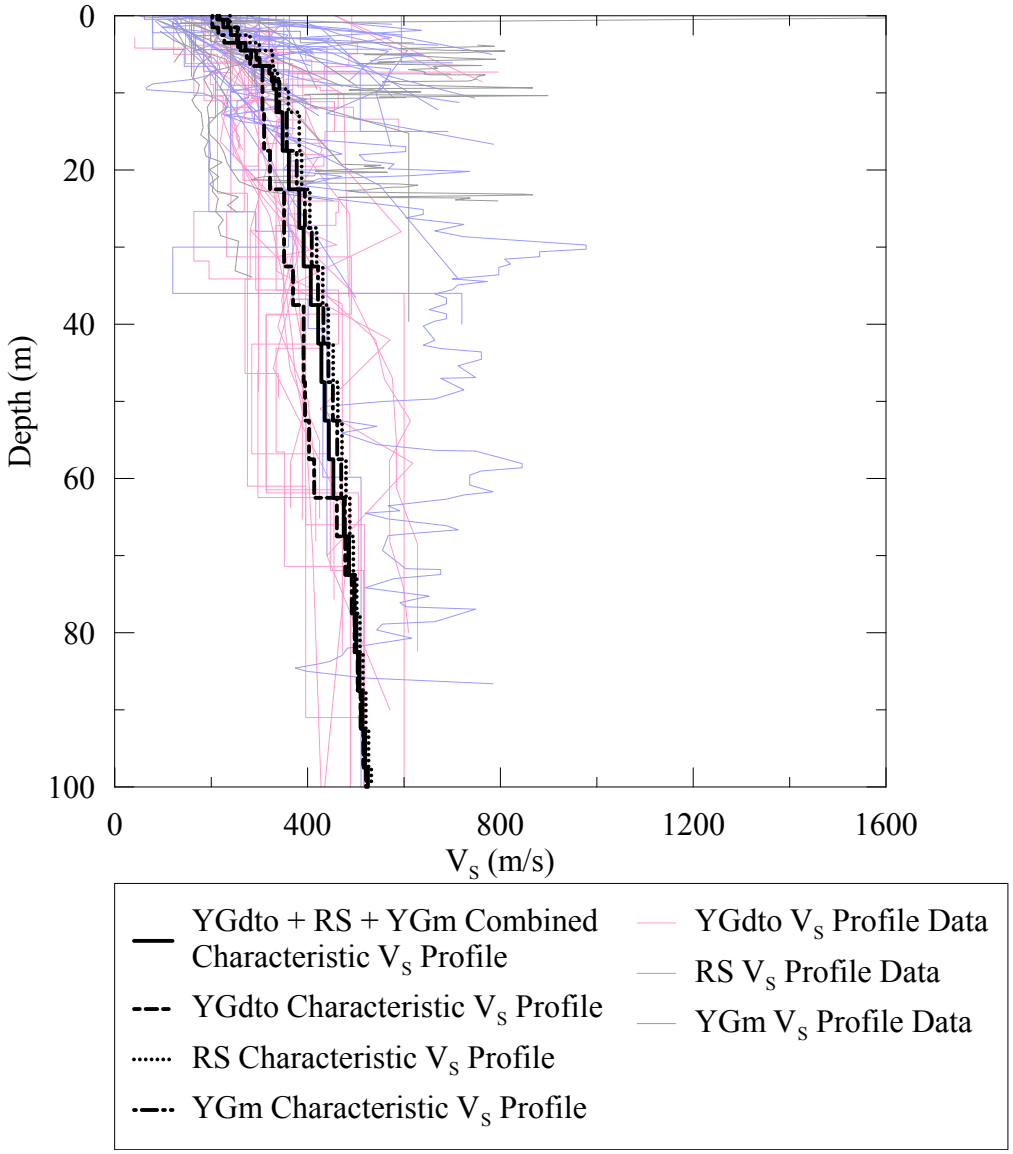

Figure 91: Combination of YGd-YGt-YGo, RS, and YGm profiles to form YGdto+RS+YGm characteristic profile

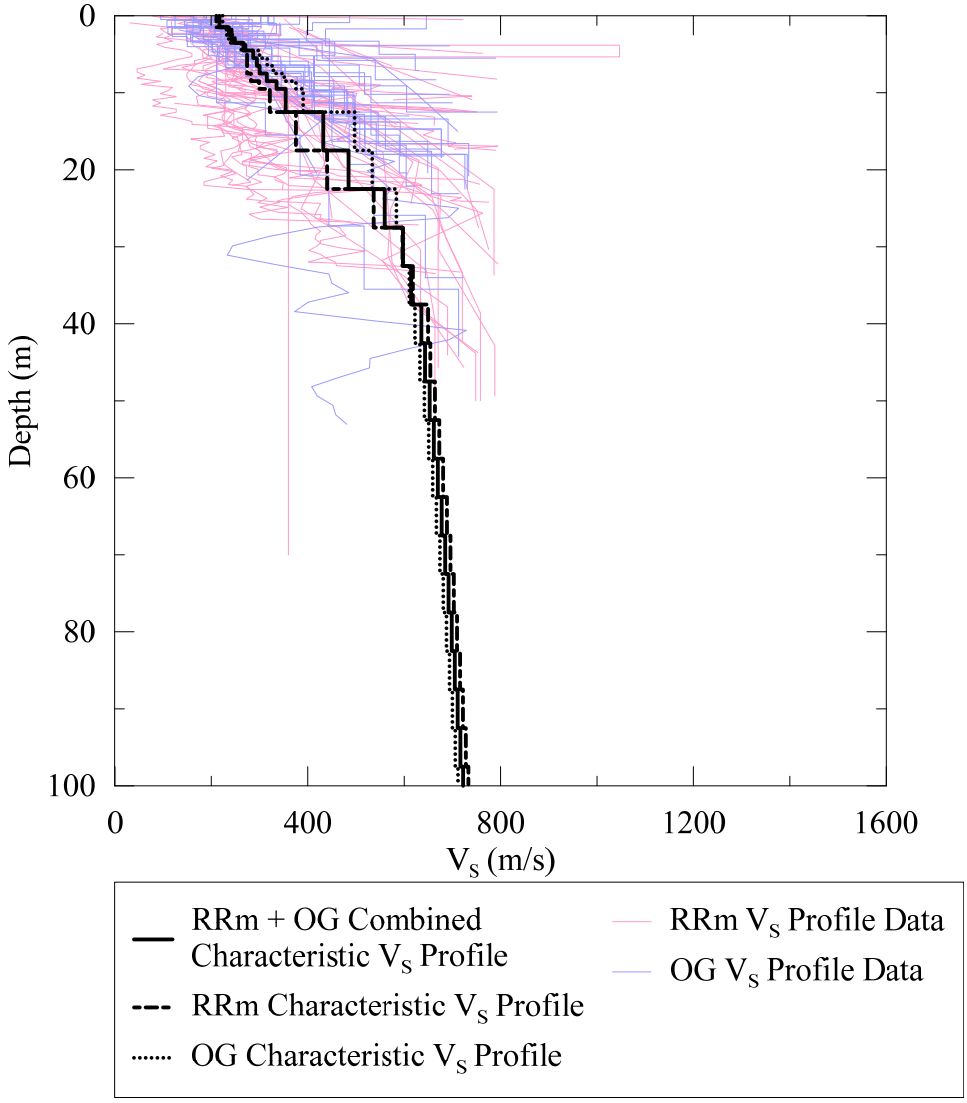

Figure 92: Combination of RRm and OG profiles to form RRm+OG characteristic profile

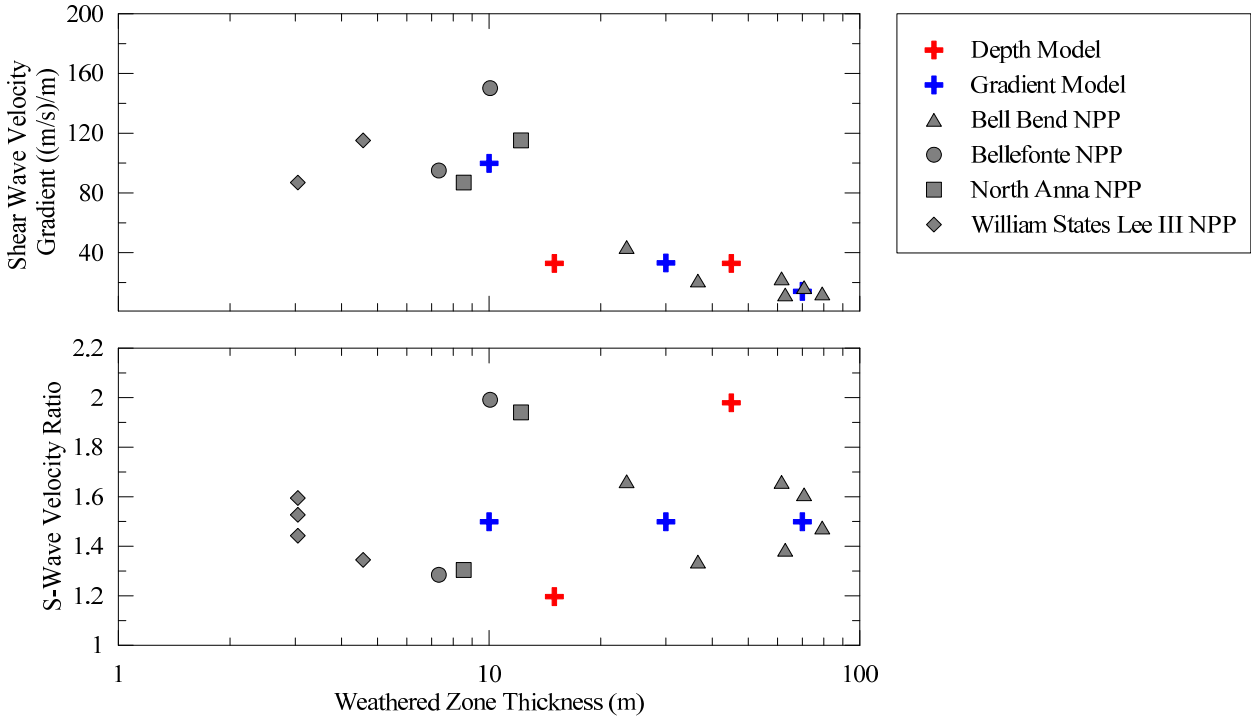

Figure 93: Weathered Rock Zone Properties (Data from Hashash et al. (2014))

APPENDIX B RANDOMIZATION METHODOLOGY FOR V_S PROFILES

To capture the epistemic uncertainty associated with the shear wave velocity inputs to site response analysis, characteristic shear wave velocity profiles are often randomized as a function of depth. Commonly used is the scheme proposed by Toro (1995) which includes methods for layer thickness and correlated shear wave velocity generation from input median profiles.

B.1 DEFINITION OF LAYER THICKNESS

The layer thickness randomization scheme in the Toro (1995) model uses a nonhomogeneous Poisson process to predict the rate of soil layers with soil column depth. These layers are then assigned a V_S value from the V_S randomization model. The rate function of the Toro (1995) model is given by

$$\lambda(d) = a(d + b)^c \tag{27}$$

where λ is the expected layer rate, d is depth, and a and b are constants. Using the recommended values for a, b, and c shown in Table 23, the expected layer thickness at 1000 m is 239 m. It is unusual that the velocity structure of a soil column would have a constant velocity for over 200 m, even at great depth. Because the increase in layer thickness with depth is greatly dependent on the c exponent, if the exponent is increased to -0.7, and a and b are unchanged, the expected layer thickness at 1000 m is reduced to 64 m, a more reasonable unit to have a uniform V_S. The layer thickness of V_S profiles used in this study are not randomized and all have the same layer thicknesses as a function of depth, where the V_S layer thickness at each depth is the expected layer thickness for that depth given by (27) using the coefficients shown in Table 23. The V_S layer thicknesses are assigned to the characteristic V_S profiles after profile development, resulting in slightly different V_{S30} values for the characteristic V_S profiles developed from scaling the global log-mean V_S profile to 400, 500, and 600 m/s V_{S30}. The V_{S30} values of the characteristic V_S profiles after assigning layer thicknesses from Toro (1995) shown in Table 13 of the main body of this study and a comparison of the V_{S30} before and after layer thickness assignment is provided in Table 24 below.

B.2 RANDOMIZATION OF SHEAR WAVE VELOCITY

In the development of site amplification functions, spatial variability in soil structure is typically modeled by using randomized V_S profiles with a procedure similar to Toro (1995) in a Monte Carlo simulation. The Toro (1995) randomization scheme allows for V_S profile structures where deeper layers can have lower V_S than more shallow layers, creating a reversal with V_S as a function of depth. Statistical correlation coefficients limit the frequency with which these V_S reversals occur, but in large-scale studies, site amplification behavior for sites with V_S reversals can be systematically different than those without.

A study by Pehlivan (2015) found that reversals in shear wave can lower the median surface response up to 10% at periods shorter than the site period. The Pehlivan (2015) study used ground motions and soil columns similar to those derived for this study in 1-D EL site response analyses. The profiles randomized with coefficients of Toro (1995) that allow reversals in V_S as a function of depth showed lower median surface responses than profiles without V_S reversals.

There are two systematic problems with V_S profiles generated with the Toro (1995) scheme: individual profiles can have unrealistic shapes, and the input median profile is not returned when V_S layer thickness is randomized as noted in Pehlivan (2015).

In the Toro (1995) V_S for a soil layer is assigned from a lognormal distribution with median V_S from an input median profile and either a prescribed standard deviation as a function of depth or a standard deviation related to surficial geology or site classification recommended from the data collected for the Toro (1995) model derivation. The randomized assigned V_S is correlated to the V_S of the previous layer as a function of depth. When this model is used without layer thickness randomization, the input median and standard deviation are stable and returned when a sufficient number of random velocity profiles are generated, but the profiles may be unrealistic. V_S values at most sites increase as a function of depth and reversals in V_S are usually attributable to well-documented, specific geologic site conditions. It is possible, even with high inter-layer velocity correlation coefficients for the Toro (1995) model to generate layers with overly high or low V_S relative to the surrounding layers at any depth. The Toro (1995) model also has no built-in boundaries on reasonable soil behavior. The log-normal distribution of V_S in the model can

generate rock-like V_S values at shallow depths. If the randomization model is constrained with upper or lower bounds, the median profile and standard deviation inputs are not returned by the randomization scheme. Additionally, in nonlinear site response analysis, a sharp change in V_S with depth can create numerical difficulties, as ground motion frequency can get trapped in the soft layer.

After randomization of V_S, model layers are subdivided to control the propagation of high frequency through the soil column. The maximum frequency a model soil layer can propagate, f_{max}, is given by (28).

$$f_{max} = \frac{V_S}{4H} \tag{28}$$

where H is the thickness of the model layer, and V_S is the shear wave velocity of that layer. The maximum frequency that can be reliably propagated by an entire soil profile is the minimum f_{max} of the soil profile's layers. Soil profiles in this study were subdivided such that the maximum frequency of the soil profile was 50 Hz.

B.3 BOUNDS OF RANDOMIZATION

A V_S profile is developed similar to the other characteristic profiles and used as a lower-bound of V_S profile randomization. The lower bound profile comes from lowest value of the collected V_S profile data at the center of each sublayer used for profile averaging. This profile then has reversals removed and is extended to 1000 m the same as the other characteristic input profiles as described in APPENDIX A. The minimum bound V_S profile is shown in Figure 88. Any randomized V_S profile generated with V_S lower than the minimum bound profile at the midpoint of a layer will be discarded and a new random V_S profile will be generated.

B.4 RANDOMIZATION METHODOLOGY FOR NONLINEAR CURVES

Darendeli (2001) proposes not only empirical correlations for the development of G/G_{max} and damping curves, but also the standard deviation of the curves generated. The standard deviation model of Darendeli (2001) can be used as a means of randomization of the curves. For each randomized V_S profile, there will be three randomized nonlinear curves following a procedure

similar to the one used in the equivalent-linear site response program STRATA (Kottke and Rathje 2011).

The STRATA randomization model generates two normally distributed random ε values for each soil layer, ε_G and ε_D, where ε_G describes the distance of the G/G_{max} curve from the mean, and ε_D describes the distance of the damping curve from the mean. ε_D for a specific soil layer is negatively correlated to ε_G by a factor of -0.5. ε values between adjacent layers can be correlated in the STRATA model.

This study uses three random realizations of nonlinear soil behavior each random V_S profile. The first realization for the nonlinear soil behavior for a random V_S profile is the mean soil behavior calculated from Darendeli (2001). Two additional random nonlinear curve realizations are used to capture soil behavior with less strain softening than the mean behavior (positive ε_G) and soil behavior with more strain-softening than the mean behavior (negative ε_G). The realizations for the soil column assume perfect inter-layer correlation and perfect negative correlation between ε_G and ε_D. Both generated ε values will be constrained to $1.5 \times \sigma$, where σ is the standard deviation from Darendeli (2001). Damping values generated will be constrained to be > 0.0 and G/G_{max} values will be constrained between 0 and 1. If a value for the nonlinear curves would be generated above or below its constraints, the limiting value will be used.

B.5 TABLES

Table 23: Coefficients for use with Toro (1995) layer thickness randomization scheme

Coefficient	Toro (1995) recommended values	Values to be used in this study
a	1.98	1.98
b	10.86	10.86
c	-0.89	-0.7

Table 24: V_{S30} of characteristic profiles before and after layer thickness assignment

Characteristic Profiles	V_{S30} of Characteristic profile before layer thickness assignment (m/s)	V_{S30} of characteristic profile after layer thickness assignment (m/s)
YNm	229	240
RRs	356	356
YNa-YNl-YNs +ON	245	252
RRm + OG	380	391
YGd-YGt-YGo + RS + YGm	329	333
V_{S30} Bin = 300-500 m/s	375	383
Scaled Global Log-Mean to V_{S30}= 600 m/s	600	616
Scaled Global Log-Mean to V_{S30}= 500 m/s	500	513
Scaled Global Log-Mean to V_{S30}= 400 m/s	400	411
Judgment Soft	143	148

APPENDIX C NONLINEAR CURVES IN CENA

Modulus reduction (G/G_{max}) and damping input curves for site response analysis greatly affect calculated site amplification. Therefore, it is important that the modulus reduction and damping curves used as inputs for the site response analyses in this study reflect the range of site conditions and nonlinear curves typical of CENA, and that the constitutive soil model used in analysis be able to produce real soil behavior.

Constitutive models for use in 1-D seismic site response analyses must accurately capture initial shear modulus at small strains, shear strength of soil at large strains, and have flexible control of nonlinear soil at intermediate strains. Commonly used soil models either do not capture both large- and small-strain soil behavior or are not usable in site response analyses. Failure to capture either the large or small strain behavior of soil can lead to both under- and over- estimation of site amplification. The GQ/H model proposed by Groholski et al. (2015), Groholski et al. (2016) is a model derived from the bivariate quadratic equation to both accurately capture initial soil stiffness and large-strain shear soil strength behavior.

Current site response analysis calculations involve solving equations of motion and require shear strain-controlled soil models, commonly known as Kondner and Zelasko (1963) derived models after the original formulation. Modifications to the Kondner and Zelasko derived models over time have typically included improvements in capturing small-strain shear behavior (such as in the model of Matasovic (1993), the MKZ model) or have included terms to capture additional effects on the shear strength behavior of the soil (such as the formulation of Hashash and Park (2001) to include the effects of confining pressure). These models have typically improved or preserved shear-strain behavior in the region most commonly of interest to engineers at the expense of being unable to capture shear strength response of soil at large strains.

Models that can capture both small-strain soil behavior and large-strain shear strength behavior by combining hysteretic curves such as the Yee et al. (2013) have been proposed. These models typically include a model curve similar to the MKZ model for low shear strains, a hyperbolic model curve asymptotic to a prescribed shear strength for large shear strains, and a transition function between that weights each model curve to ensure smooth behavior. These models, while

typically successful in capturing shear stress behavior at both large and small shear strains, are particularly difficult to implement in 1-D site response analysis codes because they lack rules for hysteretic unload-reload behavior.

The GQ/H soil model uses a smooth hyperbolic curve to control the shear stress-strain behavior of a soil for use in 1-D site response analysis. The functional form is asymptotic to a prescribed shear strength and includes model coefficients to provide control of soil nonlinearity.

Nonlinear curves for soil columns for analysis are generated using the empirically-derived model for modulus reduction and damping curves from Darendeli (2001). To account for the epistemic uncertainty of the soil properties in CENA, random realizations of the Darendeli (2001) model for each random velocity profile will be used. To ensure compatibility of dynamic curve strength and V_S, the strength-controlled hyperbolic GQ/H model developed by Groholski (2016) will be used for soil layers with compatible V_S and shear strength.

C.1 SELECTION OF CEUS SOIL PROPERTY DATA

An effort was undertaken to collect G/G_{max} and damping curves for sites in CENA. However, because of a lack of diversity in the geologic conditions and material properties of the collected dynamic curves, characteristic site properties were determined for use with correlation-based procedures for generating dynamic curves such as the formulations presented by Darendeli (2001). To characterize nonlinear soil behavior from Darendeli (2001), soil characteristics needed are: mean stress, plasticity index (PI), overconsolidation ratio (OCR), number of cycles (N), and frequency of cycles (f). For site response analyses, N and f are typically equal to 10 and 1, respectively and the values have little impact on the shape of empirical nonlinear curves.

Soil property information from a small selection of geotechnical design reports at sites in CENA was collected. Table 25 shows a summary of the collected data and sources for the data are given in Table 26. Sites were selected to provide coverage of the geologic classifications given in Kottke et al. (2012). Soil properties used for empirical generation of nonlinear curves are shown in Table 25. Differences between the site characteristics shown in Tables 25 and Table 27 are the result of judgement decisions about the relative soil properties between geologic classifications and the combination of geologic classifications for characteristic V_S profiles. Figure 94 shows a

comparison of the PI and friction angles selected for this study to other clays. The mean stress for use in empirical correlations is calculated from the friction angle of the selected material through the at-rest coefficient of lateral earth pressure, K_0, as shown in eq. 4

$$K_0 = (1 - \sin\varphi) \times OCR^{\sin\varphi} \tag{29}$$

where φ is the material friction angle. The selected material friction angle will also be used in the GQ/H model to influence soil strength.

C.2 STRENGTH CONTROL OF NONLINEAR CURVES

Randomized G/G_{max} nonlinear soil behavior can result in unrealistic shear stress-strain behavior. V_S, density, and G/G_{max} behavior of soil implies a shear stress-strain response that soil. The maximum observed implied shear stress from the G/G_{max} curve between 0 % shear strain and a limiting upper value (typically 10 % shear strain) is known as the implied shear strength of the soil layer. The implied shear stress of a soil layer can be calculated by:

$$\tau_{implied} = \rho \cdot {V_S}^2 \cdot \frac{G}{G_{max}} \cdot \gamma \tag{30}$$

where ρ is the soil density, and γ is the shear strain.

The strength-controlled GQ/H model places an asymptote on implied shear stress as shown in Figure 95. This model is preferable to the commonly used MKZ model (Matasovic (1993) after Kondner and Zelasko(1963)) because the MKZ model does not allow for control of large-strain soil strength, which can be seen in Figure 95. However, one of the limitations of the GQ/H model is its inability to fit soil behavior with an incompatible V_S, G/G_{max} curve, and model shear strength. If the implied shear strength of a nonlinear curve is significantly different than the prescribed model shear strength asymptote, the GQ/H model will be unable to fit the nonlinear curves. This can occur in material with high V_S and low target shear strength when using Darendeli (2001) or other empirical correlations that do not consider V_S or shear strength.

The nonlinear curves in Darendeli (2001) include confining stress as an input parameter and therefore change as a function of depth. Curves from Darendeli (2001) are not V_S dependent, so to capture the connection between implied shear strength and V_S, a model for soil strength is

needed that is both a function of confining stress and V_S. A strength model dependent only on confining stress using the friction angles shown in Table 27 is insufficient, as in the context of randomization it implies that a layer with a V_S typical of a soft surficial soil has the same shear strength as a layer with a rock-like V_S if they occur at the same depth. For shallow material, it is also often insufficient to describe strength with just a friction angle for use in site response. Fitting to the strength of material with confining stresses near the surface with just a friction angle will generate overly soft layer response.

To account for these strength considerations in a parametric study of site response analyses, a model is proposed that uses the friction angles in Table 27 to describe the increase in soil strength as function of depth, but adds in a small amount of cohesion based on the V_S as described by

$$c = \rho \cdot {V_S}^2 \cdot 0.80 \cdot 0.1\% \geq 10\ kPa \tag{31}$$

where c is the cohesion component of the shear strength. This formulation is based on the equation for implied shear strength (30).

This equation assumes that the soil being modeled will have some amount of strength equal to the shear stress developed at 0.1% shear strain from a linear response of the soil with a shear modulus reduced by 20 %. The total shear strength of the soil is described by

$$\tau_{target,implied} = c + \sigma_v' \tan(\varphi) \tag{32}$$

This model is shown as a function of depth in Figure 96 for soil with a friction angle of 30°. The "cohesionless friction angle" shows the total soil strength relative to overburden is calculated by

$$\tan(\varphi_{cohesionless}) = \frac{\tau_{target,implied}}{\sigma_v'} \tag{33}$$

Where σ_v' is the effective vertical stress, and $\varphi_{cohesionless}$ is the cohesionless friction angle.

Even with correction shown in (32) applied to shear strength behavior, it is still possible for high-V_S layers with little strain-softening behavior to be generated by the randomization

procedure for nonlinear curves which the GQ/H model is unable to fit. For these layers, the MKZ nonlinear model can be used. In these layers, strains are expected to be small and exhibit little nonlinearity. Nonlinear curves generated with Darendeli (2001) and the corresponding best-fit MKZ and GQ/H curves are shown in Figure 95. Target shear strength for the GQ/H soil model in Figure 95 includes the cohesional strength from (31). A summary of all randomized G/G_{max} and damping curves after fitting to the GQ/H model across all analyses and geologic classes as a function of depth is shown in Figure 97 The mean and standard deviation of each geologic class and V_S profile at a depth of 22.5 m is shown in Figure 98

C.3 GQ/H FITTING PROCEDURE

The GQ/H model requires a selection of a range of strains for fitting G/G_{max} and damping curves. It is recommended in Groholski et al. (2016) that the damping curve be fit over the entire strain range of interest, and that the G/G_{max} curve be fit to the small-strain range of the nonlinear curve up to 0.1 % shear strain. The GQ/H model will always be asymptotic to a maximum desired shear strength, and Groholski et al. (2016) recommends that the fitting bound of the curves reach a threshold of 95 % of the asymptotic shear strength at 10 % shear strain (i.e. the implied shear strength at 10 % shear strain should be 95 % of the asymptotic shear strength). These recommendations are not applicable for all possible combinations of G/G_{max} curves and V_S combinations, and a modified fitting routine was required for use in this study to generate reasonably-shaped G/G_{max} curves for the randomized soil profile layers.

The shear strength given in (32) is the desired soil strength for strains up to 10 %, the target implied shear strength. To produce reasonable fits to the randomized soil curves with the GQ/H model, the GQ/H asymptotic shear strength is set to be higher than the target implied shear strength by the following procedure:

1. Fit the randomized G/G_{max} curve to GQ/H parameters with the model asymptotic shear strength equal to the target implied shear strength from (32) and no threshold for the implied shear strength of the resulting fit.
2. Fit the randomized G/G_{max} curve to GQ/H parameters with the model asymptotic shear strength $\tau'_{asymptote}$ as given by:

$$\tau'_{asymptote} = \frac{\tau_{target,implied}}{\left(\frac{\tau_{target,implied}}{\tau'_{implied}}\right)} \quad (34)$$

where $\tau'_{implied}$ is the implied shear strength from the first stage of fitting. The minimum threshold of shear strength for the second stage of fitting, δ, is given by:

$$\delta = \frac{\tau_{target,implied}}{\tau'_{asymptote}} \times 100\ \% \quad (35)$$

This procedure ensures that the implied shear strength at 10% will always be greater than or equal to the desired shear strength. This procedure is shown visually in Figure 99 for a soil layer with V_{S30} = 500 m/s, 50 m depth, γ = 19.0 kN/m^3, PI = 15 %, and OCR = 1.5 for the mean and +/- 1 σ G/G_{max} and damping curves from Darendeli (2001)

Parameters of the GQ/H model must be defined such that the resulting behavior does not violate any of the model's boundary conditions for numerical stability (Groholski et al. 2016). The fits of the G/G_{max} to the GQ/H model in the above steps were done over several ranges of shear strains as given in Table 28 to ensure that the GQ/H fits were valid under the model constrains. Each range of shear strains were fit until a valid set of parameters for the GQ/H model was produced

.

C.4 TABLES

Table 25: Summary of soil property data collected for CENA sites

Geologic Class	PI (%)			Overburden (pcf)			Data Source
	Mean	Range	# of data	Mean	Range	# of data	
OGm	19	0-52	28	118.7	104.4-127.2	6	1, 13
OGo							
OGt							
YGm	10	1-23	163	133.8	106.4-145.4	27	2, 3
YGo	17	9-30	21	120.1	111.3-125.4	12	17, 18
YGt							
YGd							
ONa	28	2-91	81	120	100.7-134.9	72	4, 5
ONc							
ONl							
ONm							
YNc	17	8-34	4	125.9	123.9-127.3	3	6, 15
YNm	37	9-59	42	123.2	98.32-141.25	57	7
YNa	18	4-34	16	111.1	86.02-136.28	36	8, 9
YNl							
YNs							
RRm	10	1-26	250	117.5	117.5	1	10, 16
RRs	20	6-44	10	123.7	115.7-130.8	10	11
RSs	27	4-47	15	122.6	116.96-130.1	3	12, 14

Table 26: Sources for data presented in Table 25

Data Source	Geotechnical Design Report
1	HNTB Corporation. "T.H. 52 ORONOCO DESIGN-BUILD ORONOCO, MINNESOTA", 2005
2	Northeast Ohio Regional Sewer District. "Euclid creek tunnel", 2010
3	Parsons Brinckerhoff. "Rochester Intermodal Transportation Center Improvement Geotechnical Investigation Preliminary Design Phase Monroe County, New York", 2013
4	HVJ ASSOCIATES, Inc."PART 1 GEOTECHNICAL INVESTIGATION BATTLESHIP TEXAS DRY BERTH", 2011
5	HVJ ASSOCIATES, Inc. "GREEN WATER TREATMENT DECOMMISSIONING AUSTIN, TEXAS ",2007
6	BBC&M Engineering, Inc."Muddy Creek East Branch Interceptor – West Half Hamilton County, Ohio", 2007
7	Fugro Consultants, Inc." Pegasus Project, Phace One I-30 Bridge Over the Trinity River Dallas, Texas", 2009
8	ISG & Associates, inc. "Geotechnical Engineering Report Council Bluffs, Iowa", 2008
9	TTL, "Geotechnical Exploration Buffalo Wild Wings Restaurant Des Moines, Iowa", 2013
10	Florecnce & Hutcheson."I-85/I-385 Interchange Improvements Greenville County, SC", 2013
11	S&ME, Inc."Louisville-Southern Indiana Ohio River Bridges Project Vertical Borings Jefferson County, Kentucky", 2012
12	HBC/Terracon, "Geotechnical Engineering Report Classic BMW Dealership Spring Creek Parkway and North Dallas Tollway Plano, Texas", 2004
13	Terracon. "Geothechnical Engineering report proposed lift station south maple streetm SE of south 4th street west branch, Iowa", 2012
14	Schnabel, "Geotechnical report 1000 Mosby street Richmond, VA", 2010
15	Michael Baker Jr., Inc,"PRE-FINAL GEOTECHNICAL ENGINEERING REPORT LOWER HILL REDEVELOPMENT PROJECT PITTSBURGH, ALLEGHENY COUNTY, PENNSYLVA" , 2012
16	S&ME, "Proposed Building Sites Hunter Industrial Park Laurens, South Carolina", 2008
17	Haley & Aldrich, Inc. "SUPPLEMENTAL GEOTECHNICAL DATA REPORT PROPOSED SIBLEY POND BRIDGE REPLACEMENT MAINEDOT PIN 15618.00 CANAAN / PITTSFIELD,
18	MaineDOT "BRIDGE PROGRAM GEOTECHNICAL SECTION AUGUSTA,MAINE", 2010

Table 27 Selected soil properties for use in parametric study

Material	PI (%)	Unit Weight (kN/m^3)	OCR	Friction Angle (φ°)	Associated Characteristic V_S Profiles		
General	15	19	1.5	25	Scaled Global	V_{S30}-Binned	Judgement Soft
Weathered Rock Zone	5	21	3	40	Weathered Rock Zone		
Young Glaciated	15	18.9	1.3	30	YGd-YGt-YGo + RS + YGm		
Old Glaciated	20	18.6	3	30	RRm + OG		
Young Nonglaciated	20	18.5	1.3	30	YNa-YNl-YNs + ON	YNm	
Old Nonglaciated	30	19	2	30	YNa-YNl-YNs + ON		
Residual Soil from Sedimentary Rock	24	19.4	3	25	RRs		
Residual Soil from Metamorphic Rock	10	19	3	25	RRm + OG		
Residual Soil	30	19.3	3	25	YGd-YGt-YGo + RS + YGm		

Table 28: GQ/H Strain Fitting Ranges for G/G_{max} curves

Randomization	Iteration	Min Bound Strain (%)	Max Bound Strain (%)
H (G/G_{max} $\varepsilon > 0$)	1	0.001	0.1
H (G/G_{max} $\varepsilon > 0$)	2	0.01	0.1
H (G/G_{max} $\varepsilon > 0$)	3	0.03	0.1
H (G/G_{max} $\varepsilon > 0$)	4	0.003	0.03
H (G/G_{max} $\varepsilon > 0$)	5	0.003	0.01
M (G/G_{max} $\varepsilon = 0$)	1	0.001	0.1
M (G/G_{max} $\varepsilon = 0$)	2	0.001	0.03
M (G/G_{max} $\varepsilon = 0$)	3	0.0001	0.01
M (G/G_{max} $\varepsilon = 0$)	4	0.003	0.03
M (G/G_{max} $\varepsilon = 0$)	5	0.008	0.03
L (G/G_{max} $\varepsilon < 0$)	1	0.001	0.1
L (G/G_{max} $\varepsilon < 0$)	2	0.0001	0.003
L (G/G_{max} $\varepsilon < 0$)	3	0.001	0.01
L (G/G_{max} $\varepsilon < 0$)	4	0.001	0.003
L (G/G_{max} $\varepsilon < 0$)	5	0.003	0.03

C.5 FIGURES

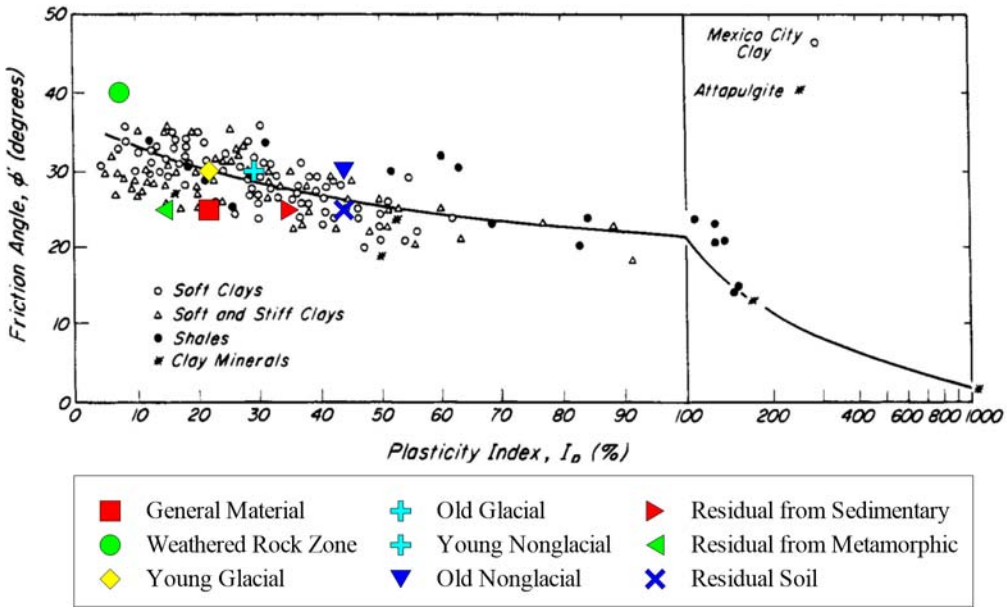

Figure 94: Comparison of material properties for this study compared to Figure 19.7 of Terzaghi et al. (1996)

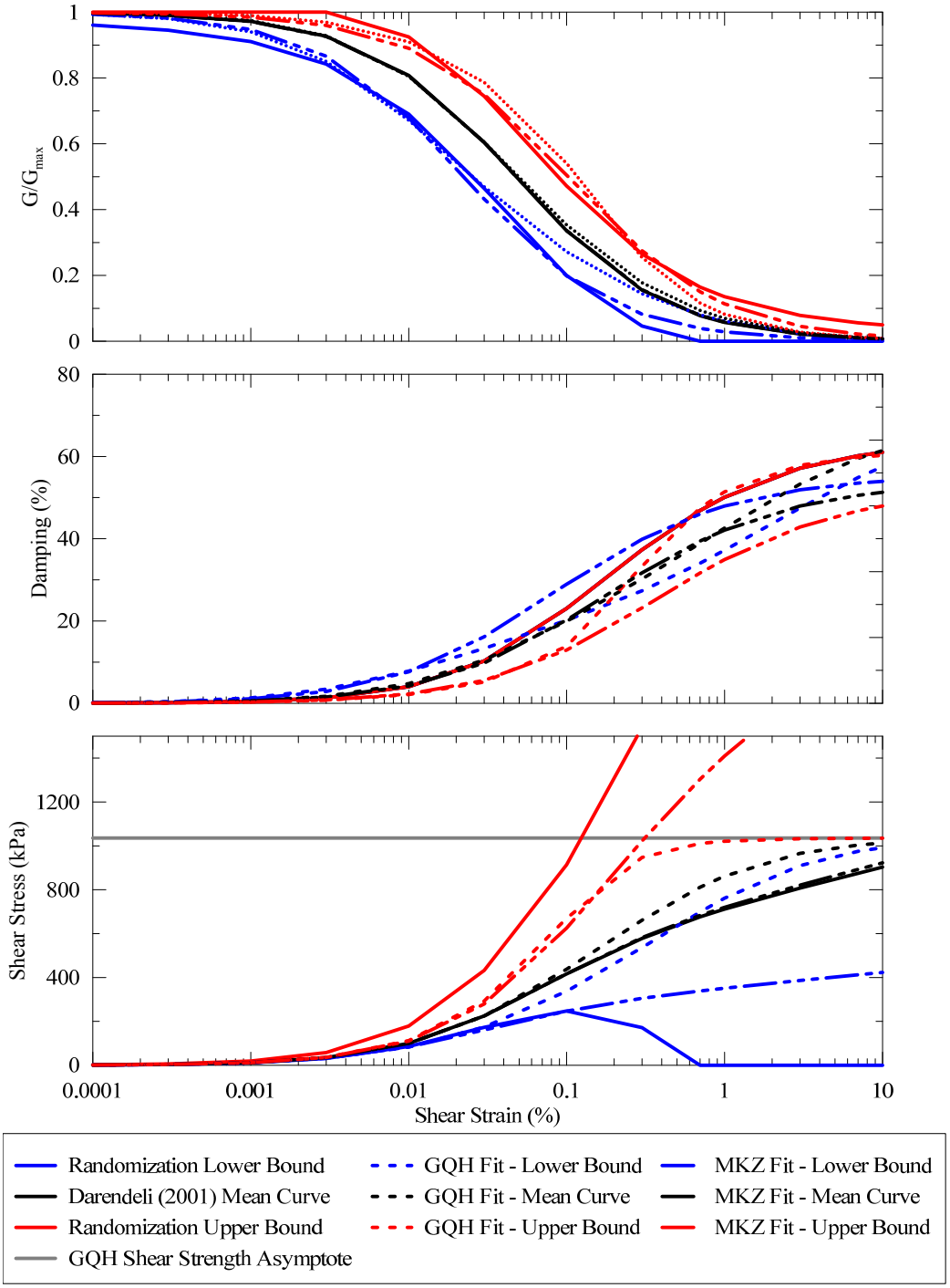

Figure 95: Dynamic Curves generated with Darendeli (2001) for a soil layer 5 m deep with PI = 10%, φ = 25°, σ'_v = 95 kPa, and V_S = 800 m/s. MKZ and GQ/H fits shown for GQ/H asymptote strength of 1035 kPa.

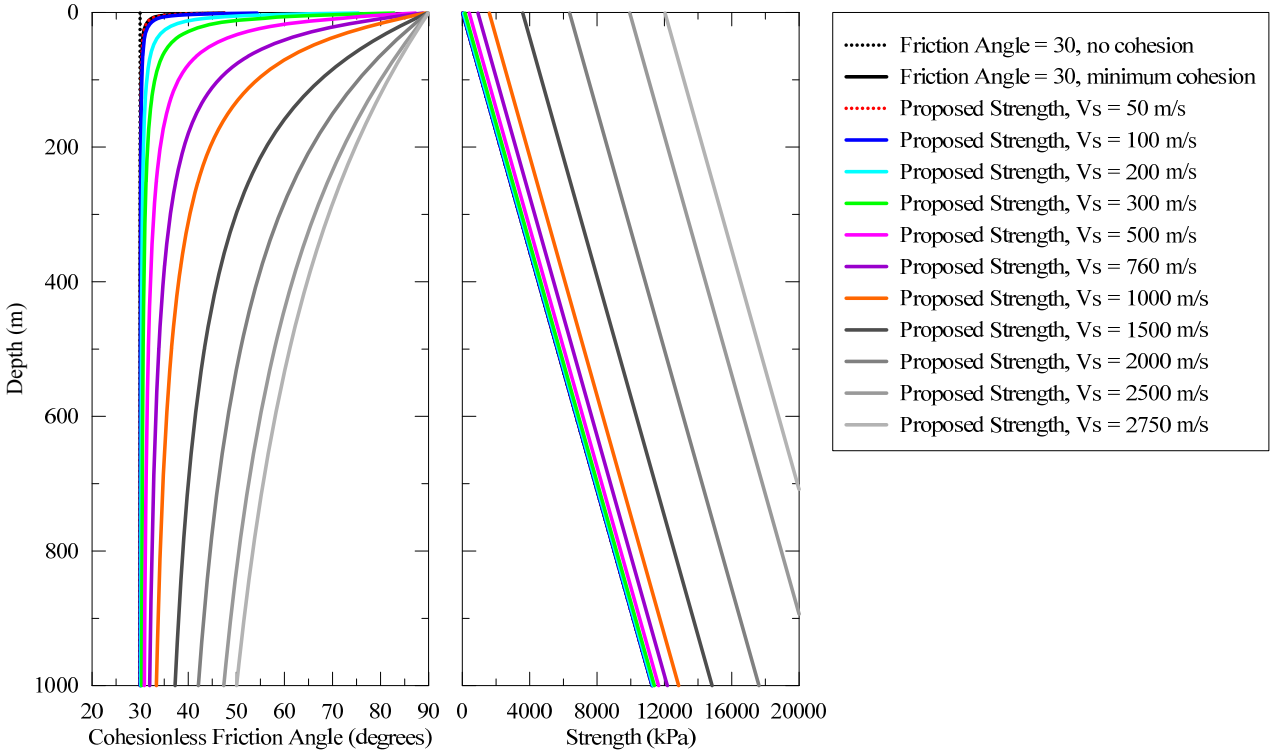

Figure 96: Proposed Vs-based cohesion model for implied shear strength as a function of depth for a soil with a friction angle of 30° and unit weight of 19 kPa.

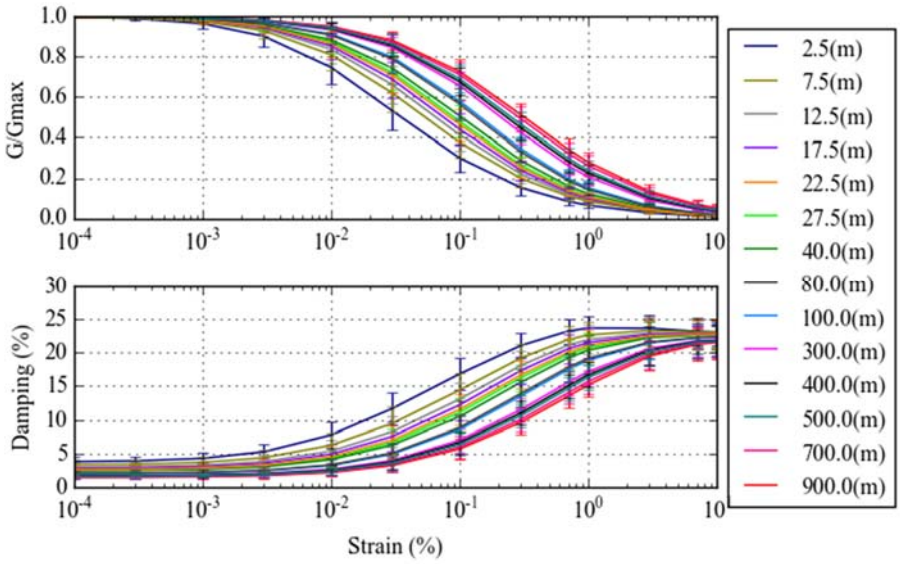

Figure 97: Summary of randomized G/G_{max} and damping curves as a function of depth. Error bars represent +/- 1 standard deviation

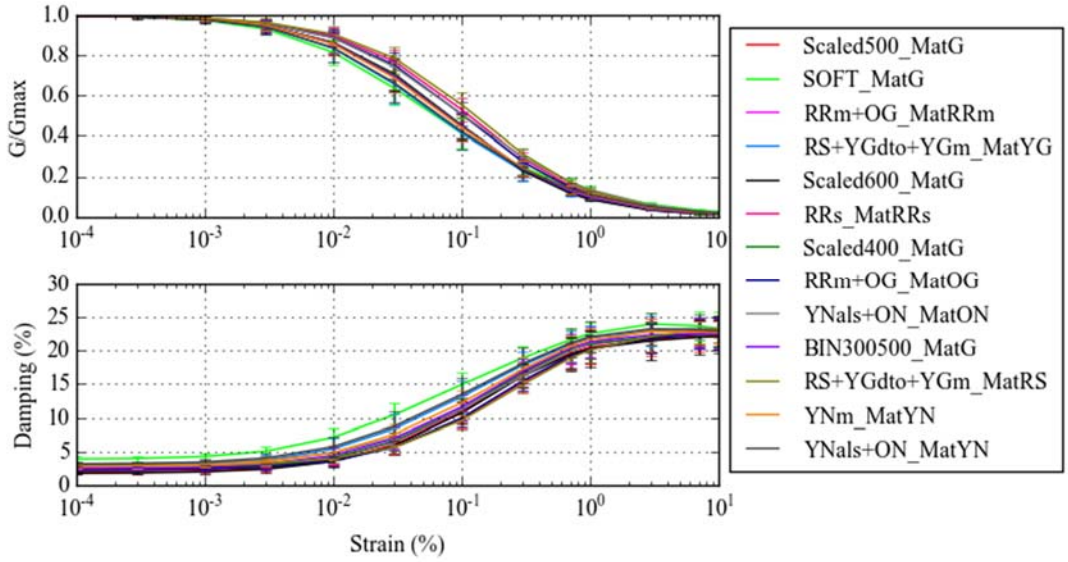

Figure 98: Average G/G_{max} and damping curves for each material and V_S profile combination at 22.5 m depth. Error bars show +/- 1 standard deviation

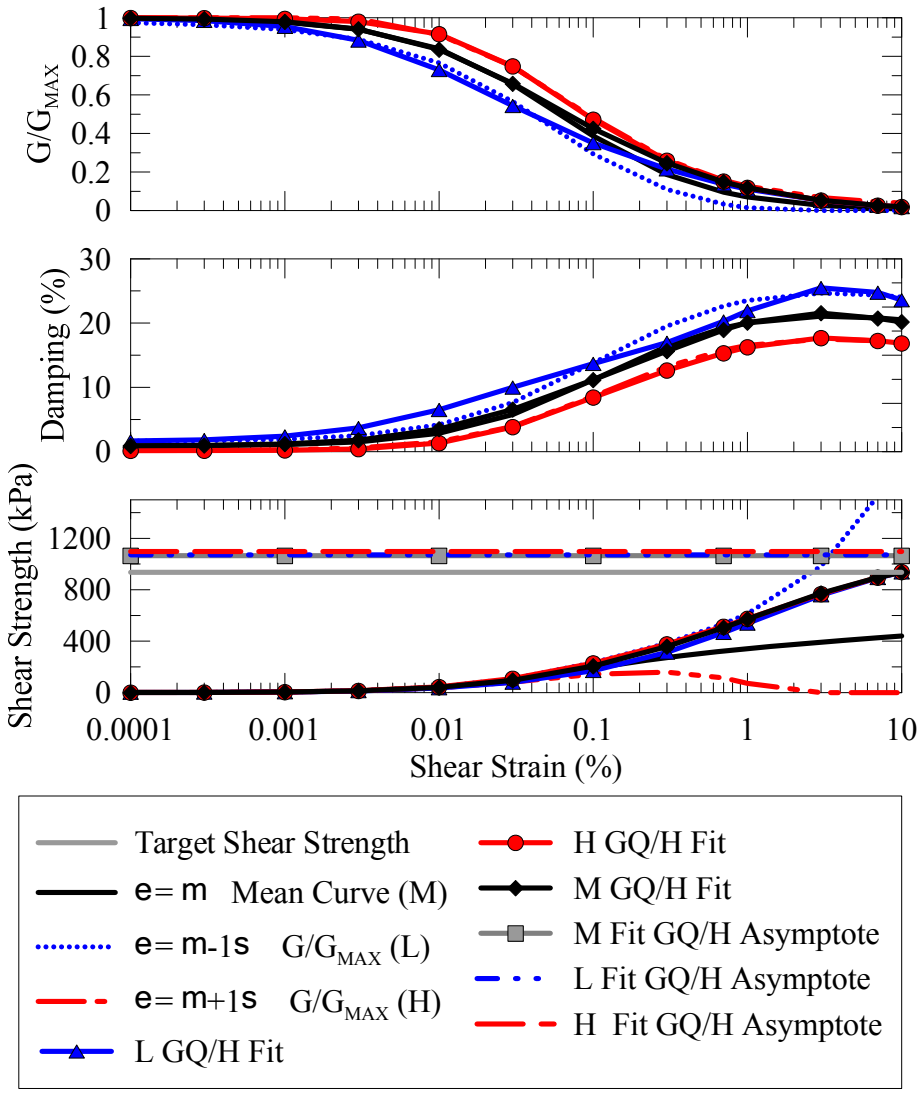

Figure 99: GQ/H Fitting Procedure for a soil layer with V_{S30} = 500 m/s, 50 m depth, γ = 19.0 kN/m^3, PI = 15 %, and OCR = 1.5 for the mean and +/- 1 σ G/G_{max} and damping curves from Darendeli (2001)

APPENDIX D RESPONSE SPECTRAL MODEL COEFFICIENTS AND BOUNDS

This appendix presents the fitting methodology of the site amplification coefficients in the main body of the report. Coefficients are presented for 22 RS and FAS periods between 0.001 s and 10 s. The coefficients and bounding values used in the fitting of the coefficients for the site

amplification model terms presented in this study are shown in Figures 100, 101, 102, and 103 as a function of response spectral period. Coefficients at 22 RS and FAS periods are provided in Tables 29, 30, 31, 32, 33, and 34.

Coefficients for the amplification models were developed through nonlinear regression model with bounds using the 'port' algorithm of a nonlinear least-squared solver in R (R Core Team 2015). Regression bounds were selected to provide consistent model behavior between response spectral periods. Coefficients for each model at each period were regressed independently, and no smoothing between periods was performed after coefficient fitting.

Figure 100 shows the regressed linear amplification coefficients and fitting bounds for $f(V_{S30})$ for the L1, L4, L5, K1, and K2 coefficient models. Reparameterization during regression was needed to simultaneously constrain the coefficients V_c and V_L into the coefficient *diff* as shown in (36).

$$V_L = \frac{V_c}{10^{diff}} \tag{36}$$

V_L must be less than V_c and cannot be constrained with fixed values unless the maximum allowable value for V_L is less than the minimum allowable value of V_c. The regression coefficient *diff* can be constrained with values that are unaffected by V_c. Two different bounds are used for $f(V_{S30})$ fitting: one set of upper and lower bounds for the L1 coefficient model and one set for the L4, L5, K1, and K2 coefficient models based on the results of the L1 model fits.

The functional form selected for $f(V_{S30})$ is more complicated than models such as the Seyhan and Stewart (2014) model with only two fitting coefficients, the value of V_c and the slope of the linear scaling with $\ln(V_{S30})$. Because of the curved region in $f(V_{S30})$ the functional form presented in this study can have combinations of parameters that produce similar amplification shapes, particularly when factors other than V_{S30} are considered as for the L4, L5, K1, and K2 coefficient models. If the curved region has a gradual enough curve (e.g. low values of c_3) for high enough values of V_L it approximates the shape of the linear region of $f(V_{S30})$ (e.g. between V_c and V_L). This trade off can be seen in Figure 48 of the main body of this report in at 0.3 s and 0.6 s The region of the amplification of both periods between 1000 m/s and 300 m/s. is similar in

magnitude, though the curved quadratic region of 0.3 s covers a much wider range of V_{S30} values because of the higher V_L.

Figure 101 shows the regressed linear amplification coefficient and fitting bounds for $f(Z_{Soil})$ for the L2 and L4 coefficient models. Positive values of c_4 indicate an increase in amplification as a function of depth while negative values indicate a decrease in amplification as a function of depth. Figure 101 shows similar trends in the depth effects of amplification for the L2 and L4 coefficient models as expected.

Figure 102 shows the regressed linear amplification coefficients and fitting bounds for $f(T_{nat})$ for the L3, L5, K1, and K2 coefficient models. The c_5 and c_6 coefficients in the $f(T_{nat})$ amplification model linearly scale the Riker wavelet and amplification with T_{nat}, respectively, and the α coefficient modifies the width of the Riker wavelet. The c_6 coefficient has a similar effect on site amplification as the c_4 coefficient in the $f(Z_{Soil})$ amplification term. At low periods, the negative c_6 term causes a reduction in amplification for very soft or deep sites with high natural period, and at higher periods, the positive c_6 term causes a relative increase in amplification for those sites.

Figure 103 shows the regressed nonlinear amplification coefficients and fitting bounds for $f(NL)$ for the N1, N2, K1, and K2 coefficient models. Two sets of coefficient bounds were used for $f(NL)$, one set for the fitting of N1 and N2 coefficient models, and one set for the K1 and K2 coefficient models. The N models were developed independently of linear site amplification or residuals of linear site amplification after model fitting. In order to reproduce similar trends in soil nonlinearity and well-behaved regression coefficients, the K models needed fairly tight constraints as seen for long periods in f_4 and short periods in f_5, Figure 103 (b) and (c), respectively.

Table 29: Model coefficients for models L1, L2, and L3

Model:	L1					L2	L3		
Period (s)	c_1	c_2	c_3	V_c (m/s)	V_L (m/s)	c_4	c_5	c_6	α
0.001	-1.6980	0.0000	-1.7223	2990	1887	-7.46E-07	0.0000	-0.0992	0.0000
0.01	-1.5262	0.0000	-1.6995	2990	1887	-7.81E-07	-0.0100	-0.1033	0.1039
0.02	-1.4527	0.0000	-2.0614	2990	1887	-1.02E-06	-0.0100	-0.1328	0.1500
0.03	-1.6467	0.0000	-2.2725	2990	1887	-1.15E-06	0.0448	-0.1515	0.0940
0.1	-2.0550	0.0000	-2.0486	2990	1887	-8.21E-07	0.1332	-0.1118	0.1329
0.2	-2.1000	-1.0252	-3.6786	1318	832	-5.12E-07	0.1753	-0.0717	0.1486
0.25	-2.0000	-1.3930	-4.0008	1152	727	-4.46E-07	0.1750	-0.0662	0.1526
0.3	-1.9710	-1.1749	-5.1962	1018	429	-3.79E-07	0.1755	-0.0594	0.1463
0.35	-1.9551	-1.2432	-6.6761	970	340	-3.03E-07	0.1802	-0.0507	0.1504
0.4	-1.8624	-1.7079	-7.5559	939	314	-2.19E-07	0.1851	-0.0400	0.1581
0.45	-1.7838	-2.0511	-8.3895	917	290	-1.51E-07	0.1931	-0.0299	0.1643
0.5	-1.7923	-2.1951	-10.1934	883	252	-7.89E-08	0.2076	-0.0193	0.1665
0.55	-1.7577	-2.2040	-9.8400	862	243	-2.28E-08	0.2208	-0.0102	0.1688
0.6	-1.7153	-2.0608	-8.4902	849	239	2.55E-08	0.2283	-0.0016	0.1746
0.65	-1.6044	-1.7476	-5.9314	832	235	6.19E-08	0.2312	0.0054	0.1815
0.7	-1.0000	-0.7890	-0.0531	974	388	9.52E-08	0.2347	0.0122	0.1883
0.8	-1.0000	-0.6569	0.1420	951	466	1.59E-07	0.2374	0.0285	0.2166
0.9	-1.0000	-0.2500	0.4236	862	485	2.77E-07	0.2377	0.0617	0.2985
1	-1.0000	0.0000	-0.4034	894	564	2.53E-07	0.2448	0.0546	0.2969
2	-1.0000	0.0000	-0.4152	837	528	3.37E-07	0.3262	0.0129	0.3734
3	-1.6980	0.0000	-1.7223	2990	1887	4.57E-07	0.3859	0.0019	0.4531
10	-1.5262	0.0000	-1.6995	2990	1887	3.77E-07	0.2508	0.0378	0.6000

Table 30: L4 model Coefficients

Period (s)	c_1	c_2	c_3	c_4	V_c (m/s)	V_L (m/s)
0.001	-1.7790	0.0000	-1.6379	-9.02E-07	2990	1887
0.01	-1.6112	0.0000	-1.6111	-9.45E-07	2990	1887
0.02	-1.5632	0.0000	-1.9463	-1.23E-06	2990	1887
0.03	-1.7715	0.0000	-2.1425	-1.39E-06	2990	1887
0.1	-2.1442	0.0000	-1.9557	-9.94E-07	2990	1887
0.2	-2.7029	0.0000	-3.1997	-6.24E-07	1487	938
0.25	-2.1000	-1.3202	-3.8849	-5.44E-07	1326	837
0.3	-2.0000	-1.6557	-4.1811	-4.62E-07	1166	736
0.35	-2.0826	-1.3411	-4.6336	-3.69E-07	1081	554
0.4	-2.0455	-1.2226	-5.1989	-2.67E-07	1020	439
0.45	-2.0248	-1.1696	-6.6804	-1.85E-07	969	339
0.5	-1.8963	-1.6660	-7.5246	-9.62E-08	939	314
0.55	-1.7932	-2.0370	-8.3796	-2.78E-08	918	289
0.6	-1.7828	-2.2139	-10.2098	3.11E-08	882	253
0.65	-1.7351	-2.2729	-10.0502	7.54E-08	859	242
0.7	-1.6850	-2.1814	-8.9215	1.16E-07	843	237
0.8	-1.5502	-1.9727	-6.6452	1.94E-07	822	232
0.9	-1.0000	-0.7890	-0.0531	2.06E-07	974	388
1	-1.0000	-0.5385	0.3093	3.08E-07	897	450
2	-1.0000	-0.2500	0.4236	4.13E-07	862	485
3	-1.0000	0.0000	-0.7009	5.49E-07	760	480
10	-1.0000	0.0000	-0.7123	4.40E-07	760	480

Table 31: L5 Model Coefficients

Period (s)	c_1	c_2	c_3	c_5	c_6	V_c (m/s)	V_L (m/s)
0.001	-1.7560	0.0000	-1.3778	0.0000	-0.1747	2990	1887
0.01	-1.5970	0.0000	-1.3596	-0.0100	-0.1814	2990	1887
0.02	-1.5571	0.0000	-1.6491	-0.0100	-0.2324	2990	1887
0.03	-1.7749	0.0000	-1.8180	0.0622	-0.2648	2990	1887
0.1	-2.1330	0.0000	-1.6389	0.1752	-0.2051	2880	1817
0.2	-2.5544	0.0000	-2.4265	0.1830	-0.1243	1492	941
0.25	-2.1000	-0.9821	-2.9443	0.1713	-0.1048	1344	848
0.3	-2.0000	-1.3961	-3.3419	0.1651	-0.0933	1199	756
0.35	-1.9053	-1.0889	-3.5836	0.1790	-0.0721	1195	550
0.4	-1.8183	-0.9399	-4.1570	0.1930	-0.0522	1154	409
0.45	-1.7192	-0.9946	-5.3409	0.2102	-0.0343	1127	320
0.5	-1.6000	-1.3663	-6.1138	0.2303	-0.0174	1099	295
0.55	-1.4755	-1.6409	-6.8557	0.2476	-0.0021	1094	274
0.6	-1.4355	-1.7561	-8.7579	0.2574	0.0116	1059	236
0.65	-1.4061	-1.7632	-9.2207	0.2609	0.0204	1032	226
0.7	-1.3722	-1.6487	-8.8175	0.2653	0.0296	1012	221
0.8	-1.2835	-1.3981	-7.1177	0.2724	0.0501	982	215
0.9	-1.0000	-0.6312	-0.0637	0.2476	0.0597	991	432
1	-1.0000	-0.6569	0.1420	0.2448	0.0420	951	466
2	-1.0000	0.0000	-0.1402	0.2680	0.0473	811	512
3	-1.0000	0.0000	-0.4841	0.4495	-0.0224	1073	677
10	-1.0000	0.0000	-0.4982	0.1662	0.0531	760	480

Table 32: N1 and N2 model coefficients

Model	N1			N2		
Period (s)	f_3	f_4	f_5	f_3	f_4	f_5
0.001	0.0916	-0.4482	-0.0018	0.0894	-0.4489	-0.0018
0.01	0.0932	-0.4387	-0.0013	0.0752	-0.4375	-0.0013
0.02	0.1265	-0.4325	-0.0009	0.0566	-0.4151	-0.0010
0.03	0.2289	-0.4885	-0.0013	0.1036	-0.4987	-0.0013
0.1	0.2546	-0.4415	-0.0033	0.1508	-0.4466	-0.0033
0.2	0.1850	-0.3163	-0.0048	0.1282	-0.3048	-0.0049
0.25	0.1881	-0.3055	-0.0056	0.1329	-0.2751	-0.0056
0.3	0.1964	-0.2790	-0.0066	0.1307	-0.2282	-0.0065
0.35	0.1368	-0.1872	-0.0077	0.1064	-0.1605	-0.0077
0.4	0.1087	-0.1320	-0.0089	0.0941	-0.1159	-0.0087
0.45	0.1141	-0.1172	-0.0098	0.0932	-0.0927	-0.0096
0.5	0.1044	-0.0922	-0.0106	0.0989	-0.0779	-0.0103
0.55	0.0776	-0.0597	-0.0117	0.0820	-0.0537	-0.0113
0.6	0.0738	-0.0466	-0.0126	0.0759	-0.0401	-0.0122
0.65	0.0643	-0.0340	-0.0136	0.0652	-0.0286	-0.0131
0.7	0.0397	-0.0202	-0.0147	0.0463	-0.0181	-0.0142
0.8	0.0336	-0.0128	-0.0162	0.0736	-0.0159	-0.0151
0.9	0.0171	-0.0052	-0.0185	0.0603	-0.0084	-0.0169
1	0.0100	-0.0027	-0.0200	0.0437	-0.0048	-0.0182
2	0.0100	-0.0023	-0.0165	0.0016	-0.0024	-0.0130
3	0.0100	-0.0100	-0.0097	0.0533	-0.0063	-0.0140
10	0.0100	-0.0042	-0.0158	0.0894	-0.4489	-0.0018

Table 33: K1 Model Coefficients

T (s)	c_1	c_2	c_3	c_5	c_6	V_c (m/s)	V_L (m/s)	f_3	f_4	f_5	α
0.001	-1.911	0.000	-1.814	0.000	-0.141	2990	1887	0.180	-0.609	-0.001	0.0000
0.01	-1.701	0.000	-1.690	0.013	-0.143	2990	1887	0.157	-0.562	-0.001	0.0400
0.02	-1.575	0.000	-1.670	-0.010	-0.176	2990	1887	0.110	-0.451	-0.001	0.1500
0.03	-1.794	0.000	-1.980	0.053	-0.223	2990	1887	0.344	-0.608	-0.001	0.0910
0.1	-2.285	0.000	-2.000	0.090	-0.191	2963	1870	0.450	-0.599	-0.002	0.1291
0.2	-2.662	0.000	-2.813	0.095	-0.128	1625	1025	0.354	-0.452	-0.004	0.1329
0.25	-2.100	-0.991	-3.083	0.101	-0.113	1507	951	0.331	-0.431	-0.005	0.1416
0.3	-2.000	-1.396	-3.506	0.096	-0.103	1336	843	0.309	-0.391	-0.005	0.1414
0.35	-1.900	-1.407	-3.584	0.107	-0.092	1261	733	0.290	-0.311	-0.006	0.1503
0.4	-2.069	-0.940	-4.157	0.111	-0.079	1153	552	0.273	-0.259	-0.007	0.1689
0.45	-1.852	-0.995	-5.341	0.124	-0.065	1164	411	0.259	-0.235	-0.008	0.2000
0.5	-1.728	-1.366	-6.045	0.143	-0.054	1126	364	0.246	-0.197	-0.009	0.2000
0.55	-1.648	-1.641	-8.052	0.174	-0.037	1101	276	0.094	-0.099	-0.010	0.2312
0.6	-1.651	-1.756	-9.275	0.194	-0.023	1059	236	0.044	-0.068	-0.010	0.2455
0.65	-1.608	-1.763	-9.514	0.203	-0.014	1034	226	0.037	-0.052	-0.011	0.2500
0.7	-1.571	-1.649	-9.211	0.212	-0.007	1019	223	0.029	-0.041	-0.011	0.2500
0.8	-1.440	-1.398	-7.118	0.254	0.021	999	219	0.016	-0.032	-0.011	0.3000
0.9	-1.000	-0.631	-0.064	0.273	0.026	1169	555	0.010	-0.028	-0.012	0.3000
1	-1.000	-0.657	0.142	0.245	0.042	951	466	0.010	-0.003	-0.020	0.3000
2	-1.000	0.000	-0.140	0.257	0.026	925	584	0.010	-0.026	-0.010	0.4000
3	-1.000	-0.200	-0.403	0.245	0.042	894	564	0.010	-0.010	-0.010	0.3000
10	-1.000	0.000	-0.498	0.150	0.054	818	516	0.010	-0.118	-0.010	0.6000

Table 34: K2 Model Coefficients

T (s)	c_1	c_2	c_3	c_5	c_6	V_c (m/s)	V_L (m/s)	f_3	f_4	f_5	α
0.001	-1.908	0.000	-1.813	0.000	-0.141	2990	1887	0.178	-0.612	-0.001	0.0000
0.01	-1.655	0.000	-1.654	0.013	-0.143	2990	1887	0.127	-0.534	-0.001	0.0400
0.02	-1.572	0.000	-1.649	-0.010	-0.176	2990	1887	0.039	-0.395	-0.001	0.1500
0.03	-1.760	0.000	-1.986	0.052	-0.223	2990	1887	0.184	-0.641	-0.001	0.0903
0.1	-2.275	0.000	-2.006	0.089	-0.191	2976	1877	0.287	-0.615	-0.002	0.1290
0.2	-2.653	0.000	-2.772	0.095	-0.127	1625	1025	0.194	-0.380	-0.004	0.1329
0.25	-2.100	-0.942	-3.074	0.102	-0.113	1507	951	0.303	-0.418	-0.005	0.1419
0.3	-2.000	-1.396	-3.567	0.095	-0.103	1329	839	0.283	-0.358	-0.005	0.1403
0.35	-1.900	-1.367	-3.584	0.106	-0.092	1259	732	0.290	-0.280	-0.006	0.1504
0.4	-2.056	-0.940	-4.157	0.111	-0.080	1154	553	0.273	-0.227	-0.007	0.1687
0.45	-1.836	-0.995	-5.341	0.123	-0.066	1164	405	0.259	-0.183	-0.008	0.2000
0.5	-1.730	-1.366	-6.045	0.144	-0.055	1126	352	0.220	-0.150	-0.009	0.2000
0.55	-1.663	-1.641	-6.712	0.179	-0.037	1101	276	0.060	-0.067	-0.010	0.2313
0.6	-1.644	-1.756	-8.155	0.195	-0.023	1059	236	0.055	-0.055	-0.011	0.2440
0.65	-1.593	-1.763	-8.019	0.203	-0.015	1034	226	0.050	-0.040	-0.012	0.2500
0.7	-1.559	-1.649	-7.561	0.214	-0.007	1019	223	0.046	-0.032	-0.012	0.2500
0.8	-1.415	-1.398	-6.025	0.254	0.021	999	219	0.038	-0.025	-0.013	0.3000
0.9	-1.000	-0.631	-0.064	0.269	0.026	1169	510	0.031	-0.020	-0.013	0.3000
1	-1.000	-0.657	0.142	0.245	0.042	951	466	0.044	-0.005	-0.018	0.3000
2	-1.000	0.000	-0.140	0.258	0.025	917	579	0.001	-0.006	-0.010	0.4000
3	-1.024	0.000	-0.484	0.408	-0.027	1073	677	0.001	-0.005	-0.010	0.5272
10	-1.000	0.000	-0.498	0.150	0.058	809	511	0.001	-0.007	-0.010	0.6000

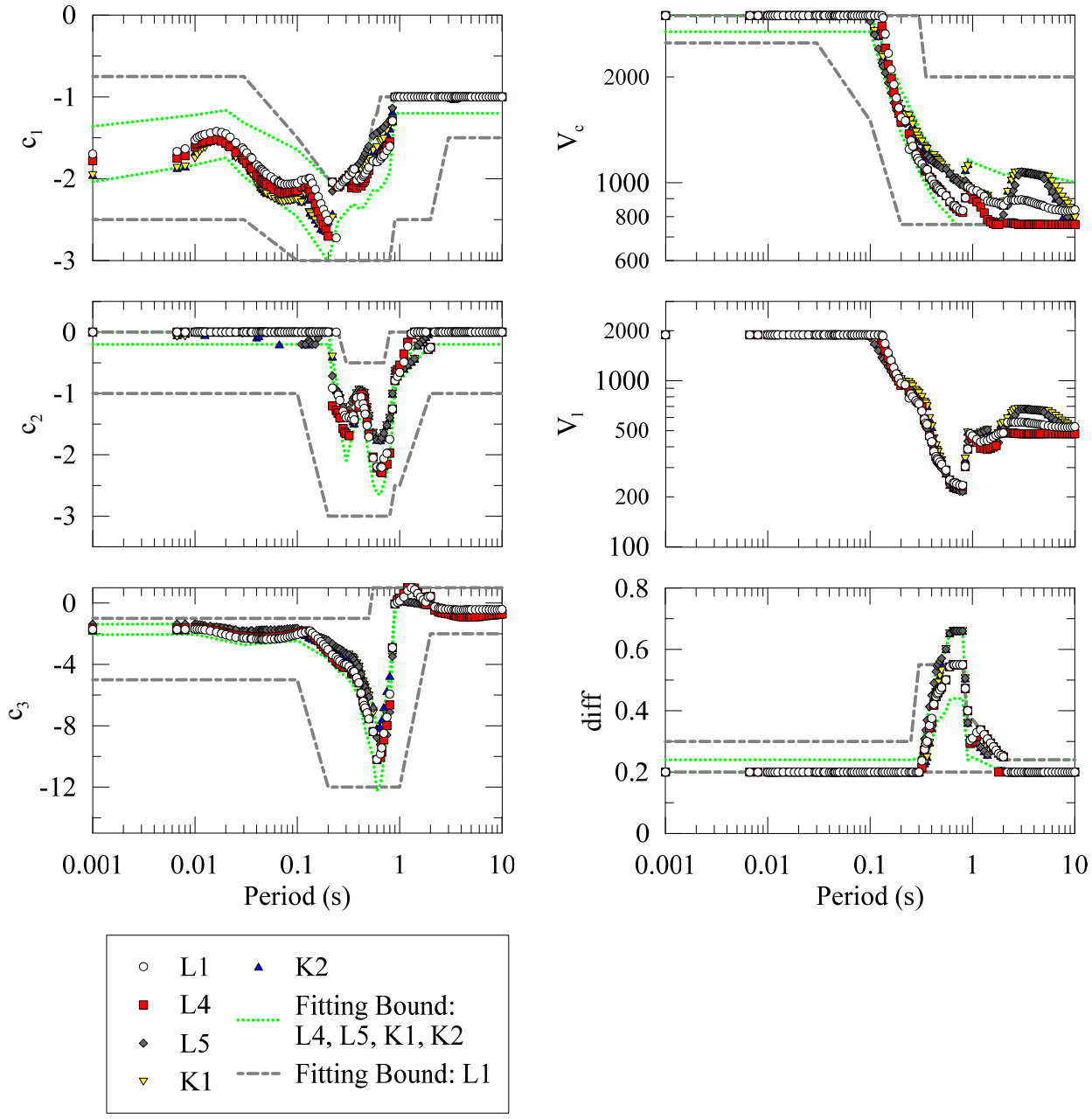

Figure 100: c1, c2, c3, V_c, and V_l, and *diff* fits from the L1, L4, L5, K1, and K2 coefficient models

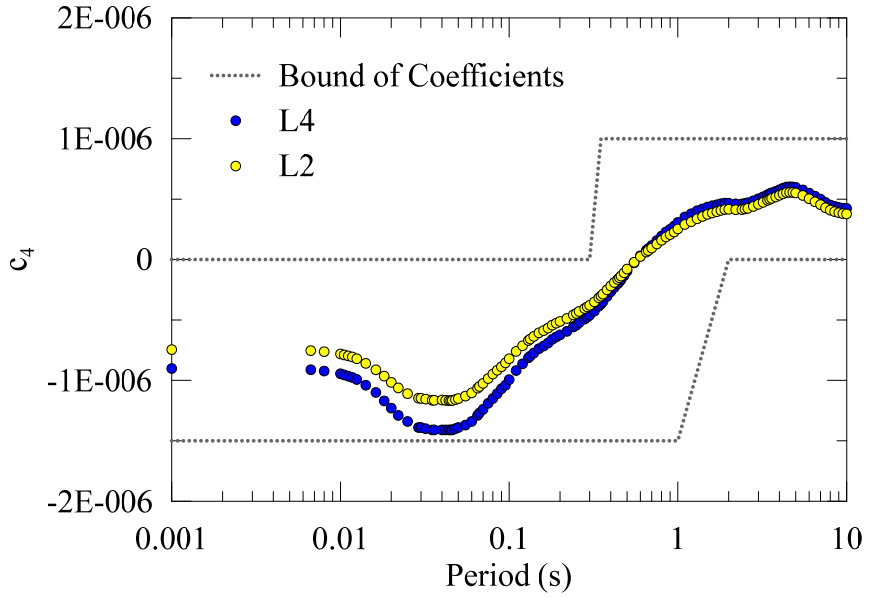

Figure 101: c4 coefficient fit of L2 and L4 models as a function of period shown with bound of coefficient fitting

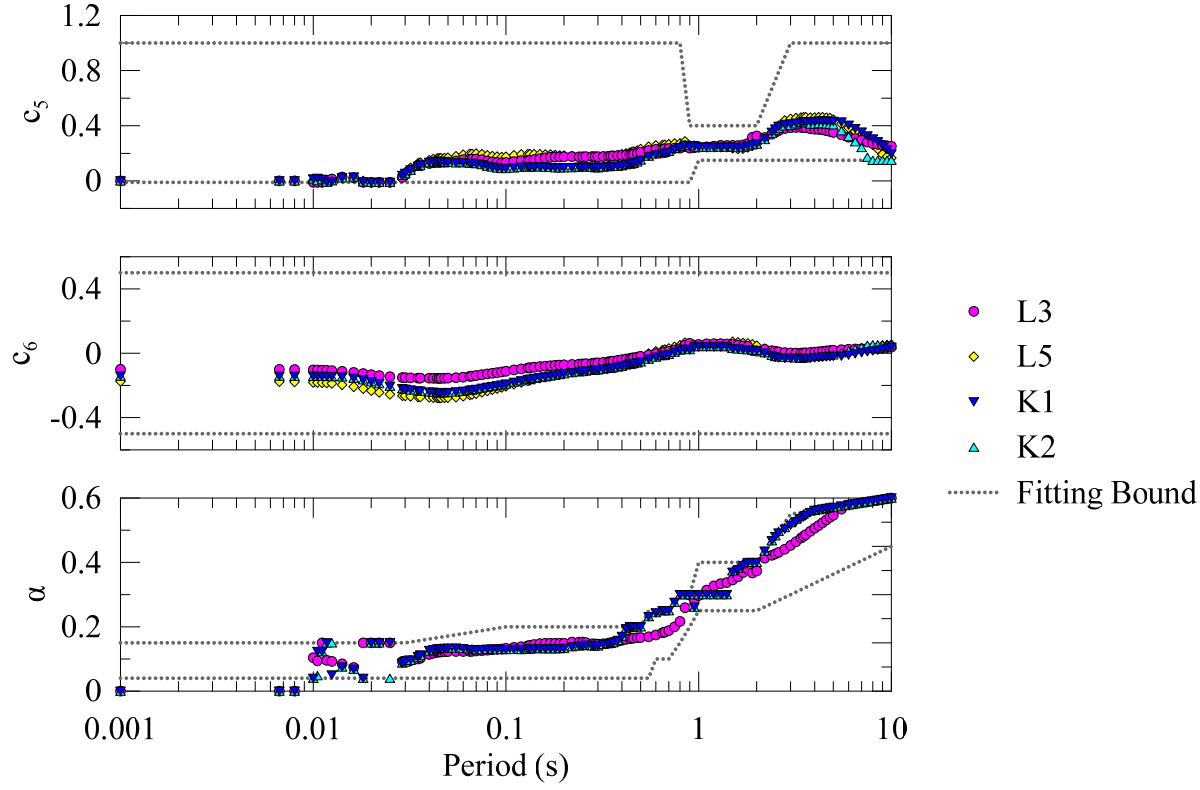

Figure 102: c5, c6, and α coefficient fit of L3, L5, K1, and K2 models with bounds of coefficient fitting

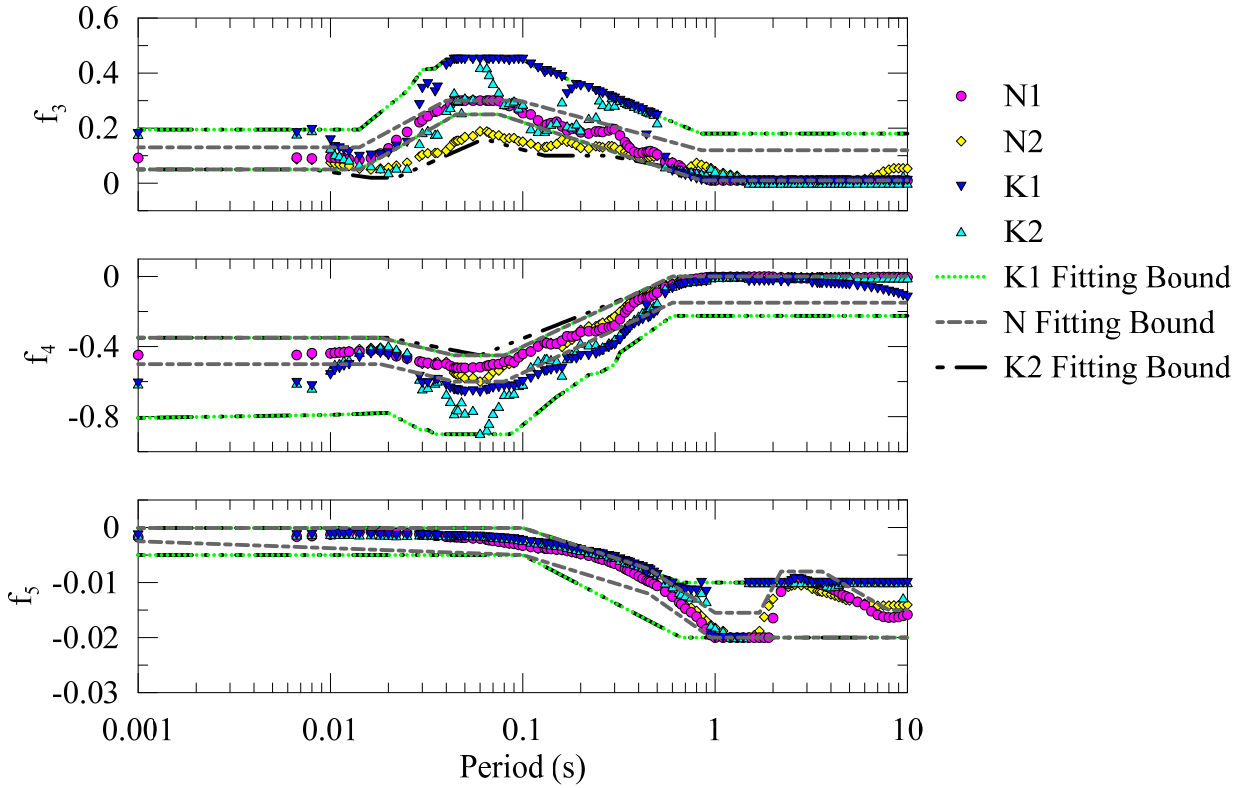

Figure 103: f3, f4, and f5 coefficients for N1, N2, K1, and K2 model terms with bounds of coefficient fitting

APPENDIX E DEPTH DEPENDENT AMPLIFICATION OF 760 M/S V_{S30} SITES

Table 35: Period-dependent values of ln(amp) of linear elastic simulations of simulations with 700 m/s < V_{S30} < 800 m/s as a function of depth. The DI (Depth-Independent) column is the average amplilfication of all simulations with 700 m/s < V_{S30} < 800 m/s.

T (s)	DI Correction	5 m	10 m	15 m	20 m	25 m	30 m	50 m	100 m	50 m	1000 m
0.001	0.822	0.913	0.861	0.838	0.811	0.792	0.773	0.756	0.710	0.466	0.285
0.01	0.728	0.806	0.766	0.760	0.740	0.724	0.708	0.681	0.620	0.321	0.119
0.02	0.662	0.741	0.673	0.750	0.762	0.697	0.671	0.654	0.578	0.116	-0.209
0.03	0.739	0.764	0.751	0.832	0.866	0.850	0.776	0.708	0.652	0.262	-0.069
0.1	1.172	1.480	1.270	1.127	1.013	0.899	0.850	0.731	0.803	0.726	0.588
0.2	0.667	0.630	0.643	0.656	0.678	0.719	0.719	1.090	0.624	0.727	0.629
0.25	0.471	0.423	0.426	0.436	0.448	0.475	0.470	0.832	0.826	0.685	0.600
0.3	0.358	0.307	0.308	0.312	0.325	0.346	0.341	0.622	0.938	0.605	0.561
0.35	0.288	0.238	0.238	0.242	0.253	0.266	0.263	0.476	0.904	0.526	0.569
0.4	0.236	0.188	0.186	0.191	0.200	0.210	0.208	0.386	0.776	0.613	0.494
0.45	0.208	0.163	0.160	0.161	0.167	0.174	0.171	0.319	0.653	0.642	0.524
0.5	0.178	0.138	0.134	0.139	0.143	0.149	0.146	0.255	0.549	0.548	0.529
0.55	0.156	0.122	0.119	0.123	0.128	0.131	0.128	0.222	0.472	0.457	0.466
0.6	0.140	0.108	0.106	0.111	0.116	0.119	0.118	0.196	0.415	0.399	0.422
0.65	0.133	0.104	0.102	0.106	0.110	0.113	0.109	0.178	0.367	0.369	0.440
0.7	0.125	0.096	0.093	0.096	0.099	0.102	0.100	0.166	0.337	0.363	0.485
0.8	0.118	0.088	0.085	0.087	0.091	0.092	0.088	0.143	0.270	0.422	0.543
0.9	0.112	0.083	0.081	0.081	0.085	0.084	0.079	0.125	0.230	0.497	0.490

1	0.106	0.077	0.075	0.075	0.079	0.077	0.074	0.114	0.203	0.576	0.416
2	0.094	0.067	0.066	0.065	0.066	0.064	0.062	0.085	0.123	0.463	0.555
3	0.091	0.069	0.069	0.069	0.071	0.067	0.066	0.089	0.114	0.303	0.509
10	0.094	0.080	0.079	0.078	0.081	0.076	0.072	0.102	0.137	0.256	0.322

APPENDIX F RESPONSE SPECTRAL SITE AMPLIFICATION MODEL ERROR EVALUATION

The linear and nonlinear site amplification modes developed in this study are modular functions intended to be usable with different amounts of site information. If site natural period or depth to weathered rock are available, more advanced model forms for linear (L models) amplification can be used. The nonlinear site amplification models (L+N models and K models) are provided for two different drivers of nonlinearity: PSA and PGA. Of the suite of models provided, only the L5+N1 and K1 models and L5+N2 and K2 models are derived for the same site and motion information (V_{S30}, T_{nat}, and either PSA or PGA, respectively).

The sum of squares error for the linear models L1-L5 is shown in Figure 104. The error is not normalized to the number of degrees of freedom of each of the models and is calculated from the difference between the LE simulations and estimated response from the regressed linear amplification models. The L1 model which only uses V_{S30} as a parameter has the highest error of all other linear models. The effect on total error of adding depth to weathered rock (Z) and T_{nat} to the regressed L1 V_{S30} model is shown in the L2 and L3 lines, respectively in Figure 104. In the range from 0.2 to 0.7 s there is little dependency of the soil column depth on amplification in the L2 model. Above this period range the reduction in model error comes from the increase in site amplification for deeper sites, and below this range, the reduction in model error comes from the reduction in site amplification for deeper sites. The L3 model shows a decrease in model error by including the effects of T_{nat} at all periods from the L1 model. Below 0.1 s the L2 model has lower error than the L3 model, but the L3 model has lower total error at higher periods.

The effect on total error of simultaneously regressing Z and T_{nat} with V_{S30} is shown in the L4 and L5 lines, respectively, in Figure 104. The L4 and L5 models show improvement in total error from the L2 and L3 models, respectively. The model coefficients for the L4 and L5 models are regressed simultaneously instead of sequentially, so improvement in total error at each period is expected. At 3 s, the L5 model has higher error than the L3 model as a result of the resolution of

regression coefficient convergence. For frequencies in the range from 0.2 to 0.7 s, the L4 model shows little improvement to the L1 model in capturing site amplification. Above and below this period range, the L4 model has lower total error than the L1 and L2 models. The L5 model has the lowest total error of all models. The L5 model has lower total error at periods below 0.2 s than all other models. Above 0.2 s, the L5 model has similar total error to the L3 model, but still has lower total error than the L1, L2, and L4 models.

The effects of regressing additional linear models including the effects of V_{S30}, Z, and T_{nat} were additionally evaluated. No significant improvement for the amplification models as a function of V_{S30}, Z, and T_{nat} were observed over the models as a function of just V_{S30} and T_{nat}. The functional form for the T_{nat}-dependent amplification includes not just effects around the natural period (the Riker wavelet component) but also a component of site amplification that scales linearly with T_{nat}. The linear component of the T_{nat} functional form is sufficient to capture the depth-dependent site amplification effects. For model usage, if the V_S profile is available for a site so the depth to weathered rock is known, then the natural period of the site can also be calculated or reasonably estimated from the V_S and depth information. Model coefficients for the combined Z and T_{nat} models are not provided.

The sum of squares error for the purely nonlinear components of the site amplification models (N component of amplification) is shown in Figure 105. The sum of squared error is calculated by comparing the difference between the NL and LE analyses and the regressed N models. The difference between PSA and PGA as the driver of nonlinearity for the N1 and N2 models, respectively, has little effect on the error on the nonlinear component of amplification.

The sum of squares error for the nonlinear amplification models (L+N and K amplification models) is shown in Figure 106. Figure 106(a) shows the nonlinear amplification models using PSA as the driver of nonlinearity (L+N2 and K2 models) and Figure 106(b) shows the nonlinear amplification models using PGA as the driver of nonlinearity. The sum of squares error is calculated from the difference between the NL simulation data and the regressed amplification models. The L+N nonlinear amplification models demonstrate similar trends as the L linear amplification models. The models with the highest error are the models where the linear component is dependent only V_{S30} and the linear component of models with the lowest error are

dependent on V_{S30} and T_{nat} with T_{nat} being more effective than Z when regressed simultaneously with V_{S30}. The similarity in the error of the N1 and N2 amplification models shown in Figure 105 is evidenced in Figure 106 by the similarity between of the L+N amplification models in Figure 106(a) and Figure 106(b), respectively. The error of the K nonlinear amplification models shown in Figure 106 is lower than any of the L+N nonlinear amplification models. The linear and nonlinear model coefficients of the K models are regressed simultaneously, and, as expected, have the lowest total error of all nonlinear amplification models. The K1 and K2 amplification models are shown together in Figure 107. The K2 model using PGA as the driver of nonlinearity has lower total error than the K1 nonlinear amplification model using PSA as the driver of nonlinearity.

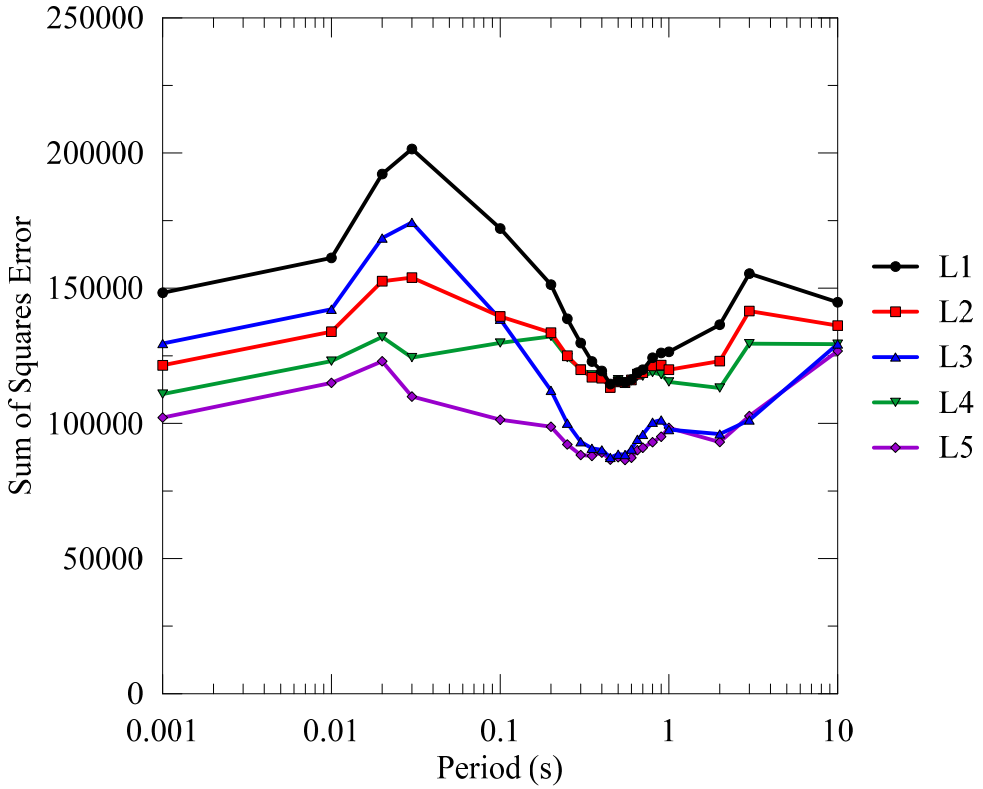

Figure 104: Total sum of squares error for linear site amplification models

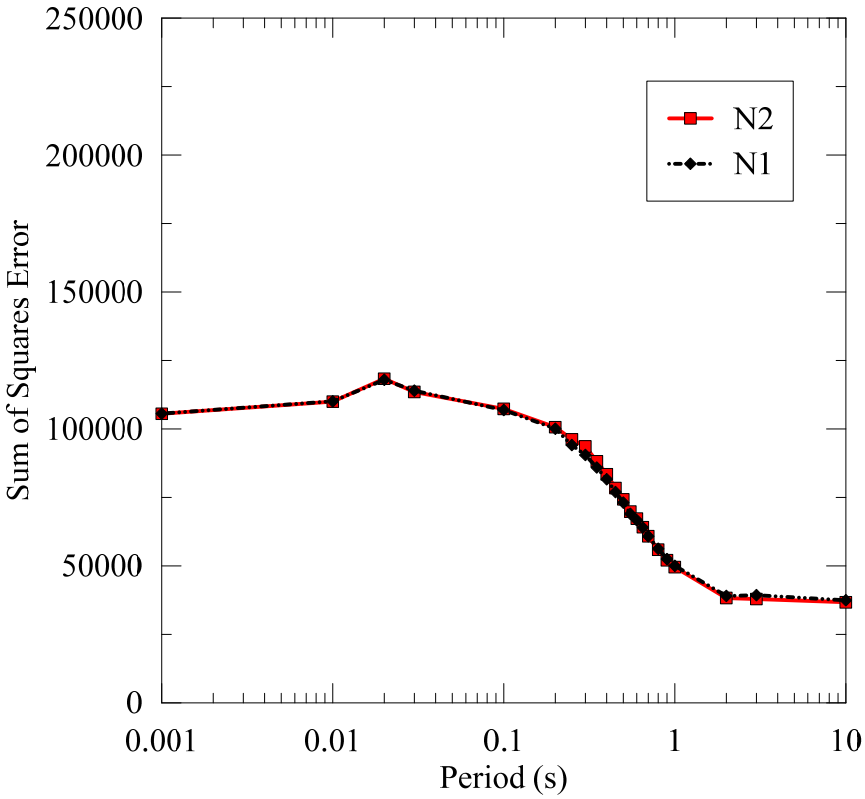

Figure 105: Total sum of squares error for nonlinear site amplification terms (N-Terms)

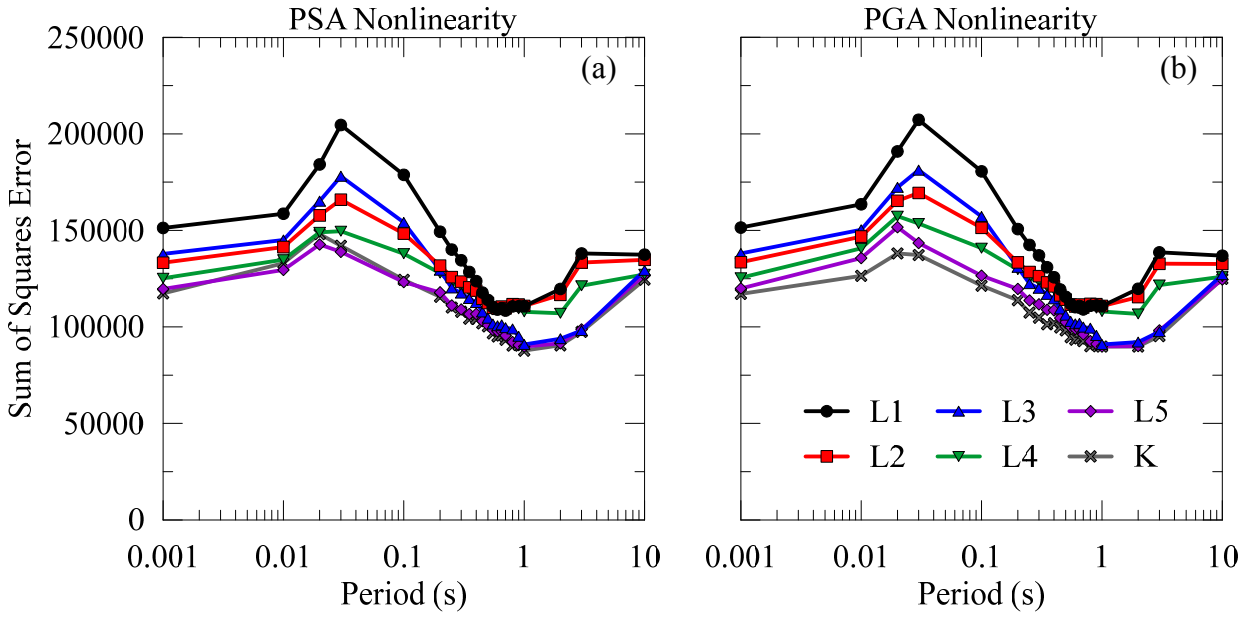

Figure 106: Total sum of squares error for L+N- and K-type nonlinear site amplification models with PSA as the driver of nonlinearity (a) and PGA as the driver of nonlinearity (b)

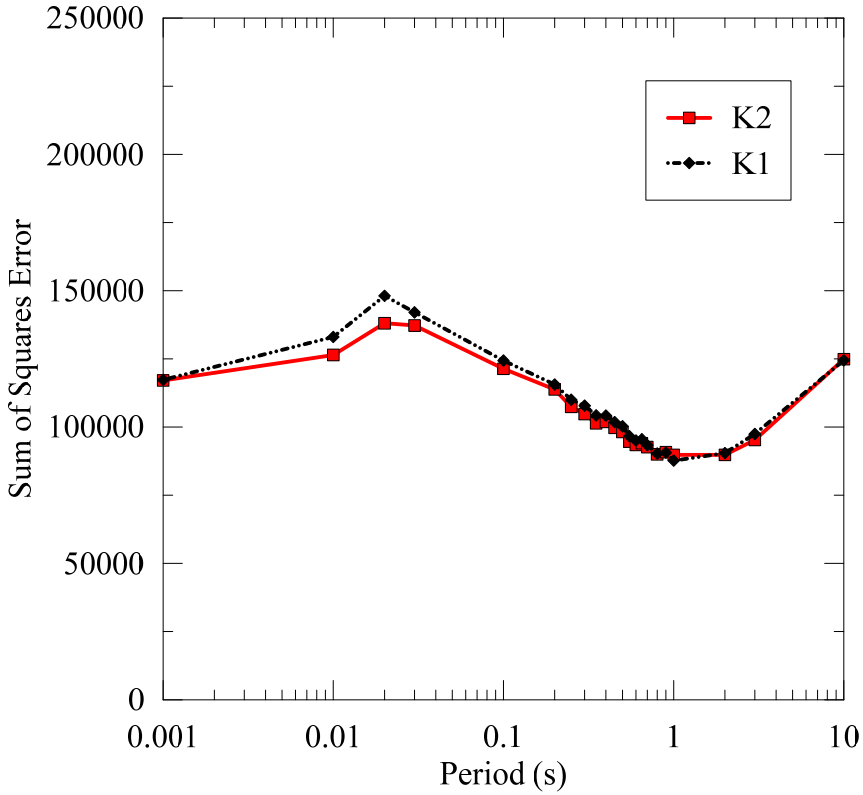

Figure 107: Sum of squares error for K-type nonlinear site amplification models